# Relativistic effects : applications to multiferroic materials

Anant Dixit




**THÈSE DE DOCTORAT**

pour obtenir le titre de

**DOCTEUR EN PHYSIQUE DE LA MATIÈRE CONDENSÉE**

# Relativistic Effects: Applications to Multiferroic Materials

Anant DIXIT

soutenue le 18 décembre, 2015

## Jury

| | | |
|---|---|---|
| Directeurs de thèse | : | Mébarek ALOUANI |
| | : | Giovanni MANFREDI |
| Rapporteurs externes | : | Hubert EBERT |
| | : | Olle ERIKSSON |
| Examinateurs | : | Jean-Yves BIGOT |
| | : | Mattias MARKLUND |

*To Aleksandra, I couldn't have done this without you.*
*Thank you for your support, patience and belief in me all the way!*

*E pur si muove.*

Galileo Galilei

*If it looks like a duck, and quacks like a duck, we have at least to consider the possibility that we have a small aquatic bird of the family anatidae on our hands.*

Douglas Adams

*The history of science shows that theories are perishable. With every new truth that is revealed we get a better understanding of Nature and our conceptions and views are modified.*

Nikola Tesla

# Acknowledgements

This PhD work was carried out between the *Quantum Dynamics of Nano-Objects* (DYNO) group, part of the *Department of Optics and Nano-photonics* (DON), and the *Department of Magnetic Objects on the NanoScale* (DMONS).

I express my sincere gratitude to my thesis supervisors, Prof. Mébarek Alouani and Prof. Giovanni Manfredi, whose patience and advice on numerous occasions, including during many difficult times, enabled me to complete my thesis.

I thank Prof. Jean-Yves Bigot, Prof. Hubert Ebert, Prof. Olle Eriksson and Prof. Mattias Marklund, for participating in the jury of my PhD defence.

I extend my gratitude to Prof. Paul-Antoine Hervieux, Daniel Stoeffler, Yannick Hinschberger, Yves Henry, Omar Morandi, Jens Zamanian, Saber Gueddida, Nathalie Viart and Bohdan Kundys for guiding me and helping me with the thousands of my questions.

I thank Mébarek Alouani, Olivier Bengone and Sébastien Harlepp for helping me with my teaching activities. It was a wonderful experience.

I thank the IT department, especially Christine Tugène, Dominique Quince and Xavier Ledoux for providing technical assistance with many of my calculations. I also thank Véronique Wernher for her support with a lot of my bureaucratic activities.

In addition, I thank Etienne, Ziyad, Jérôme, Michał, Dimitra, Beata, Marwan, Burak, Manuel, Assil, Ufuk, Florian, Wojciech and Filip for the countless discussions on physics and otherwise. Special shout-outs to Michał for helping me understand X-ray spectroscopy techniques from an experimental perspective, and to Etienne for the neodymium magnets.

# Contents

# 1 General Introduction

Relativistic effects play an important role in areas of modern research on condensed matter physics. The interaction of a femtosecond electromagnetic pulse with the electron spin in a ferromagnetic metal has been the object of intense investigations, both theoretical[1,2] and experimental,[3,4] during the past two decades. Experiments have shown the existence of a coherent coupling between a femtosecond laser pulse and the demagnetisation of ferromagnetic thin film.[4] This is clearly distinguished from the demagnetisation associated to thermalisation of the spins. The underlying interaction requires higher order relativistic corrections to be explained accurately.

In molecules and solids, relativistic effects manifest mainly in the form of a spin-orbit coupling (SOC), which lowers the symmetry of a system and lifts energy degeneracies by coupling the spin and orbital degrees of freedom. In this way, the SOC has a profound influence on the electronic structure of magnetic systems giving rise to a variety of effects such as the magneto-optical Kerr effect, Faraday effect and magnetic dichroism.[5] In addition, the inclusion of the SOC in theoretical calculations introduces a scalar product of the spin and orbital moments, which contains the angle between the crystallographic and the magnetisation axis.[6] This gives rise to the phenomenon of the magneto-crystalline anisotropy, the dependence of the total energy on the magnetisation orientation. Relativistic effects also couple the electric and magnetic fields and are responsible for the direct magnetoelectric effects. Together with the magneto-crystalline anisotropy, the SOC can be a major contribution to the indirect magnetoelectric effects as well.

The aim of this thesis is to understand relativistic effects, and use them to study multiferroic materials. In the second chapter, we present a self-consistent model that can describe semi-relativistic electron dynamics in a mean-field approximation, with or without external electromagnetic fields. The self-consistency comes from the single-particle wavefunction depending on the mean-fields, which are themselves described by the Maxwell's equations where the single-particles form the sources. The model was developed through a Lagrangian approach, which allowed us to derive the analytical form of the sources in terms of the single particle wavefunctions.
The third chapter deals with the theoretical tools, namely the density functional theory (DFT) in the projector augmented wave (PAW) basis, used for the *ab initio* calculations of gallium ferrite (GFO) and chromium oxide. A brief description of the LDA+$U$, used to correctly describe the 3$d$ electrons in these materials, and the SOC, used to probe the orbital moments and the magnetoelectric effects, is also provided.
The results of our *ab initio* calculations for GFO are presented in the fourth chapter. Our first task

was to find the value of $U$ that best describes experimental values of the energy band gap and magnetic moments. We then performed cationic site disorder studies to probe the origin of ferrimagnetism in GFO. To understand the magnetic order of the $3d$ orbitals in GFO, we present our implementation of the crystal-field analysis and our results analysed with a point-charge model. Then we show and discuss our results for the calculations of the temperature dependent electric polarisation are discussed. Towards the end of the chapter, we present our results for the direct magnetoelectric effect in GFO.
The fifth chapter is dedicated to our *ab initio* results of chromium oxide. Like with GFO, we first performed simulations to find the value of $U$ that best reproduces the experimental results of the energy band gap and the magnetic moments. To mimic the experimental conditions of $Cr_2O_3$ embedded in MgO, calculations with biaxial compressive strains were done with the intention of studying the origin of ferromagnetism and ferroelectricity in the system. Our results of bulk $Cr_2O_3$ failed to reproduce the experimental results, indicating that perhaps size and surface effects are responsible for the observed magnetoelectric behaviour.
In the sixth chapter we present our implementation of the computation of the x-ray absorption spectra (XAS) and the x-ray magnetic circular dichroism (XMCD). This was done in the dipole approximation using both the momentum and the position operators. After discussing the theory and implementation details, our results for two test cases, Fe L-edges and Fe K-edge, are shown. We then applied the method to calculate the XAS and XMCD at the $L_{2,3}$-edges of Fe in GFO. We end the thesis with general conclusions and perspectives.

# 2 Lagrangian Approach to Semi-Relativistic Electron Dynamics

## Contents



## 2.1 Introduction

In the latest technological developments, relativistic effects play an important role. These developments include, and are not limited to, multiferroic materials, femto-second lasers and spintronic devices. In all these cases, the influence of external electromagnetic fields on different materials has been very crucial to understanding their behaviour under realistic situations. For example, one can control the magnetisation in magnetoelectric materials with external electric fields.[7] In addition, the

interaction of a femto-second electromagnetic pulse with the electron spin in a ferromagnetic metal has been the subject of much research, both theoretical[1,2,8] and experimental.[3,4,9,10] At the same time, relativistic corrections are taken into account in quantum chemistry, particularly for heavy elements.[11] As is described in Section 3.3, there are also relativistic versions of density functional theory.[12]

In this chapter, we present a time-dependent semi-relativistic mean-field model[13] that is based on two-component wavefunctions (spinors), and thus considerable more tractable than the four-component bispinors relying on the fully-relativistic Dirac equation. The mean-fields used in the model are described using the Maxwell's equations and can be trivially extended to include external fields. The model is developed with an intention to preserve the mathematical structure of the Schrödinger and Kohn-Sham equations, which have been implemented in many numerical codes, so that these implementations can be extended to include semi-relativistic mean-field and external field effects.

We begin with the fully-relativistic many-electron ($N$ electrons) Dirac equation under the Born-Oppenheimer approximation,[14–16] where the ionic motion are considered classical and decoupled from the electron motion, and the mean-field approach, where the electron-electron interaction on a given electron is replaced by an effective field generated by the *other* electrons, given by,

$$i\hbar\frac{\partial\Psi_D^i}{\partial t} = c\boldsymbol{\alpha}\cdot(\hat{\boldsymbol{p}} - q\boldsymbol{A})\Psi_D^i + \beta mc^2\Psi_D^i + q\phi\Psi_D^i, \tag{2.1}$$

where, $A^\mu = (\phi/c, \boldsymbol{A})$ is the four-vector potential (mean-field potential) with the scalar potential $\phi$ and vector potential $\boldsymbol{A}$ described by the Maxwell's equations under the minimal coupling, $\hat{\boldsymbol{p}} \to \hat{\boldsymbol{p}} - q\boldsymbol{A}$ and $i\hbar\partial_t \to i\hbar\partial t - q\phi$, where $\partial_\mu = \frac{\partial}{\partial x^\mu}$. For simplicity, we work in the Lorentz gauge,

$$\boldsymbol{\nabla}\cdot\boldsymbol{A} + \frac{\partial\phi}{c^2\partial t} = 0, \tag{2.2}$$

where the Maxwell's equations can be written as,

$$\begin{aligned} -\Delta\phi + \frac{1}{c^2}\frac{\partial^2\phi}{\partial t^2} &= \frac{q\rho}{\varepsilon_0}, \\ -\Delta\boldsymbol{A} + \frac{1}{c^2}\frac{\partial^2\boldsymbol{A}}{\partial t^2} &= \mu_0 q\boldsymbol{j}, \end{aligned} \tag{2.3}$$

and the sources are given by the Dirac four-current as,

$$J^\mu = (c\rho, \boldsymbol{j}) = c\sum_i^N \left(\Psi_D^{i\dagger}\Psi_D^i,\ \Psi_D^{i\dagger}\boldsymbol{\alpha}\Psi_D^i\right). \tag{2.4}$$

Here, $\Psi_D^i$ represents the four-component Dirac bispinor for the $i^{\text{th}}$ electron, $m$ and $q$ are the particle rest mass and charge (for electrons, $m = m_e$ and $q = -e$), $\varepsilon_0$ and $\mu_0$ are the electric permittivity and magnetic permeability in vacuum ($\varepsilon_0\mu_0c^2 = 1$), $c$ is the speed of light in vacuum, $\hbar$ is the Planck constant, $\rho$ is the probability density, and $\boldsymbol{j}$ is the probability current. $\boldsymbol{\alpha}$ and $\beta$ are the $4\times4$ Dirac matrices expressed as,

$$\begin{aligned} \boldsymbol{\alpha} &= \begin{pmatrix} 0 & \boldsymbol{\sigma} \\ \boldsymbol{\sigma} & 0 \end{pmatrix}, \\ \beta &= \begin{pmatrix} \mathbf{I}_2 & 0 \\ 0 & \mathbf{I}_2 \end{pmatrix}, \end{aligned} \tag{2.5}$$

where, $\boldsymbol{\sigma}$ are the Pauli matrices defined as:

$$\sigma_x = \begin{pmatrix} 0 & 1 \\ 1 & 0 \end{pmatrix}; \qquad \sigma_y = \begin{pmatrix} 0 & -i \\ i & 0 \end{pmatrix}; \qquad \sigma_z = \begin{pmatrix} 1 & 0 \\ 0 & -1 \end{pmatrix}; \tag{2.6}$$

and $\mathbf{I}_2$ is a $2 \times 2$ identity matrix. Equations 2.1-2.4 constitute a fully-relativistic, Lorentz-invariant model for the quantum dynamics of a system of $N$ electrons in the mean-field generated by these electrons. However, these equations couple the particle and anti-particle states of the Dirac bispinor through the $\boldsymbol{\alpha}$ matrices, which have off-diagonal terms. To develop a low-energy semi-relativistic limit, where only the electrons are considered as two-component spinors, one must perform semi-relativistic expansions in powers of $1/c$. Our model was developed up to second order in $1/c$, using the Foldy-Wouthuysen transformation[17–19] described in the following section.

## 2.2 Foldy-Wouthuysen Transformation

The Foldy-Wouthuysen transformation was formulated by Foldy and Wouthuysen[17] to investigate the non-relativistic and semi-relativistic limits of the Dirac equation. This transformation uses the Hadamard Lemma which, for an operator $\hat{Q}$ and a unitary transformation $S$: $\widetilde{\Psi} = e^{iS}\Psi$, is given by:

$$\begin{aligned} e^{iS}\hat{Q}e^{-iS} =& \hat{Q} + i[S,\hat{Q}] + \frac{i^2}{2!}[S,[S,\hat{Q}]] + \frac{i^3}{3!}[S,[S,[S,\hat{Q}]]] + \cdots \\ & - \left(\dot{S} + \frac{i}{2!}[S,\dot{S}] + \frac{i^2}{3!}[S,[S,\dot{S}]] + \cdots\right). \end{aligned} \tag{2.7}$$

To reach the non-relativistic and semi-relativistic limits of the Dirac equation, we have to 'push' the coupling of the particle and anti-particle states to higher orders in $1/c$. For that purpose, it is useful to term operators that couple the upper and lower energy states as *odd* operators and operators that do not couple the energy states as *even* operators. Thus, in Eq. 2.1 the operator $\hat{O} = c\boldsymbol{\alpha}\cdot(\hat{\boldsymbol{p}} - q\boldsymbol{A})$ is an odd operator and the remaining terms are even operators.

To eliminate odd operators up to the zeroth order (non-relativistic limit) in $1/c$, the unitary transformation $S$ is done with $\widetilde{\Psi} = e^{iS}\Psi$ and $\widetilde{H} = e^{iS}(\hat{H} - i\hbar\partial_t)e^{-iS}$, such that $i[S,\beta mc^2] = -\hat{O}$ to ensure the presence of only even operators up to this order. It can be seen that $S = \frac{-i\beta\hat{O}}{2mc^2}$ satisfies this condition. Using the Hadamard Lemma (Eq. 2.7) and keeping only the zeroth order terms in $1/c$, we get,

$$\widetilde{H} = \hat{H} + i[S,\hat{H}] + \frac{i^2}{2!}[S,[S,\hat{H}]], \tag{2.8}$$

which on further simplification gives us,

$$\widetilde{H} = \beta mc^2 + q\phi + \frac{i}{2}[S,\hat{O}]. \tag{2.9}$$

Using the definition of $S$ and the fact that $\beta$ anticommutes with the $\boldsymbol{\alpha}$ matrices, and hence with $\hat{O}$, we get,

$$\widetilde{H} = \beta mc^2 + q\phi + \frac{\beta\hat{O}^2}{2mc^2}, \tag{2.10}$$

where the term $\frac{\hat{O}^2}{c^2}$ can be simplified as,

$$\begin{aligned}\frac{\hat{O}^2}{c^2} &= (\boldsymbol{\alpha}\cdot(\hat{\boldsymbol{p}}-q\boldsymbol{A}))(\boldsymbol{\alpha}\cdot(\hat{\boldsymbol{p}}-q\boldsymbol{A})) \\ &= \sum_i \alpha_i^2(\hat{p}_i - qA_i)^2 + \sum_{i\neq j}\alpha_i\alpha_j(\hat{p}_i-qA_i)(\hat{p}_j-qA_j) \\ &= (\hat{\boldsymbol{p}}-q\boldsymbol{A})^2 + \frac{1}{2}\sum_{i\neq j}(\alpha_i\alpha_j-\alpha_j\alpha_i)(\hat{p}_i-qA_i)(\hat{p}_j-qA_j) \\ &= (\hat{\boldsymbol{p}}-q\boldsymbol{A})^2 + \frac{1}{2}\sum_{i\neq j}\alpha_i\alpha_j[(\hat{p}_i-qA_i),(\hat{p}_j-qA_j)],\end{aligned} \tag{2.11}$$

where, the identities $\alpha_i^2 = 1$ and $\alpha_i\alpha_j + \alpha_j\alpha_i = 0$, and a change of indexes (in the last step) were used to reach the final result. Now, $\alpha_i\alpha_j = i\epsilon_{ijk}\Sigma_k$, where $\epsilon_{ijk}$ is the completely anti-symmetric Levi-Civita tensor (eqal to $+1$ for even permutations of $ijk$, $-1$ for odd permutations, and 0 if any index is repeated) and $\boldsymbol{\Sigma}$ is the four-component spin matrix with $\boldsymbol{S} = \frac{\hbar}{2}\boldsymbol{\Sigma}$ as the spin operator acting on four-component bispinors. Further, the commutator can be simplified as $iq\hbar\,(\partial_i A_j - \partial_j A_i)$ and thus,

$$\begin{aligned}\sum_{i\neq j}\alpha_i\alpha_j[(\hat{p}_i-qA_i),(\hat{p}_j-qA_j)] &= -q\hbar\sum_{i\neq j}\epsilon_{ijk}\Sigma_k\,(\partial_i A_j - \partial_j A_i) \\ &= -2q\hbar\Sigma_k\sum_{i\neq j}\epsilon_{ijk}\partial_i A_j \\ &= -2q\hbar\Sigma_k(\boldsymbol{\nabla}\times\boldsymbol{A})_k = -2q\hbar\boldsymbol{\Sigma}\cdot\boldsymbol{B},\end{aligned} \tag{2.12}$$

where $\boldsymbol{B} = \boldsymbol{\nabla}\times\boldsymbol{A}$ is the magnetic field. Thus, the Hamiltonian becomes,

$$\widetilde{H} = \beta mc^2 + \frac{\beta}{2m}(\hat{\boldsymbol{p}}-q\boldsymbol{A})^2 + q\phi - \frac{\beta q\hbar}{2m}\boldsymbol{\Sigma}\cdot\boldsymbol{B}, \tag{2.13}$$

which for positive energy states (only particles), i.e. $\beta = \mathbf{I}_2$, gives,

$$\widetilde{H} = mc^2 + \frac{1}{2m}(\hat{\boldsymbol{p}}-q\boldsymbol{A})^2 + q\phi - \frac{q\hbar}{2m}\boldsymbol{\sigma}\cdot\boldsymbol{B}. \tag{2.14}$$

This is the non-relativistic Schrödinger equation with a spin term, also known as the Pauli equation. This spin term describes the electron spins coupled to a magnetic field $\boldsymbol{B}$. In the mean-field picture, the electron spins themselves would generate the field. However, in the case of external electromagnetic fields $(\phi_{\text{external}}/c, \boldsymbol{A}_{\text{external}})$ as well, the term would be present and thus this Hamiltonian can be applied for self-generated mean-fields and external fields. The advantage of the Foldy-Wouthuysen transformation is that the order of expansion can be controlled as desired. We use it to perform an expansion up to second order in $1/c$, the derivation of which follows closely to that performed by Foldy and Wouthuysen,[17] and recently expanded to higher orders by Hinschberger and Hervieux.[19] Since these two works use an expansion of $1/m$ rather than $1/c$, an independent derivation up to the second order in $1/c$ is provided in Appendix A, and the second order Hamiltonian is given below:

$$\begin{aligned}\hat{H} =& mc^2 + q\phi + \frac{(\hat{\boldsymbol{p}}-q\boldsymbol{A})^2}{2m} - \frac{q\hbar}{2m}\boldsymbol{\sigma}\cdot\boldsymbol{B} - \frac{(\hat{\boldsymbol{p}}-q\boldsymbol{A})^4}{8m^3c^2} - \frac{q\hbar^2}{8m^2c^2}\boldsymbol{\nabla}\cdot\boldsymbol{E} \\ &- \frac{q\hbar}{8m^2c^2}\boldsymbol{\sigma}\cdot\left[\boldsymbol{E}\times(\hat{\boldsymbol{p}}-q\boldsymbol{A}) - (\hat{\boldsymbol{p}}-q\boldsymbol{A})\times\boldsymbol{E}\right],\end{aligned} \tag{2.15}$$

which we term as the *extended* Pauli equation and where, the electromagnetic fields are defined as usual as $\boldsymbol{E} = -\boldsymbol{\nabla}\phi - \partial_t \boldsymbol{A}$ and $\boldsymbol{B} = \boldsymbol{\nabla} \times \boldsymbol{A}$. Here, the first term on the right-hand side is the rest-mass energy of the electron, the next two terms are the standard Schrödinger Hamiltonian in presence of an electromagnetic field $(\phi/c, \boldsymbol{A})$ with minimal coupling, the fourth term is the Pauli spin term (Zeeman effect), also present in the zeroth order expansion (Eq. 2.14), the fifth term $(\hat{\boldsymbol{p}} - q\boldsymbol{A})^4$ is the first relativistic correction to the electron mass (expansion of the Lorentz factor $\gamma$ up to second order), the $\boldsymbol{\nabla} \cdot \boldsymbol{E}$ is the Darwin term and the last two terms represent the spin-orbit coupling (SOC). In this scheme so far, the electromagnetic fields (mean-field) are generated by the electrons themselves as described in the Maxwell's equations in the Lorentz gauge (Eq. 2.3). The sources of the fields, the density and current density, in the fully-relativistic case are given by Eq. 2.4, which should also be expanded up to the second order in $1/c$, since the wavefunctions were transformed as well through the transformation $S$ as $\tilde{\Psi} = e^{iS}\Psi$. In principle one could expand the exponential, and obtain the density and current density up to second order in $1/c$. However, we use the Lagrangian formalism to couple the Maxwell's equations and the extended Pauli equation, and obtain the sources directly from the equations of motions obtained through the Euler-Lagrange equations. This is developed in further detail in the subsequent section.

## 2.3 Lagrangian Approach

The purpose of the present chapter is to develop a semi-relativistic self-consistent dynamic model coupling the electromagnetic fields, described by the Maxwell's equations, and the electron states, described by the extended Pauli Hamiltonian. The advantage of the Lagrangian approach is that self-consistency can be incorporated in the model simply by constructing a Lagrangian density that is the sum of the Lagrangian densities corresponding to the extended Pauli equation, $\mathcal{L}_P$, and the electromagnetic fields, $\mathcal{L}_{\mathrm{EM}}$. To find $\mathcal{L}_P$, we begin by rewriting the extended Pauli equation (Eq. 2.15) in terms of the scalar and vector potentials, where the operators act only on the terms to their immediate right and the relativistic correction term, $(\hat{\boldsymbol{p}} - q\boldsymbol{A})^4$, is neglected,

$$\begin{aligned}\hat{H} = mc^2 + q\phi + \frac{(\hat{\boldsymbol{p}} - q\boldsymbol{A})^2}{2m} - \frac{q\hbar}{2m}\boldsymbol{\sigma} \cdot (\boldsymbol{\nabla} \times \boldsymbol{A}) + \frac{q\hbar^2}{8m^2c^2}\Delta\phi + \frac{q\hbar^2}{8m^2c^2}\boldsymbol{\nabla} \cdot \partial_t \boldsymbol{A} \\ + \frac{q\hbar}{4m^2c^2}\boldsymbol{\sigma} \cdot [(\boldsymbol{\nabla}\phi + \partial_t \boldsymbol{A}) \times (\hat{\boldsymbol{p}} - q\boldsymbol{A})] - \frac{q\hbar}{8m^2c^2}\boldsymbol{\sigma} \cdot (\hat{\boldsymbol{p}} \times \partial_t \boldsymbol{A}).\end{aligned} \tag{2.16}$$

The relativistic correction term, though second order in $1/c$, introduces fourth order derivatives in the evolution equation, unlike the other terms, which only contain derivatives up to second order. Nevertheless, a Lagrangian density and the corresponding corrections for this term can be found, as shown in Section 2.7. The resulting extended Pauli equation,

$$i\hbar\partial_t \Psi = \hat{H}\Psi, \tag{2.17}$$

can be derived from a Lagrangian density, $\mathcal{L}_P$, by applying the Euler-Lagrange equations. There are at least two forms of the Lagrangian density,

$$\mathcal{L}_P = \frac{1}{2}\Psi^\dagger \left[(i\hbar\partial_t - \hat{H})\Psi\right] + \frac{1}{2}\left[(-i\hbar\partial_t - \hat{H}^\dagger)\Psi^\dagger\right]\Psi, \tag{2.18}$$

$$\mathcal{L}_P = \Psi^\dagger(i\hbar\partial_t - \hat{H})\Psi, \tag{2.19}$$

which yield the same extended Pauli equation. Moreover, terms like $(\hat{\boldsymbol{p}} - q\boldsymbol{A})^2$ can be included as $\left[(\hat{\boldsymbol{p}} - q\boldsymbol{A})^\dagger \Psi^\dagger\right] \left[(\hat{\boldsymbol{p}} - q\boldsymbol{A})\Psi\right]$. The Lagrangian density we propose is based on a combination of the above forms and is defined as,

$$\begin{aligned}\mathcal{L}_P =& \frac{i\hbar}{2}\left(\Psi^\dagger\dot{\Psi} - \dot{\Psi}^\dagger\Psi\right) - \Psi^\dagger(mc^2 + q\phi)\Psi - \frac{1}{2m}\left[(i\hbar\partial_k - qA_k)\Psi^\dagger(-i\hbar\partial_k - qA_k)\Psi\right] \\ &+ \Psi^\dagger\left[\frac{q\hbar}{2m}\epsilon_{ijk}\sigma_i\partial_j A_k - \frac{q\hbar^2}{8m^2c^2}\partial_k^2\phi - \frac{q\hbar^2}{8m^2c^2}\partial_t\partial_k A_k\right]\Psi \\ &+ \Psi^\dagger\epsilon_{ijk}\left[\frac{q\hbar}{4m^2c^2}\sigma_i\partial_j\phi q A_k + \frac{q\hbar}{4m^2c^2}\sigma_i\partial_t A_j q A_k\right]\Psi \\ &- \frac{q\hbar}{8m^2c^2}\epsilon_{ijk}\left[(\Psi^\dagger\sigma_i\partial_j\phi\hat{p}_k\Psi - \partial_j\phi\hat{p}_k\Psi^\dagger\sigma_i\Psi) + (\Psi^\dagger\sigma_i\partial_t A_j\hat{p}_k\Psi - \partial_t A_j\hat{p}_k\Psi^\dagger\sigma_i\Psi)\right].\end{aligned} \tag{2.20}$$

Here, we have assumed the Einstein summation convention, where a repetition of an index implies a summation over the index. An additional point to note is that the electron index and the summation over the different electrons have been dropped for simplicity of notation. The Lagrangian density indeed returns the extended Pauli equation and its Hermitian conjugate form when the Euler-Lagrange equations with respect to variations in $\Psi^\dagger$ and $\Psi$, a proof of which is shown in Appendix B.

The Lagrangian density for the electromagnetic fields in the Lorentz gauge is given by,

$$\mathcal{L}_{\text{EM}} = \frac{\varepsilon_0}{2}(\partial_k\phi)^2 - \frac{\varepsilon_0}{2c^2}(\partial_t\phi)^2 - \frac{1}{2\mu_0}(\partial_j A_k)^2 + \frac{1}{2\mu_0 c^2}(\partial_t A_k)^2, \tag{2.21}$$

and the total Lagrangian density $\mathcal{L}(\Psi, \Psi^\dagger, \phi, \boldsymbol{A})$, i.e. particles and fields, is then,

$$\begin{aligned}\mathcal{L} =& \mathcal{L}_P + \mathcal{L}_{\text{EM}} \\ =& \frac{i\hbar}{2}\left(\Psi^\dagger\dot{\Psi} - \dot{\Psi}^\dagger\Psi\right) - \Psi^\dagger(mc^2 + q\phi)\Psi - \frac{1}{2m}\left[(i\hbar\partial_k - qA_k)\Psi^\dagger(-i\hbar\partial_k - qA_k)\Psi\right] \\ &+ \Psi^\dagger\left[\frac{q\hbar}{2m}\epsilon_{ijk}\sigma_i\partial_j A_k - \frac{q\hbar^2}{8m^2c^2}\partial_k^2\phi - \frac{q\hbar^2}{8m^2c^2}\partial_t\partial_k A_k\right]\Psi \\ &+ \Psi^\dagger\epsilon_{ijk}\left[\frac{q\hbar}{4m^2c^2}\sigma_i\partial_j\phi q A_k + \frac{q\hbar}{4m^2c^2}\sigma_i\partial_t A_j q A_k\right]\Psi \\ &- \frac{q\hbar}{8m^2c^2}\epsilon_{ijk}\left[(\Psi^\dagger\sigma_i\partial_j\phi\hat{p}_k\Psi - \partial_j\phi\hat{p}_k\Psi^\dagger\sigma_i\Psi) + (\Psi^\dagger\sigma_i\partial_t A_j\hat{p}_k\Psi - \partial_t A_j\hat{p}_k\Psi^\dagger\sigma_i\Psi)\right] \\ &+ \frac{\varepsilon_0}{2}(\partial_k\phi)^2 - \frac{\varepsilon_0}{2c^2}(\partial_t\phi)^2 - \frac{1}{2\mu_0}(\partial_j A_k)^2 + \frac{1}{2\mu_0 c^2}(\partial_t A_k)^2.\end{aligned} \tag{2.22}$$

By taking the Euler-Lagrange equations with respect to the scalar and vector potentials, we obtain the Maxwell's equations (Eq. 2.3), with certain, yet undetermined, expressions on the right-hand side of the equations, which can be identified as the density and current density of the our system, the dynamics of which are governed by the extended Pauli equation. Thus, we have a systematic and straightforward method to obtain the second order relativistic corrections to the non-relativistic expressions of the density and current density. The Euler-Lagrange equation for a Lagrangian density depending on up to the second derivatives of a field $\varphi$, is:[20,21]

$$\frac{\partial\mathcal{L}}{\partial\varphi} - \sum_\mu \partial_\mu\frac{\partial\mathcal{L}}{\partial(\partial_\mu\varphi)} + \sum_\mu \partial_\mu^2\frac{\partial\mathcal{L}}{\partial(\partial_\mu^2\varphi)} + \sum_{\substack{\mu,\nu \\ \mu\neq\nu}} \partial_\mu\partial_\nu\frac{\partial\mathcal{L}}{\partial(\partial_\mu\partial_\nu\varphi)} = 0, \tag{2.23}$$

where the Greek subscripts $\mu$ and $\nu$ denote the space-time coordinates $(ct, x, y, z)$ and the field $\varphi$ for the Lagrangian $\mathcal{L}(\Psi, \Psi^\dagger, \phi, \boldsymbol{A})$ is either the scalar potential $\phi$, one Cartesian component of the vector potential $A_k$, the electron wavefunction $\Psi$ or its Hermitian conjugate $\Psi^\dagger$. The first two terms in Eq. 2.23 are the standard ones for a Lagrangian that depends only on the first derivatives. This general form of the Euler-Lagrange equation is required for our system since we encounter mixed derivatives up to second order.

As mentioned earlier, one could obtain the sources (density and current) for the Maxwell's equations by applying the Foldy-Wouthuysen transformations on the Dirac four-current (Eq. 2.4), a procedure which would be mathematically complicated. Here, we show that the correct results can be obtained by means of the Lagrangian approach outlined above. As we shall see, the obtained sources contain several terms beyond the result of the standard relativistic density functional theory.[22]

### 2.3.1 Probability Density

To compute the probability density, we compute each term appearing in the Euler-Lagrange equation (Eq. 2.23), with the scalar potential $\phi$ as the field variable. Thus,

$$\begin{aligned}
\frac{\partial \mathcal{L}}{\partial \phi} &= -q\Psi^\dagger\Psi, \\
\partial_t \frac{\partial \mathcal{L}}{\partial(\partial_t \phi)} &= -\frac{\varepsilon_0}{c^2}\partial_t^2 \phi, \\
\partial_j \frac{\partial \mathcal{L}}{\partial(\partial_j \phi)} &= \partial_j \left\{ \frac{q\hbar}{4m^2c^2}\left[q\boldsymbol{A} \times (\Psi^\dagger \boldsymbol{\sigma}\Psi)\right]_j - \frac{iq\hbar^2}{8m^2c^2}\left[(\boldsymbol{\nabla}\Psi^\dagger)\times\boldsymbol{\sigma}\Psi + \Psi^\dagger\boldsymbol{\sigma}\times(\boldsymbol{\nabla}\Psi)\right]_j + \varepsilon_0 \partial_j \phi \right\}, \\
\partial_j^2 \frac{\partial \mathcal{L}}{\partial(\partial_j^2 \phi)} &= -\frac{q\hbar^2}{8m^2c^2}\Delta(\Psi^\dagger\Psi).
\end{aligned}$$

Combining these terms together and rearranging for comparison with the Maxwell's equation for $\phi$ (Eq. 2.3) gives us,

$$\begin{aligned}
-\varepsilon_0\Delta\phi + \frac{\varepsilon_0}{c^2}\partial_t^2\phi &= q\rho \\
&= q\Psi^\dagger\Psi + \frac{q\hbar}{4m^2c^2}\boldsymbol{\nabla}\cdot\left[\frac{q}{m}\boldsymbol{A}\times(\Psi^\dagger\boldsymbol{\sigma}\Psi) - \frac{i\hbar}{2m}\{(\boldsymbol{\nabla}\Psi^\dagger)\times\boldsymbol{\sigma}\Psi + \Psi^\dagger\boldsymbol{\sigma}\times(\boldsymbol{\nabla}\Psi)\}\right] \\
&\quad + \frac{q\hbar^2}{8m^2c^2}\Delta(\Psi^\dagger\Psi),
\end{aligned} \tag{2.24}$$

which allows us to define the probability density as,

$$\begin{aligned}
\rho = \Psi^\dagger\Psi &+ \frac{\hbar}{4mc^2}\boldsymbol{\nabla}\cdot\left[\frac{q}{m}\boldsymbol{A}\times(\Psi^\dagger\boldsymbol{\sigma}\Psi) - \frac{i\hbar}{2m}\left\{(\boldsymbol{\nabla}\Psi^\dagger)\times\boldsymbol{\sigma}\Psi + \Psi^\dagger\boldsymbol{\sigma}\times(\boldsymbol{\nabla}\Psi)\right\}\right] \\
&+ \frac{\hbar}{4mc^2}\boldsymbol{\nabla}\cdot\left[\frac{\hbar}{2m}\boldsymbol{\nabla}(\Psi^\dagger\Psi)\right].
\end{aligned} \tag{2.25}$$

At zeroth order in $1/c$, we recover the standard Schrödinger or Pauli density $\Psi^\dagger\Psi$. Furthermore, all corrections at second order can be written as the divergence of a vector $\boldsymbol{P}/q$, which can be interpreted as a polarisation density. The physical interpretations of the different contributions to this term is discussed in Section 2.4.

### 2.3.2 Probability Current Density

In order to obtain the expression of the probability current density, we compute the Euler-Lagrange, Eq. 2.23, for the $k^{\text{th}}$ component of the vector potential $A_k$. This yields,

$$\begin{aligned}
\frac{\partial \mathcal{L}}{\partial A_k} &= \frac{iq\hbar}{2m}\left[(\boldsymbol{\nabla}\Psi^\dagger)\Psi - \Psi^\dagger(\boldsymbol{\nabla}\Psi)\right]_k - \frac{q^2}{m}A_k\Psi^\dagger\Psi - \frac{q^2\hbar}{4m^2c^2}\left[(\boldsymbol{\nabla}\phi + \partial_t\boldsymbol{A})\times(\Psi^\dagger\boldsymbol{\sigma}\Psi)\right]_k, \\
\partial_t\frac{\partial \mathcal{L}}{\partial(\partial_t A_k)} &= \frac{q^2\hbar}{4m^2c^2}\partial_t\left[\boldsymbol{A}\times(\Psi^\dagger\boldsymbol{\sigma}\Psi)\right]_k - \frac{qi\hbar^2}{8m^2c^2}\partial_t\left[(\boldsymbol{\nabla}\Psi^\dagger)\times\boldsymbol{\sigma}\Psi + \Psi^\dagger\boldsymbol{\sigma}\times(\boldsymbol{\nabla}\Psi)\right]_k + \frac{1}{\mu_0 c^2}\partial_t^2 A_k, \\
\partial_j\frac{\partial \mathcal{L}}{\partial(\partial_j A_k)} &= \frac{q\hbar}{2m}\epsilon_{ijk}\partial_j(\Psi^\dagger\sigma_i\Psi) - \frac{1}{\mu_0}\partial_j^2 A_k, \\
\partial_t\partial_j\frac{\partial \mathcal{L}}{\partial(\partial_t\partial_j A_k)} &= -\frac{q\hbar^2}{8m^2c^2}\partial_t\partial_j(\delta_{jk}\Psi^\dagger\Psi) = -\partial_t\partial_k(\Psi^\dagger\Psi),
\end{aligned}$$

which on combining and rearranging in the form of the Maxwell's equation for $\boldsymbol{A}$ (Eq. 2.3) gives,

$$\begin{aligned}
\frac{1}{\mu_0 c^2}\partial_t^2\boldsymbol{A} - \frac{1}{\mu_0}\Delta\boldsymbol{A} = {} & \frac{iq\hbar}{2m}\left[(\boldsymbol{\nabla}\Psi^\dagger)\Psi - \Psi^\dagger(\boldsymbol{\nabla}\Psi)\right] - \frac{q^2}{m}\boldsymbol{A}\Psi^\dagger\Psi - \frac{q^2\hbar}{4m^2c^2}\partial_t\left[\boldsymbol{A}\times(\Psi^\dagger\boldsymbol{\sigma}\Psi)\right] \\
& - \frac{q^2\hbar}{4m^2c^2}\left[(\boldsymbol{\nabla}\phi + \partial_t\boldsymbol{A})\times(\Psi^\dagger\boldsymbol{\sigma}\Psi)\right] + \frac{q\hbar}{2m}\left[\boldsymbol{\nabla}\times(\Psi^\dagger\boldsymbol{\sigma}\Psi)\right] \\
& + \frac{qi\hbar^2}{8m^2c^2}\partial_t\left[(\boldsymbol{\nabla}\Psi^\dagger)\times\boldsymbol{\sigma}\Psi + \Psi^\dagger\boldsymbol{\sigma}\times(\boldsymbol{\nabla}\Psi)\right] - \frac{q\hbar^2}{8m^2c^2}\partial_t\left[\boldsymbol{\nabla}(\Psi^\dagger\Psi)\right].
\end{aligned} \tag{2.26}$$

We thus obtain a probability current density defined as,

$$\begin{aligned}
\boldsymbol{j} = {} & \frac{i\hbar}{2m}\left[(\boldsymbol{\nabla}\Psi^\dagger)\Psi - \Psi^\dagger(\boldsymbol{\nabla}\Psi)\right] - \frac{q}{m}\boldsymbol{A}\Psi^\dagger\Psi + \frac{\hbar}{2m}\left[\boldsymbol{\nabla}\times(\Psi^\dagger\boldsymbol{\sigma}\Psi)\right] + \frac{q\hbar}{4m^2c^2}\left[\boldsymbol{E}\times(\Psi^\dagger\boldsymbol{\sigma}\Psi)\right] \\
& - \frac{\hbar}{4m^2c^2}\partial_t\left[\frac{q}{m}\boldsymbol{A}\times(\Psi^\dagger\boldsymbol{\sigma}\Psi) - \frac{i\hbar}{2m}\left\{(\boldsymbol{\nabla}\Psi^\dagger)\times\boldsymbol{\sigma}\Psi + \Psi^\dagger\boldsymbol{\sigma}\times(\boldsymbol{\nabla}\Psi)\right\}\right] - \frac{\hbar}{4mc^2}\partial_t\left[\frac{\hbar}{2m}\boldsymbol{\nabla}(\Psi^\dagger\Psi)\right],
\end{aligned} \tag{2.27}$$

where the terms are arranged for easy comparison with the probability density in Eq. 2.25. At zeroth order in $1/c$, we recover the Schrödinger or Pauli current density along with the usual spin current term $\frac{\hbar}{2m}\boldsymbol{\nabla}\times(\Psi^\dagger\boldsymbol{\sigma}\Psi)$ as can be seen in the book by Landau and Lifshitz.[23] This is the curl of a magnetisation vector and therefore does not appear in the continuity equation. Additionally, we see that the all the terms of the second order, except one, are the same as obtained in the expression of the probability density in Eq. 2.25, but as a time derivative instead of a divergence, and an opposite sign, and therefore these terms indeed form a polarisation density vector $\boldsymbol{P}/q$. In the forthcoming section, we provide a physical interpretation of all the corrections at second order.

## 2.4 Interpretation of Sources

The charge and current density sources can be rewritten as a sum of free and bound sources as,

$$q\rho = q\rho^{\text{free}} - \boldsymbol{\nabla}\cdot\boldsymbol{P}, \tag{2.28}$$

$$q\boldsymbol{j} = q\boldsymbol{j}^{\text{free}} + \boldsymbol{\nabla}\times\boldsymbol{M} + \partial_t\boldsymbol{P}, \tag{2.29}$$

where,

$$\rho^{\text{free}} = \Psi^\dagger\Psi, \tag{2.30}$$

$$\boldsymbol{j}^{\text{free}} = \frac{i\hbar}{2m}\left[(\boldsymbol{\nabla}\Psi^\dagger)\Psi - \Psi^\dagger(\boldsymbol{\nabla}\Psi)\right] - \frac{q}{m}\boldsymbol{A}\Psi^\dagger\Psi + \frac{q\hbar}{4m^2c^2}\left[\boldsymbol{E}\times(\Psi^\dagger\boldsymbol{\sigma}\Psi)\right], \tag{2.31}$$

$$\boldsymbol{M} = \boldsymbol{M}_{\text{spin}} = \frac{q\hbar}{2m}(\Psi^\dagger\boldsymbol{\sigma}\Psi), \tag{2.32}$$

$$\boldsymbol{P}_{\text{spin}} = -\frac{q\hbar}{4mc^2}\left[\frac{q}{m}\boldsymbol{A}\times(\Psi^\dagger\boldsymbol{\sigma}\Psi) - \frac{i\hbar}{2m}\left\{(\boldsymbol{\nabla}\Psi^\dagger)\times\boldsymbol{\sigma}\Psi + \Psi^\dagger\boldsymbol{\sigma}\times(\boldsymbol{\nabla}\Psi)\right\}\right], \tag{2.33}$$

$$\boldsymbol{P}_{\text{Darwin}} = -\frac{q\hbar^2}{8m^2c^2}\boldsymbol{\nabla}(\Psi^\dagger\Psi). \tag{2.34}$$

The polarisation density $\boldsymbol{P} = \boldsymbol{P}_{\text{spin}} + \boldsymbol{P}_{\text{Darwin}}$ has been written as the sum of a *spin* polarisation density and a *Darwin* polarisation density, hinting at the origin of these two terms. Additionally, there is no second order correction to the free probability density, $\rho^{\text{free}}$, but instead, the free current density $\boldsymbol{j}^{\text{free}}$ displays a correction term that can be written as $\frac{1}{2mc^2}\boldsymbol{E}\times\boldsymbol{M}_{\text{spin}}$. This term was already obtained in the past from semi-relativistic kinetic models (Wigner equation).[24]

Once written as a sum of free and bound sources, it is possible to probe the origins of the different terms at second order. Let us start with the spin polarisation. We consider two reference frames moving with a velocity $\boldsymbol{v}$ with respect to each other. The Lorentz transformations for the magnetisation density $\boldsymbol{M}$ and polarisation density $\boldsymbol{P}$ vectors in the fully-relativistic case read as,[25]

$$\boldsymbol{P} = \gamma\left(\boldsymbol{P}' + \frac{\boldsymbol{v}\times\boldsymbol{M}'}{c^2}\right) - \frac{\gamma^2}{1+\gamma}\left(\frac{\boldsymbol{P}'\cdot\boldsymbol{v}}{c}\right)\frac{\boldsymbol{v}}{c}, \tag{2.35}$$

$$\boldsymbol{M} = \gamma(\boldsymbol{M}' - \boldsymbol{v}\times\boldsymbol{P}') - \frac{\gamma^2}{1+\gamma}\left(\frac{\boldsymbol{M}'\cdot\boldsymbol{v}}{c}\right)\frac{\boldsymbol{v}}{c}, \tag{2.36}$$

where $\gamma = \frac{1}{\sqrt{1-v^2/c^2}}$ is the Lorentz factor. For $v \ll c$ and $|\boldsymbol{M}| \gg c|\boldsymbol{P}|$ (electric limit), the above transformations become,

$$\boldsymbol{P} = \boldsymbol{P}' + \frac{\boldsymbol{v}\times\boldsymbol{M}'}{c^2}, \tag{2.37}$$

$$\boldsymbol{M} = \boldsymbol{M}'. \tag{2.38}$$

For our system, in the rest frame of the electron (primed variables), there is a magnetisation density $\boldsymbol{M}' = \boldsymbol{M}_{\text{spin}}$, but no polarisation, $\boldsymbol{P}' = 0$. Thus, in the laboratory frame (unprimed variables), we have,

$$\boldsymbol{P} = \frac{\boldsymbol{v}\times\boldsymbol{M}_{\text{spin}}}{c^2}, \tag{2.39}$$

$$\boldsymbol{M} = \boldsymbol{M}_{\text{spin}}. \tag{2.40}$$

This line of reasoning is purely classical, since $\boldsymbol{v}$, $\boldsymbol{M}$ and $\boldsymbol{P}$ are real numbers, not operators. To compare with the quantum result,[24] we define the velocity operator as,

$$\hat{\boldsymbol{v}} = \frac{(\hat{\boldsymbol{p}} - q\boldsymbol{A})}{m}, \tag{2.41}$$

and the magnetisation density operator as,

$$\hat{\boldsymbol{M}}_{\text{spin}} = \frac{q\hbar}{2m}\boldsymbol{\sigma}. \tag{2.42}$$

Thus, we can then define the polarisation density operator in the lab frame as,

$$\begin{aligned}\hat{\boldsymbol{P}}_{\text{spin}} &= \frac{\hat{\boldsymbol{v}} \times \hat{\boldsymbol{M}}_{\text{spin}}}{c^2} \\ &= -\frac{q\hbar}{2m^2c^2}\left(q\boldsymbol{A}\times\boldsymbol{\sigma} - \frac{1}{2}\hat{\boldsymbol{p}}\times\boldsymbol{\sigma} + \frac{1}{2}\boldsymbol{\sigma}\times\hat{\boldsymbol{p}}\right).\end{aligned} \tag{2.43}$$

Multiplying on the right by $\Psi$ and on the left by $\Psi^\dagger$ gives us,

$$\Psi^\dagger\hat{\boldsymbol{P}}_{\text{spin}}\Psi = -\frac{q\hbar}{2mc^2}\left[\frac{q}{m}\boldsymbol{A}\times(\Psi^\dagger\boldsymbol{\sigma}\Psi) - \frac{i\hbar}{2m}\left\{(\boldsymbol{\nabla}\Psi^\dagger)\times\boldsymbol{\sigma}\Psi + \Psi^\dagger\boldsymbol{\sigma}\times(\boldsymbol{\nabla}\Psi)\right\}\right], \tag{2.44}$$

which is identical to the spin polarisation density vector $\boldsymbol{P}_{\text{spin}}$ obtained earlier, except for a factor of 2. This factor has the same origin as the well-known Thomas correction in the spin-orbit Hamiltonian. Thus, we have seen that the spin polarisation density is a manifestation of the spin magnetisation density in the laboratory frame of reference.

The Darwin polarisation density is named after the Darwin term, which appears in the Hamiltonian as a manifestation of the *Zitterbewegung*, a quivering motion of the electron around its mean path.[26] This is generally assumed due to the interference between the positive and negative states, which produce fluctuations of the position of the particle. By considering only the positive (or negative) states, the interference is replaced with an equivalent potential, the Darwin term. To understand further how the second order Darwin polarisation density is a manifestation of the *Zitterbewegung*, we consider fluctuations $\delta\boldsymbol{r}(t)$ around the mean trajectory $\overline{\boldsymbol{r}(t)}$:

$$\boldsymbol{r}(t) = \overline{\boldsymbol{r}(t)} + \delta\boldsymbol{r}(t), \tag{2.45}$$

where $\boldsymbol{r}(t)$ is the instantaneous position of the particle at time $t$. We expand the probability distribution of the particle around the mean position. We then obtain,

$$\rho(\boldsymbol{r}) = \Psi^\dagger(\overline{\boldsymbol{r}})\Psi(\overline{\boldsymbol{r}}) + \boldsymbol{\nabla}\left[\Psi^\dagger(\overline{\boldsymbol{r}})\Psi(\overline{\boldsymbol{r}})\right]\cdot\delta\boldsymbol{r} + \frac{1}{2}\frac{\partial^2\left[\Psi^\dagger(\overline{\boldsymbol{r}})\Psi(\overline{\boldsymbol{r}})\right]}{\partial r_i\partial r_j}\delta r_i\delta r_j + \cdots, \tag{2.46}$$

where we have neglected the time dependence and used the Einstein's summation convention for simplicity of notation. The perturbation due to the *Zitterbewegung* is $\rho_Z = \overline{\rho(\boldsymbol{r})} - \Psi^\dagger(\overline{\boldsymbol{r}})\Psi(\overline{\boldsymbol{r}})$. When we take the average, the linear term vanishes since the *Zitterbewegung* is isotropic, and we get,

$$\rho_Z = \overline{\rho(\boldsymbol{r})} - \Psi^\dagger(\overline{\boldsymbol{r}})\Psi(\overline{\boldsymbol{r}}) = \frac{1}{2}\frac{\partial^2\left[\Psi^\dagger(\overline{\boldsymbol{r}})\Psi(\overline{\boldsymbol{r}})\right]}{\partial r_i\partial r_j}\delta r_i\delta r_j. \tag{2.47}$$

The amplitude of the oscillations can be estimated to be of the order of the Compton wavelength, i.e.,

$$\overline{\delta\boldsymbol{r}^2} \equiv \frac{\hbar^2}{m^2c^2}. \tag{2.48}$$

Using this estimate and the fact that the *Zitterbewegung* is isotropic, we get,

$$\rho_Z \equiv \frac{\hbar^2}{6m^2c^2}\delta_{ij}\frac{\partial^2\left[\Psi^\dagger(\overline{\boldsymbol{r}})\Psi(\overline{\boldsymbol{r}})\right]}{\partial r_i \partial r_j} = \frac{\hbar^2}{6m^2c^2}\Delta(\Psi^\dagger\Psi) = -\boldsymbol{\nabla}\cdot\left[-\frac{\hbar^2}{6m^2c^2}\boldsymbol{\nabla}(\Psi^\dagger\Psi)\right], \tag{2.49}$$

which yields a polarisation density,

$$\boldsymbol{P}_Z = -\frac{\hbar^2}{6m^2c^2}\boldsymbol{\nabla}(\Psi^\dagger\Psi), \tag{2.50}$$

to be compared with the expression of $\boldsymbol{P}_{\text{Darwin}}$. The functional dependence is correct, and the multiplicative constant only differs by a factor equal to 3/4. This discrepancy is due to the crude estimate value for the amplitude of the fluctuations.

To conclude this section, we recall that a similar partition of the probability density and probability current density into free and bound parts can be formally obtained through a Gordon decomposition.[25] The latter is an exact result that re-expresses the four-current as the sum of an external (*free*) and an internal (*bound*) contribution. It can be further shown that the internal part can be written in terms of a polarisation and magnetisation density. Nevertheless, the Gordon decomposition is a formal procedure that relies on the Dirac bispinors. In order to recover our result (based on two-component Pauli spinors), one should apply a Foldy-Wouthuysen transformation on the bispinor, which is not an easy task and has been done only for the lower order terms. Furthermore, the Lagrangian approach automatically couples the particle evolution equation (extended Pauli) to the field evolution equation (Maxwell's), allowing us to treat coupled self-consistent systems, as shown in Section 2.6. In the following section, we verify the sources obtained using the continuity equation.

## 2.5 Continuity Equation

A closed system of charged particles must obey the conservation law for electric charge. Conservation laws are usually written in the form of a continuity equations. Indeed, Maxwell's equations implicitly contain such a continuity equation and therefore automatically satisfy the conservation of electric charge, whose four-vector form is $\partial_\mu J^\mu = 0$, and when expressed in terms of $\rho$ and $\boldsymbol{j}$ is given as,

$$\partial_t\rho + \boldsymbol{\nabla}\cdot\boldsymbol{j} = 0. \tag{2.51}$$

If we allow for free and bound sources as in our system, i.e., $q\rho = q\rho^{\text{free}} - \boldsymbol{\nabla}\cdot\boldsymbol{P}$ and $\boldsymbol{j} = \boldsymbol{j}^{\text{free}} + \boldsymbol{\nabla}\times\boldsymbol{M} + \partial_t\boldsymbol{P}$, we can see that the continuity equation must be satisfied by the *free* sources. Thus,

$$\partial_t\rho^{\text{free}} + \boldsymbol{\nabla}\cdot\boldsymbol{j}^{\text{free}} = 0. \tag{2.52}$$

Using the definitions of the free sources obtained in the previous section, we get the following continuity equation:

$$\partial_t(\Psi^\dagger\Psi) + \frac{i\hbar}{2m}\left[(\Delta\Psi^\dagger)\Psi - \Psi^\dagger(\Delta\Psi)\right] - \frac{q}{m}\boldsymbol{\nabla}\cdot(\boldsymbol{A}\Psi^\dagger\Psi) + \frac{q\hbar}{4m^2c^2}\boldsymbol{\nabla}\cdot\left[\boldsymbol{E}\times(\Psi^\dagger\boldsymbol{\sigma}\Psi)\right] = 0, \tag{2.53}$$

where the only second order correction comes from the free current. This continuity equation refers to the conservation of charge dictated by the Maxwell's equations. But this conservation law should be compatible with the relevant equation of motion, i.e. the extended Pauli equation. In order to check this compatibility, we derive the continuity equation directly from the extended Pauli equation and from the Lagrangian density, and show that both methods yield the same result as Eq. 2.53.

### 2.5.1 Continuity Equation from the Extended Pauli Equation

This method involves manipulating the Hamiltonian of the system. From the evolution equation,

$$i\hbar\partial_t\Psi = \hat{H}\Psi, \tag{2.54}$$

one can easily deduce that,

$$\partial_t(\Psi^\dagger\Psi) = \frac{1}{i\hbar}\left[\Psi^\dagger(\hat{H}\Psi) - (\hat{H}^\dagger\Psi^\dagger)\Psi\right], \tag{2.55}$$

where $\hat{H}$ is the extended Pauli Hamiltonian (Eq. 2.15), with the relativistic kinetic energy correction $(\hat{\boldsymbol{p}} - q\boldsymbol{A})^4$ term neglected, and $\hat{H}^\dagger$ is its Hermitian conjugate. Thus, we obtain,

$$\begin{aligned} i\hbar\partial_t(\Psi^\dagger\Psi) &= \Psi^\dagger(\hat{H}\Psi) - (\hat{H}^\dagger\Psi^\dagger)\Psi \\ &= \Psi^\dagger\left[\frac{\hat{\boldsymbol{p}}^2}{2m}\Psi - \frac{q\boldsymbol{A}\cdot\hat{\boldsymbol{p}}}{m}\Psi - \frac{q\hbar}{4m^2c^2}\boldsymbol{\sigma}\cdot\{(\boldsymbol{\nabla}\phi + \partial_t\boldsymbol{A})\times\hat{\boldsymbol{p}}\Psi\}\right] \\ &\quad - \left[\frac{\hat{\boldsymbol{p}}^2}{2m}\Psi^\dagger + \frac{q\boldsymbol{A}\cdot\hat{\boldsymbol{p}}}{m}\Psi^\dagger + \frac{q\hbar}{4m^2c^2}\left\{(\boldsymbol{\nabla}\phi + \partial_t\boldsymbol{A})\times\hat{\boldsymbol{p}}\Psi^\dagger\right\}\cdot\boldsymbol{\sigma}\right]\Psi \\ &\quad + \Psi^\dagger\left[-\frac{\hat{\boldsymbol{p}}}{m}\cdot(q\boldsymbol{A}) - \frac{q\hbar}{4m^2c^2}\boldsymbol{\sigma}\cdot(\hat{\boldsymbol{p}}\times\partial_t\boldsymbol{A})\right]\Psi. \end{aligned} \tag{2.56}$$

The last term $\hat{\boldsymbol{p}}\times\partial_t\boldsymbol{A}$ can be written as $\hat{\boldsymbol{p}}\times(\boldsymbol{\nabla}+\partial_t\boldsymbol{A})$, since the curl of a gradient is zero. Rearranging the terms, we get,

$$i\hbar\partial_t(\Psi^\dagger\Psi) = -\frac{1}{2m}\left[(\hat{\boldsymbol{p}}^2\Psi^\dagger)\Psi - \Psi^\dagger(\hat{\boldsymbol{p}}^2\Psi)\right] - \frac{\hat{\boldsymbol{p}}}{m}\cdot(q\boldsymbol{A}\Psi^\dagger\Psi) + \frac{q\hbar}{4m^2c^2}\hat{\boldsymbol{p}}\cdot\left[\boldsymbol{E}\times(\Psi^\dagger\boldsymbol{\sigma}\Psi)\right], \tag{2.57}$$

which is identical to the continuity equation in Eq. 2.53. It is important to point out that by using this method the actual sources cannot be obtained, because the bound sources (magnetisation and polarisation) cancel each other out in the continuity equation. The Lagrangian procedure detailed in the previous sections was therefore necessary to derive the actual sources of the Maxwell's equations.

### 2.5.2 Continuity Equation from Noether's Theorem

Noether's theorem holds a special place in Lagrangian mechanics. It states that we have a conserved quantity whenever there is a symmetry in the system (invariance under some type of transformation). In the present case, the relevant symmetry is gauge invariance and the corresponding conserved quantity is the electric charge. The theorem allows us to calculate the continuity equation directly from the Lagrangian density and can be written in a four-vector form as,

$$\partial_\mu J^\mu = \partial_\mu\left(\Psi^\dagger\frac{\partial\mathcal{L}}{\partial(\partial_\mu\Psi^\dagger)} - \frac{\partial\mathcal{L}}{\partial(\partial_\mu\Psi)}\Psi\right) = 0, \tag{2.58}$$

where $\partial_\mu = (\partial_{ct}, \boldsymbol{\nabla})$, and the Einstein summation convention is used. For the continuity equation, only the terms depending on the derivatives of $\Psi$ and $\Psi^\dagger$ are relevant. Thus, we rewrite the Lagrangian density as,

$$\begin{aligned} \mathcal{L} &= \mathcal{L}' + \frac{i\hbar}{2}(\Psi^\dagger\dot{\Psi} - \dot{\Psi}^\dagger\Psi) - \frac{1}{2m}\left[(i\hbar\partial_k\Psi^\dagger)(-i\hbar\partial_k - qA_k)\Psi + i\hbar qA_k\Psi^\dagger\partial_k\Psi\right] \\ &\quad - \frac{q\hbar}{8m^2c^2}\epsilon_{ijk}\left[\Psi^\dagger\sigma_i\partial_j\phi\hat{p}_k\Psi - \partial_j\phi\hat{p}_k\Psi^\dagger\sigma_i\Psi + \Psi^\dagger\sigma_i\partial_tA_j\hat{p}_k\Psi - \partial_tA_j\hat{p}_k\Psi^\dagger\sigma_i\Psi\right], \end{aligned} \tag{2.59}$$

where $\mathcal{L}'$ contains all the remaining terms of the Lagrangian density. The time component yields,

$$\partial_{ct}\left[\Psi^\dagger \frac{\partial \mathcal{L}}{\partial(\partial_{ct}\Psi^\dagger)} - \frac{\partial \mathcal{L}}{\partial(\partial_{ct}\Psi)}\right] = -i\hbar\partial_t(\Psi^\dagger\Psi), \tag{2.60}$$

and the space components give,

$$\Psi^\dagger \frac{\partial \mathcal{L}}{\partial(\partial_k\Psi^\dagger)} = \frac{i\hbar}{2m}\Psi^\dagger(i\hbar\partial_k + qA_k)\Psi - \frac{q\hbar(i\hbar)}{8m^2c^2}\epsilon_{ijk}(\partial_j\phi + \partial_t A_j)\Psi^\dagger\sigma_i\Psi \tag{2.61}$$

$$-\frac{\partial \mathcal{L}}{\partial(\partial_k\Psi^\dagger)}\Psi = -\frac{i\hbar}{2m}(i\hbar\partial_k\Psi^\dagger - qA_k)\Psi - \frac{q\hbar(i\hbar)}{8m^2c^2}\epsilon_{ijk}(\partial_j\phi + \partial_t A_j)\Psi^\dagger\sigma_i\Psi. \tag{2.62}$$

Combining the above terms gives,

$$\begin{aligned}\partial_k\left[\Psi^\dagger \frac{\partial \mathcal{L}}{\partial(\partial_k\Psi^\dagger)} - \frac{\partial \mathcal{L}}{\partial(\partial_k\Psi^\dagger)}\Psi\right] = &-\frac{(i\hbar)^2}{2m}\left[(\partial_k^2\Psi^\dagger)\Psi - \Psi^\dagger(\partial_k^2\Psi)\right] + \frac{qi\hbar}{m}\partial_k(A_k\Psi^\dagger\Psi) \\ &+ \frac{q\hbar(i\hbar)}{4m^2c^2}\epsilon_{ijk}\partial_k\left[(\partial_j\phi + \partial_t A_j)\Psi^\dagger\sigma_i\Psi\right].\end{aligned} \tag{2.63}$$

Substituting Eqs. 2.60 and 2.63 into Eq. 2.58, we get the same continuity equation as Eq. 2.53. We again stress that the full density and current corrections could not have been obtained from Noether's theorem, as the theorem only provides the conservation law, but not the sources themselves. That the conservation laws obtained from the extended Pauli Hamiltonian and Noether's theorem coincide with the charge conservation implicit in Maxwell's equations with second order sources is an attractive feature of our model and strengthens our confidence in its validity.

In the following section, we highlight a shortcoming in the model, namely the fact that the extended Pauli equation is a second order (in $1/c$) approximation, while the Maxwell's equations are fully exact in $1/c$. To properly couple the particles and fields, we describe a procedure to expand the electromagnetic fields in the Maxwell's equations so that a consistent model can be developed. Towards the end of the following section, we provide three ways to use the self-consistent model.

## 2.6 Coupled Particle-Field Equations

In the previous sections, a model for obtaining the sources to the Maxwell's equations and the equation of motions for the electrons (extended Pauli Hamiltonian) with a Lagrangian approach was developed. The extended Pauli equation is a second order (in $1/c$) approximation for the positive energy states of the Dirac equation. However, there is an inconsistency here. The charge and current densities were derived by putting together the Pauli and Maxwell parts of the Lagrangian, i.e. by assuming that the extended Pauli equation acts as some sort of source to the Maxwell equations. But the latter are exact to all orders in $1/c$, whereas the extended Pauli equation is only valid up to second order. While this procedure yields the correct results as far as the charge and current densities are concerned, it would be desirable to construct a model that treats on the same footing (i.e. at the same order) both the equation of motion of the particles (extended Pauli equation) and the equations for the fields (Maxwell's equations).

It has been known for a long time[27–30] that the Maxwell's equations possess two independent non-relativistic limits, which correspond to situations where either $|\boldsymbol{E}| \gg c|\boldsymbol{B}|$ (electric limit) or

$|\boldsymbol{E}| \ll c|\boldsymbol{B}|$ (magnetic limit). Each of these two limits is Galilean invariant. In practice, the electric limit amounts to neglecting the time derivative of the magnetic field in Faraday's law of induction, whereas the magnetic limit is obtained by dropping the displacement current in Ampère's equation. Both limits can be derived in a rigorous and gauge-independent way by using a non-dimensional version of the Maxwell's equations.[31] In our model we work with the SI units and the Lorentz gauge. Moreover, we are concerned with the electric limit only, since the magnetic limit is neutral in charge by construction, and thus requires the presence of two mobile species of opposite charge. The electric limit can be viewed as the case where $c \to \infty$, while $\varepsilon_0$ remains finite. We rewrite the Maxwell's equations as,

$$-\Delta\phi + \frac{1}{c^2}\partial_t^2\phi = \frac{q\rho}{\varepsilon_0}, \tag{2.64}$$

$$-\Delta\boldsymbol{A} + \frac{1}{c^2}\partial_t^2\boldsymbol{A} = \frac{q\boldsymbol{j}}{\varepsilon_0 c^2}. \tag{2.65}$$

We then expand all variables, $\phi$, $\boldsymbol{A}$, $\rho$ and $\boldsymbol{j}$ in powers of $c^-2$ as,

$$\phi = \phi_0 + \phi_2 + \cdots, \tag{2.66}$$

$$\boldsymbol{A} = \boldsymbol{A}_0 + \boldsymbol{A}_2 + \cdots, \tag{2.67}$$

$$\rho = \rho_0 + \rho_2 + \cdots, \tag{2.68}$$

$$\boldsymbol{j} = \boldsymbol{j}_0 + \boldsymbol{j}_2 + \cdots. \tag{2.69}$$

We need only *even* powers of $1/c$ the sources we obtained were only at even powers and the fields in the Maxwell's equations can only couple fields like $\phi_0$ and $\phi_2$. This is purely because of the system of units we choose to work in, which in our case are the SI units. Once the fields and sources are expanded, we can match the appropriate orders and we obtain at zeroth and second order,

$$\Delta\boldsymbol{A}_0 = 0, \tag{2.70}$$

$$-\Delta\phi_0 = \frac{q\rho_0}{\varepsilon_0}, \tag{2.71}$$

$$-\Delta\phi_2 + \frac{1}{c^2}\partial_t\phi_0 = \frac{q\rho_2}{\varepsilon_0}, \tag{2.72}$$

$$-\Delta\boldsymbol{A}_2 = \frac{q\boldsymbol{j}_0}{\varepsilon_0 c^2}, \tag{2.73}$$

where we assumed zero boundary conditions at infinity to set $\boldsymbol{A}_0 = 0$. This is also in agreement with the electric limit where there is no magnetic field at leading order. If we do a similar expansion of the electric and magnetic fields, $\boldsymbol{E}$ and $\boldsymbol{B}$, we have the following simplified Maxwell's equations at zeroth order,

$$\boldsymbol{\nabla}\cdot\boldsymbol{E}_0 = \frac{q\rho_2}{\varepsilon_0}, \tag{2.74}$$

$$\boldsymbol{\nabla}\times\boldsymbol{E}_0 = \boldsymbol{\nabla}\cdot\boldsymbol{B}_0 = \boldsymbol{\nabla}\times\boldsymbol{B}_0 = 0, \tag{2.75}$$

and with $\boldsymbol{B}_0 = 0$ and $\boldsymbol{E}_0 = -\boldsymbol{\nabla}\phi_0$, which return Eqs. 2.70 and 2.71. At second order we get,

$$\boldsymbol{\nabla}\cdot\boldsymbol{E}_2 = \frac{q\rho_2}{\varepsilon_0}, \tag{2.76}$$

$$\boldsymbol{\nabla}\times\boldsymbol{E}_2 = \partial_t\boldsymbol{B}_2, \tag{2.77}$$

$$\boldsymbol{\nabla}\cdot\boldsymbol{B}_2 = 0, \tag{2.78}$$

$$\boldsymbol{\nabla}\times\boldsymbol{B}_2 = \frac{q\boldsymbol{j}_0}{\varepsilon_0 c^2} + \frac{1}{c^2}\partial_t\boldsymbol{E}_0. \tag{2.79}$$

Using $\boldsymbol{E}_2 = -\boldsymbol{\nabla} - \partial_t \boldsymbol{A}_2$ and the Lorentz gauge condition,

$$\boldsymbol{\nabla} \cdot \boldsymbol{A}_2 + \frac{1}{c^2}\partial_t \phi_0 = 0, \tag{2.80}$$

we get the Eqs. 2.72 and 2.73. If we take the divergence of Eq. 2.79, we obtain the continuity equation at the zeroth order,

$$\partial_t \rho_0 + \boldsymbol{\nabla} \cdot \boldsymbol{j}_0 = 0. \tag{2.81}$$

To obtain the continuity equation at second order, one must pursue a similar expansion up to fourth order and the equation is,

$$\partial_t \rho_2 + \boldsymbol{\nabla} \cdot \boldsymbol{j}_2 = 0. \tag{2.82}$$

We can now try to match the above sources with those found with the general Lagrangian approach, i.e. Eqs. 2.30–2.34. For the charge density, it is clear that $\rho_0$ coincides with the free density, while $\rho_2$ can be identified with the bound density. For the current density, things are subtler since the free current contains zeroth as well as second order terms. We have for the zeroth order,

$$q\boldsymbol{j}_0 = \underbrace{\frac{i\hbar}{2m}\left[(\boldsymbol{\nabla}\Psi^\dagger)\Psi - \Psi^\dagger(\boldsymbol{\nabla}\Psi)\right]}_{q\boldsymbol{j}_0^{\text{free}}} + \underbrace{\boldsymbol{\nabla} \times \boldsymbol{M}_{\text{spin}}}_{q\boldsymbol{j}_0^{\text{bound}}}, \tag{2.83}$$

and for the second order,

$$q\boldsymbol{j}_2 = \underbrace{-\frac{q}{m}\boldsymbol{A}_2\Psi^\dagger\Psi - \frac{q\hbar}{4m^2c^2}\left[\boldsymbol{\nabla}\phi_0 \times (\Psi^\dagger\boldsymbol{\sigma}\Psi)\right]}_{q\boldsymbol{j}_2^{\text{free}}} + \underbrace{\partial_t(\boldsymbol{P}_{\text{spin}} + \boldsymbol{P}_{\text{Darwin}})}_{q\boldsymbol{j}_2^{\text{bound}}}, \tag{2.84}$$

where the order of the potentials are explicitly indicated. Furthermore, the term depending on the vector potential in $\boldsymbol{P}_{\text{spin}}$ in Eq. 2.33 can be neglected because it is of at least fourth order.

In principle, only the current $\boldsymbol{j}_0$ should go into Ampère's equation in Eq. 2.73. However, by doing so the continuity equation (Eq. 2.53) would no longer be satisfied, an undesirable property. For this reason, we shall keep both zeroth and second order currents in this equation, even though certain fourth order terms are introduced. The Maxwell's equations then become,

$$\begin{aligned}
\boldsymbol{A}_0 &= 0, && (2.85)\\
-\Delta\phi_0 &= \frac{q\rho_0}{\varepsilon_0}, && (2.86)\\
-\Delta\phi_2 + \frac{1}{c^2}\partial_t^2\phi_0 &= \frac{q\rho_2}{\varepsilon_0}, && (2.87)\\
-\Delta\boldsymbol{A}_2 &= \frac{q}{\varepsilon_0 c^2}(\boldsymbol{j}_0 + \boldsymbol{j}_2). && (2.88)
\end{aligned}$$

We can now write down a family of useful models that can be viewed as self-consistent expansions of the original Dirac-Maxwell equations up to second order in $1/c$.

### 2.6.1 Purely Internal Electromagnetic Fields

If we assume purely internal electromagnetic fields, with $\boldsymbol{A}_0 = 0$, the extended Pauli Hamiltonian becomes after neglecting the $mc^2$ term,

$$\begin{aligned}\hat{H} =& q(\phi_0 + \phi_2) + \frac{\hat{\boldsymbol{p}}^2}{2m} - \frac{q}{2m}(\hat{\boldsymbol{p}} \cdot \boldsymbol{A}_2 + \boldsymbol{A}_2 \cdot \hat{\boldsymbol{p}}) + \frac{q\hbar}{2m}\boldsymbol{\sigma} \cdot (\boldsymbol{\nabla} \times \boldsymbol{A}_2) \\ &- \frac{q\hbar^2}{8m^2c^2}\Delta\phi_0 - \frac{q\hbar}{4m^2c^2}\boldsymbol{\sigma} \cdot (\boldsymbol{\nabla}\phi_0 \times \hat{\boldsymbol{p}}).\end{aligned} \tag{2.89}$$

This is coupled to the Maxwell's equations Eqs. 2.85–2.88. Using the Maxwell's equations or Noether's theorem or by manipulating the extended Pauli equation, the continuity equation becomes,

$$\partial_t(\Psi^\dagger\Psi) + \frac{i\hbar}{2m}\left[(\Delta\Psi^\dagger)\Psi - \Psi^\dagger(\Delta\Psi)\right] - \frac{q}{m}\boldsymbol{\nabla} \cdot (\boldsymbol{A}_2\Psi^\dagger\Psi) + \frac{q\hbar}{4m^2c^2}\boldsymbol{\nabla} \cdot \left[\boldsymbol{\nabla}\phi_0 \times (\Psi^\dagger\boldsymbol{\sigma}\Psi)\right] = 0, \tag{2.90}$$

which is consistent with,

$$\partial_t(\rho_0 + \rho_2) + \boldsymbol{\nabla} \cdot (\boldsymbol{j}_0 + \boldsymbol{j}_2) = 0, \tag{2.91}$$

where the currents are as defined in Eqs. 2.83 and 2.84.

### 2.6.2 Minimal Self-Consistent Model

We have seen that self-consistent electric effects appear at zeroth order in the Maxwell's equations, whereas magnetic effects are of second order. It may be reasonable (although not mathematically rigorous) to neglect self-consistent electrostatic corrections at second order. We shall see that this entails significant simplifications to the model. The relevant Hamiltonian becomes after $\phi_2$ is neglected in Eq. 2.89,

$$\begin{aligned}\hat{H} =& q\phi_0 + \frac{\hat{\boldsymbol{p}}^2}{2m} - \frac{q}{2m}(\hat{\boldsymbol{p}} \cdot \boldsymbol{A}_2 + \boldsymbol{A}_2 \cdot \hat{\boldsymbol{p}}) + \frac{q\hbar}{2m}\boldsymbol{\sigma} \cdot (\boldsymbol{\nabla} \times \boldsymbol{A}_2) \\ &- \frac{q\hbar^2}{8m^2c^2}\Delta\phi_0 - \frac{q\hbar}{4m^2c^2}\boldsymbol{\sigma} \cdot (\boldsymbol{\nabla}\phi_0 \times \hat{\boldsymbol{p}}).\end{aligned} \tag{2.92}$$

The Maxwell's equations on the other hand reduce to,

$$-\Delta\phi_0 = \frac{q\rho_0}{\varepsilon_0}, \tag{2.93}$$

$$-\Delta\boldsymbol{A}_2 = \frac{q}{\varepsilon_0 c^2}(\boldsymbol{j}_0 + \boldsymbol{j}_2^{\text{free}}). \tag{2.94}$$

We see that the Maxwell's equations are now a set of two elliptic (i.e., Poisson-like) equations where no time derivatives appear. The last term in the current is needed to ensure that the continuity equation (Eq. 2.90) derived from the Hamiltonian in Eq. 2.92 is consistent with,

$$\partial_t\rho_0 + \boldsymbol{\nabla} \cdot (\boldsymbol{j}_0 + \boldsymbol{j}_2^{\text{free}}) = 0. \tag{2.95}$$

An additional welcome property of the above set of equations is that the particle density is simply $\rho_0 = \Psi^\dagger\Psi$, as in the Schrödinger or Pauli equations. Finally, one can show that the self-consistent vector potential $\boldsymbol{A}_2$, when re-injected into Eq. 2.92 yields all the terms present in the Breit equation for a many-electron system in the mean-field approximation, like the spin-spin, the spin-same-orbit and the spin-other-orbit interactions.[32]

### 2.6.3 Internal and External Electromagnetic Fields

If some external electromagnetic fields are also present, e.g. a laser pulse, these can be assumed to be of zeroth order. For the scalar potential, nothing needs to be changed since $\phi$ already contains a zeroth order term, and one just rewrites $\phi_0 = \phi_0^{\text{internal}} + \phi_0^{\text{external}}$. For the vector potential however, we now have a zeroth order term, $\boldsymbol{A}_0 = \boldsymbol{A}_0^{\text{external}}$, and we cannot make simplifications that lead to Eq. 2.89. Thus, one should use the full Hamiltonian of Eq. 2.16 and the corresponding continuity equation Eq. 2.53, although one could neglect the self-consistent vector potential $\boldsymbol{A}_2$ in the second order terms. The sources to be used in the reduced Maxwell's equations would be those of Eqs. 2.30–2.34.

## 2.7 Inclusion of the Relativistic Mass Correction

To include the relativistic correction term to the Lagrangian density, we use the form $\langle\Psi|\hat{\boldsymbol{p}}^2\hat{\boldsymbol{p}}^2|\Psi\rangle$. This is similar to the way the $\frac{\hat{p}^2}{2m}$ is used in the original Lagrangian density $\langle\Psi|(\hat{\boldsymbol{p}}-q\boldsymbol{A})(\hat{\boldsymbol{p}}-q\boldsymbol{A})|\Psi\rangle$. We use a highly reduced Pauli equation to compute the contribution by this term which is given as,

$$i\hbar\partial_t\Psi = \frac{(\hat{\boldsymbol{p}}-q\boldsymbol{A})^4}{8m^3c^2}\Psi. \tag{2.96}$$

The Lagrangian density for this Pauli equation coupled to the Maxwell's equations is,

$$\begin{aligned}\mathcal{L} =& \frac{i\hbar}{2}(\Psi^\dagger\dot{\Psi} - \dot{\Psi}^\dagger\Psi) + \frac{1}{8m^3c^2}(-\hat{p}_i - qA_i)(-\hat{p}_i - qA_i)\Psi^\dagger(\hat{p}_j - qA_j)(\hat{p}_j - qA_j)\Psi \\ &+ \frac{\varepsilon}{2}(\partial_k\phi)^2 - \frac{\varepsilon}{2c^2}(\partial_t\phi)^2 - \frac{1}{2\mu}(\partial_j A_k)^2 + \frac{1}{2\mu c^2}(\partial_t A_k)^2.\end{aligned} \tag{2.97}$$

One can easily check that the probability density does not change. Thus, we rewrite the Lagrangian density as one consisting of terms containing only the Maxwell's equations for the vector field and the relativistic correction. The current density that is obtained from this term is simply added to the previously obtained current density. Thus,

$$\mathcal{L} = \mathcal{L}' - \frac{1}{2\mu}(\partial_j A_k)^2 + \frac{1}{2\mu c^2}(\partial_t A_k)^2 + \frac{1}{8m^3c^2}(\hat{p}_i + qA_i)(\hat{p}_i + qA_i)\Psi^\dagger(\hat{p}_j - qA_j)(\hat{p}_j - qA_j)\Psi, \tag{2.98}$$

where $\mathcal{L}'$ contains all the other terms. The momentum operator can act on the field and the wavefunction. Simplifying this and putting the $\hat{p}_i\hat{p}_i\Psi^\dagger\hat{p}_j\hat{p}_j\Psi$ term in $\mathcal{L}'$ gives,

$$\begin{aligned}\mathcal{L} =& \mathcal{L}' - \frac{1}{2\mu}(\partial_j A_k)^2 + \frac{1}{2\mu c^2}(\partial_t A_k)^2 + \frac{1}{8m^3c^2}[\hat{p}_i\hat{p}_i\Psi^\dagger q^2 A_j A_j\Psi + q^2 A_i A_i\Psi^\dagger\hat{p}_j\hat{p}_j\Psi] \\ &+ \frac{1}{8m^3c^2}\left[\{2qA_i\hat{p}_i + (\hat{p}_i qA_i) + q^2A_iA_i\}\Psi^\dagger\{q^2A_jA_j - 2qA_j\hat{p}_j - (\hat{p}_j qA_j)\}\Psi\right].\end{aligned} \tag{2.99}$$

The Euler-Lagrange equations for $A_k$ gives us the current density. However, care must be taken while computing them since there are two indices $i$ and $j$. Computing for a single component (say,

$k^{th}$) gives a $\delta_{ik}$ and $\delta_{jk}$. Thus,

$$\begin{aligned}\frac{\partial\mathcal{L}}{\partial A_k} =&\frac{\delta_{ik}}{8m^3c^2}[4q^4A_iA_j^2\Psi^\dagger\Psi + 4i\hbar q^3A_iA_j\Psi^\dagger(\partial_j\Psi) + 2q^3i\hbar A_i(\partial_jA_j)\Psi^\dagger\Psi]\\ &+\frac{\delta_{ik}}{8m^3c^2}[-2q^3i\hbar A_j^2(\partial_i\Psi^\dagger)\Psi - 4(qi\hbar)^2A_j(\partial_i\Psi^\dagger)(\partial_j\Psi) - 2(qi\hbar)^2(\partial_i\Psi^\dagger)(\partial_jA_j)\Psi]\\ &+\frac{\delta_{jk}}{8m^3c^2}[4q^4A_i^2A_j\Psi^\dagger\Psi - 4q^3i\hbar A_iA_j(\partial_i\Psi^\dagger)\Psi - 2q^3i\hbar A_j(\partial_iA_i)\Psi^\dagger\Psi]\\ &+\frac{\delta_{jk}}{8m^3c^2}[2q^3i\hbar A_i^2\Psi^\dagger(\partial_j\Psi) - 4(qi\hbar)^2A_i(\partial_i\Psi^\dagger)(\partial_j\Psi) - 2(qi\hbar)^2(\partial_iA_i)\Psi^\dagger(\partial_j\Psi)]\\ &+\frac{\delta_{ik}}{8m^3c^2}2q^2A_i\Psi^\dagger\hat{p}_j\hat{p}_j\Psi + \frac{\delta_{jk}}{8m^3c^2}2\hat{p}_i\hat{p}_i\Psi^\dagger q^2A_j\Psi.\end{aligned} \tag{2.100}$$

The first and the seventh terms are identical when we remove the Kronecker delta by proper substitution of the indices. The third and the ninth terms are also the same and cancel each other out. Combining like terms by substitution of the indices,

$$\begin{aligned}\frac{\partial\mathcal{L}}{\partial A_k} =&\frac{1}{8m^3c^2}\left[8q^2(q\boldsymbol{A}\cdot q\boldsymbol{A})\Psi^\dagger\Psi A_k + 4i\hbar q^2\left\{q\boldsymbol{A}\cdot[\Psi^\dagger(\boldsymbol{\nabla}\Psi) - (\boldsymbol{\nabla}\Psi^\dagger)\Psi]\right\}A_k\right]\\ &+\frac{1}{8m^3c^2}\left[-2qi\hbar(q\boldsymbol{A}\cdot q\boldsymbol{A})[(\partial_k\Psi^\dagger)\Psi - \Psi^\dagger(\partial_k\Psi)] - 2(qi\hbar)^2(\boldsymbol{\nabla}\cdot\boldsymbol{A})\partial_k(\Psi^\dagger\Psi)\right]\\ &+\frac{1}{8m^3c^2}\left[-4(qi\hbar)^2\left\{(\partial_k\Psi^\dagger)(\boldsymbol{A}\cdot\boldsymbol{\nabla}\Psi) + (\boldsymbol{A}\cdot\boldsymbol{\nabla}\Psi^\dagger)(\partial_k\Psi)\right\}\right]\\ &+\frac{1}{8m^3c^2}2(qi\hbar)^2\{A_k\Psi^\dagger(\Delta\Psi) + (\Delta\Psi^\dagger)A_k\Psi\}.\end{aligned} \tag{2.101}$$

For the first time-derivative components,

$$\partial_t\frac{\partial\mathcal{L}}{\partial(\partial_tA_k)} = \frac{1}{\mu c^2}\partial_t^2A_k. \tag{2.102}$$

For the space-derivatives, when we calculate the component with the index $i$, we replace $j$ by $i$. Thus,

$$\begin{aligned}\frac{\partial\mathcal{L}}{\partial(\partial_jA_k)} =&-\frac{1}{\mu}\partial_jA_k + \frac{1}{8m^3c^2}\delta_{jk}\left[-qi\hbar\Psi^\dagger\{q^2(\boldsymbol{A}\cdot\boldsymbol{A}) + 2qi\hbar\boldsymbol{A}\cdot\boldsymbol{\nabla} + qi\hbar(\boldsymbol{\nabla}\cdot\boldsymbol{A})\}\Psi\right]\\ &+\frac{1}{8m^3c^2}\delta_{jk}\left[\{q^2\boldsymbol{A}\cdot\boldsymbol{A} - 2qi\hbar\boldsymbol{A}\cdot\boldsymbol{\nabla} - qi\hbar(\boldsymbol{\nabla}\cdot\boldsymbol{A})\}\Psi^\dagger qi\hbar\Psi\right].\end{aligned} \tag{2.103}$$

Simplifying,

$$\begin{aligned}\partial_j\frac{\partial\mathcal{L}}{\partial(\partial_jA_k)} =&-\frac{1}{8m^3c^2}\partial_k\left[2(qi\hbar)^2\{\Psi^\dagger(\boldsymbol{A}\cdot\boldsymbol{\nabla}\Psi) + (\boldsymbol{A}\cdot\boldsymbol{\nabla}\Psi^\dagger)\Psi\} + 2(qi\hbar)^2(\boldsymbol{\nabla}\cdot\boldsymbol{A})\Psi^\dagger\Psi\right]\\ &-\frac{1}{\mu}\Delta A_k.\end{aligned} \tag{2.104}$$

Substituting these terms in the Euler-Lagrange equation and rearranging,

$$\begin{aligned}8m^3c^2\left\{-\frac{1}{\mu}\Delta A_k+\frac{1}{\mu c^2}\partial_t^2 A_k\right\}=&2(qi\hbar)^2\partial_k\boldsymbol{\nabla}\cdot(\boldsymbol{A}\Psi^\dagger\Psi)+8q^2(q\boldsymbol{A}\cdot q\boldsymbol{A})\Psi^\dagger\Psi A_k\\&+4i\hbar q^2\left\{q\boldsymbol{A}\cdot[\Psi^\dagger(\boldsymbol{\nabla}\Psi)-(\boldsymbol{\nabla}\Psi^\dagger)\Psi]\right\}A_k\\&-2qi\hbar(q\boldsymbol{A}\cdot q\boldsymbol{A})[(\partial_k\Psi^\dagger)\Psi-\Psi^\dagger(\partial_k\Psi)]\\&-2(qi\hbar)^2[(\partial_k\Psi^\dagger)\{\boldsymbol{\nabla}\cdot(\boldsymbol{A}\Psi)\}+\{\boldsymbol{\nabla}\cdot(\boldsymbol{A}\Psi^\dagger)\}(\partial_k\Psi)]\\&-2(qi\hbar)^2[(\boldsymbol{A}\cdot\boldsymbol{\nabla}\Psi^\dagger)(\partial_k\Psi)+(\partial_k\Psi^\dagger)(\boldsymbol{A}\cdot\boldsymbol{\nabla}\Psi)]\\&+2(qi\hbar)^2\{A_k\Psi^\dagger(\Delta\Psi)+(\Delta\Psi^\dagger)A_k\Psi\}\\=&8m^3c^2qj_k^{\rm rel},\end{aligned}\tag{2.105}$$

which by converting to vector form to rewrite the current, we get the relativistic mass correction to the current density as,

$$\begin{aligned}\boldsymbol{j}^{\rm rel}=&-\frac{q(i\hbar)^2}{4m^3c^2}[(\boldsymbol{\nabla}\Psi^\dagger)\boldsymbol{\nabla}\cdot(\boldsymbol{A}\Psi)+\boldsymbol{\nabla}\cdot(\boldsymbol{A}\Psi^\dagger)(\boldsymbol{\nabla}\Psi)+(\boldsymbol{A}\cdot\boldsymbol{\nabla}\Psi^\dagger)(\boldsymbol{\nabla}\Psi)+(\boldsymbol{\nabla}\Psi^\dagger)(\boldsymbol{A}\cdot\boldsymbol{\nabla}\Psi)]\\&+\frac{q(i\hbar)^2}{4m^3c^2}\boldsymbol{\nabla}\{\boldsymbol{\nabla}\cdot(\boldsymbol{A}\Psi^\dagger\Psi)\}+\frac{q^3}{m^3c^2}(\boldsymbol{A}\cdot\boldsymbol{A})(\Psi^\dagger\boldsymbol{A}\Psi)+\frac{i\hbar q^2\boldsymbol{A}}{2m^3c^2}[\Psi^\dagger(\boldsymbol{A}\cdot\boldsymbol{\nabla}\Psi)-(\boldsymbol{A}\cdot\boldsymbol{\nabla}\Psi^\dagger)\Psi]\\&-\frac{q^2i\hbar}{2m^3c^2}(\boldsymbol{A}\cdot\boldsymbol{A})[(\boldsymbol{\nabla}\Psi^\dagger)\Psi-\Psi^\dagger(\boldsymbol{\nabla}\Psi)]+\frac{q(i\hbar)^2}{4m^3c^2}[\Psi^\dagger(\Delta\Psi)+(\Delta\Psi^\dagger)\Psi]\boldsymbol{A}.\end{aligned}\tag{2.106}$$

This is current density contribution due to the relativistic correction to the kinetic energy up to $\Theta(\cdot)=c^{-2}$. Thus, the total current is,

$$\begin{aligned}\boldsymbol{j}^{\rm rel}=&\partial_t\left\{-\frac{\hbar}{4mc^2}\left[\frac{q}{m}\boldsymbol{A}\times(\Psi^\dagger\boldsymbol{\sigma}\Psi)-\frac{i\hbar}{2m}[(\boldsymbol{\nabla}\Psi^\dagger)\times\boldsymbol{\sigma}\Psi+\Psi^\dagger\boldsymbol{\sigma}\times(\boldsymbol{\nabla}\Psi)]+\frac{\hbar}{2m}\boldsymbol{\nabla}(\Psi^\dagger\Psi)\right]\right\}\\&+\frac{i\hbar}{2m}[(\boldsymbol{\nabla}\Psi^\dagger)\Psi-\Psi^\dagger(\boldsymbol{\nabla}\Psi)]-\frac{q}{m}\boldsymbol{A}\Psi^\dagger\Psi+\frac{q\hbar}{4m^2c^2}[\boldsymbol{E}\times(\Psi^\dagger\boldsymbol{\sigma}\Psi)]+\frac{\hbar}{2m}[\boldsymbol{\nabla}\times(\Psi^\dagger\boldsymbol{\sigma}\Psi)]\\&-\frac{q(i\hbar)^2}{4m^3c^2}[(\boldsymbol{\nabla}\Psi^\dagger)\boldsymbol{\nabla}\cdot(\boldsymbol{A}\Psi)+\boldsymbol{\nabla}\cdot(\boldsymbol{A}\Psi^\dagger)(\boldsymbol{\nabla}\Psi)+(\boldsymbol{A}\cdot\boldsymbol{\nabla}\Psi^\dagger)(\boldsymbol{\nabla}\Psi)+(\boldsymbol{\nabla}\Psi^\dagger)(\boldsymbol{A}\cdot\boldsymbol{\nabla}\Psi)]\\&+\frac{q(i\hbar)^2}{4m^3c^2}\boldsymbol{\nabla}\{\boldsymbol{\nabla}\cdot(\boldsymbol{A}\Psi^\dagger\Psi)\}+\frac{q^3}{m^3c^2}(\boldsymbol{A}\cdot\boldsymbol{A})(\Psi^\dagger\boldsymbol{A}\Psi)+\frac{i\hbar q^2\boldsymbol{A}}{2m^3c^2}[\Psi^\dagger(\boldsymbol{A}\cdot\boldsymbol{\nabla}\Psi)-(\boldsymbol{A}\cdot\boldsymbol{\nabla}\Psi^\dagger)\Psi]\\&-\frac{q^2i\hbar}{2m^3c^2}(\boldsymbol{A}\cdot\boldsymbol{A})[(\boldsymbol{\nabla}\Psi^\dagger)\Psi-\Psi^\dagger(\boldsymbol{\nabla}\Psi)]+\frac{q(i\hbar)^2}{4m^3c^2}[\Psi^\dagger(\Delta\Psi)+(\Delta\Psi^\dagger)\Psi]\boldsymbol{A}.\end{aligned}\tag{2.107}$$

This correction is algebraically cumbersome and its practical usefulness in numerical computations may be questioned. It must be pointed out that all terms in $\boldsymbol{j}^{\rm rel}$ dependon the vector potential at least linearly. As we have seen that the self-consistent (internal) vector potential is a second-order quantity, we conclude that, for a purely self-consistent magnetic field, $\boldsymbol{j}^{\rm rel}$ does not contain any contribution at second order. Things could be different, of course, in the case of an external magnetic field, which can be arbitrarily large.

## 2.8 Discussion

Relativistic effects are very important to understand electron dynamics in multiferroics, heavy atoms, dense plasmas, and condensed matter systems excited with intense ultrafast laser pulses. Up to the

order shown in the chapter, the electron spin can couple to the electric field of the static nuclei as well as the self-consistent mean-field generated by other electrons and if present, directly to the magnetic and electric fields of the incident laser pulse. As a result, it may be necessary to go beyond the lowest order description of an electron with spin, i.e. the Pauli equation.

In this chapter, we derived certain models that couple the semi-relativistic Schrödinger or Pauli equation to the Maxwell's equations using the Lagrangian approach. This approach allows us to determine the sources that should be used in the description of the self-generated electromagnetic fields. These sources were derived using the Lorentz gauge, but the results are gauge-invariant, since the exact same sources were derived using Landau's variational principle,[13,23] where the sources were defined as,

$$\delta_\phi \langle H(\phi, \boldsymbol{A}) \rangle = \int q\rho\delta\phi \, \mathrm{d}\tau, \tag{2.108}$$

$$\delta_{\boldsymbol{A}} \langle H(\phi, \boldsymbol{A}) \rangle = \int q\boldsymbol{j} \cdot \delta\boldsymbol{A} \, \mathrm{d}\tau, \tag{2.109}$$

where $\int \mathrm{d}\tau = \int \mathrm{d}\boldsymbol{r} \int \mathrm{d}t$ denotes integration over space and time, $\delta_\phi \langle H(\phi, \boldsymbol{A}) \rangle$ and $\delta_{\boldsymbol{A}} \langle H(\phi, \boldsymbol{A}) \rangle$ denote variations of the expectation value of the energy with respect to the scalar and vector potentials respectively, and the expectation value of the energy $\langle H \rangle$ is given by,

$$\langle H \rangle = \int \Psi^\dagger \hat{H} \Psi \, \mathrm{d}\tau. \tag{2.110}$$

The identical sources obtained by this method, which is gauge-independent, affirms the models developed in this chapter. The Lagrangian method developed is nevertheless much simpler to implement, since the Lagrangian approach uses a single scalar function of the various fields, whereas Landau's method is based on the expectation value of the energy, which involves computing very complicated integrals.

Recently, Hinschberger *et al.* showed that the model derived in this chapter is equivalent to the Breit-Pauli model in the mean-field approximation, or the Hartree-Breit-Pauli model.[32] The Dirac-Breit model is a quantum version for treating a system of $N$ charged particles interacting through electromagnetic fields up to second order in $1/c$, which accounts for magnetic interactions and retardation effects up to second order in $1/c$. Its semi-relativistic expansion up to $c^{-2}$ gives us the Breit-Pauli model, which can point out the different types of two-particle interactions. If the interactions are treated on a mean-field level, we get the Hartree-Breit-Pauli model. However the effective mean-field potential in this model is very large in the number of terms and integrations. It was shown that the current and charge densities that act as sources in the Maxwell's equations are related to the microscopic two-electron interactions in the Breit-Pauli model via the one-electron light-matter operators in the mean-field Hamiltonian. This also lends credence to our model and can eventually be used for systems difficult to compute numerically.

An additional advantage of the Lagrangian approach is the relative ease with which transformations of the wavefunction can be put in. As an example, we consider Lagrangian density for the non-relativistic Schrödinger equation:

$$\mathcal{L}_{\mathrm{S}} = \frac{i\hbar}{2}\left(\Psi^\dagger\dot{\Psi} - \dot{\Psi}^\dagger\Psi\right) - \Psi^\dagger(mc^2 + q\phi)\Psi - \frac{1}{2m}\left[(i\hbar\partial_k - A_k)\Psi^\dagger(-i\hbar\partial_k - qA_k)\Psi\right] \tag{2.111}$$

Using the Madelung transformation, we can study quantum fluid dynamics,[33–38] for instance dense and weakly degenerate electron plasmas created via intense laser pulses as well as astrophysical plasmas.[39] The transformation is given by,

$$\Psi = \sqrt{n}e^{i\chi}, \tag{2.112}$$

where $n$ is the density and $\chi$ the phase. This transformation can be easily inserted in the Lagrangian density $\mathcal{L}_{\mathrm{S}}(\Psi, \Psi^{\dagger}, \phi, \boldsymbol{A}) \rightarrow \mathcal{L}_{\mathrm{S}}(n, \chi, \phi, \boldsymbol{A})$. Using the Euler-Lagrange for $n$ and $\chi$, one can obtain the equations of motion for the density and phase of the fluid. Moreover, these equations already contain the self-consistent or external electromagnetic fields. Extending the Madelung transformation to include spinors can be done[37] and spin dynamics under the influence of internal or external electromagnetic fields can be probed using the Lagrangian approach.

It should be noted that the models developed are limited to the mean-field approximation, although as compared to many mean-field models, the *magnetic* mean-field is included. Extending to account for *beyond-mean-field* phenomena requires exchange and correlation functionals, which are very hard to obtain in the relativistic or semi-relativistic regime.

## 2.9 Conclusions and Perspectives

The purpose of this chapter was to derive a self-consistent mean-field model that incorporates quantum and relativistic effects with spin up to second order in $1/c$. We started with the Foldy-Wouthuysen transformation that gave us the extended Pauli equation from the Dirac equation. We then constructed a Lagrangian density that reproduces the extended Pauli equation through the Euler-Lagrange equations. We added the standard electromagnetic Lagrangian density to include the coupling of the electromagnetic fields described by the Maxwell's equations with the extended Pauli equation that generate the fields. The advantages of this approach is that we automatically got the analytical expressions for the charge and current densities up to second order.
A physical interpretation was then given for each new term appearing in the sources. At zeroth order, we recovered the standard expressions for the Schrödinger density and current. The second order sources contained a free current correction, as well as other terms that were written in the form of a polarisation and a magnetisation density. The magnetisation is linked to the divergence-free *spin current* that already appears in the standard Pauli equation. The polarisation terms were split into a *Darwin* part and a *spin* part. The Darwin polarisation density was shown to originate from the relativistic *Zitterbewegung* (rapid oscillations of the electron trajectory around its mean value), which causes the density to smear out on a distance of the order of the Compton wavelength. The spin polarisation density was interpreted as a Lorentz transformation of the magnetisation density from the electron rest frame to the laboratory frame.
The charge and current densities were derived by using the extended Pauli equation, which is exact up to second order in $1/c$, and coupling it with the Maxwell's equations, which are exact to all orders in $1/c$. In order to treat both on the same footing, the Maxwell's equations were also expanded in orders of $1/c$. With this, we were able to construct a fully self-consistent set of equations that are valid up to second order and maintain certain conservation laws. Several versions of such a model were discussed.

The models derived in this chapter should be useful, for instance, for applications to dense and

weakly degenerate electron plasmas created via intense laser pulses. Other possible areas of application involve inertial confinement fusion, astrophysical plasmas, and nanoparticles or thin films excited with intense ultrafast lasers in the femto- or atto-second domain. Since the magnetic mean-field and time dependence are included, the current density functional theory can be extended to describe electron dynamics with or without external electromagnetic fields.

# 3 Density Functional Theory and PAW Method

## Contents



## 3.1 Introduction

Understanding the properties of different materials requires understanding the behaviour of the electrons in those materials. This is best achieved by studying the electronic structure and thus, development of theoretical approaches that describe a system of interacting electrons and atomic nuclei, is still a challenge in theoretical physics. The main hurdle in achieving this goal is the overwhelming complexity faced when accurately solving a many-body Schrödinger equation that accounts for all interactions, nucleus-nucleus, electron-nucleus and electron-electron. One important approximation that significantly reduces the complexity of the many-body Schrödinger equation is the Born-Oppenheimer approximation,[14,15] itself developed from the *adiabatic approximation*, which is based on the observation that the time-scale associated with the motion of nuclei is usually much slower than that associated with the motion of electrons. The validity of the adiabatic approximation can be seen through the mass ratio of the electron and the nucleus, which, in the worst case of a hydrogen atom, corresponds to a value of about 1:1836, i.e. less than 0.1%. Within a classical picture, this would imply that the average electron velocity is much higher than the nucleic or ionic velocity and for all practical purposes, the ions can be considered stationary during the evolution of the electrons. Since the electrons in this picture follow the nucleic motion, the electronic and nucleic wavefunctions can be decoupled. If the nucleic motion is treated classically as was suggested by Born and Oppenheimer, the approximation is called the Born-Oppenheimer approximation, and the many-body problem reduces to a *many-electron* problem in an external electric field. The correction to the electronic energy

levels due to the quantum nature of the nuclei is calculable and has been shown to be smaller than 0.5%.[16] In this work, as well as in the VASP package, the Born-Oppenheimer approximation is used and the electron and nuclei are decoupled and the nuclei are treated classically. The complete Hamiltonian of the $N$-body electron system and $n$ nuclei (with atomic number $Z_i$, $i = 1, n$) under the Born-Oppenheimer approximation is given by:

$$\hat{H} = -\frac{\hbar^2}{2m}\sum_{i=1}^{N}\nabla_i^2 - \frac{e^2}{4\pi\varepsilon_0}\sum_{i=1}^{N}\sum_{j=1}^{n}\frac{Z_j}{|\boldsymbol{r}_i - \boldsymbol{R}_j|} + \frac{e^2}{8\pi\varepsilon_0}\sum_{i=1}^{N}\sum_{\substack{j=1,\\ j\neq i}}^{N}\frac{1}{|\boldsymbol{r}_i - \boldsymbol{r}_j|}, \tag{3.1}$$

where, $\boldsymbol{r}_i$, $i = 1, N$ are the electron coordinates and $\boldsymbol{R}_i$, $i = 1, n$ are the nuclear coordinates. There are three terms in the above equation, the first is the kinetic energy of the electronic system, the second is the energy contribution due to the nuclear-electron interaction and the last is the energy contribution due to the electron-electron interaction. The electron-electron interaction is very hard to solve in practice and requires further approximations in order to be tractable. This interaction is the focus of intense research, since it, almost single-handedly, defines the electronic structure and thus the properties of different materials.

One of the first approximations developed for solving the many-electron problem was proposed by Hartree,[40] where it was assumed that the many-electron wavefunction can be written as a product of one-electron wavefunctions or orbitals. He also assumed the electrostatic force on each electron would be due to the central potential of the nuclei (the second term in Eq. 3.1) and the field created by the other electrons, also called the Hartree self-consistent field or Hartree potential. Slater[41] showed with the variational principle that the Hatree potential can be obtained from the electron-electron interaction in the many-electron problem by writing the many-electron wavefunction as,

$$\Psi(\boldsymbol{r}_1, \boldsymbol{r}_2, ..., \boldsymbol{r}_N) = \prod_{i=1}^{N}\psi_i(\boldsymbol{r}_i). \tag{3.2}$$

Here, the many-electron wavefunction is expressed as a product of individual one-electron orbitals. Using the variational principle, we get $N$ Schrödinger-like equations for each of the $N$ electrons, typical of single-particle pictures. The single-particle Hamiltonian for the electron $i$ is then given by,

$$\begin{aligned}\hat{H}_i &= -\frac{\hbar^2}{2m}\nabla_i^2 - \frac{e^2}{4\pi\varepsilon_0}\sum_{j=1}^{n}\frac{Z_j}{|\boldsymbol{r}_i - \boldsymbol{R}_j|} + \frac{e^2}{4\pi\varepsilon_0}\int\sum_{\substack{j=1,\\ j\neq i}}^{N}\frac{|\psi_j(\boldsymbol{r}')|^2}{|\boldsymbol{r}_i - \boldsymbol{r}'|}\,\mathrm{d}\boldsymbol{r}' \\ &= -\frac{\hbar^2}{2m}\nabla_i^2 - \frac{e^2}{4\pi\varepsilon_0}\sum_{j=1}^{n}\frac{Z_j}{|\boldsymbol{r}_i - \boldsymbol{R}_j|} + V_H(\boldsymbol{r}_i),\end{aligned} \tag{3.3}$$

where, $V_H(\boldsymbol{r}_i)$ is the Hartree potential due to the other electrons. The single-particle orbitals can be obtained through the Hartree potential in a self-consistent way to construct the many-electron wavefunction. While relatively easy to compute, this approximation has one major issue. Electrons are indistinguishable spin-1/2 fermions, and Pauli's exclusion principle states that two fermions cannot occupy the same quantum state since the many-fermion wavefunction is antisymmetric upon particle exchange. Thus, if two electrons in the many-electron wavefunction are exchanged, the many-electron wavefunction changes sign. The many-electron wavefunction under the Hartree approximation however, can be shown to not change sign under particle exchange and thus the many-electron wavefunction given in Eq. 3.2 is not antisymmetric. Consequently, this approximation fails to provide

the complete description of the electrons. To overcome this, one must include the Pauli's exclusion principle, which can be done by proposing an antisymmetric wave function in the form of a Slater determinant:

$$\Psi(\boldsymbol{r}_1, \boldsymbol{r}_2, ..., \boldsymbol{r}_N) = \frac{1}{\sqrt{N!}} \begin{vmatrix} \psi_1(\boldsymbol{r}_1) & \psi_2(\boldsymbol{r}_1) & \cdots & \psi_N(\boldsymbol{r}_1) \\ \psi_1(\boldsymbol{r}_2) & \psi_2(\boldsymbol{r}_2) & \cdots & \psi_N(\boldsymbol{r}_2) \\ \vdots & \vdots & \ddots & \vdots \\ \psi_1(\boldsymbol{r}_N) & \psi_2(\boldsymbol{r}_N) & \cdots & \psi_N(\boldsymbol{r}_N) \end{vmatrix}, \tag{3.4}$$

where, $\psi_i(\boldsymbol{r}_j)$ is the $i^{\text{th}}$ electron with spatial coordinates $\boldsymbol{r}_j$. The Slater determinant can be easily extended to include the spin quantum number $\sigma_i$ as well. Such a formalism is not fully general, but includes the particle exchange in an exact manner, i.e. the many-electron wavefunction changes sign when the coordinates (or spin) of two electrons are exchanged.[42,43] The approximation of postulating the wavefunction as shown in Eq. 3.4 is known as the Hartree-Fock approximation. The Hamiltonian for a single-particle orbital in this approximation is then given by,

$$\begin{aligned} \hat{H}_i\psi_i(\boldsymbol{r}) = &-\frac{\hbar^2}{2m}\nabla_i^2\psi_i(\boldsymbol{r}) - \frac{e^2}{4\pi\varepsilon_0}\sum_{j=1}^{n}\frac{Z_j}{|\boldsymbol{r}-\boldsymbol{R}_j|}\psi_i(\boldsymbol{r}) + \frac{e^2}{4\pi\varepsilon_0}\int\sum_{\substack{j=1,\\ j\neq i}}^{N}\frac{|\psi_j(\boldsymbol{r}')|^2}{|\boldsymbol{r}-\boldsymbol{r}'|}\psi_i(\boldsymbol{r})\,\mathrm{d}\boldsymbol{r}' \\ &- \frac{e^2}{4\pi\varepsilon_0}\int\sum_{\substack{j=1,\\ j\neq i}}^{N}\frac{\psi_j^\star(\boldsymbol{r}')\psi_i(\boldsymbol{r}')}{|\boldsymbol{r}-\boldsymbol{r}'|}\psi_j(\boldsymbol{r})\,\mathrm{d}\boldsymbol{r}'. \end{aligned} \tag{3.5}$$

Comparing it with Eq. 3.3, we observe that there is an additional term, the last term, called the *exchange* integral, which arises due to the antisymmetric nature of the many-electron wavefunction. Additionally, this term is non-local, i.e. it depends on the location of the other electrons. This statement can be understood by considering an additional quantum number, the spin quantum number. Due to the Pauli's exclusion principle, electrons with the same spin do not like to be close to each other and an electron with spin $\sigma_i$ at position $\boldsymbol{r}_i$ is 'pushed away' from an electron with the same spin at position $\boldsymbol{r}_j$. Therefore, the non-locality of the exchange interaction is fully taken into account in this approximation. However, the Hartree-Fock picture still describes a single-particle in a mean-field generated by the other electrons, and there are many Post-Hartree-Fock methods, like the configuration interaction method,[44] multi-configurational methods, perturbative methods and explicity correlated methods.[15] For our calculations, we continue to work within the single-particle picture, but based on a line of thought different from that developed by Hartree. Known as the density functional theory (DFT), it was initially developed by Thomas and Fermi[45,46] who proposed that the full electronic density was the fundamental variable of the many-electron problem and independently gave a prescription for calculating the energy of an electronic system in terms of the electronic density. Both of them gave an expression for the total energy, where the kinetic, exchange and correlation contributions were developed from the homogenous electron gas solution, for which very good solutions were known. Though intuitively developed in the hopes that the energy can be written completely in terms of the electron density, the solid mathematical foundation required for DFT was only proved in 1964 by Hohenberg and Kohn,[47] the development of which is shown in the subsequent section.

## 3.2 Density Functional Theory

The development of the post-Thomas-Fermi DFT began with the Hohenberg-Kohn theorems[47] shown below:

**Theorem 1:** The external potential is univocally determined by the electron density, up to a trivial additive constant.
**Corollary:** Since the electron density uniquely determines the external potential, it also determines the ground state wave function through the Schrödinger equation and thus, all the ground state properties of the system.

**Theorem 2:** The ground state energy is obtained variationally, and the density that minimises the total energy is the ground state density.

These two theorems form the backbone of the DFT framework, whose main idea is that instead of dealing with the many-electron problem, one deals with the electron density problem. To understand this in a more formal way, we consider a many-electron Hamiltonian under the Born-Oppenheimer approximation (Eq. 3.1) and rewrite it as,

$$\hat{H} = \hat{T} + \hat{V}_{\text{ext}} + \hat{U}_{ee}, \tag{3.6}$$

where, $\hat{T}$ is the kinetic energy operator, $\hat{V}_{\text{ext}}$ is the external potential mentioned in Theorem 1, which also includes the contribution of the Coulomb interaction between the electrons and ions, and $\hat{U}_{ee}$ is the electron-electron interaction. The external potential for an electronic system with atomic nuclei is given by,

$$\hat{V}_{\text{ext}}(\boldsymbol{r}) = -\frac{e^2}{4\pi\varepsilon_0}\sum_{j=1}^{n}\frac{Z_j}{|\boldsymbol{r}-\boldsymbol{R}_j|} \tag{3.7}$$

similar in form as shown earlier. Under the DFT formalism, we have the total energy of the system, $E[\rho(\boldsymbol{r})]$, represented as a functional of the density $\rho(\boldsymbol{r})$ and expressed as,

$$E[\rho] = \langle\Psi[\rho]|\hat{H}|\Psi[\rho]\rangle = F[\rho] + \int \hat{V}_{\text{ext}}\rho(\boldsymbol{r})\,\mathrm{d}\boldsymbol{r}, \tag{3.8}$$

where, $\Psi[\rho]$ is the ground state of a potential with $\rho(\boldsymbol{r})$ as its ground state density and $F[\rho] = \langle\Psi[\rho]|\hat{T}+\hat{U}_{ee}|\Psi[\rho]\rangle$. Knowledge of $F[\rho]$ implies the knowledge of the solution of the many-electron Schrödinger equation. Moreover, $F[\rho]$ is a *universal* functional, which does not depend on the external potential, but only on the electron density. Thus, using DFT, it is possible to determine the electronic ground state density and energy exactly, and thereby the other ground state properties, if $F[\rho]$ is known. In fact, since the ground state density uniquely determines the external potential, it is possible to determine the many-electron wavefunctions, both ground and *excited* states. In this work, we focus on DFT related to ground state, a scheme that was developed by Kohn and Sham in 1965,[48] and there are many extensions and generalisations of this scheme for excited states, such as ensemble DFT,[49] time-dependent density functional theory (TDDFT),[50] the GW approximation[51] and other generalisations of the Kohn-Sham formalism.[52]

### 3.2.1 Kohn-Sham Approach

As described earlier, the knowledge of $F[\rho]$ is very critical to understand electron behaviour and thereby ground state properties of the system. However, even though $F[\rho]$ is universal, the exact functional forms of the kinetic energy and the electron-electron interaction in terms of the density

are unknown. In 1965, Kohn and Sham proposed an approach, which replaces the interacting many-electron system with a fictitious system of non-interacting electrons in a fictitious effective potential $v_{\text{eff}}$. This fictitious non-interacting system generates the same ground state density as that of the original interacting system. Thus, the Schrödinger equations for the Kohn-Sham non-interacting particles $\psi_i(\boldsymbol{r})$ are,

$$\hat{H}\psi_i(\boldsymbol{r}) = \left[-\frac{\hbar^2}{2m}\nabla_i^2 + v_{\text{eff}}\right]\psi_i(\boldsymbol{r}) = \epsilon_i\psi_i(\boldsymbol{r}), \tag{3.9}$$

where the effective potential is given by,

$$v_{\text{eff}} = \hat{V}_{\text{ext}} + V_H + V_{xc}, \tag{3.10}$$

with $\hat{V}_{\text{ext}}$ as the external potential generated by the nuclei as in Eq. 3.7, $V_H$ as the Hartree potential corresponding to the electron-electron electrostatic interaction similar in form to that in Eq. 3.3 and $V_{xc}$ as the exchange-correlation potential, which contains all the difficult many-electron interactions. The density of the Kohn-Sham fictitious system is constructed from the non-interacting particles as,

$$\rho(\boldsymbol{r}) = \sum_i^N |\psi_i(\boldsymbol{r})|^2, \tag{3.11}$$

which, based on the Kohn-Sham *ansatz*, is the same as the density of the interacting system. The ground state energy functional in the Kohn-Sham approach is given as,

$$E_{\text{KS}}[\rho(\boldsymbol{r})] = T_0[\rho(\boldsymbol{r})] + \int \left(\hat{V}_{\text{ext}} + V_H\right)\rho(\boldsymbol{r})\,\mathrm{d}\boldsymbol{r} + E_{xc}[\rho(\boldsymbol{r})], \tag{3.12}$$

where the exchange-correlation potential $V_{xc}$ contributes $E_{xc}[\rho]$ to the energy functional and the kinetic energy contribution $T_0[\rho]$ is represented as a functional of the density as follows:

$$T_0[\rho(\boldsymbol{r})] = \sum_{\substack{i \\ \text{occupied}}} -\frac{\hbar^2}{2m}\langle\psi_i|\nabla^2|\psi_i\rangle. \tag{3.13}$$

To extend the Kohn-Sham approach to spin-polarised systems, it is sufficient to consider the total electron density as a sum of the two independent spin densities, $\rho = \rho_\uparrow + \rho_\downarrow$. The interaction between the two spin components can be transferred into the exchange-correlation contribution $E_{xc}[\rho_\uparrow, \rho_\downarrow]$. The total ground state energy is written as,

$$E_{\text{KS}}[\rho_\uparrow, \rho_\downarrow] = T_0[\rho_\uparrow, \rho_\downarrow] + \int \left(\hat{V}_{\text{ext}} + V_H\right)\rho(\boldsymbol{r})\,\mathrm{d}\boldsymbol{r} + E_{xc}[\rho_\uparrow, \rho_\downarrow], \tag{3.14}$$

with the kinetic energy term given as,

$$T_0[\rho(\boldsymbol{r})] = \sum_{\substack{i,s \\ \text{occupied}}} -\frac{\hbar^2}{2m}\langle\psi_{i,s}|\nabla^2|\psi_{i,s}\rangle, \tag{3.15}$$

where $s = 1, 2$ denotes the spin. The spin-polarised DFT is also known as the spin-density functional theory (SDFT) and it assumes that the spin is a good quantum number.

The self-consistent nature of the problem arises due to the fact that the Kohn-Sham particle states $\psi_i$ depend on the effective potential $v_{\text{eff}}$, which is a function of the density $\rho$ that depends on the Kohn-Sham particle states. The accuracy of the ground state density and energy is highly limited by the approximation in the exchange-correlation functional, since its exact form is unknown. Even though, the energy contribution due to the term $E_{xc}$ is small, it plays a vital role in defining the mechanisms of chemical bonding. It is hence necessary to describe expressions of the exchange-correlation potential used in this work.

### 3.2.2 Exchange-Correlation Potentials

As described previously, the exchange-correlation potential defines the chemical bonding between ions. Of the different expressions that approximate this potential, two were used in our work, the *local density approximation* (LDA) and the *generalised gradient approximation* (GGA). The expression for the LDA was first proposed by Kohn and Sham,[48] but the philosophy was present in the early DFT approach by Thomas and Fermi. The idea of the LDA is to consider a general inhomogeneous electron system as locally homogeneous, and then use the exchange-correlation potential corresponding to the homogeneous electron gas, the expression of which is known to an excellent accuracy through Quantum Monte Carlo methods by Ceperley and Alder,[53] and parametrisation by Perdew and Zunger.[54] The density functional for the exchange-correlation energy under the LDA is expressed as,

$$E_{xc}^{\text{LDA}}[\rho(\boldsymbol{r})] = \int \rho(\boldsymbol{r})\, \epsilon_{xc}^{\text{homo}}[\rho(\boldsymbol{r})]\, \mathrm{d}\boldsymbol{r}, \tag{3.16}$$

where, $\epsilon_{xc}^{\text{homo}}$ is the exchange-correlation energy density in a homogeneous electron gas. To extend the LDA to spin-polarised systems (local spin density approximation or LSDA), the expression of the exchange-correlation energy density is replaced with a spin-polarised expression,

$$E_{xc}^{\text{LSDA}}[\rho(\boldsymbol{r})] = \int \left[\rho_{\uparrow}(\boldsymbol{r}) + \rho_{\downarrow}(\boldsymbol{r})\right]\, \epsilon_{xc}^{\text{homo}}[\rho_{\uparrow}(\boldsymbol{r}), \rho_{\downarrow}(\boldsymbol{r})]. \tag{3.17}$$

Due to the fact that the LDA is derived from a homogeneous gas, it is exact for a system with uniform density, and good enough for systems with densities that vary slowly in space. Thus, it is generally valid for describing systems with relatively homogeneous densities, like simple crystalline metals, and fails for systems with higher inhomogeneity, like isolated atoms, molecules, semi-conductors and insulators. The limitations of the LDA-LSDA are discussed by Kohanoff and the interested reader is directed to it for further information.[15]

The failure of the LDA to describe inhomogeneous systems is usually overcome by using the generalised gradient approximation (GGA), where along with the local density, the local gradient of the density is included in the expression of the exchange-correlation functional. There are many ways proposed for this functional that modify the behaviour at large gradient values to preserve desired properties. However, exchange-correlation functional under the GGA has a common expression of the form,

$$E_{xc}^{\text{GGA}}[\rho(\boldsymbol{r})] = \int \rho(\boldsymbol{r})\, \epsilon_{xc}^{\text{homo}}[\rho(\boldsymbol{r})]\; F_{xc}\left[\rho(\boldsymbol{r}), |\boldsymbol{\nabla}\rho(\boldsymbol{r})|\right]\, \mathrm{d}\boldsymbol{r}, \tag{3.18}$$

where the functional $F_{xc}$ is an enhancement factor that modifies the LDA expression in Eq. 3.16, according to the variation of the density, $\boldsymbol{\nabla}\rho(\boldsymbol{r})$, in the neighbourhood of the considered point, $\boldsymbol{r}$. Hence, the GGA corrections intuitively provide semi-local corrections, and would thus fail to account

for non-local effects at longer ranges. There are three most widely used forms of expressing $F_{xc}$, by Becke (called B88),[55] by Perdew and Wang (called PW91),[56] and by Perdew, Burke and Enzerhof (called PBE).[57,58] Extension to spin-polarised cases is similar to as done previously with the LSDA expression in Eq. 3.17, with the enhancement factor modified as $F_{xc}[\rho, \zeta, s]$, where $\rho = \rho_\uparrow + \rho_\downarrow$ is the total density, $\zeta = \rho_\uparrow - \rho_\downarrow$ is the magnetisation density and $s = \frac{|\boldsymbol{\nabla}\rho(\boldsymbol{r})|}{2k_\mathrm{F}\rho}$ is the dimensionless density gradient, with $k_\mathrm{F}$ as the Fermi wave-vector.

Both LDA and GGA, along with their spin-polarised analogs, break down in treating materials in which electrons are localised and strongly correlated, such as transition metal oxides and rare earth elements.[59,60] These systems have localised atomic-like electron states from the $d$ and $f$ atomic states, and de-localised band-like electron states from the $s$ and $p$ atomic states. Both LDA and GGA provide orbital-independent potentials, which produce incorrect occupancies for the localised states, thereby leading to an incorrect description of the physical properties of such materials. To circumvent this, the LDA+$U$ method and its derivatives as proposed by Anisimov *et al.* are generally used.[61] In this work, the method as proposed by Lichtenstein *et al.* is used and described in the following subsection.[62]

### 3.2.3 LDA+$U$ Method

The Hubbard model, also known as the LDA+$U$ or LSDA+$U$ model, is used to correctly describe strongly correlated, localised $d$ and $f$ electrons. In typical implementations, two 'free' parameters are available, $U$, the screened Coulomb parameter, and $J$, the exchange parameter. In the original work by Lichtenstein *et al.*,[62] the generalised LSDA+$U$ functional was described as,

$$E^{\mathrm{LDA}+U}[\rho_s(\boldsymbol{r}), \{\rho_s\}] = E^{\mathrm{LSDA}}[\rho_s(\boldsymbol{r})] + E^U[\{\rho\}] - E_{dc}[\{\rho_s\}], \tag{3.19}$$

where, $E^{\mathrm{LSDA}}[\rho_s(\boldsymbol{r})]$ is the standard LSDA functional, $\rho_s(\boldsymbol{r})$ is the charge density for electrons with spin $s$, and $\{\rho_s^{mm'}\}$ form the density matrix for the correlated electrons with $m$ of the $d$ or $f$ correlated electrons, the magnetic quantum number. $E^U$ is described by the mean-field (Hartree-Fock) type of theory and contains the *screened* Coulomb electron-electron interactions, which is given by,

$$\begin{aligned} E^U[\{\rho\}] =& \frac{1}{2}\sum_{\{m\},s} \langle m, m''|\hat{U}_{ee}|m', m'''\rangle \rho_s^{mm'}\rho_{-s}^{m''m'''} - \langle m, m''|\hat{U}_{ee}|m', m'''\rangle \rho_s^{mm'}\rho_s^{m''m'''} \\ &- \langle m, m''|\hat{U}_{ee}|m''', m'\rangle \rho_s^{mm'}\rho_s^{m''m'''}, \end{aligned} \tag{3.20}$$

where $\hat{U}_{ee}$ is the screened Coulomb interaction among the localised electrons. The last term $E_{dc}$ corrects for double counting and is given by,

$$E_{dc}[\{\rho_s\}] = \frac{U}{2}n(n-1) - \frac{J}{2}\left[n_\uparrow(n_\uparrow - 1) + n_\downarrow(n_\downarrow - 1)\right], \tag{3.21}$$

where $n_s = \mathrm{Tr}(\rho_s^{mm'})$ and $n = n_\uparrow + n_\downarrow$. $U$ and $J$ are the screened Coulomb and exchange parameters respectively. The effective single particle Hamiltonian is,

$$\hat{H} = \hat{H}^{\mathrm{LDA}} + \sum_{mm'} |in\ell ms\rangle V^s_{mm'} \langle in\ell m's|, \tag{3.22}$$

where $i$ denotes the site, $n$ the main quantum number and $\ell$ the orbital quantum number, and the effective single particle potential is expressed as,

$$\begin{aligned} V^s_{mm'} = &\sum_{\{m\}} \langle m, m''|\hat{U}_{ee}|m', m'''\rangle \rho^{m''m'''}_{-s} - \langle m, m''|\hat{U}_{ee}|m', m'''\rangle \rho^{m''m'''} \\ &- \langle m, m''|\hat{U}_{ee}|m''', m'\rangle \rho^{m''m'''} - U\left(n - \frac{1}{2}\right) + J\left(n^s - \frac{1}{2}\right). \end{aligned} \tag{3.23}$$

The values of $U$ and $J$ could be determined using constrained DFT calculations.[63–65] In typical implementations however, $U$ and $J$ are treated as parameters, adjusted to reach agreement with experiment, for example, with the equilibrium volume, magnetic moment or energy band gap. This model reproduces the behaviour of Mott-Hubbard insulators, where strong correlations induce the opening of an energy gap. Since, LDA and GGA typically underestimate band gaps, the LDA+$U$ is generally used to improve the band gap. The accuracy of the LDA+$U$ approach is limited by the treatment of strong correlations with a mean-field. Moreover, the $U$ and $J$, if used parametrically, may not necessarily reflect the actual physical phenomena in different materials, since they change the localisation and thus, the hybridisation and chemical bonding of the $d$ and $f$ electrons.

## 3.3 Relativistic DFT

DFT and spin-polarised DFT are incomplete in that the spin and orbital angular momenta are not coupled. This is because they are Galilean invariant and not Lorentz invariant. To treat the core electrons for larger atoms or very fast valence electrons, one needs to perform fully-relativistic calculations employing the Dirac equation, where the spin and orbital angular momenta are coupled through spin-orbit coupling (SOC). This means that the spin or the magnetic quantum numbers are not good quantum numbers, and the projection of the *total* angular momentum on the $z$-axis is a good quantum number. Moreover, relativistic calculations explain magnetic anisotropy by coupling the spins to the orbital momenta and thereby to the lattice. In non-relativistic calculations, the orbital moments are always quenched in solids and the electron spins are free to rotate (together) without any energy cost. By including relativistic effects, this freedom of the spins is removed and the orbital moments in certain systems take on non-zero values.[6] As a result, DFT was extended to the relativistic density functional theory (RDFT, also the Kohn-Sham-Dirac formalism),[12] where analogous to the Schrödinger equations for the Kohn-Sham particles in an effective potential $v_{\text{eff}}$, one has the Dirac equation for the fictitious particles in an effective four-vector field $A^\mu_{\text{eff}} = (v_{\text{eff}}/ec, \boldsymbol{A}_{\text{eff}})$ given by,

$$\hat{H}_i\psi_i = \left[c\boldsymbol{\alpha}\cdot(\hat{\boldsymbol{p}} - e\boldsymbol{A}_{\text{eff}}) + \beta mc^2 + e\phi_{\text{eff}}\right]\psi_i(\boldsymbol{r}) = \epsilon_i\psi_i \tag{3.24}$$

where $\phi_{\text{eff}} = v_{\text{eff}}/e$ is the scalar potential, $\boldsymbol{A}_{\text{eff}}$ is the vector potential and $c$ is the speed of light in vacuum. $\psi_i(\boldsymbol{r})$ is the four-component Dirac bi-spinor with corresponding particle energies $\epsilon_i$. $\boldsymbol{\alpha}$ and $\beta$ are the $4\times 4$ Dirac matrices expressed as,

$$\begin{aligned} \boldsymbol{\alpha} &= \begin{pmatrix} 0 & \boldsymbol{\sigma} \\ \boldsymbol{\sigma} & 0 \end{pmatrix}, \\ \beta &= \begin{pmatrix} \mathbf{I}_2 & 0 \\ 0 & \mathbf{I}_2 \end{pmatrix}, \end{aligned} \tag{3.25}$$

where, $\boldsymbol{\sigma}$ are the Pauli matrices defined as:

$$\sigma_x = \begin{pmatrix} 0 & 1 \\ 1 & 0 \end{pmatrix}; \qquad \sigma_y = \begin{pmatrix} 0 & -i \\ i & 0 \end{pmatrix}; \qquad \sigma_z = \begin{pmatrix} 1 & 0 \\ 0 & -1 \end{pmatrix}; \tag{3.26}$$

and $\mathbf{I}_2$ is a $2 \times 2$ identity matrix. Analogous to the density in non-relativistic DFT, one has the four-component current $J^\mu = (c\rho, \boldsymbol{j})$, where $\rho$ is the electron density and $\boldsymbol{j}$ is the probability current density given by,

$$\begin{aligned} \rho &= -\sum_i \psi_i^\dagger \psi_i, \\ \boldsymbol{j} &= -\sum_i \psi_i^\dagger \boldsymbol{\alpha} \psi_i. \end{aligned} \tag{3.27}$$

While, the RDFT treats the spin and orbital momenta coupling exactly, this is computationally very demanding. With the intention of making electronic structure calculations faster while maintaining certain relativistic features, one needs to enter semi-relativistic limits, where the particle and anti-particle states are decoupled and we get Schrödinger-type and Pauli-type equations up to different orders in $1/c$. As was shown in the previous chapter, this can be achieved with the Foldy-Wouthuysen transformation, where we get an extended Pauli-type equation, this time with $A^\mu_{\text{eff}}$ as the fields,

$$\begin{aligned} \hat{H} =& mc^2 + e\phi_{\text{eff}} + \frac{(\hat{\boldsymbol{p}} - e\boldsymbol{A}_{\text{eff}})^2}{2m} - \frac{e\hbar}{2m}\boldsymbol{\sigma} \cdot (\boldsymbol{\nabla} \times \boldsymbol{A}_{\text{eff}}) + \frac{e\hbar}{4m^2c^2}\boldsymbol{\sigma} \cdot [(\boldsymbol{\nabla}\phi_{\text{eff}} + \partial_t \boldsymbol{A}_{\text{eff}}) \times (\hat{\boldsymbol{p}} - e\boldsymbol{A}_{\text{eff}})] \\ &+ \frac{e\hbar^2}{8m^2c^2}\left[\Delta\phi_{\text{eff}} + \boldsymbol{\nabla} \cdot \partial_t \boldsymbol{A}_{\text{eff}} - \boldsymbol{\sigma} \cdot (\hat{\boldsymbol{p}} \times \partial_t \boldsymbol{A}_{\text{eff}})\right]. \end{aligned} \tag{3.28}$$

To reach a formalism for DFT with some relativistic effects, we can set $\boldsymbol{A}_{\text{eff}} = 0$, which is similar to non-relativistic DFT under only $v_{\text{eff}}$. Thus, using $e\phi_{\text{eff}} = v_{\text{eff}}$ and some algebra, we have,

$$\hat{H} = mc^2 + \frac{\hat{\boldsymbol{p}}^2}{2m} + v_{\text{eff}} + \frac{\hbar}{4m^2c^2}\boldsymbol{\sigma} \cdot (\boldsymbol{\nabla} v_{\text{eff}} \times \hat{\boldsymbol{p}}) + \frac{\hbar^2}{8m^2c^2}\Delta v_{\text{eff}}, \tag{3.29}$$

where the first term is the energy due to the rest mass, the second and third terms are those also present in the non-relativistic DFT, the fourth term is the SOC and the last term is the Darwin term. The rest mass term is a constant and merely shifts the energy of the electronic structure and thus can be removed from the calculations. If we consider that the effective potential is mainly created by the external potential of the ions and that these potentials vary very slowly, then the Darwin term can be neglected. The SOC term can be written as,

$$\hat{H}_{\text{SOC}} = \frac{\hbar}{4m^2c^2}\boldsymbol{\sigma} \cdot (\boldsymbol{\nabla} v_{\text{eff}} \times \hat{\boldsymbol{p}}) = \frac{\hbar}{4m^2c^2}\frac{1}{r}\frac{\partial v_{\text{eff}}}{\partial r}\boldsymbol{\sigma} \cdot (\hat{\boldsymbol{r}} \times \hat{\boldsymbol{p}}) = \frac{\hbar}{4m^2c^2}\frac{1}{r}\frac{\partial v_{\text{eff}}}{\partial r}\boldsymbol{L} \cdot \boldsymbol{\sigma}. \tag{3.30}$$

This term is relatively easy to compute since the term $\frac{1}{r}\frac{\partial v_{\text{eff}}}{\partial r}$ is important only near the nucleus, where the effective potential changes rapidly, and thus in codes which use augmented basis sets, this term only needs to be computed for the augmentation regions. In this work, we employed the *projector augmented wave* (PAW) method, an augmented basis set proposed by Blöchl,[66] which is described in the following section.

## 3.4 Projector Augmented Wave Method

The projector augmented wave (PAW) method is a general augmentation scheme that combines the linear augmented plane wave (LAPW) and the pseudopotential methods. Proposed by Blöchl in

1994,[66] it uses the frozen core approximation, wherein the core states are 'frozen' to the isolated atom states, since they are slightly affected upon bond formation. This is similar to the pseudopotential methods, where only the valence electrons participate to chemical bonding under a pseudopotential generated by the nucleus and the frozen core electrons. The electron wavefunction is decomposed in two regions, the augmentation and interstitial regions, thereby generalising the LAPW method. The idea of PAW is based on the observation used in other augmented schemes that the electron wavefunctions have different form in different regions of space: they vary smoothly between the atoms due to weak potentials, while they oscillate rapidly near the nuclei due to the strong potential and the nodes generated by the atomic-like orbitals to maintain orthogonality. This gives us two regions:

- *Augmentation Region* – consists of non-overlapping atom-centred spheres of cutoff radius $r_c^a$, where $a$ is the atom's index.
- *Interstitial Region* – covers all the remaining space outside the augmented region.

The idea is then to expand the wavefunctions of the valence electrons as plane waves in the interstitial region, and as atomic-like partial waves in the augmentation region. It is imperative that the wavefunctions and their derivatives are assured to be continuous at the boundaries of the augmented spheres to maintain a continuity of the wavefunction and its derivative across all space. The PAW formalism is based on a linear transformation $\hat{T}$ that transforms the all-electron wavefunction $|\psi_{n\boldsymbol{k}}\rangle$ into a fictitious pseudo-wavefunction $|\widetilde{\psi_{n\boldsymbol{k}}}\rangle$,

$$|\psi_{n\boldsymbol{k}}\rangle = \hat{T}|\widetilde{\psi_{n\boldsymbol{k}}}\rangle, \tag{3.31}$$

where $n$ and $\boldsymbol{k}$ represent the band and $\boldsymbol{k}$-vector indexes respectively. The transformation is defined as:

$$\hat{T} = 1 + \sum_a \hat{T}^a, \tag{3.32}$$

where $\hat{T}^a$ are transformations which act only within the augmentation region of an atom with index $a$. This ensures that the all-electron wavefunction and the pseudo-wavefunctions match outside the augmentation regions. Inside the augmentation region, the all-electron wavefunction is expanded into all-electron partial waves $|\phi_i^a\rangle$, to each of which is defined a smooth pseudo-partial waves $|\widetilde{\phi_i^a}\rangle$ such that,

$$|\phi_i^a\rangle = (1 + \hat{T}^a)|\widetilde{\phi_i^a}\rangle, \tag{3.33}$$

where $i$ represents the atomic quantum numbers. Thus, each all-electron partial wave matches its corresponding pseudo-partial wave. Further, these pseudo-partial waves form a complete set within the augmentation region so that every pseudo-wavefunction can be expanded into pseudo-partial waves:

$$|\widetilde{\psi_{n\boldsymbol{k}}}\rangle = \sum_{i,a} c_{i,a}^{n\boldsymbol{k}} |\widetilde{\phi_i^a}\rangle, \tag{3.34}$$

with $c_{i,a}^{n\boldsymbol{k}}$ being the expansion coefficients. For the transformation $\hat{T}$ to remain linear, the coefficients should be linear functionals of the pseudo-wavefunction. Thus,

$$c_{i,a}^{n\boldsymbol{k}} = \langle \widetilde{p_{i,a}} | \widetilde{\psi_{n\boldsymbol{k}}} \rangle, \tag{3.35}$$

where $\widetilde{|p_{i,a}\rangle}$ are some functions called projector functions such that there is exactly one projector function for each pseudo-partial wave. Moreover, inside the augmentation region, they satisfy the following conditions:

$$\begin{aligned} \sum_i \widetilde{|\phi_i^a\rangle}\widetilde{\langle p_{i,a}|} &= 1, \\ \widetilde{\langle p_{i,a}|}\widetilde{|\phi_j^a\rangle} &= \delta_{i,j}. \end{aligned} \tag{3.36}$$

Thus, the linear transformation is written as:

$$\hat{T} = 1 + \sum_{i,a} \left( |\phi_i^a\rangle - \widetilde{|\phi_i^a\rangle} \right) \widetilde{\langle p_{i,a}|}, \tag{3.37}$$

and the all-electron Kohn-Sham wavefunction is obtained from the pseudo-wavefunction as:

$$|\psi_{n\boldsymbol{k}}\rangle = \widetilde{|\psi_{n\boldsymbol{k}}\rangle} + \sum_{i,a} \left( |\phi_i^a\rangle - \widetilde{|\phi_i^a\rangle} \right) \langle \widetilde{p_{i,a}}|\widetilde{\psi_{n\boldsymbol{k}}}\rangle. \tag{3.38}$$

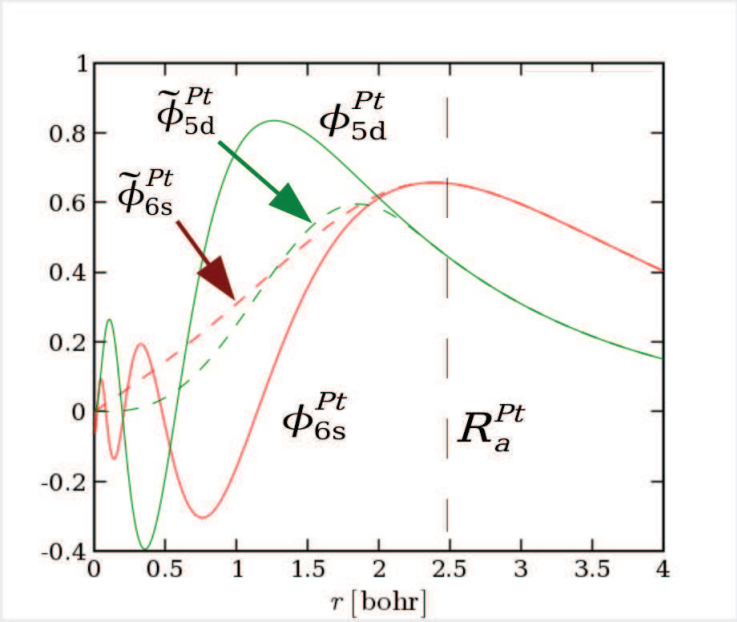


**Figure 3.1:** An illustration of the radial partial waves and the corresponding pseudo-partial waves for Platinum in the PAW basis with $R_a^{Pt}$, called $r_c{}^{Pt}$ in the text, as the radius of the augmentation sphere.

The advantage of this representation is that the pseudo-partial waves can be chosen to be smooth and not oscillating like the all-electron partial waves, which are computationally easier to treat, an illustration of which is shown in Fig. 3.1. In the PAW representation, it is thus the pseudo-wavefunction $\widetilde{|\psi_{n\boldsymbol{k}}\rangle}$ that is computed and the physical all-electron wavefunction is obtained through the transformation in Eq. 3.37. As a result, the observables must be given in the form of expectation values of the pseudo-wavefunction. A detailed description of how to compute the expectation value of any operator $A$ and the charge density is provided in the original work by Blöchl[66] and only the basic steps are shown here. We begin by calculating the expectation value of an operator $A$, which is transformed into a pseudo-operator $\widetilde{A}$ acting on the pseudo-wavefunction with the same expectation value. Thus,

$$\langle A \rangle = \sum_{n\boldsymbol{k}} f_{n\boldsymbol{k}} \langle \psi_{n\boldsymbol{k}}|A|\psi_{n\boldsymbol{k}}\rangle = \sum_{n\boldsymbol{k}} f_{n\boldsymbol{k}} \langle \widetilde{\psi_{n\boldsymbol{k}}}|\widetilde{A}|\widetilde{\psi_{n\boldsymbol{k}}}\rangle, \tag{3.39}$$

where $f_{n\boldsymbol{k}}$ is the Fermi distribution of the state $|n,\boldsymbol{k}\rangle$. Using the definition of $\hat{T}$, we get $\widetilde{A} = \hat{T}^\dagger A \hat{T}$ which when expanded using Eq. 3.37 gives us,

$$\begin{aligned}\widetilde{A} =& A + \sum_{i,j} |\widetilde{p}_i\rangle \left( \langle\phi_i|A|\phi_j\rangle - \langle\widetilde{\phi}_i|A|\widetilde{\phi}_j\rangle \right) \langle\widetilde{p}_j| \\ &+ \sum_i \left\{ |\widetilde{p}_i\rangle \left( \langle\phi_i| - \langle\widetilde{\phi}_i| \right) A \left( 1 - \sum_j |\widetilde{\phi}_j\rangle\langle\widetilde{p}_j| \right) + \left( 1 - \sum_j |\widetilde{p}_j\rangle\langle\widetilde{\phi}_j| \right) A \left( |\phi_i\rangle - |\widetilde{\phi}_i\rangle \right) \langle\widetilde{p}_i| \right\},\end{aligned} \tag{3.40}$$

where the first two terms in the last are the local contribution and the last term is the non-local contribution. Thus, for local operators, only the first two terms are required. An example would be the density operator $|\boldsymbol{r}\rangle\langle\boldsymbol{r}|$, the expectation value of which is the charge density $\rho(\boldsymbol{r})$. Since it is local, we use only the first two terms of Eq. 3.40 to get,

$$\begin{aligned}\rho(\boldsymbol{r}) =& \sum_{n\boldsymbol{k}} f_{n\boldsymbol{k}} \langle\psi_{n\boldsymbol{k}}|\boldsymbol{r}\rangle\langle\boldsymbol{r}|\psi_{n\boldsymbol{k}}\rangle = \sum_{n\boldsymbol{k}} f_{n\boldsymbol{k}} \langle\widetilde{\psi_{n\boldsymbol{k}}}|\widetilde{\boldsymbol{r}}\rangle\langle\widetilde{\boldsymbol{r}}|\widetilde{\psi_{n\boldsymbol{k}}}\rangle \\ =& \sum_{n\boldsymbol{k}} f_{n\boldsymbol{k}} \left\{ \langle\widetilde{\psi_{n\boldsymbol{k}}}|\boldsymbol{r}\rangle\langle\boldsymbol{r}|\widetilde{\psi_{n\boldsymbol{k}}}\rangle + \sum_{i,j} \langle\widetilde{\psi_{n\boldsymbol{k}}}|\widetilde{p}_i\rangle\langle\phi_i|\boldsymbol{r}\rangle\langle\boldsymbol{r}|\phi_j\rangle\langle\widetilde{p}_j|\widetilde{\psi_{n\boldsymbol{k}}}\rangle - \sum_{i,j} \langle\widetilde{\psi_{n\boldsymbol{k}}}|\widetilde{p}_i\rangle\langle\widetilde{\phi}_i|\boldsymbol{r}\rangle\langle\boldsymbol{r}|\widetilde{\phi}_j\rangle\langle\widetilde{p}_j|\widetilde{\psi_{n\boldsymbol{k}}}\rangle \right\} \\ =& \widetilde{\rho}(\boldsymbol{r}) + \rho^1(\boldsymbol{r}) - \widetilde{\rho}^1(\boldsymbol{r}).\end{aligned} \tag{3.41}$$

In other words, a pseudo-charge density $\widetilde{\rho}$ is constructed, which is identical to the charge density outside the augmentation region, and is smooth inside. The electron density $\rho^1$ contains the contribution due to the all-electron partial waves and $\widetilde{\rho}^1$ removes the contribution of $\widetilde{\rho}$ inside the augmentation region.

Other operators can be similarly transformed into pseudo-operators and the contributions due to the different regions can be summed up. The charge density as computed in Eq. 3.41 was essentially due to a local operator and hence had a more compact expression. The total energy as well as any other local operator can be computed using a similar expression.

# 4 Electronic, Magnetic and Magnetoelectric Properties of Gallium Ferrite

## Contents



## 4.1 Introduction

Magnetoelectric materials are multiferroic materials, which have coupled magnetic and electric ferroic orders. The coupling of the electric and magnetic fields in materials was speculated by Curie[67,68] as early as in 1894. However, due to the difficulty of combining magnetic and electric ferroic orders, there was not much development in this field. The first theoretical prediction of the magnetoelectric coupling was done by Dzyaloshinskii[69] in 1959 for chromium oxide, $Cr_2O_3$. This was soon observed by Astrov[70] in 1960.

The cross-play of the ferroic properties has motivated further research into potential technological devices, especially those where the electric properties are controlled with magnetic fields or *vice versa*.[7] Few materials have been reported to show a sizeable magnetoelectric effect, among which gallium

ferrite ($Ga_{2-x}Fe_xO_3$ or GFO) appears to be of considerable significance due to its being a ferrimagnet and ferroelectric at room temperature, these being demonstrated experimentally. With an aim to better understand these properties, we performed *ab initio* studies, under different approximations, including spin-orbit coupling, to probe the electronic, magnetic and magnetoelectric properties of bulk GFO for the iron concentration, $x = 1$. We first provide an introductory overview of GFO and its properties. We then describe the calculation details used to obtain the electronic and magnetic properties. Next, we provide the results of these calculations and determine the origin of ferrimagnetism in GFO. The subsequent part addresses the crystal-field analysis, where the theory, implementation and results are discussed. The last part is dedicated to the description of the electric properties of GFO and eventually, its magnetoelectric properties.

## 4.2 GFO: An Overview

The first gallium ferrite crystals, $Ga_{2-x}Fe_xO_3$ with $0.7 \leq x \leq 1.4$, were synthesised by Remeika in 1959, and were described as a ferromagnetic-piezoelectric material.[71] The structural characterisation was determined by Wood, who found the crystallographic space group for GFO to be $Pc2_1n$.[72] This was confirmed by Abrahams *et al.* in 1965, with the lattice constants to be $a = 8.7512 \pm 0.00008$ Å, $b = 9.3993 \pm 0.00003$ Å and $c = 5.0806 \pm 0.0002$ Å.[73] There are four different cationic sites occupied by Fe and Ga cations: three irregular (distorted) octahedral sites (Fe1, Fe2 and Ga2) and a regular tetrahedral site (Ga1) oriented along the $b$-axis. The O anions are positioned in six different sites in a double hexagonal compact arrangement (Fig. 4.1).

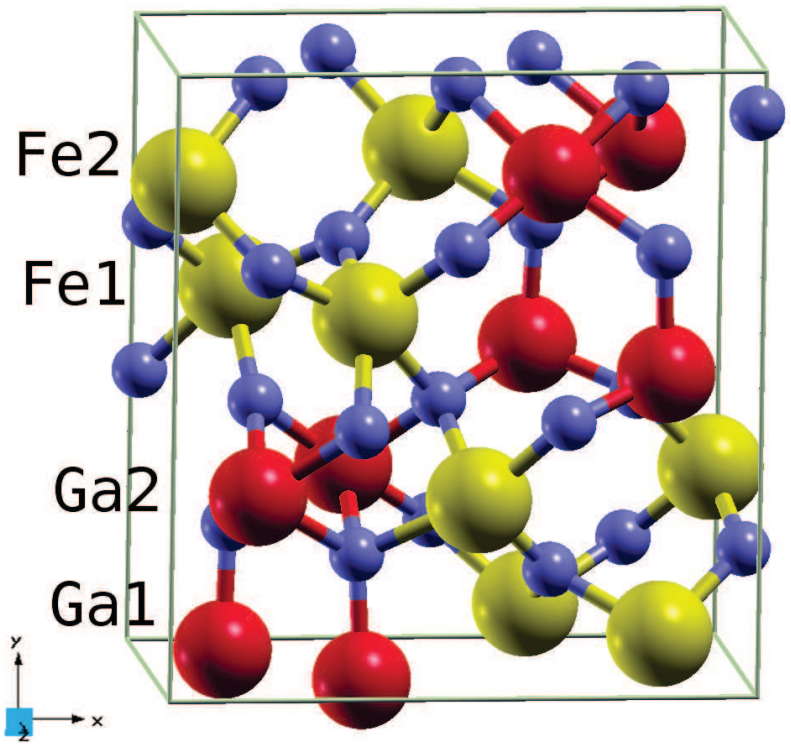


**Figure 4.1:** $GaFeO_3$ unit cell with Fe, Ga and O atoms in yellow, red and blue respectively. The cationic sites are also labelled.

Other studies[74–76] were carried out to probe the magnetic structure and magnetoelectric characteristics of GFO. However, it was in 1965 that Frankel *et al.* using Mössbauer spectroscopy, showed a ferrimagnetic order with magnetic moments close to or along the *c*-axis, instead of a canted antiferromagnetic order.[77] Both cationic sites Ga1 and Fe1 are antiferromagnetically coupled to the Ga2 and Fe2 sites, which should result in a net antiferromagnetic configuration for Fe composition $x = 1$. The presence of ferrimagnetism without the presence of a canted antiferromagnetic hints at a possible existence of site disorder. In 2004, Arima *et al.* found that the GFO preparation method influenced the magnetic transition temperature, which were likely caused by the change in the Ga/Fe occupations at the four cationic sites.[78] The origin of ferrimagnetism was interpreted as follows – the magnetic Fe cations at the Ga1 and Fe1 sites adopt a magnetic orientation antiparallel to the magnetic cations at the Ga2 and Fe2 sites through a super-exchange mechanism mediated through the O anions. Since, the amount of Fe at the Fe2 and Ga2 sites is larger than that at the Fe1 and Ga1 sites, there is a net non-zero magnetic moment along the *c*-axis (along Fe2). They also demonstrated experimentally that the magnetic transition temperature could be tuned with the Fe/Ga ratio and it increased with Fe content to room temperature for $x \geq 1.1$. In addition, a large linear magnetoelectric effect was measured for GFO single crystals, which was larger than one order of magnitude than the value reported for $Cr_2O_3$.
In 2006, Kim *et al.* reported a large orbital moment in GFO.[79] This was unusual because Fe in $GaFeO_3$ has a formal valence of +3 (half-filled $d^5$ configuration), for which the orbital moment is expected to be zero. The mechanism behind the orbital moment could help provide a better understanding of the magnetoelectric coupling in this material. However, despite the several experimental studies, very few theoretical reports investigating the properties of GFO are present in literature. Early density-functional theory (DFT) calculations carried out on the ideal structure revealed a stable antiferromagnetic state with zero net spin and orbital moments.[80] Han *et al.* also showed that the energy difference between an ideal GFO structure and a structure with an Fe interchanged with the Ga2 site can be as small as 1 meV per unit cell, thereby implying that this kind of site disorder is highly probable and in accord with the presence of Fe at the Ga2 sites reported in experiments. With the help of first-principle calculations, Roy *et al.* showed that the site disorders are not favoured in the ground state and that available thermal energy at room temperature ($kT \sim 25$ meV) is of the order of the energy difference for the Fe2-Ga2 site disorder, hinting towards the role of thermally induced defects.[81] The same group calculated the electronic structure and the Born effective charges, which showed a largely ionic character of the Ga/Fe-O bonds and a lack of significant anomaly in the Born effective charges.[82] Stoeffler calculated the electric polarisation of the system to be $-25\mu C/cm^2$, an order of magnitude larger than the value estimated by Arima *et al.*[83] along the *b*-axis.

In the following, the *ab initio* calculations carried out in this study are described. The results for the electronic properties and magnetic properties for the ideal structure of GFO are then analysed. With the intention of finding the origin of ferrimagnetism in the system, a structure with cationic site disorders is used and the results compared with those obtained by Hatnean *et al.*[84] Then, the crystal-field analysis is performed on the ideal GFO structure and the results for the different Fe cationic sites shown. These results are confirmed with a simple point-charge model. Towards the end, we build on the results obtained by Stoeffler to probe the magnetoelectric effects in the ideal structure by changing the direction of the magnetic field. We do not allow ionic relaxation and hence, the effect obtained would be a purely direct magnetoelectric effect.

## 4.3 Calculation Details

Our DFT calculations were carried out using the VASP package.[85,86] We used the projector augmented wave basis set[66,87] and the exchange-correlation functional was described using the local density approximation (LDA) as parametrised by Perdew and Zunger,[54] and the generalised gradient approximation (GGA) as parametrised by Perdew, Becke and Ernzerhof.[57,58] Earlier calculations done showed that a minimum k-point mesh size of $7 \times 7 \times 9$ (441 k-points) in the irreducible Brillouin zone was required for proper convergence of the ground state energy and the magnetocrystalline anisotropy energy to within 10 $\mu$eV.[88] Hence, we used this k-point mesh for our calculations. For the plane wave cut-off, a value of 550 eV was used and the convergence criterion for the electronic self-consistent loop was set to 10 $\mu$eV. Both LDA and GGA underestimate the energy band gap and magnetic moments of GFO as compared to the experimental values. This failure of LDA and GGA is known in strongly correlated systems like transition metal oxides.[59–61] To more accurately account for the strong on-site Coulomb interaction among the localised Fe 3*d* electrons, we used the rotationally invariant approach introduced by Lichtenstein *et al.*, represented by the Hubbard-like term $U$ and the exchange term $J$ (see Section 3.2.3).[62] This led to an improvement of the ground state properties of GFO. Based on an earlier theoretical study, the value of J was set to 0.9 eV.[88] In this work, two specific values of $U$ were used, $U = 4$ and 8 eV, chosen so as to probe the ground state properties as well as the hybridisation of the localised orbitals with the remaining de-localised states. The spin-orbit coupling (SOC) was included in some of our calculations as implemented in VASP to improve the magnetic properties of the system.[89]

To study the origin of ferrimagnetism in GFO, the ionic occupancies provided by Hatnean *et al.* were used.[84] In addition, a simple predictive model was developed that allows one to compute the net spin and orbital magnetic moments in a disordered structure with the help of the cationic occupancies. The predictions of this model were then compared with the values obtained by the *ab initio* calculations and experiment.

For the crystal-field analysis, the global frame $\ell, m$-site-projected basis set were rotated to the local octahedral or tetrahedral frame of reference to better understand the symmetries of the $e_g$ and $t_{2g}$ sub-orbitals. The rotation was first defined directly using the Euler angles and the real spherical harmonics (also known as the cubic harmonics) and then implemented in the VASP code. To study the effect of crystal-field an hybridisation on the $e_g$-$t_{2g}$ splitting on the octahedral Fe sites, both values of $U$ were used. The $e_g$-$t_{2g}$ splitting was modelled using a point-charge model, where the Coulomb potential at the octahedral centre was expanded in terms of spherical harmonics. Such a model allows one to construct a matrix consisting of the overlap of the *d*-orbitals. Diagonalising this matrix gave us an $e_g$-$t_{2g}$ splitting in good qualitative agreement with those obtained from our *ab initio* calculations.

The electric polarisation of GFO was computed as implemented in the VASP code.[90–95] The preliminary calculations were done with the aim to study the temperature dependent electric polarisation on a path between the experimental positions at 4 K and 230 K provided by Arima *et al.*,[78] and to verify the polarisation calculations done by Stoeffler.[83] Finally, to probe the magnetoelectric effect, the magnetisation axis was rotated for different angles along the *c*-*b* plane.

## 4.4 Electronic and Magnetic Properties of Ideal GFO

In this section, we present the electronic and magnetic properties of ideal GFO. The lattice parameters and the atomic positions were based on the values reported by Arima *et al.*,[78] which were obtained with neutron diffraction studies at 4 K. The values obtained at 230 K were used in the later magnetoelectric studies. The lattice parameters are $a = 8.719$ Å, $b = 9.368$ Å and $c = 5.067$ Å. The atoms were not relaxed since the parameters were obtained from experiment. Two values of $U$ were used for the Fe $3d$ orbitals: 4 eV and 8 eV, for both LDA and GGA, to improve ground state properties like the energy band gap and magnetic moments. The calculations including the SOC does not significantly affect the physical properties of interest, but allows us to compute the orbital magnetic moments. In later sections pertaining to magnetoelectric effects, the SOC is of high importance.

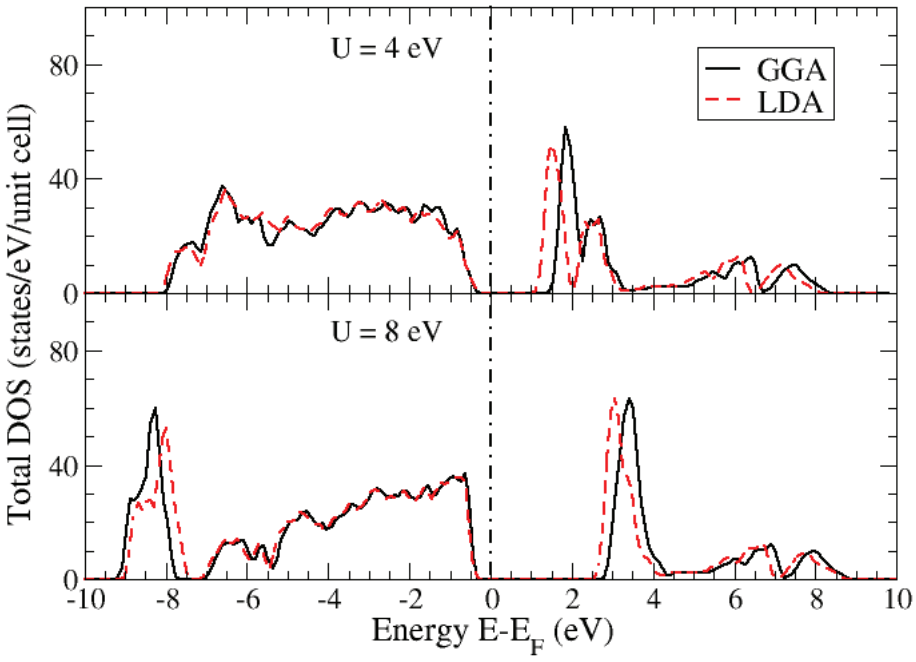


**Figure 4.2:** GGA+$U$ and LDA+$U$ calculated total DOS for GFO for $U = 4$ and 8 eV.

To understand the electronic structure, we plot the total electronic density of states (DOS) in Fig. 4.2. When the value of $U$ under both LDA and GGA approximations is increased, the Fe $3d$ orbitals are spilled further. This is in accordance with the Hubbard model, where the higher value of $U$ tends to localise the $d$ orbitals. Increasing the $U$ value beyond 8 eV will eventually produce the electronic structure of an isolated Fe atom. Also, it should be noted that under both approximations, though the value of $U = 8$ eV gives good values of the energy band gap and the spin magnetic moments, the hybridisation of the Fe $3d$ orbitals with the $2p$ orbitals of the neighbouring O atoms is drastically reduced and may not be physical. Since we do not have photoemission experimental data to compare with our DOS, we used the value of $U$ that best describes the experimentally observed properties like the energy band gap and the magnetic moments, i.e. $U = 8$ eV. The values for these properties are

tabulated in Table 4.1.

**Table 4.1:** Energy band gap (in eV) and spin and orbital moments of the Fe cations in GFO for different $U$ in LDA+$U$ and GGA+$U$, compared to experiment.

| Property | Exp. | LDA | | GGA | |
|---|---|---|---|---|---|
| | | $U = 4$ eV | $U = 8$ eV | $U = 4$ eV | $U = 8$ eV |
| Energy band gap (eV) | 3.2[96] | 1.5 | 3.0 | 2.0 | 3.2 |
| Spin magnetic moment Fe1 ($\mu_B$) | -3.9[78] | -4.02 | -4.41 | -4.10 | -4.44 |
| Spin magnetic moment Fe2 ($\mu_B$) | 4.5[78] | 4.02 | 4.41 | 4.10 | 4.44 |
| Orbital magnetic moment ($\mu_B$) | - | $\pm$0.027 | $\pm$0.020 | $\pm$0.022 | $\pm$0.017 |

It can be seen that value of $U = 8$ eV for LDA+$U$ and GGA+$U$ yields an energy band gap in very good agreement with experiment. We also observe an improvement in the prediction of the magnetic moment for the Fe2 site. However, the magnetic moment at the Fe1 site does not agree with experiment. As is shown in the subsequent section, this discrepancy arises due to the partial iron occupancy at the Fe1 site, which was estimated experimentally to be 84%. Assuming a spin moment at 84% of $-4.44$ $\mu_B$ gives us a value of $-3.73$ $\mu_B$, closer to experiment. In addition, we notice that the orbital moments decrease with an increase in the value of $U$. This is not surprising as the higher values of $U$ localise the Fe 3$d$ electrons more, thereby reducing their hybridisation and thus, their orbital moments. Kim *et al.*[79] had performed X-ray magnetic circular dichroism (XMCD) experiments at the Fe $L_{23}$-edges of GFO and found a net orbital magnetic moment of 0.017$\mu_B$ at a temperature of 190 K. Assuming that the individual spin and orbital magnetic moments behave as their total magnetisation curves, we estimate the net orbital magnetic moment to be 0.034 $\mu_B$ at 4 K. They estimate their Fe occupancy at the Ga1, Ga2, Fe1 and Fe2 sites to be 0, 0.35, 0.825 and 0.825 respectively. Assuming that the Ga1 and Ga2 moments are parallel to the Fe1 and Fe2 sites respectively, we obtain net orbital moments of 0.007 $\mu_B$ and 0.006 $\mu_B$ for the LDA+$U$ and GGA+$U$ respectively, which are much smaller than experiment. This level of discrepancy is known to be present in LDA/GGA methods and there is no general solution to improve the theoretical orbital moments.[97]

It is important to point out that the net magnetisation obtained theoretically in GFO is zero and hence, we always obtain a perfect antiferromagnetic system. To explain the origin of ferrimagnetism, we performed *ab initio* calculations for cationic site disorders and present our work in the following section.

## 4.5 Origin of Ferrimagnetism in GFO

There are three ways that a material with an antiferromagnetic ordering may be ferrimagnetic:

1. The individual magnetic moments are not the same on the two antiferromagnetic sites, thereby giving a net non-zero magnetic moment. Such behaviour is seen in magnetite, $Fe_3O_4$, where there are two Fe states, $Fe^{+2}$ and $Fe^{+3}$, which have different moments, and thus give rise to a ferrimagnetic system.[98] In the case of GFO, the Fe ionic state on the cationic sites is $Fe^{+3}$.

2. The individual magnetic moments are canted towards a particular direction and give rise to a non-zero magnetic moment along that direction. GFO was thought to be ferrimagnetic due to

this reason,[75,76] but the experimental observation by Frankel *et al.*[77] showed that the moments lie along the *c*-axis.

3. Site disorders in an antiferromagnetic system where a magnetic atom is replaced with a non-magnetic atom, would leave an uncompensated magnetic moment and the system would appear to be ferrimagnetic. Experimental observations on GFO indicate that the Ga and Fe atoms tend to swap places with a preference for the Ga2 site.[78] This might produce an uncompensated moment and hence a ferrimagnetic ground state.

To explain the origin of ferrimagnetism in GFO, we investigated the third possibility concerning site disorders. This is not an easy task because each experimental paper on GFO describes different Fe occupancies at the cationic sites, as can be noticed in the few examples shown in Table 4.2. Moreover, given a set of occupancies, it is not computationally practical to consider larger supercells or even every possible atomic arrangement in the unit cell. However, all experiments show that there is a higher preference of Fe occupying the Ga2 site over the Ga1 site. This could be due to the fact that the Ga1 site is tetrahedral, which would require further investigation to confirm. In addition, the Fe occupancies at the Fe1 and Fe2 sites seem to be identical in all cases. For these reasons, we consider exactly one such case, where the Fe occupancies are as those provided by Hatnean *et al.*,[84] with Fe@Ga1 = 0 and are possible to simulate in the same cell as earlier. There are obviously many more cells that provide the same occupancies, but those were not considered.

**Table 4.2:** Different Fe occupancies at cationic sites in GFO from different experimental data.

| | Arima *et al.*[78] | Hatnean *et al.*[84] | Kim *et al.*[79] |
|---|---|---|---|
| Fe@Fe1 | 0.84 | 0.75 | 0.825 |
| Fe@Fe2 | 0.83 | 0.75 | 0.825 |
| Fe@Ga1 | 0.10 | 0.00 | 0.000 |
| Fe@Ga2 | 0.24 | 0.50 | 0.350 |

Before we present our results, it might be important to first understand the magnetic coupling between the different cationic sites. Given that the Fe1 and Fe2 sites are antiferromagnetically coupled, we have two possible cases for the coupling between the Fe sites and the Ga sites:

1. *Case 1:* Fe1 is antiferromagnetically coupled to Ga1 and Fe2 is antiferromagnetically coupled to Ga2.

2. *Case 2:* Fe1 is antiferromagnetically coupled to Ga2 and Fe2 is antiferromagnetically coupled to Ga1.

A quick calculation using the occupancies provided in Table 4.2 and the magnetic moments for both cases provides us with a net magnetisation. Comparing this with the magnetic moments obtained in the corresponding experiments[78,79,84] indicates that the second case is more likely. Using the occupancies as reported by Hatnean *et al.* and the magnetic moments of 4.5 $\mu_B$ for Fe, we get the magnetic moments at the Fe1, Fe2 and Ga2 (since the occupation at Ga1 is zero) as -3.375, +3.375 and +2.250 $\mu_B$ respectively as compared to the corresponding experimental values of -4.0, +3.5 and +2.7 $\mu_B$. It should be noted that this calculation helps understand the origin of ferrimagnetism in GFO intuitively and does not consider hybridisation effects and exchange mechanisms beyond those mentioned, and hence may not be accurate quantitatively. The disordered unit cell that was used in

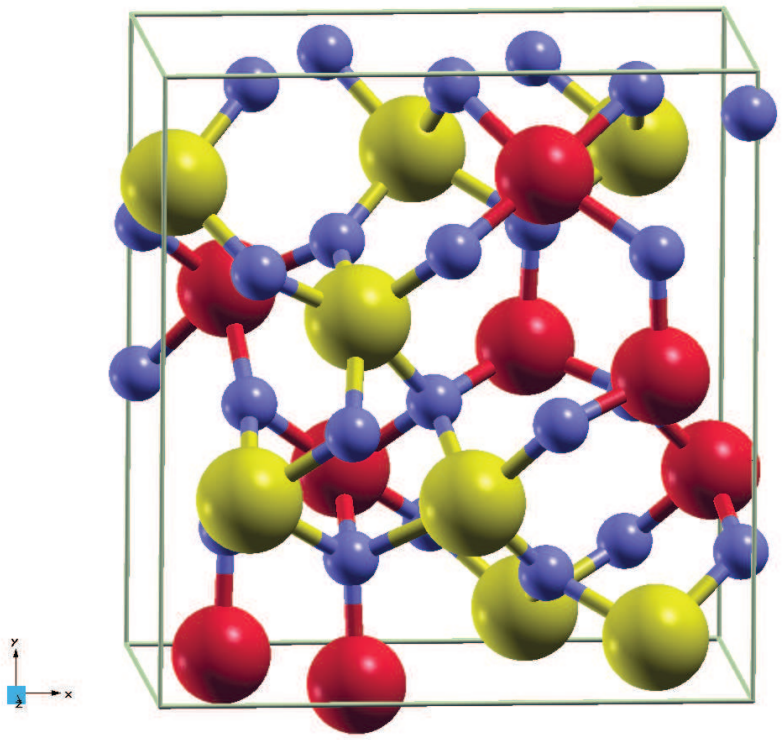

**Figure 4.3:** Disordered unit cell to understand the origin of ferrimagnetism in GFO.

our *ab initio* calculation is given in Fig. 4.3. Table 4.3 shows our average site magnetisation results with *ab initio* techniques and compares them to the experimental and the simple calculation results.

**Table 4.3:** *Ab initio* site magnetisation results for a disordered system compared with experiment and simple calculation based on site occupations.

| Site | Experiment[84] | Super cell | Simple averaging |
|---|---|---|---|
| Fe1 | -4.0 | -3.335 | -3.375 |
| Fe2 | 3.5 | 3.346 | 3.375 |
| Ga1 | 0.0 | 0.00 | 0.0 |
| Ga2 | 2.7 | 2.243 | 2.250 |

The table shows that the *ab initio* super cell site disorder calculations agree relatively well with experiment. Note that the experimental values are different from the table 4.1 since they are from different experiments. We see a disagreement of $-0.665\ \mu_B$ and $0.457\ \mu_B$ for the magnetic moments on the Fe1 and Ga2 sites. However, the magnetic moment on the Fe2 site is in good agreement with experiment as well as the net magnetisation, which differs from experiment by $-0.619\ \mu_B$ per unit cell. Moreover, the simple calculation scheme described earlier is a very good indicator of the site magnetisation as compared to the *ab initio* results. These results are similar to those obtained by Roy *et al.*,[99] who predicted that the individual Fe1 and Fe2 moments do not change by a large amount with respect to the perfect structure. However, they observed that the Fe ion at the Ga2 site has a relatively lower moment of $4.11\ \mu_B$, in contrast to our observed moment of $4.486\ \mu_B$. The corresponding individual moments of the Fe ion at the Ga2 sites based on experimental average values of 2.7

$\mu_B$ are 5.4 $\mu_B$, which does not seem likely considering that the maximum magnetic moment Fe can possess is 5 $\mu_B$. The same is true for the value of $-4.0$ $\mu_B$ reported for the Fe1 site, which corresponds to individual moments of $-5.33$ $\mu_B$ based on the iron occupancy of 0.75. The net magnetic moment obtained is about 10 $\mu_B$ per unit cell, and thus, we infer that the origin of ferrimagnetism in GFO is due to cationic site disorders. When we compare the ground state energies between the ideal structure in Fig. 4.1 and the disordered structure in Fig. 4.3, we obtain a difference of 231 meV ($\sim$ 2700 K), which is lower than the sum of the predicted values of 25 meV and 400 meV for the Fe2-Ga2 and Fe1-Ga2 disorders respectively as reported by Roy *et al.*[99]

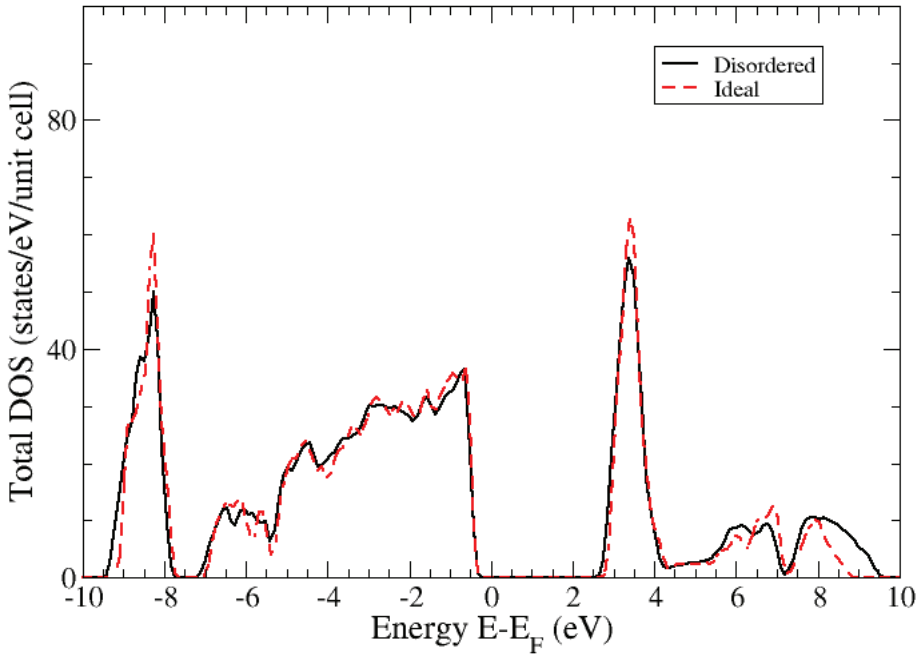


**Figure 4.4:** Comparison of the total DOS for the ideal and disordered structures of GFO

To study the changes in the electronic structure we plot the total DOS for the ideal and disordered structures in Fig. 4.4. The figure shows that the two systems are similar in their electronic structure and energy band gaps. Additionally, our calculations indicate that the orbital moments for Fe remain parallel to the corresponding spin moments with a magnitude of 0.017 $\mu_B$. Thus, the net orbital magnetisation in the system is 0.034 $\mu_B$ with a direction parallel to the next spin magnetisation. Since we considered Fe at the octahedral Fe1, Fe2 and Ga2 sites only, the similarity of DOS and magnitudes of the spin and orbital magnetic moments indicate that the octahedral sites all behave similarly. It might be of interest to study the electronic structure of Fe at the tetrahedral Ga1 site. Another point that should be made is that the ions were not relaxed and the net forces on the individual atoms increased by a factor of 3 as compared to those in the ideal structure. Performing ionic relaxations might reduce the ground state energy of the disordered system to the point where the thermal energy ($\sim$ 1000-1500 K) available during synthesis of the experimental samples might be sufficient to cause cationic disorders. These cationic site disorders are statistical and might require larger supercells and

more swappings, leading to impractical computational requirements, which is why the ionic relaxation or further investigation of different site disorders were not carried out.

In this section, we attributed the origin of ferrimagnetism in GFO to cationic site disorders. The energy difference is of the order of hundreds of meV and might be available from the environment during synthesis. Additionally, we showed that there is very little change in the electronic structure and the magnetic moments of the cationic sites, indicating the absence of any exchange mechanism beyond the second neighbour. In the following section, we investigate the magnetic order on the distorted octahedral sites by performing the crystal-field analysis and studying the $3d$ orbitals of Fe in these environments.

## 4.6 Crystal-Field Analysis – Theory, Implementation and Results

Crystal-field theory helps describe the splitting of the electron orbitals of an atom, usually a $d$ or $f$ cation, in the presence of a Coulomb potential generated by neighbouring atoms, usually anions. This model has been very successful in analysing $d$ and $f$ splitting for different magnetic orders and when combined with molecular orbitals, has successfully explained spin crossover phenomena, where the energy gap of the splitting can be of the order of the pairing energy between the electrons. In GFO we have two types of crystal-field environments in the system – octahedral and tetrahedral. An Fe atom at the centre of these environments would be influenced by six and four O anions respectively and the splitting of the degenerate $3d$ orbitals of Fe would reflect this interaction. In case of an octahedral environment, the $d_{xy}$, $d_{yz}$ and $d_{xz}$ orbitals would feel a stronger attraction towards the O anions than the $d_{z^2}$ and $d_{x^2-y^2}$ orbitals, and would thus have a lower energy. This would lead to splitting of the five $d$-orbitals into two sub-shells, called $t_{2g}$, consisting of the $d_{xy}$, $d_{yz}$ and $d_{xz}$ orbitals, and $e_g$ consisting of the $d_{z^2}$ and $d_{x^2-y^2}$ orbitals, with the former being lower in energy. For a tetrahedral environment, the $e_g$ orbitals tend to be lower in energy than the $t_{2g}$ orbitals. This effect is purely due to the crystal geometry and can be schematically visualised as shown in Fig. 4.5.

Two important details should be pointed out here, firstly, that the $e_g$ and $t_{2g}$ orbitals are described using real spherical harmonics, also known as cubic harmonics, and secondly, that these are defined through their $m$ quantum number, i.e. the eigenvalue of the $\hat{L}_z$ operator, which depends on the coordinate system. The second point is visualised in Fig. 4.5 in the reference frame. If the coordinate system is not as shown in the figure, up to a rotation of $\pi/2$, then the $d$-orbitals obtained would be a superposition of the maximally split sub-orbitals and can not be clearly defined as $e_g$ and $t_{2g}$. To obtain the correct crystal-field splitting from an arbitrary reference frame, the real spherical harmonics or the coordinate system should be rotated to align the anions appropriately. We thus have a rotation matrix for the real spherical harmonics analogous to the rotation matrix for the Cartesian coordinate system. Using *ab initio* techniques, there are at least two ways this can be achieved.
In the first approach, we rotate the crystal structure completely for a cation under study, wherein the wavefunctions obtained would describe the crystal-field splitting on the given cation appropriately. Such an approach can be used effectively for certain cases only, for example, if there is one cation in a molecular system. In general however, a crystal does not consist of only one cation surrounded by anions in a given crystal geometry, and thus, the rotations that need to be performed for different cations might be many and different.

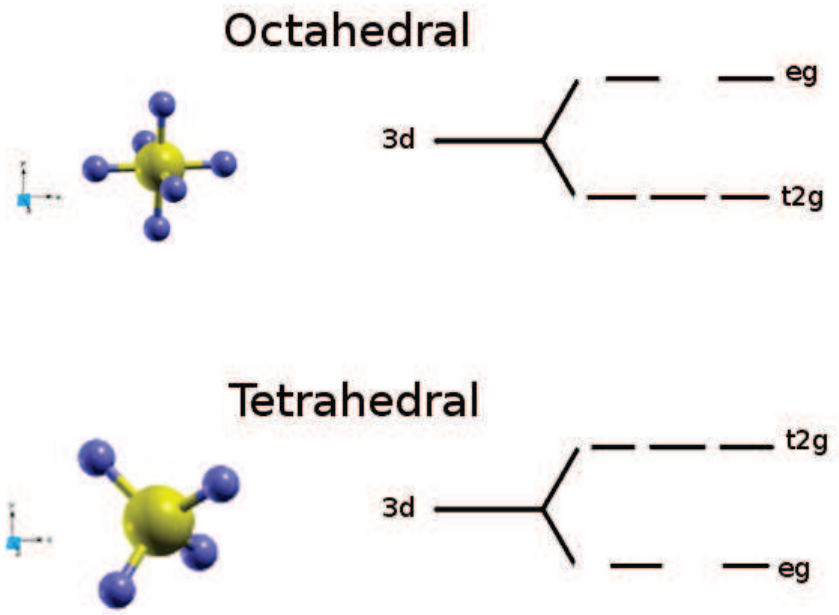


**Figure 4.5:** Crystal-field splitting of 3*d* orbitals in octahedral and tetrahedral fields

In the second approach, we rotate the projected spherical harmonics of the cation under study. This can be done during the same self-consistent cycle and is computationally faster since only the local orbitals are rotated. Since this feature has not been implemented in VASP, we implemented the local rotation. We present below the implementation details and our results for the octahedral cationic Fe1 site in GFO. To understand our results, we also developed a point-charge model, the details of which follow the results of the local rotation.

### 4.6.1 Implementation Details

Rotation of the real spherical harmonics can be done in two ways – firstly by rotating the spherical harmonics using the Wigner D-matrices and then rewriting them as the real spherical harmonics, and secondly by rotating the real spherical harmonics directly by using the rotation matrix of the coordinate system. The Wigner D-matrices are well described by Bradley and Cracknell and the interested reader is directed to their work.[100] In our implementation, the second method is used.

Our implementation involves rotation of the *d*-orbitals following a rotation $\hat{R}(\alpha, \beta, \gamma)$ of the Cartesian coordinate system. Thus, we have a $5 \times 5$ rotation matrix $\hat{A}(\alpha, \beta, \gamma)$ corresponding to rotations about the $z$-, $x$- and $z$-axes by the Euler angles $\alpha$, $\beta$ and $\gamma$ respectively. The matrix elements $a_{ij}$ of $\hat{A}$ in terms of the matrix elements $R_{ij}$ of $\hat{R}$ are derived by writing the rotated real spherical harmonics, $\overline{\mathcal{Y}_{\ell m}}$ in terms of the rotated Cartesian coordinates $(x', y', z')$ and then rewriting these in terms of a superposition of the original real spherical harmonics $\mathcal{Y}_{\ell m}$. To demonstrate this, we provide one example of obtaining the transformation for $m = -2$. The rest of the rotated real spherical harmonics are derived in Appendix C.

Consider a generalised $3 \times 3$ Cartesian rotation matrix $\hat{R}$ which then gives us,

$$r_i' = \sum_j R_{ij} r_j. \tag{4.1}$$

We define the corresponding $5 \times 5$ rotation matrix $\hat{A}$ for the real spherical harmonics with $\ell = 2$, and by manipulating the indices $a_{ij}$, we can write $\overline{\mathcal{Y}_{\ell m}} = \sum_{m'} a_{mm'} \mathcal{Y}_{\ell m'}$. If we write out the full form of the real spherical harmonics with $r_i' = \sum_j R_{ij} r_j$ and use $|\boldsymbol{r}'| = |\boldsymbol{r}|$, we have,

$$\begin{bmatrix} \frac{1}{2}\sqrt{\frac{15}{\pi}}\frac{x'y'}{r^2} \\ \frac{1}{2}\sqrt{\frac{15}{\pi}}\frac{y'z'}{r^2} \\ \frac{1}{4}\sqrt{\frac{5}{\pi}}\frac{2z'^2 - x'^2 - y'^2}{r^2} \\ \frac{1}{2}\sqrt{\frac{15}{\pi}}\frac{z'x'}{r^2} \\ \frac{1}{4}\sqrt{\frac{15}{\pi}}\frac{x'^2 - y'^2}{r^2} \end{bmatrix} = \begin{bmatrix} a_{11} & a_{12} & a_{13} & a_{14} & a_{15} \\ a_{21} & a_{22} & a_{23} & a_{24} & a_{25} \\ a_{31} & a_{32} & a_{33} & a_{34} & a_{35} \\ a_{41} & a_{42} & a_{43} & a_{44} & a_{45} \\ a_{51} & a_{52} & a_{53} & a_{54} & a_{55} \end{bmatrix} \begin{bmatrix} \frac{1}{2}\sqrt{\frac{15}{\pi}}\frac{xy}{r^2} \\ \frac{1}{2}\sqrt{\frac{15}{\pi}}\frac{yz}{r^2} \\ \frac{1}{4}\sqrt{\frac{5}{\pi}}\frac{2z^2 - x^2 - y^2}{r^2} \\ \frac{1}{2}\sqrt{\frac{15}{\pi}}\frac{zx}{r^2} \\ \frac{1}{4}\sqrt{\frac{15}{\pi}}\frac{x^2 - y^2}{r^2} \end{bmatrix}. \tag{4.2}$$

As an example, we show how to obtain the first row elements, $a_{1i}$. The remaining matrix elements $a_{ij}$ are derived in Appendix C. We multiply the matrix to obtain the expression of $\overline{\mathcal{Y}_{2,-2}}$,

$$\begin{aligned} \overline{\mathcal{Y}_{2,-2}} &= \frac{1}{2}\sqrt{\frac{15}{\pi}}\frac{x'y'}{r^2} = \frac{1}{2}\sqrt{\frac{15}{\pi}}\frac{(R_{11}x + R_{12}y + R_{13}z)(R_{21}x + R_{22}y + R_{23}z)}{r^2} \\ &= a_{11}\frac{1}{2}\sqrt{\frac{15}{\pi}}\frac{xy}{r^2} + a_{12}\frac{1}{2}\sqrt{\frac{15}{\pi}}\frac{yz}{r^2} + a_{13}\frac{1}{4}\sqrt{\frac{5}{\pi}}\frac{2z^2 - x^2 - y^2}{r^2} + a_{14}\frac{1}{2}\sqrt{\frac{15}{\pi}}\frac{zx}{r^2} + a_{15}\frac{1}{4}\sqrt{\frac{15}{\pi}}\frac{x^2 - y^2}{r^2}. \end{aligned} \tag{4.3}$$

By comparing the coefficients, we get for $m = -2$,

$$\begin{aligned} a_{11} &= R_{11}R_{22} + R_{12}R_{21} \\ a_{12} &= R_{12}R_{23} + R_{13}R_{22} \\ a_{13} &= \sqrt{3}R_{13}R_{23} = -\sqrt{3}(R_{11}R_{21} + R_{12}R_{22}) \\ a_{14} &= R_{11}R_{23} + R_{13}R_{21} \\ a_{15} &= R_{11}R_{21} - R_{12}R_{22} \end{aligned} \tag{4.4}$$

We see that there are two solutions for $a_{13}$. As seen in Appendix C, we get two solutions for matrix elements of the form $a_{i3}$. This is due to the fact that we have six quadratic terms $(x^2, y^2, z^2, xy, yz, zx)$ and only five coefficients $a_{mm'}$ for a given $m$. However, it can be easily verified that these two solutions are identical for rotations along each Cartesian axis and since every general rotation can be represented as rotations along the different axes, these two solutions are also identical for any general rotation.

The first step of our implementation is determination of the crystal-field geometry, since the final positions after rotation depend on the geometry (see Fig. 4.5). To distinguish between the octahedral and tetrahedral geometries, we first find the nearest neighbours and sort them by their distances. If the distance of the sixth neighbour is over 35% of the closest, the crystal-field geometry is most likely tetrahedral. If this condition is not met, we determine the angles between the 'arms' of the

octahedron. If these angles are within 35% of $\pi/2$, then the crystal-field is most likely octahedral. The reason we keep the relative angle and distance conditions to 35% is to include highly distorted octahedral configurations like those in GFO.
Once the crystal-field geometries are determined, we perform appropriate rotations about the $z$-, $x$- and $z$-axes by the Euler angles $\alpha$, $\beta$ and $\gamma$. These angles are obtained by using trigonometric relations between the final and initial positions. The final positions are 'known' since the neighbours of the cation have an arrangement as shown in Fig. 4.5. For an octahedral field, the six neighbours lie on the arms of the new coordinate system with the cation at the origin and their positions are along $(\pm1, 0, 0)$, $(0, \pm1, 0)$ and $(0, 0, \pm1)$. In the case of a tetrahedral field, the four neighbours lie at the four vertexes of the two long diagonals in a cube with the cation at its centre and the sides parallel to the axes of the new coordinate system. The positions are along $\left(\frac{1}{\sqrt{3}}, \frac{1}{\sqrt{3}}, \frac{1}{\sqrt{3}}\right)$, $\left(-\frac{1}{\sqrt{3}}, \frac{1}{\sqrt{3}}, -\frac{1}{\sqrt{3}}\right)$, $\left(-\frac{1}{\sqrt{3}}, -\frac{1}{\sqrt{3}}, \frac{1}{\sqrt{3}}\right)$ and $\left(\frac{1}{\sqrt{3}}, -\frac{1}{\sqrt{3}}, -\frac{1}{\sqrt{3}}\right)$.

For rotating the locally site projected wavefunctions, only the Euler angles to reach the final positions are required and not the final positions themselves. However, the final positions help us understand the amount of distortion in the geometry, and are important while developing the point-charge model, where the Coulomb potential due to the anions is expanded as a series of spherical harmonics. As described in section 3.4, the all-electron wavefunction in the projector augmented wave basis (PAW) is given as,

$$|n, \boldsymbol{k}, s\rangle = \widetilde{|n, \boldsymbol{k}, s\rangle} + \sum_{p,\ell,m} \left( |p, \ell, m\rangle - \widetilde{|p, \ell, m\rangle} \right) P^{n\boldsymbol{k}s}_{p\ell m}, \tag{4.5}$$

where $\widetilde{|n, \boldsymbol{k}, s\rangle}$ is the pseudo-wavefunction for band $n$, wave vector $\boldsymbol{k}$ and spin $s$. $|p, \ell, m\rangle$ and $\widetilde{|p, \ell, m\rangle}$ are the partial and pseudo-partial waves corresponding to projector type $p$, angular momentum quantum number $\ell$ and magnetic quantum number $m$. $P^{n\boldsymbol{k}}_{p\ell m}$ are the projector coefficients. In this equation, SOC is not included, which is why the spin quantum number $s$ appears explicitly. The inclusion of SOC is trivial and does not affect the final results in our work. The local site projected DOS is defined within the augmentation region, where the all-electron wavefunction is given only by the partial waves as,

$$|n, \boldsymbol{k}, s\rangle = \sum_{p,\ell,m,s} P^{n\boldsymbol{k}s}_{p\ell m} |p, \ell, m\rangle. \tag{4.6}$$

When the Cartesian reference frame is rotated, the new real spherical harmonics maintain their $\ell$ quantum number and the total DOS for a given $\ell$ remains unchanged. Hence, we have,

$$|\Psi^{n\boldsymbol{k}}_{\ell}\rangle = \sum_{p,m,s} P^{n\boldsymbol{k}s}_{p\ell m} |p, \ell, m\rangle = \sum_{p,m,s} \overline{P}^{n\boldsymbol{k}s}_{p\ell m} \overline{|p, \ell, m\rangle}, \tag{4.7}$$

where the 'barred' objects are the rotated quantities. To find how the new projector coefficients transform, we express the rotated real spherical harmonics in terms of the original basis set. This is trivial since the radial functions do not change, and only the spherical harmonics are rotated. Thus,

$$\overline{|p, \ell, m\rangle} = \sum_{m'} a_{mm'} |p, \ell, m'\rangle. \tag{4.8}$$

When we substitute this in Eq. 4.7, we get,

$$
\begin{aligned}
|\Psi_\ell^{n\boldsymbol{k}}\rangle &= \sum_{p,m,s} \overline{P}_{p\ell m}^{n\boldsymbol{k}s} \overline{|p,\ell,m\rangle} = \sum_{p,m,s} \overline{P}_{p\ell m}^{n\boldsymbol{k}s} \sum_{m'} a_{mm'} |p,\ell,m'\rangle \\
&= \sum_{p,m',s} \left( \sum_{m} a_{mm'} \overline{P}_{p\ell m}^{n\boldsymbol{k}s} \right) |p,\ell,m'\rangle = \sum_{p,m',s} P_{p\ell m'}^{n\boldsymbol{k}s} |p,\ell,m'\rangle. \qquad (4.9) \\
\Rightarrow P_{p\ell m}^{n\boldsymbol{k}s} &= \sum_{m'} a_{m'm} \overline{P}_{p\ell m'}^{n\boldsymbol{k}s} \qquad \text{or} \qquad \overline{P}_{p\ell m}^{n\boldsymbol{k}s} = \sum_{m'} a_{mm'}^{\star} P_{p\ell m}^{n\boldsymbol{k}s}.
\end{aligned}
$$

Thus, the rotation matrix for the new projector coefficients is the complex conjugate of the $\hat{A}$ rotation matrix. However, we are dealing with the real spherical harmonics, whose rotation matrices are completely real (see Appendix C). This implies that both the new projector coefficients and the real spherical harmonics transform using the same rotation matrix $\hat{A}$.

The implementation was done with the intention of studying the splitting of the $e_g$ and $t_{2g}$ orbitals of a $3d$ cation in an octahedral or a tetrahedral environment. It is capable of handling distortions of up to 35 % in terms of the arm lengths or angles, as well as handling non-spin-polarised, spin-polarised and relativistic-spin-polarised electron wavefunctions. In the following subsection we present the results obtained for the Fe1 site in GFO and provide a validation of the results using the point-charge model.

### 4.6.2 Results for GFO

The crystal-field analysis was performed on all the Fe sites in GFO. Fig. 4.6 shows the $d$-projected density of states of an Fe1 atom in GFO, which are similar to all the other Fe sites. The SOC was included in the calculations, which were done using the GGA functional with the Hubbard $U = 4$ (top) and 8 eV (bottom). The $e_g$ and $t_{2g}$ orbitals are shown in black and red respectively.
We observe that for both values of $U$, the occupied $3d$ states are split clearly with the $e_g$ orbitals lower in energy than the $t_{2g}$. The splitting between the unoccupied states seem to depend upon the value of $U$, and thus the hybridisation, with the $e_g$ orbitals slightly lower in energy than the $t_{2g}$ for $U = 8$ eV, and the $t_{2g}$ orbitals clearly lower in energy for $U = 4$ eV. Since the Fe1 site (and Fe2 and Ga2 sites as well) is an octahedral site, the results obtained for the occupied states contradict the splitting expected for octahedral sites.

Using the crystal-field splitting, it is possible to probe the filling of $d$-orbitals and understand why Fe in GFO possesses a non-zero orbital magnetic moment and why the spin magnetic moment of Fe is less than 5 $\mu_B$. To do so, we plot the $(\ell, m, s)$-projected DOS of the $3d$ electrons of the same atom in Fig. 4.7. Also shown are the effects of the SOC on the DOS. This is an Fe1 site which is why the majority spins are of *spin-down* nature. Moreover, there are some *spin-up* states, mainly of $t_{2g}$ character, which belong to the neighbouring oxygen atoms. These states oppose the moments on the Fe sites and create a small non-zero orbital moment as well as a spin magnetic moment less than 5 $\mu_B$. This would indicate that the bonding between the Fe and O ions in GFO has a covalent character. As a result of this covalent character, certain spin-polarised states should be present on the oxygen ions. Our calculations indeed agree with this prediction, indicating small spin magnetic moments between 0.010 $\mu_B$ and 0.087 $\mu_B$ for $U = 4$ eV, and between 0.008 $\mu_B$ and 0.065 $\mu_B$ for $U = 8$ eV on the oxygen atoms. These values are more affected by the level of hybridisation controlled by $U$ than

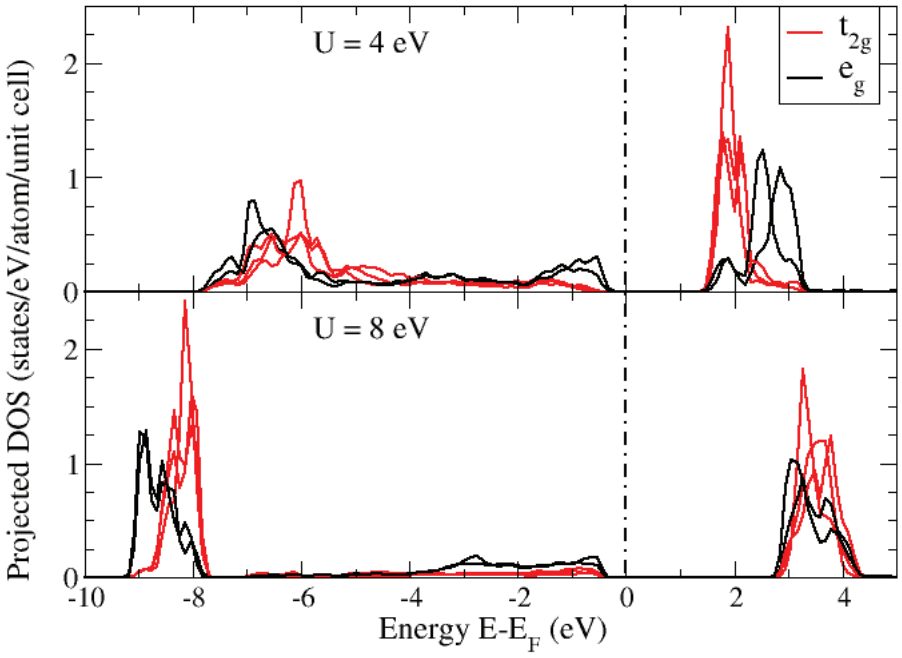


**Figure 4.6:** Crystal-field splitting using *ab initio* techniques

the SOC. We thus conclude that increasing the value of $U$ drives the Fe system to a +3 state and that the bonding between the Fe and O atoms is partly ionic. Furthermore, our results show that this bonding is not influenced by the SOC, with the exception of creating a non-zero orbital moment. The conclusions drawn here support the calculations done by Ibrahim and Alouani,[88] where they obtained Bader charges of +1.63 to +1.73 on the Fe atoms depending on $U$, instead of +2 as expected for an ionic crystal, and concluded a partial ionic bonding.

To understand the mechanism causing a tetrahedral-type splitting in an octahedral environment, a point-charge model was developed, in which the effects of hybridisation can be fully neglected. Such a model would help us understand the $e_g$-$t_{2g}$ splitting obtained for the occupied states with $U = 8$ eV, where the $3d$ orbitals are highly localised. Qualitatively, the electrons in the model can only interact through the Coulomb interaction with the neighbouring negatively charged oxygen ions. With this requirement in mind, we assumed ionic charges of +3 on the central atom and −2 on the neighbouring atoms forming the octahedral. For maintaining consistency between the *ab initio* calculation and the point-charge model, the octahedron was oriented in the same way as in the rotated frame of reference, i.e. with the octahedral arms aligned maximally along the axes. We then rewrite the Coulomb potential felt at the central atom in terms of the spherical harmonics as,[101]

$$V(\boldsymbol{r}) = \sum_{i=1}^{6} \frac{q_i}{|\boldsymbol{r} - \boldsymbol{R}_i|} = \sum_{i=1}^{6} \sum_{\ell=0}^{\infty} \sum_{m=-\ell}^{\ell} (-1)^m \frac{4\pi q_i}{2\ell+1} \mathcal{Y}_\ell^{-m}(\boldsymbol{r})\, \mathcal{Y}_\ell^m(\boldsymbol{R}_i)\, \frac{R_i^\ell}{r^{\ell+1}}, \tag{4.10}$$

where $q_i$ is the charge on the neighbouring ligand atoms, $-2e$ for the oxygen ions in GFO, the $\mathcal{Y}_\ell^m$ are the spherical harmonics, and $\boldsymbol{R}_i$ are the distance vectors connecting the central atom to the ligand $i$.

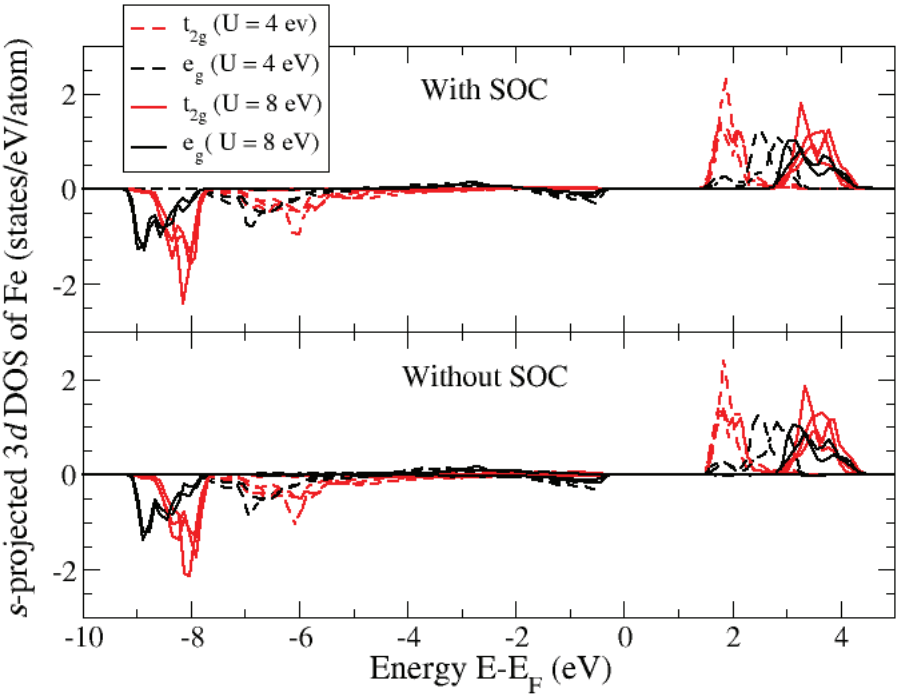


**Figure 4.7:** Effect of SOC and $U$ on the crystal-field splitting

Using the above expression, we can calculate the matrix elements $M_{m,m''}$ that are the overlaps of the $3d$ orbitals as,

$$\begin{aligned} M_{m,m''} &= \langle \mathcal{Y}^{m}_{\ell=2} | V(\boldsymbol{r}) | \mathcal{Y}^{m''}_{\ell=2} \rangle \\ &= \int \sum_{i=1}^{6} \sum_{\ell,m'} (-1)^{m}\, \mathcal{Y}^{-m}_{2}(\boldsymbol{r})\, |r\phi|^2 \frac{(-1)^{m'} 4\pi q_i}{2\ell+1}\, \mathcal{Y}^{-m'}_{\ell}(\boldsymbol{r})\, \mathcal{Y}^{m'}_{\ell}(\boldsymbol{R}_i)\, \frac{R_i^{\ell}}{r^{\ell+1}}\, \mathcal{Y}^{m''}_{2}(\boldsymbol{r})\, \mathrm{d}\boldsymbol{r}, \end{aligned} \tag{4.11}$$

where $\phi(r)$ is the radial function corresponding to the $3d$ orbitals, with $\int |r\phi|^2\, \mathrm{d}\boldsymbol{r} = 1$. The identity $\mathcal{Y}^{m\star}_{\ell} = (-1)^m \mathcal{Y}^{-m}_{\ell}$ was used to arrive at the final result. The above expression contains a product of three spherical harmonics and their integration, which can be simplified using the Gaunt coefficients, which in terms of the Wigner 3-$j$ symbols are,

$$M_{m,m''} = \int \sum_{i=1}^{6} \sum_{\ell,m'} (-1)^{m+m'} \frac{5 q_i R_i^{\ell}}{r^{\ell+1}} \sqrt{\frac{4\pi}{2\ell+1}} |r\phi|^2 \begin{pmatrix} 2 & 2 & \ell \\ 0 & 0 & 0 \end{pmatrix} \begin{pmatrix} 2 & 2 & \ell \\ m'' & -m & -m' \end{pmatrix} \mathrm{d}r, \tag{4.12}$$

where $\begin{pmatrix} j_1 & j_2 & j_3 \\ m_1 & m_2 & m_3 \end{pmatrix}$ are the Wigner 3-$j$ symbols linked to the Clebsch-Gordon coefficients as,

$$\begin{pmatrix} j_1 & j_2 & j_3 \\ m_1 & m_2 & m_3 \end{pmatrix} = \frac{(-1)^{j_1 - j_2 - m_3}}{\sqrt{2j_3+1}} \langle j_3, -m_3 | j_1, m_1; j_2, m_2 \rangle. \tag{4.13}$$

The Wigner 3-$j$ symbols are used for their symmetry properties. They are invariant under even permutations of the columns and obtain a phase factor $(-1)^{j_1+j_2+j_3}$ for every odd permutation. Additionally,

they are non-zero only for the following conditions:

$$m_1 + m_2 + m_3 = 0, \tag{4.14}$$
$$j_1 + j_2 + j_3 \quad \text{is an integer , an even integer if } m_1 = m_2 = m_3 = 0, \tag{4.15}$$
$$|m_i| \leq j_i. \tag{4.16}$$

These conditions allow us to restrict the summation over $\ell, m'$ in Eq. 4.12 to $\ell = 0, 2, 4$ and $m' = m'' - m$. For $\phi$, we use the hydrogen-like radial functions given as,

$$\phi_{n,\ell}(r) = \left(\frac{2Z}{na_0}r\right)^{\ell} \sum_{k=0}^{n-\ell-1} a_k \left(\frac{2Z}{na_0}r\right)^{k} e^{-\frac{Zr}{na_0}}, \tag{4.17}$$

where $a_0 = \frac{4\pi\varepsilon_0}{me^2}$ is the Bohr radius, $n$ is the principle quantum number (3 for $3d$ orbitals) and $a_k$ are coefficients that can be obtained through recursion as,

$$a_{k+1} = \frac{k + \ell + 1 - n}{(k+1)(k+2\ell+2)} a_k, \tag{4.18}$$

which terminates for $k = n - \ell - 1$. For the $3d$ orbitals, corresponding to the third orbit of Fe with atomic number $Z = 26$ and $\ell = 2$, we have,

$$\phi_{3d} = \frac{2\sqrt{2}}{27\sqrt{5}} \left(\frac{Z}{3a_0}\right)^{\frac{3}{2}} \left(\frac{Zr}{a_0}\right)^{2} e^{-\frac{Zr}{3a_0}}. \tag{4.19}$$

Using this in Eq. 4.12 and rewriting the matrix elements in terms of the Wigner 3-$j$ symbols, we have,

$$M_{m,m''} = \sum_{i=1}^{6} \sum_{\ell=0,2,4} \sum_{m'} (-1)^{m+m'} \frac{Z}{a_0} \frac{(5-\ell)!}{216} q_i \left(\frac{2Z}{3a_0}R_i\right)^{\ell} \sqrt{\frac{4\pi}{2\ell+1}} \begin{pmatrix} 2 & 2 & \ell \\ 0 & 0 & 0 \end{pmatrix} \begin{pmatrix} 2 & 2 & \ell \\ m'' & -m & -m' \end{pmatrix}. \tag{4.20}$$

For the $3d$ orbitals, we have five $m$ values and thus, $M$ is a $5 \times 5$ matrix. Note that the spin degrees of freedom are not included. This is justified by the fact that Fe in GFO has essentially a +3 ionic charge and a large band gap, where the states of one spin interact mainly among themselves than with the other spin states. However, if one wishes to include the spin quantum number and the SOC, it can be done using a $10 \times 10$ matrix, where the off-diagonal $5 \times 5$ matrices would contain the couplings (exchange, SOC) between the two spin states.
We then diagonalise the matrix $M$ to obtain the eigenvalues and the corresponding eigenvectors in the $(\ell, m)$ basis. Since the $e_g$ correspond to $m = 0, 2$ and $t_{2g}$ correspond to $m = -2, -1, 1$, we can plot the eigenvalues in terms of the proportion of $e_g$ and $t_{2g}$ orbitals.

The results were calculated for the same Fe1 atom as described in Fig. 4.6, and are plotted in Fig. 4.8. The figure shows that there is very low mixing of the $e_g$ and $t_{2g}$ orbitals. We also obtain a similar behaviour as obtained for the occupied states using the *ab initio* splittings, with the $e_g$ orbitals lower in energy than the $t_{2g}$ orbitals. Since the point-charge model is mainly based on unscreened Coulomb interaction with the point-like ionic neighbours without hybridisation, the crystal-field splitting obtained for the Fe octahedral atoms can be said to arise mainly from the geometry of the distorted octahedral environment. There are at least two inferences one can draw from the results obtained in this section,

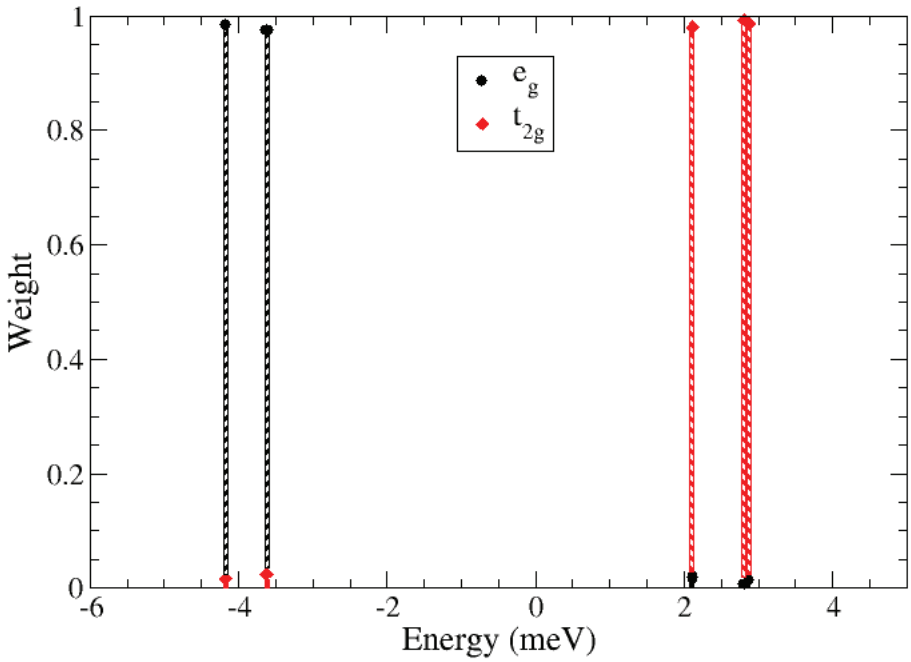


**Figure 4.8:** Crystal-field splitting using the point-charge model

- The conventional meaning of $e_g$ and $t_{2g}$ orbitals is no longer valid since the splitting is not in accord with what is expected (Fig. 4.5).
- The octahedral environment is so distorted that the ligands behave as a tetrahedron with unbalanced charges.

While the first point seems right, we point out that even though the conventional splitting is not preserved, it is possible to distinguish *clearly* the $e_g$ and $t_{2g}$ orbitals within the full *ab initio* model as well as the point-charge model, due to the low mixing of the orbitals. The second argument becomes more intuitive when one considers that the Fe central atom is displaced away from the centre as was shown by Ibrahim and Alouani in an earlier work.[88] This might cause a tetrahedral sort of behaviour, simply due to the high amount of distortion of the octahedral environment.

The point-charge model is not an exact model and can only provide a qualitative understanding of the crystal-field splitting for systems which are mainly ionic and the hybridisation between the central atom orbitals and neighbouring ligands is low. As the amount of hybridisation increases (lowering of $U$), the model is less appropriate to study the orbital splitting behaviour, since the neighbouring ions can no longer be considered as fully ionic or point-like. However, the point-charge model is very general and can be used for the splitting of the $d$, $f$ and higher orbitals.

In this section, we demonstrated that the $3d$ orbitals on the octahedral Fe sites in GFO have a tetrahedral-like splitting due to the high amount of distortion of the octahedron. To ensure that this is not an artefact, a point-charge model was developed that gave the same qualitative splitting of the

orbitals, thereby strengthening the validity of the results. The crystal-field splitting is also useful to study how the orbitals are filled to provide an understanding of the magnetic order in the system.
In the following section, the focus turns to probing the electric properties, mainly the electric polarisation, of GFO. Once the linear temperature dependence results of the electric polarisation are explained, we study the magnetoelectric properties of GFO using two mechanisms – direct magnetoelectric effect and indirect (magnetostrictive) magnetoelectric effect. The results for the indirect effect are not provided since they are still being computed.

## 4.7 Magnetoelectric Properties

GFO has been known as a ferrimagnetic and ferroelectric material, i.e. it contains a spontaneous magnetisation and a spontaneous electric polarisation. Additionally, these two ferroic orders have been known to be coupled to one another.[71,74–76,78,102] However, a theoretical understanding of the mechanism driving this coupling is missing and until recently, even the electric polarisation of the GFO system was not computed using *ab initio* techniques.[82,83] With an aim of understanding the coupling between the magnetic and electric ferroic orders, we performed *ab initio* calculations for the electric polarisation and its dependence on the magnetisation direction as implemented in VASP.[90–95] A brief overview of the modern theory of polarisation is provided in Appendix D. This section first presents our results for the electric polarisation on a path following a linear interpolation between the atomic positions at 4 K and 230 K provided by Arima *et al.*,[78] which would imitate a linear temperature dependence. In the second part of the section, we provide the results of the magnetoelectric effect obtained by rotating the magnetisation direction in the $y$-$z$ plane. Two kinds of effects were probed, direct, where the ions were not relaxed, and indirect (magnetostrictive), where the ions were relaxed.

### 4.7.1 Temperature Dependence of Electric Polarisation

To simulate a temperature dependence, we assume a linear interpolation of the atomic positions and lattice vectors between those at 4 K and 230 K. The initial (at 4 K) and final (at 230 K) positions were measured with neutron diffraction patterns by Arima *et al.* and are given in Table 4.4. It can be observed from this data that there is very little change in the atomic positions and the lattice vectors, for example, change in volume is less than 0.2 %, and thus, we can work in the linear regime between these temperatures.

To simplify work in the linear regime, we defined a parameter $\lambda$ between 0 and 1 defining the temperature and positions at 4 K and 230 K respectively. For example, the temperature is then defined as,

$$T(\lambda) = 4 + (230 - 4)\lambda \tag{4.21}$$

$\lambda$ was varied in steps of 0.1 and we calculated the electric polarisation for the atomic positions at these points. A small description of how the polarisation is calculated is given in Appendix D. Since the initial and final positions are obtained from experiment, the ionic relaxation was not carried out. Additionally, the electric polarisation is multi-valued differing by integral values of the polarisation quanta.[93,103] To resolve this, it is necessary to calculate the polarisation on a path connecting the non-polar structure (centrosymmetric) and the polar structure (non-centrosymmetric). As a result, the electric polarisation values were already manipulated based on the method developed by Stoeffler,[83] who had performed the calculation for the GFO structure at 4K along a polarisation lattice

branch connecting the corresponding non-polar and polar structures.

**Table 4.4:** Experimental positions (relative) of GFO ions at 4 K and 230 K with $a = 8.71932$ Å, $b = 9.36838$ Å and $c = 5.06723$ Å at 4 K and $a = 8.72569$ Å, $b = 9.37209$ Å and $c = 5.07082$ Å at 230 K.[78]

| Site | 4 K | | | 230 K | | |
|---|---|---|---|---|---|---|
| | $x$ | $y$ | $z$ | $x$ | $y$ | $z$ |
| Ga1 | 0.1500 | 0.0000 | 0.1781 | 0.1501 | 0.0000 | 0.1761 |
| Ga2 | 0.1593 | 0.3073 | 0.8106 | 0.1597 | 0.3067 | 0.8091 |
| Fe1 | 0.1538 | 0.5831 | 0.1886 | 0.1525 | 0.5827 | 0.1893 |
| Fe2 | 0.0346 | 0.7998 | 0.6795 | 0.0351 | 0.7992 | 0.6787 |
| O1 | 0.3228 | 0.4262 | 0.9716 | 0.3223 | 0.4260 | 0.9740 |
| O2 | 0.4864 | 0.4311 | 0.5142 | 0.4877 | 0.4313 | 0.5168 |
| O3 | 0.9979 | 0.2022 | 0.6541 | 0.9963 | 0.2008 | 0.6521 |
| O4 | 0.1593 | 0.1974 | 0.1480 | 0.1593 | 0.1961 | 0.1475 |
| O5 | 0.1695 | 0.6717 | 0.8437 | 0.1715 | 0.6714 | 0.8410 |
| O6 | 0.1736 | 0.9383 | 0.5166 | 0.1725 | 0.9379 | 0.5153 |

The absolute values of the electric polarisation for the ideal system as a function of temperature are shown in Fig. 4.9. The polarisation vector is aligned along the negative $y$-axis, with a magnitude of about 23.5 $\mu$C/cm$^2$, close to the value of 25 $\mu$C/cm$^2$ as reported by Stoeffler.[83] It is seen that as the temperature increases, the magnitude of the polarisation decreases. This is expected since increase in temperature leads to an increase of the inter-atomic distances, which causes hybridisation to decrease and electrons to be more localised near the parent atom and the bonding becomes more ionic. Since polarisation is a measure of how far apart the charges are, a localisation of electrons near the ions implies a lowering of the magnitude of the electric polarisation.

This can be understood with the help of Fig. 4.10, which shows the electronic and ionic components of the electric polarisation in GFO. The polarisation is plotted along the positive $y$-axis, which is why the net polarisation is negative. The ionic part of the polarisation increases in magnitude with temperature. Since, the ionic part of the polarisation is the sum of the dipole moments per unit cell as shown in Eq. D.6, an increase of temperature would drive the atoms apart, thereby increasing the dipole moments and thus, the electric polarisation.

The electronic part of the polarisation also increases with temperature, however in the opposite direction, due to the charge. To understand this behaviour, we look at the expression given in Eq. D.11. If we consider that the Wannier centres are located at the positions of the ions, then increasing the temperature would drive the ions apart and the Wannier centres, hence increasing the polarisation. However, if this were the only factor, we would expect no change in the net polarisation since the ionic positions and the Wannier centres would be driven apart by exactly the same amount. The other factor is the electron hybridisation, which decreases with increase in the inter-atomic distances. As a result of this, the electronic density becomes more localised and the bonding becomes more ionic, which increases the electric polarisation. Since the electronic polarisation and the ionic polarisation are in opposition, the net polarisation, parallel to the ionic polarisation, reduces in magnitude with increase in temperature.

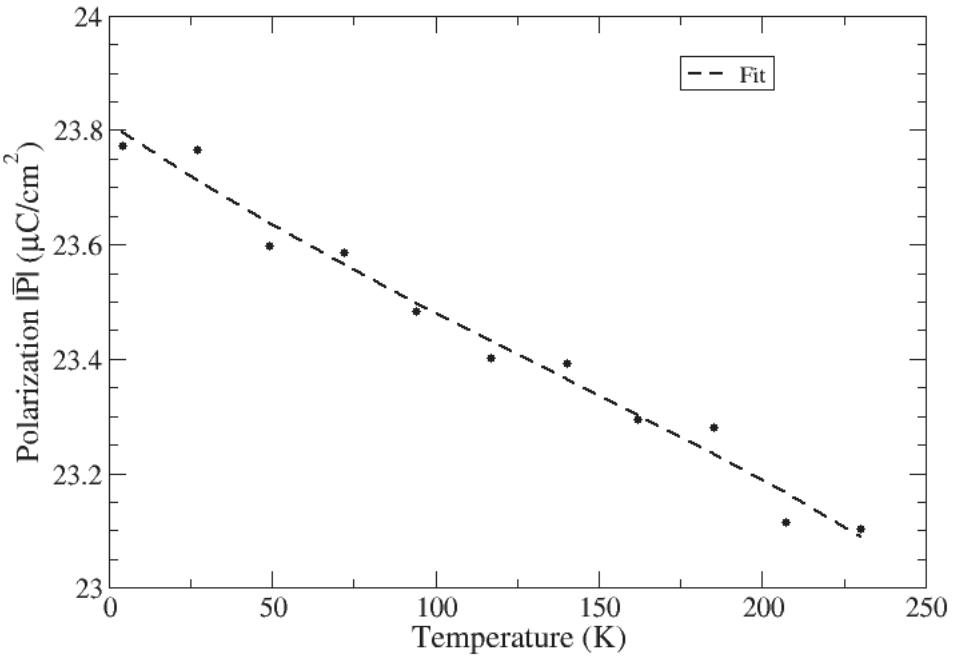


**Figure 4.9:** Electric polarisation in GFO as a function of temperature

### 4.7.2 Rotation of Magnetisation Direction

The electric polarisation obtained in the previous subsection are in good agreement with what was found by earlier theoretical studies.[83] Recent experimental studies[104] were performed on $Ga_{2-x}Fe_xO_3$ with $x = 1.1$, which indicate polarisation values around 33 $\mu C/cm^2$, not very far from ours. These confirmations support our calculations and allow us to study magnetoelectric effects in GFO. Magnetoelectric effects form a class of phenomena that arise due to the coupling between the magnetic and electric ferroic orders, which are the ferrimagnetic and ferroelectric orders in GFO. In our work, we probe the effect of rotation of the magnetisation axis on the electric polarisation.

There are two types of magnetoelectric effects – direct and indirect. The direct magnetoelectric effect arises from the SOC, that couples the spin and the lattice. When an external magnetic field is applied, the electrons move to a different ground state that causes the electronic polarisation to change. This effect does not require the ionic positions to change and is a direct consequence of the external magnetic field, hence the term *direct*. On the other hand, the indirect magnetoelectric effect is a consequence of the external magnetic field moving the ions and altering the volume of the cell, thus changing the electric polarisation. This effect is also called the magnetostrictive magnetoelectric effect. Based on experiments conducted in the 1960's, it was hypothesised that the magnetoelectric effects observed in GFO are due to the indirect mechanism.[75] However, in the 1990's, Popov *et al.* indicated that the direct mechanism is responsible for the observed magnetoelectric effects in GFO.[105] In spite of the unresolved problem for over half a century, there has been no systematic theoretical study trying to probe this phenomenon to the best of our knowledge.

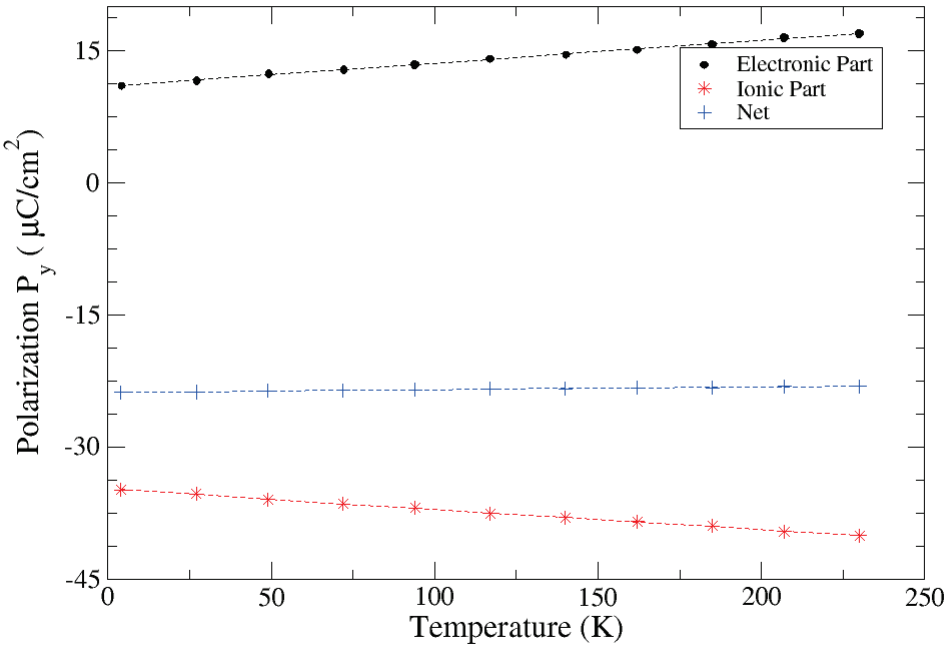


**Figure 4.10:** Electronic (black circles), ionic (red stars) and net (blue pluses) electric polarisations in GFO as a function of temperature

We begin by rotating the magnetisation axis in the $y$-$z$ plane, starting from the $+z$-axis, the original configuration, to the $-z$-axis through the $+y$-axis. Rotation of the magnetisation axis is akin to rotation of the moments such that they remain parallel (or anti-parallel) to the magnetisation axis. Since we can not include external magnetic fields in our calculation, we fix the moments along a rotated magnetisation axis to simulate a saturation external magnetic field in the $y$-$z$ plane that will rotate the moments in the same way. By maintaining an antiferromagnetic system, we assume that the exchange energy, i.e. the energy to overcome the antiferromagnetic coupling between the Fe ions, is always higher than the energy of the corresponding external magnetic field. To check whether the direct mechanism is responsible for the observed magnetoelectric effects, the calculations were performed keeping the ions fixed. As a result, any change in the electric polarisation is due to the change in the electronic polarisation only.

Fig. 4.11 shows the change of the electric polarisation along the $y$- and $z$-axes in GFO. While a clear pattern exists in both curves, the change is less than 0.4 nC/cm$^2$, five orders of magnitude lower than the spontaneous electric polarisation determined in the previous subsection at 23.5 $\mu$C/cm$^2$. Moreover, it is very hard to measure these small values experimentally. Thus, quantitatively speaking, the direct mechanism is far from sufficient to explain the magnetoelectric effects in GFO. The indirect mechanism on the other hand might be the main cause for the observed magnetoelectric effects. This is supported by the temperature dependence calculations done in the previous subsection, where the volume change of about 0.2 % caused the electric polarisation to change by about 0.6

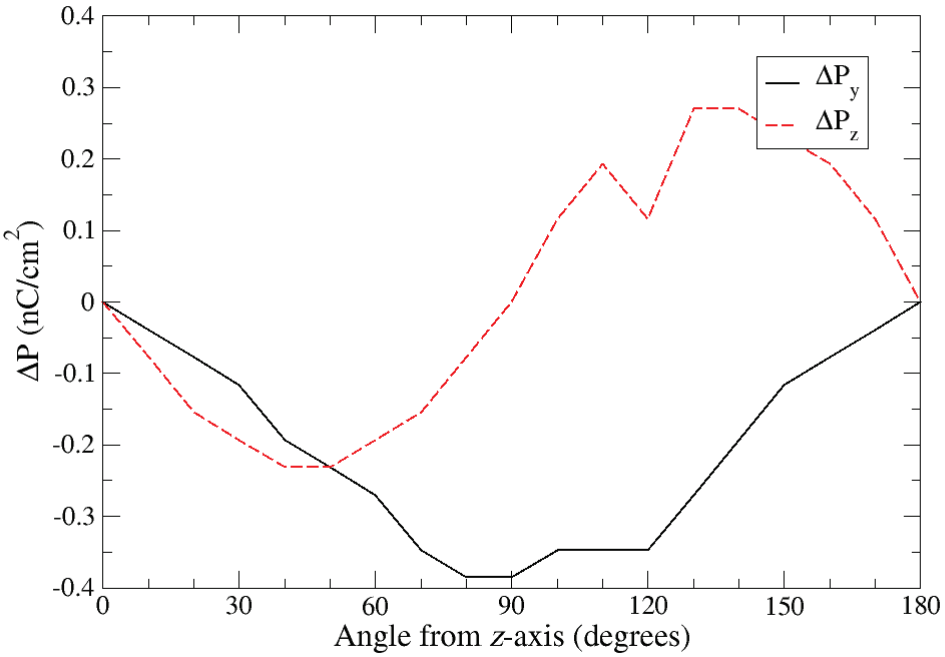


**Figure 4.11:** Change in the electric polarisations along the $y$- and $z$-axes in GFO as a function of rotation of the magnetisation axis

$\mu$C/cm$^2$ or 2.5 %.
To properly determine the main mechanism for the magnetoelectric effects, it is hence important to perform similar calculations while allowing the unit cell volume and ionic positions to change, which might be very expensive since GFO is a relatively large system. These calculations can be done by performing only a volume relaxation to minimise the computational effort, and have not yet been carried out.

## 4.8 Discussion

In this chapter, we presented the results of our *ab initio* calculations on GFO. To correctly account for the strongly correlated $3d$ electrons the LDA+$U$ model was used, where we found that the value of $U = 8$ eV best reproduced the experimental values of the energy band gap and the site magnetisations. We also found that the inclusion of the SOC did not change the electronic properties drastically and allowed us to obtain a non-zero orbital moment in GFO.
By performing site disorder studies based on cationic occupancies we confirmed earlier hypotheses attributing these disorders to the cause of ferrimagnetism in the system. The difference between the ground state energies of the ideal and disordered systems is below that previously estimated and much closer to the thermal energy available during synthesis of the system. This indicates that site disorders can not be completely controlled using current synthesis methods. Further studies using excess-Fe might provide clues to better control the electronic and magnetic properties, in spite of the

site disorders, to help the development of practical devices.
To understand the magnetic ordering of the Fe sites, we implemented the crystal-field analysis in VASP. For the octahedral Fe sites, we obtained a tetrahedral-like splitting. The origin of this was attributed to the high amount of distortion in the octahedral geometry and confirmed with a point-charge model. We also showed that bonding between Fe and O is partly covalent, thereby explaining the non-zero orbital moment and supporting earlier Bader charge calculations.
In addition, we presented our results for the linear temperature dependence of the electric polarisation. The polarisation has a monotonic decay which could be explained with the simple model of reduction of hybridisation due to increase of inter-atomic distances. This was interpreted by separating the electronic and ionic parts of the electric polarisation.
Towards the end of the chapter, we also presented the results of our direct magnetoelectric studies, where we rotated the magnetisation axis to simulate a rotation of the moments due to an external field while keeping the ions and cell volume fixed. The maximum change in the electric polarisation was under 0.4 $nC/cm^2$, and indicates that the direct mechanism is fails to explain the observed magneto-electric effects in GFO. To truly find the cause of these effects, one must perform similar studies of the electric polarisation by allowing the cell volume to change due to the change of the magnetisation axis, i.e. a magnetostriction induced polarisation.

The methods used in this chapter were targeted towards understanding a particular system, GFO. However, similar kinds of studies can be used for other multiferroic bulk systems as well. In the following chapter, we turn our focus towards chromium oxide, $Cr_2O_3$, where we use similar techniques to probe the origin of ferromagnetism and ferroelectricity in a completely antiferromagnetic system by applying large compressive biaxial strains on the unit cell. The calculations were first without SOC and then redone with SOC for all different combinations of the strains.

## 4.9 Conclusions and Perspectives

In summary, the results for the *ab initio* calculations on GFO performed under the LDA+$U$ and GGA+$U$ approximations with SOC were presented. The value of $U$=8 eV best reproduced the experimentally observed values of the energy band gap and the site magnetisations. $U$ was shown to push the 3$d$ electrons away from the Fermi level and thus played an important role in the electron hybridisation. The inclusion of SOC did not affect the electronic structure of the system. Cationic site disorder studies were then performed using experimental cationic occupancies, which reproduced the experimentally observed ferrimagnetism. The energy difference was shown to be closer to the thermal energy available during synthesis, thereby indicating difficulty of site disorder control.
The crystal-field analysis was implemented in VASP and using it, we observed that the Fe 3$d$ electrons in an octahedral field have a tetrahedral-like splitting. By invoking the point=charge model, we showed that this behaviour arises due to the high amount of distortion of the octahedron. The crystal-field analysis was also used to show the partly covalent bonding between Fe and O, and to explain the origin of the non-zero orbital moment.
We then presented the linear temperature dependence of the electric polarisation, which has a monotonic decay explained as separation of the ions with temperature. Then, we rotated the magnetisation axis of the system to simulate a rotation of the magnetic moments under an external field. By fixing the ions and cell volume, the direct magnetoelectric effect was computed. The values obtained were very small indicating that the indirect mechanism (magnetostrictive induced polarisation) might be the main cause for the observed magnetoelectric effects in GFO.

As perspectives for the system, it would be fruitful to study excess-Fe along with cationic site disorders to better control the electronic and magnetic properties of GFO. The crystal-field analysis can be redone on the Ga sites, both octahedral and tetrahedral, to understand the magnetic ordering of disordered systems. Magnetoelectric effects of the indirect nature can be studied to help understand the coupling between the ferroic orders. The methods developed here can also be applied to other multiferroic systems, such as $Cr_2O_3$ or $BiFeO_3$.

# 5 Electronic and Magnetic Properties of Chromium Oxide

## Contents



## 5.1 Introduction

Magnetoelectric materials are multiferroics with coupled magnetic and electric ferroic orders. In the previous chapter, we demonstrated a set of methods that was used to theoretically study one such material, gallium ferrite or GFO. Based on the results in the previous section, we apply these techniques to a different system, chromium oxide or $Cr_2O_3$. The first theoretical prediction of the existence of the magnetoelectric effect was provided by Dzyaloshinskii in 1959[69] for $Cr_2O_3$. The experimental observation followed quickly in 1961 by Astrov.[70] Since then, many studies have been performed on this system.[106,107]

Recent experiments by Halley *et al.* on $Cr_2O_3$ nanoclusters embedded in MgO have provided interesting results, which have potential to help development of new electronic devices. Fig. 5.1 shows the experimental schema,[108] where a size-enhanced magnetoelectric effect was observed. The strains on the $Cr_2O_3$ nanoclusters were very large and spontaneous magnetisation and electric polarisation were observed, phenomena which are absent in the normal bulk-like system. The origin of the ferromagnetism and polarisation are believed to arise from the highly strained $Cr_2O_3$ systems, rather than the MgO-$Cr_2O_3$ interface.

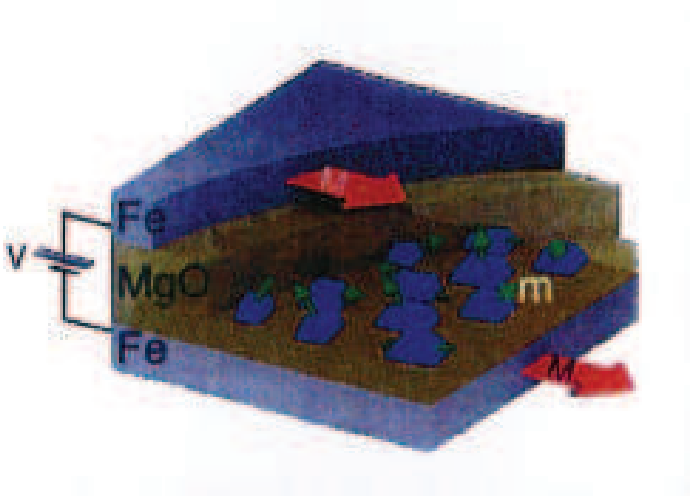


**Figure 5.1:** Experimental schema[108] of $Cr_2O_3$ nanoclusters embedded in MgO between two ferromagnetic Fe electrodes

Reprinted by permission from Macmillan Publishers Ltd: Nature Communications, 2014

With the intention of better understanding the experimentally observed phenomena, we performed *ab initio* studies to probe the electronic and magnetic properties of bulk $Cr_2O_3$. We first provide an introductory overview of $Cr_2O_3$ and its crystal structure, following which we describe the calculation details used to obtain the electronic and magnetic properties. We then provide the results of these calculations. To explain the origin of ferromagnetism, we performed strained calculations on the bulk, without and with the spin-orbit coupling (SOC).

## 5.2 Chromium Oxide: An Overview

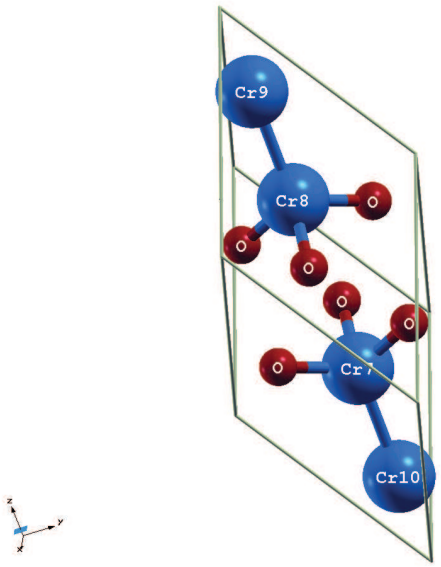


**Figure 5.2:** $Cr_2O_3$ unit cell with Cr and O atoms in blue and red respectively. The cationic sites are labelled and the lattice vectors form the parallelepiped.

Chromium oxide, $Cr_2O_3$, occurs naturally and adopts the corundum structure, like $Al_2O_3$ or $Ti_2O_3$, which is a slightly distorted hexagonal packed structure, with two-thirds of the octahedral sites occupied by chromium.[109] The lattice parameters are $a = b = 4.9607$ Å and $c = 13.5990$ Å in the hexagonal representation.[108] However, this representation requires a large unit cell that consists of 40 atoms. To reduce computational costs, the rhombohedral representation is used for this chapter, where only 10 atoms are required per unit cell and the lattice vectors are defined as:

$$\begin{aligned} \boldsymbol{t}_1 &= \frac{1}{3}(2\boldsymbol{a} + \boldsymbol{b} + \boldsymbol{c}) = \left(\frac{1}{2}a, \frac{1}{2\sqrt{3}}a, \frac{1}{3}c\right) \\ \boldsymbol{t}_2 &= \frac{1}{3}(-\boldsymbol{a} + \boldsymbol{b} + \boldsymbol{c}) = \left(-\frac{1}{2}a, \frac{1}{2\sqrt{3}}a, \frac{1}{3}c\right) \\ \boldsymbol{t}_3 &= \frac{1}{3}(-\boldsymbol{a} - 2\boldsymbol{b} + \boldsymbol{c}) = \left(0, -\frac{1}{\sqrt{3}}a, \frac{1}{3}c\right). \end{aligned} \tag{5.1}$$

The positions of the atoms represented in the rhombohedral and Cartesian coordinates are shown in Table 5.1. The values of $x$ and $z$ are 0.3056 and 0.3476 respectively. The corresponding unit cell is shown in Fig. 5.2, where the lattice vectors form the parallelepiped.

**Table 5.1:** Positions of the atoms in the Rhombohedral (relative) and Cartesian (absolute) coordinates

| Atom | Rhombohedral Coordinates | Cartesian Coordinates |
|---|---|---|
| $O_1$ | $(\frac{1}{4}+x, \frac{1}{4}-x, \frac{1}{4})$ | $(ax, 0, \frac{1}{4}c)$ |
| $O_2$ | $(\frac{1}{4}, \frac{1}{4}+x, \frac{1}{4}-x)$ | $(-\frac{1}{2}ax, \frac{\sqrt{3}}{2}ax, \frac{1}{4}c)$ |
| $O_3$ | $(\frac{1}{4}-x, \frac{1}{4}, \frac{1}{4}+x)$ | $(-\frac{1}{2}ax, -\frac{\sqrt{3}}{2}ax, \frac{1}{4}c)$ |
| $O_4$ | $(\frac{3}{4}-x, \frac{3}{4}+x, \frac{3}{4})$ | $(-ax, 0, \frac{3}{4}c)$ |
| $O_5$ | $(\frac{1}{4}, \frac{1}{4}+x, \frac{1}{4}-x)$ | $(\frac{1}{2}ax, -\frac{\sqrt{3}}{2}ax, \frac{3}{4}c)$ |
| $O_6$ | $(\frac{1}{4}, \frac{1}{4}+x, \frac{1}{4}-x)$ | $(\frac{1}{2}ax, \frac{\sqrt{3}}{2}ax, \frac{3}{4}c)$ |
| $Cr_7$ | $(z, z, z)$ | $(0, 0, cz)$ |
| $Cr_8$ | $(-z, -z, -z)$ | $(0, 0, -cz)$ |
| $Cr_9$ | $(\frac{1}{2}+z, \frac{1}{2}+z, \frac{1}{2}+z)$ | $(0, 0, \frac{1}{2}c+cz)$ |
| $Cr_{10}$ | $(\frac{1}{2}-z, \frac{1}{2}-z, \frac{1}{2}-z)$ | $(0, 0, \frac{1}{2}c-cz)$ |

There are four Cr atoms and hence four magnetic configurations for the system. We denote them as AFM1 (+, -, +, -), AFM2 (+, -, -, +), AFM3 (+, +, -, -) and FM (+, +, +, +), where the +/- sign in the parentheses denote the magnetic orientation along the $z$-axis in the order of $Cr_7$, $Cr_8$, $Cr_9$ and $Cr_{10}$. The ground state is the AFM1 state with an energy band gap of 3.4 eV.[107]

In the following, the *ab initio* calculations carried out for $Cr_2O_3$ are described. Then, the value of the Hubbard parameter $U$ that best describes experimental values is found. Using this, we probe the origin of the observed ferromagnetism and ferroelectricity[108] by performing calculations of the biaxially strained $Cr_2O_3$ system.

## 5.3 Calculation Details

The *ab initio* calculations were carried out using the VASP package.[85,86] We used the projector augmented wave basis set[66,87] and the exchange-correlation functional was described using the generalised gradient approximation (GGA) as parametrised by Perdew, Becke and Ernzerhof.[57,58] We used a k-point mesh of $8 \times 8 \times 8$ (512 k-points) for proper convergence of the ground state energy. For the plane wave cut-off, a value of 700 eV was used and the convergence criterion for the electronic self-consistent loop was set to 0.1 $\mu$eV. GGA underestimates the energy band gap and magnetic moments, especially in strongly correlated systems like transition metal oxides.[59–61] Unlike in the previous chapter, to account for the strong on-site Coulomb interaction among the localised Cr 3*d* electrons, we used the simplified rotationally invariant approach introduced by Dudarev *et al.*, represented by the Hubbard-like term $U$ and the exchange term $J$.[110] This flavour of LSDA+$U$ is of the following form:

$$E^{\mathrm{LSDA}+U} = E^{\mathrm{LSDA}} + \frac{(U-J)}{2} \sum_{s} \left[ \sum_{m} \rho_s^{mm} - \sum_{m,m'} \rho_s^{mm'} \rho_s^{m'm} \right] \tag{5.2}$$

In this approach, $U$ and $J$ do not enter separately and only the difference $(U - J)$ is meaningful. For this reason, we fixed $J$ to 0.9 eV, equal to the value in the previous chapter. Calculations were performed for $U$ = 3, 4, 6 and 8 eV to determine the value that best described the magnetic moments as well as the energy band gap. All the possible magnetic configurations, AFM1-3 and FM, were studied to determine the ground state configuration for comparison with previous studies. The spin-orbit coupling (SOC) was not included in the preliminary calculations.

With the intention of determining the origin of ferromagnetism and ferroelectric in $Cr_2O_3$, biaxial compressions of the lattice were simulated. Based on experimental values[108] the cell was compressed by 0 %, 3 %, 4 %, 5 % and 6 % along the $z$-axis, and by 0 %, 5 %, 10 % and 15 % in the $x$-$y$ plane. All combinations of compressions and magnetic orders were studied. Failing to obtain any net magnetisation or polarisation, the calculations were redone with the SOC included as implemented in VASP.[89] The electric polarisation was computed as implemented in the VASP code.[90–95]

## 5.4 Electronic and Magnetic Properties

In this section, we present the electronic and magnetic properties of $Cr_2O_3$ as a function of $U$. The values for the lattice vectors and relative shifts ($x$, $z$) are based on experimental values by Halley *et al.*,[108] so the atoms were not relaxed.

**Table 5.2:** Ground state total energy (eV) of $Cr_2O_3$ as a function of $U$. Energies are shifted to the lowest value obtained for AFM1 with $U$ = 3 eV.

| $U$ | AFM1 $+-+-$ | AFM2 $+--+$ | AFM3 $++--$ | FM $++++$ |
|---|---|---|---|---|
| 3 | 0 | 0.16 | 0.33 | 0.23 |
| 4 | 2.34 | 2.47 | 2.61 | 2.48 |
| 6 | 6.68 | 6.75 | 6.86 | 6.72 |
| 8 | 10.59 | 10.65 | 10.74 | 10.59 |

The calculations were done for $U = 3$, 4, 6 and 8 eV and the ground state energy of the system, as shown in Table 5.2. We see that for any fixed value of $U$, the AFM1 magnetic configuration has the lowest energy. However, as the value of $U$ increases, the energy of the FM configuration relative to that of the AFM1 configuration decreases. This can be understood in terms of the hybridisation between the Cr and O atoms. As $U$ increases, the hybridisation decreases, which in turn reduces the antiferromagnetic interaction. But since the long-range ferromagnetic interaction persists, the energy for the FM configuration relative to that of the AFM1 configuration decreases with increase in $U$.

**Table 5.3:** Energy band gap (eV) of $Cr_2O_3$ as a function of $U$. Experimental value is 3.4 eV[107]

| $U$ | AFM1 $+-+-$ | AFM2 $+--+$ | AFM3 $++--$ | FM $++++$ |
|---|---|---|---|---|
| 3 | 1.8 | 1.7 | 1.7 | 2.2 |
| 4 | 2.4 | 2.4 | 2.4 | 2.4 |
| 6 | 3.0 | 3.2 | 3.3 | 2.7 |
| 8 | 3.5 | 3.6 | 3.6 | 3.1 |

To find the value of $U$ that best describes the system physically, we tabulate the energy band gap as computed for different $U$ in Table 5.3. As seen in the case of GFO, the energy band gap increases with $U$ due to the lowering of the hybridisation that causes the $3d$ orbitals to be pushed away from the Fermi level. When compared to the experimental value of 3.4 eV,[107] we see that the value of $U = 8$ eV reproduces the closest value.

**Table 5.4:** Cr site magnetisation ($\mu_B$) in $Cr_2O_3$ as a function of $U$.

| $U$ | AFM1 $+-+-$ | AFM2 $+--+$ | AFM3 $++--$ | FM $++++$ |
|---|---|---|---|---|
| 3 | 2.85 | 2.85 | 2.81 | 2.98 |
| 4 | 2.91 | 2.91 | 2.88 | 3.02 |
| 6 | 3.02 | 3.02 | 2.99 | 3.09 |
| 8 | 3.10 | 3.11 | 3.09 | 3.16 |

The magnetic moments computed for the different configurations as a function of $U$ are tabulated in Table 5.4. We see that the magnetic moments increase with $U$. This is because as the hybridisation decreases, i.e. as the electrons become more localised at the atomic sites, the site magnetisation increases. This is similar to the behaviour of Fe in GFO.

At this point, we note that the net magnetic moment for the ground state configuration of $Cr_2O_3$ is zero. Experimentally, the magnetisation and electric polarisation was hypothesised to arrive from bulk $Cr_2O_3$ under high compressive stresses.[108] To test this, we performed *ab initio* calculations for compressed systems, the details of which is provided in the following section.

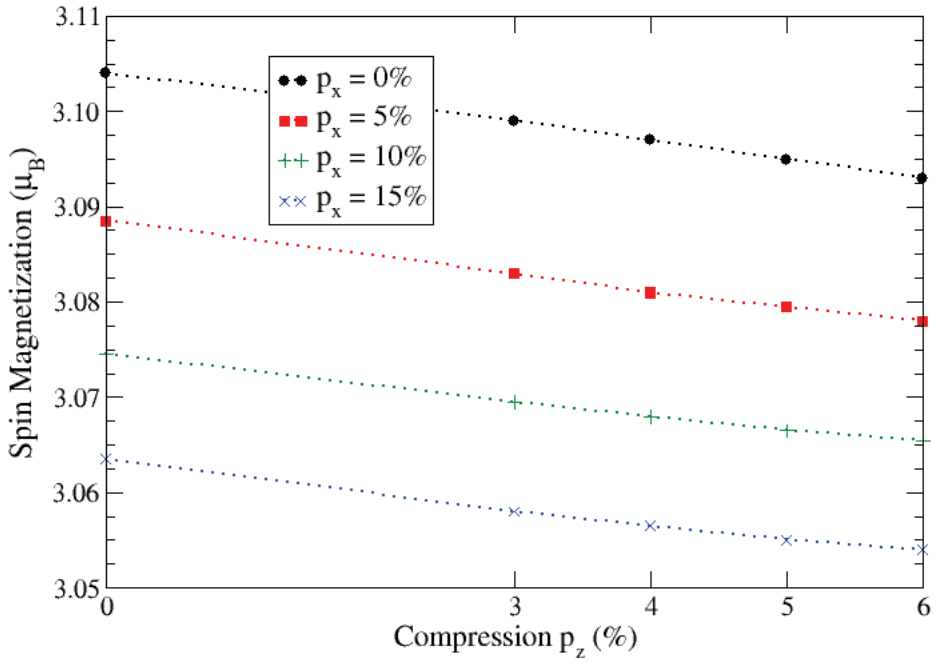


**Figure 5.3:** Cr site magnetisation as a function of compressive strain along $z$-axis. Different curves correspond to compressive strains of 0 % (black circles), 5 % (red squares), 10 % (green pluses) and 15 % (blue crosses) along $x$-axis.

## 5.5 Compression Studies

The purpose of the studies shown in this chapter is to reproduce the experimental observations of ferromagnetism and ferroelectricity. Cr was embedded in MgO and then annealed to form $Cr_2O_3$. From the x-ray magnetic dichroism spectra of the samples, it was determined that the crystals had a non-zero magnetisation and from the transport measurements, a spontaneous electric polarisation was found. The origin of the magnetisation and electric polarisation was attributed to the $Cr_2O_3$ bulk system under high compressive stresses.[108]

With the intention of verifying the hypothesis, we assume that the MgO-$Cr_2O_3$ interface can be neglected since the bulk is the main contribution. We also assume that the bulk system can take only an antiferromagnetic configuration. We justify this by pointing out that as the system is compressed, the electrons get de-localised and the Cr-O-Cr antiferromagnetic superexchange should become stronger with compression. Based on scanning tunnelling microscope measurements of the samples, it was determined that the compression along the $z$-axis ($\boldsymbol{c}$ direction) was between 3 % and 6 %. For the in-plane compression, there was a large strain of up to 18 % in one direction and almost no compression in the other. However it was determined that the large compressive strain of 18 % would relax to a value between 8-12 %. Based on this, we shrank the unit cell with compressive strains of 0, 3, 4, 5 and 6 % along $z$-axis and 0, 5, 10 and 15 % along $x$-axis. It can be easily verified that a compression along the $z$-axis requires changing only the $z$-coordinate of $\boldsymbol{t}_1$, $\boldsymbol{t}_2$ and $\boldsymbol{t}_3$ and a compression along the $x$-axis requires changing only their $x$-coordinate. The atoms were then allowed to relax with an

energy convergence criterion of 1 $\mu$eV, while the volume and shape of the cell were kept fixed. This would highly mimic the physical system where the compression of the $Cr_2O_3$ is maintained by MgO.

Our calculations showed that the ground state magnetic order is always the AFM1 configuration. For this reason, we now focus only on the results for the AFM1 configuration. The site magnetisation of Cr for all possible combinations of the strains in shown in Fig. 5.3. $p_x$, $p_y$ and $p_z$ denote compressive strains along the $x$-, $y$- and $z$-axes respectively and are defined as,

$$p_x = \frac{\Delta x}{x}; \qquad p_y = \frac{\Delta y}{y}; \qquad p_z = \frac{\Delta z}{z}. \tag{5.3}$$

We see that as the compressive strain increases, the Cr magnetic moment decreases. This is true for the in-plane compression as well. The reason for this behaviour is the de-localisation of the electrons due to stronger interaction with the neighbours with increase in lattice strain. This de-localisation causes the electrons to move away from the parent atom thereby reducing the site magnetisation. However, the system was still a perfect antiferromagnet and the electric polarisation was zero.

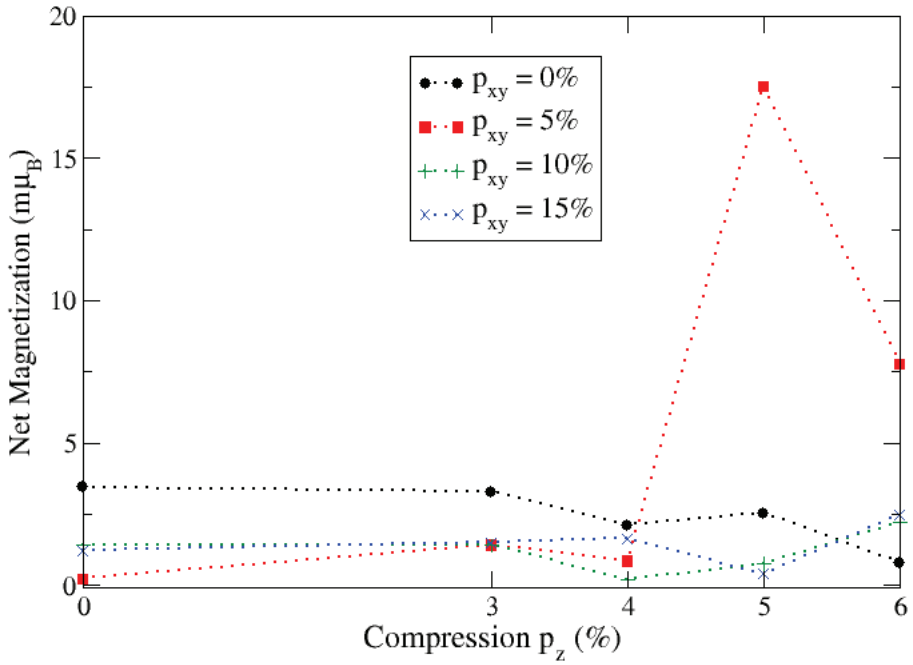


**Figure 5.4:** Net magnetisation (SOC included) as a function of compressive strain along $z$-axis. Different curves correspond to compressive strains of 0 % (black circles), 5 % (red squares), 10 % (green pluses) and 15 % (blue crosses) along $x$-axis.

Since there are no site disorders reported and our calculations showed that Cr is in a +3 configuration, we performed all the calculations again for the AFM1 configuration with the spin-orbit coupling (SOC). This would allow us to couple the spin to the lattice, which might prefer canted magnetic moments. The calculations were redone and the results did show a net magnetisation, but no electric

polarisation. Fig. 5.4 shows the net magnetisation as a function of the strain along the $z$-axis. The $z$ components are along the quantisation axis and hence maintain the AFM1 configuration. There is no discernible pattern of the coupling between the $y$ components of the individual atomic moments since they are generally too small. On the other hand the $x$ components exhibit an AFM2 type of configuration along the $-x$-axis. These $x$ components also increase with the compressive strain in the $x$ direction.

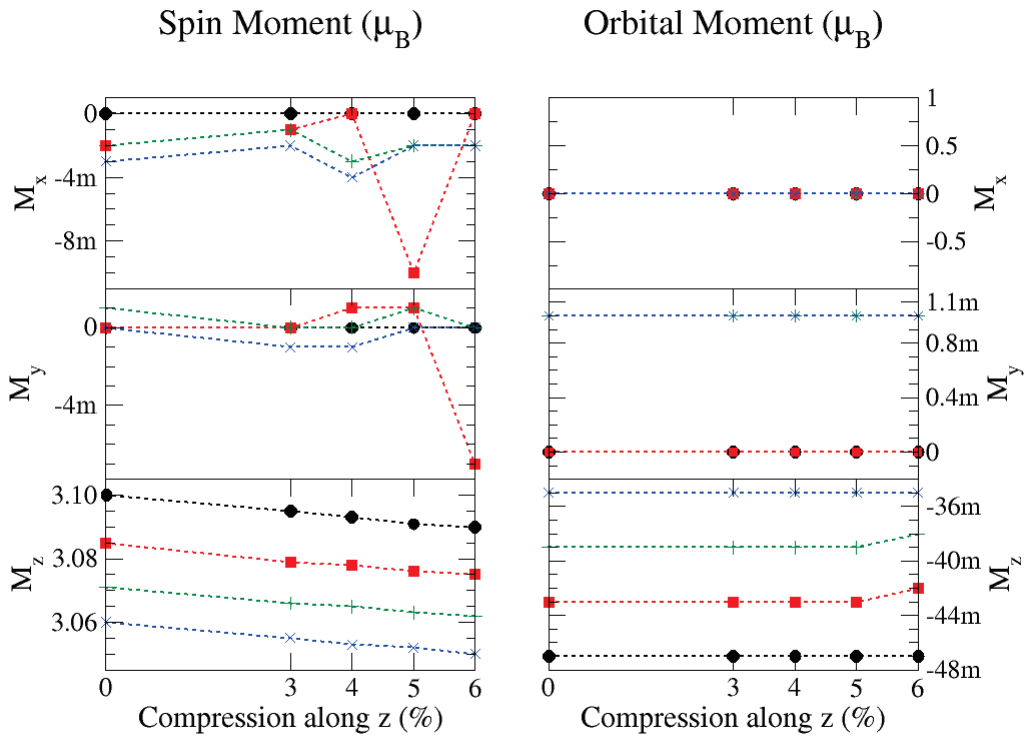


**Figure 5.5:** $x$ (top), $y$ (middle) and $z$ (bottom) components of Cr spin (left) and orbital (right) moments as a function of compressive strain along $z$-axis. Different curves correspond to compressive strains of 0 % (black circles), 5 % (red squares), 10 % (green pluses) and 15 % (blue crosses) along $x$-axis.

Fig. 5.5 shows the average spin and orbital magnetic moments for Cr as a function of compressive strains. While the $z$ component behaves similar to the case without SOC, there is no such pattern in the other components. Since Cr has a less-than-half-filled $3d$ shell, the orbital moments are anti-parallel to the spin moments. We observe an increase in the $x$ component of the spin moment for compressive strains of about 3-5 % along the $z$-axis. The maximum value is about 10 m$\mu_B$ per Cr atom, as compared to the experimentally observed 80 m$\mu_B$ per Cr atom.[108] Moreover, if the cause of a net magnetisation is ferrimagnetism as opposed to ferromagnetism, the actual physical moment per Cr atom might be higher than reported. The maximum value obtained could be an artefact caused by numerical errors, since it only happens once for a biaxial strain of 5 % along $x$ and $z$. In general, the individual Cr moments underestimate the magnetic moments by a factor of about 40.

The failure of the calculations performed for the strained $Cr_2O_3$ system to reproduce the experimentally observed ferromagnetism and polarisation raises questions on the hypotheses made for the

calculations. For these calculations we assumed that the system remains in an antiferromagnetic configuration, which may not be the case. If indeed the FM configuration is preferred at higher strains, then the system will contain a spontaneous magnetisation. However, in an FM case the magnetic moment on each Cr atom would be above 3 $\mu_B$, much higher than the experimental observation of 80 m$\mu_B$ per Cr atom.
Another issue is the validity of the hypothesis that the spontaneous ferroic orders are a result of the strained bulk. The typical size of the nanoclusters is about 5.5 nm along the $c$-axis or [001] direction, and about 2 nm along the $[\bar{1}\bar{1}0]$ direction.[108] This amounts to about 4 unit cells along the $c$-axis and about the same along the $b$-axis, making the physical cell small. Size effects might play an important role and it may not be appropriate to treat the system as a bulk crystal.
A contribution that was neglected in our calculations is the MgO-$Cr_2O_3$ interface. The nanoclusters were annealed with oxygen to prepare $Cr_2O_3$, and excess oxygen might be present at the interface, creating $CrO_2$, a known ferromagnetic material. Since the majority of the nanocluster would be antiferromagnetic, with only the surface being ferromagnetic, the average magnetic moment per Cr atom would be much lower than that for $CrO_2$.

## 5.6 Discussion

In this chapter, we presented our *ab initio* results for $Cr_2O_3$. To correctly account for the 3$d$ electrons, the GGA+$U$ approximation was used, where we found that the value of $U = 8$ eV best reproduced the experimental values of the energy band gap. By performing simulations on the different magnetic orders, AFM1-3 and FM, we observed that the AFM1 configuration is energetically the most stable. We simulated strains of the crystal to check the origin of ferromagnetism and electric polarisation. The strains were biaxial and all combinations were calculated. The calculations did not reproduce any magnetisation and hence they were redone with the SOC included. The SOC allowed the magnetic moments to be canted and produced a net moment of a few m$\mu_B$ per unit cell in the $x$-direction. The individual site magnetic moments were about 2-3 m$\mu_B$ per Cr atom in the $x$-direction, which are an underestimation of the experimental value of 80 m$\mu_B$ by a factor of 40.
The results obtained were for an infinite bulk crystal, and thus may not fully explain experimental observations. Size effects as well as the MgO-$Cr_2O_3$ interface might require to be included in the calculations to properly describe experiment. These studies are left as perspectives for the future.

## 5.7 Conclusions and Perspectives

The purpose of this chapter was to understand the origin of experimentally observed ferromagnetism and polarisation in $Cr_2O_3$ nanoclusters embedded in MgO. After determining that the value of $U = 8$ eV best reproduced the experimental energy band gap and that the AFM1 configuration is energetically the most stable, we simulated the high compressive strains of the crystal by shrinking the lattice. Our calculations failed to produce any net magnetisation without SOC, and provided an underestimation by a factor of 40 when the SOC was included. Based on this, we reject the hypothesis that the experimentally observed ferromagnetic order and electric polarisation arises from the compressed $Cr_2O_3$ bulk.

As perspectives, one might need to consider compressed super cells in vacuum to properly simulate

experimental behaviour. Other factors, such as excess-O at the surface, or the MgO-$Cr_2O_3$ interface, might play a crucial role in future calculations.

# 6 Implementation of Calculation of X-ray Absorption Spectra

## Contents



## 6.1 Introduction

X-ray absorption spectroscopy (XAS) and x-ray magnetic circular dichroism (XMCD) are excellent methods to probe the electronic and magnetic structure of materials. These methods have been under intense study, both theoretically and experimentally.[111–118] With XAS and XMCD, it is possible to obtain element-specific structure and magnetisation. The chemical selectivity of each core orbital of any atomic species in a material is what makes XAS and XMCD more capable of characterising magnetic systems than traditional magnetic techniques. This property is used to study magnetism in 3D, 2D and 1D systems. In addition to the chemical selectivity, it provides information on the magnetic spin and orbital moments of the photo-excited atoms. This information is extracted from the XMCD spectra, in particular, by means of the two sum rules,[119,120] which were developed in 1992 and 1993.

XMCD originates from the coupling between the photon helicity ($\pm\hbar$) and the atomic magnetic moments, thereby creating a difference between the absorption cross sections measured with respect

to the magnetisation axis for left and right circularly polarised light. The XMCD was originally predicted by Erskine and Stern in 1975,[121] and it was first observed by Schütz *et al.* in 1987[5] at the Fe K-edge. The dichroism at the $L_{2,3}$-edges was first measured by Chen *et al.* for Ni using soft x-rays.[122]

We have developed a package for the calculation of the XAS for left and right circularly polarised light in the VASP code, which is one of the most used and fastest *ab initio* codes for calculating electronic structure of materials.[85] Even though several implementations of XMCD are available in literature,[111,112,123,124] our implementation will allow the VASP community to calculate XMCD for systems of up to few hundreds of atoms per super cell, including complex molecular magnets, which will be difficult to perform using other methods. The implementation supports excitations from the core levels with core angular momenta up to $\ell' = 2$ and the spectra are computed under the dipole approximation using either the momentum operator $\hat{\boldsymbol{p}}$ or the position operator $\boldsymbol{r}$. We show that both methods lead to the same results which show the robustness of our implementation and the completeness of the basis-set. In this work, we present a derivation of the formulae behind the method and compare the results obtained by the two operators. We then provide two test cases under different approximations for the valence electrons to demonstrate the applicability of our code. Based on the success of the two cases, we compute the XAS and XMCD spectra for GFO with site disorders.

## 6.2 Theory

XMCD is defined as the difference between between the left and right circularly polarised absorption spectra. The directions are specified with respect to the magnetisation axis ($z$) of the system and in this chapter the term *polarisation* refers to the polarisation of light and *not* the electric polarisation. For our work, the circularly right polarised light $\hat{\varepsilon}_R$, circularly left polarised light $\hat{\varepsilon}_L$ and the $z$-polarised light are defined as:

$$\begin{aligned} \hat{\varepsilon}_R \equiv \hat{\varepsilon}_{+1} &\equiv \frac{-1}{\sqrt{2}}(\hat{\varepsilon}_x + i\hat{\varepsilon}_y), \\ \hat{\varepsilon}_L \equiv \hat{\varepsilon}_{-1} &\equiv \frac{1}{\sqrt{2}}(\hat{\varepsilon}_x - i\hat{\varepsilon}_y), \\ \hat{\varepsilon}_0 &\equiv \hat{\varepsilon}_z, \end{aligned} \tag{6.1}$$

where, $\hat{\varepsilon}_x$, $\hat{\varepsilon}_y$ and $\hat{\varepsilon}_z$ are unit vectors along $x$, $y$ and $z$ respectively.

For obtaining the expression of the polarisation dependent absorption spectrum, we assume a monochromatic plane wave for the vector potential $\boldsymbol{A}$ propagating along the direction given by the unit vector $\hat{\boldsymbol{n}}$, and defined as $\boldsymbol{A} = A_0\hat{\boldsymbol{\varepsilon}} \exp\left(\frac{i\omega\hat{\boldsymbol{n}}\cdot\boldsymbol{r}}{c} - i\omega t\right)$. $A_0$ is the amplitude of the plane wave, $\hat{\boldsymbol{\varepsilon}}$ the polarisation, $\omega$ the angular frequency of light, and $c$ the velocity of light in vacuum. Using the Fermi Golden Rule,[125,126] we get the polarisation dependent absorption rates, $\Re^{\hat{\boldsymbol{\varepsilon}}}_{i,f}(\omega)$, between an initial state $i$ at energy $\epsilon_i$ and a final state $f$ at energy $\epsilon_f$ as:

$$\Re^{\hat{\boldsymbol{\varepsilon}}}_{i,f}(\omega) = \frac{2\pi q^2 |A_0|^2}{\hbar m^2} \left| \langle i | \hat{\boldsymbol{\varepsilon}} \exp\left(\frac{i\omega\hat{\boldsymbol{n}}\cdot\boldsymbol{r}}{c}\right) \cdot \hat{\boldsymbol{p}} | f \rangle \right|^2 \delta(\hbar\omega - \epsilon_f + \epsilon_i), \tag{6.2}$$

where, $q = -e$ is the charge of the electron, $m$ its mass, $\hbar$ the reduced Planck's constant, $\hbar\omega$ the energy of the photon, $\hat{\boldsymbol{p}}$ and $\boldsymbol{r}$ the momentum operator and the position operator respectively. The absorption cross-section is defined as the ratio of the power absorbed by the atom $\hbar\omega\Re^{\hat{\boldsymbol{\varepsilon}}}_{i,f}$ to the

incident power per unit area $cU$, where $U$ is the energy density of the electromagnetic field defined as:

$$U = \frac{1}{2}\left(\frac{\varepsilon_0 E_0^2}{2} + \frac{B_0^2}{2\mu_0}\right). \tag{6.3}$$

Here, $E_0$ and $B_0$ are the amplitudes of the electric and magnetic fields respectively, $\varepsilon_0$ and $\mu_0$ are respectively the permittivity and permeability in vacuum. Using the relations $c^2\varepsilon_0\mu_0 = 1$ and $cB_0 = E_0$, we get $U = 2\varepsilon_0\omega^2|A_0|^2$. Thus, the total absorption cross-section $\sigma^{\hat{\boldsymbol{\varepsilon}}}$ is given by:

$$\sigma^{\hat{\boldsymbol{\varepsilon}}}(\omega) = \frac{4\pi\alpha\hbar}{m^2\omega}\sum_{if}\left|\langle i|\hat{\boldsymbol{\varepsilon}}\exp\left(\frac{i\omega\hat{\boldsymbol{n}}\cdot\boldsymbol{r}}{c}\right)\cdot\hat{\boldsymbol{p}}|f\rangle\right|^2\delta(\hbar\omega - \epsilon_f + \epsilon_i). \tag{6.4}$$

Here, $\alpha = \frac{1}{4\pi\varepsilon_0}\frac{q^2}{\hbar c}$ is the fine structure constant. Expanding the exponential as $e^x = 1 + x + \cdots$ and keeping only the first term produces the absorption cross-section in the electric dipole approximation:

$$\sigma^{\hat{\boldsymbol{\varepsilon}}}(\omega) \approx \frac{4\pi\alpha\hbar}{m^2\omega}\sum_{if}|\langle i|\hat{\boldsymbol{\varepsilon}}\cdot\hat{\boldsymbol{p}}|f\rangle|^2\,\delta(\hbar\omega - \epsilon_f + \epsilon_i). \tag{6.5}$$

In general, x-ray excitations are from one core level state towards the conduction states above the Fermi level, e.g. $2p$ for the $L_{2,3}$-edges in Fe. For circular x-ray dichroism, the absorption is very strongly dependent on the spin polarisation of the conduction states and the spin-orbit coupling (SOC) in the system. The left or right circularly polarised photons transfer opposite angular momentum to the core electrons and due to SOC, electrons of the opposite spin are excited. In the electric dipole approximation and without SOC, spin-flip transitions are prohibited and hence, the electron is excited to the conduction states while conserving its initial spin. If the valence states are spin-polarised, the difference between the left and right circularly polarised absorption spectra reflects the magnetic properties of the material. Even for materials with strong SOC, the spin-flip transitions are very weak and therefore often neglected.

The proper basis for the core states is thus a $|J, M\rangle$ basis and not an $|\ell', m', S', s'\rangle$ basis. Here, $J$ is the total angular momentum quantum number, $\ell'$ is the azimuthal quantum number and $S' = 1/2$ is the spin quantum number of the electrons. Their projections on the $z$-axis are respectively $M$, $m'$ and $s'$. Here, $J$ is the conserved property ('good' quantum number) and not $\ell'$ or $S'$ independently. The value of $J$ in the case of $S' = 1/2$ can take two values, viz. $J = \ell' + 1/2$ and $J = \ell' - 1/2$.[127] Thus, a degenerate $p$-orbital with 6 electrons splits into 2 sub-orbitals, with $J = 3/2$ containing 4 electrons and $J = 1/2$ containing 2 electrons. Then, the state $\langle i|$ with energy $\epsilon_i$ can be written as $\langle J, M|$ and energy $\epsilon_{JM}$. In the case of solids, the conduction states $|f\rangle$ with energy $\epsilon_f$ are represented in terms of an $|n, \boldsymbol{k}, s\rangle$ basis and energy $\epsilon_{n\boldsymbol{k}s}$ with $n$ corresponding to the band index, $\boldsymbol{k}$ to the k-point in the Brillouin zone and $s$ to the electron spin. Hence, the absorption cross-section can be written as,

$$\sigma^{\hat{\boldsymbol{\varepsilon}}}(\omega) = \frac{4\pi\alpha\hbar}{m^2\omega}\sum_{M,n,\boldsymbol{k},s}|\langle J, M|\hat{\boldsymbol{\varepsilon}}\cdot\hat{\boldsymbol{p}}|n, \boldsymbol{k}, s\rangle|^2\,\delta(\hbar\omega - \epsilon_{n\boldsymbol{k}s} + \epsilon_{JM}). \tag{6.6}$$

It is always possible to represent the wavefunctions in terms of any complete basis. One good choice for our purpose is the $|\ell', m'; 1/2, s'\rangle$ basis. Since, for our initial states, $\ell'$ is fixed, the transformation from the $|J, M\rangle$ to $|\ell', m'; 1/2, s'\rangle$ can be written as:

$$|J, M\rangle = \sum_{m',s'} C^{J,M}_{\ell',m';1/2,s'}|\ell', m'; 1/2, s'\rangle, \tag{6.7}$$

where $C^{j_3,m_3}_{j_1,m_1;j_2,m_2} = \langle j_3, m_3 | j_1, m_1; j_2, m_2 \rangle$ are the Clebsch-Gordon coefficients for angular momenta coupling. We use the $C$ notation since it is much more compact.

The connection between magnetic properties of the system, viz. the spin moment and the projection of the angular momentum on the magnetisation axis, and the integrated XMCD spectra were derived by Thole, Carra and van der Laan and are colloquially called the *sum rules*.[119,120] Derived under the dipole approximation, the sum rule for the orbital angular momentum projected on the $z$-axis $\langle L_z \rangle$ is given by:

$$\frac{\int_{J_\pm} \mathrm{d}\omega \left(\sigma^{\hat{\epsilon}-1} - \sigma^{\hat{\epsilon}+1}\right)}{\int_{J_\pm} \mathrm{d}\omega \left(\sigma^{\hat{\epsilon}-1} + \sigma^{\hat{\epsilon}+1} + \sigma^{\hat{\epsilon}0}\right)} = \frac{1}{2} \frac{\ell'(\ell'+1) - \ell(\ell+1) - 2}{\ell(\ell+1)(4\ell + 2 - n_e)} \langle L_z \rangle, \tag{6.8}$$

and the sum rule for the spin moment $\langle S_z \rangle$ and the magnetic dipole moment $\langle T_z \rangle$ is given by:

$$\begin{aligned} \frac{\int_{J_+} \mathrm{d}\omega \left(\sigma^{\hat{\epsilon}-1} - \sigma^{\hat{\epsilon}+1}\right) - \ell'(\ell'+1) \int_{J_-} \mathrm{d}\omega \left(\sigma^{\hat{\epsilon}-1} - \sigma^{\hat{\epsilon}+1}\right)}{\int_{J_\pm} \mathrm{d}\omega \left(\sigma^{\hat{\epsilon}-1} + \sigma^{\hat{\epsilon}+1} + \sigma^{\hat{\epsilon}0}\right)} &= \frac{\ell(\ell+1) - \ell'(\ell'+1) - 2}{3\ell'(4\ell + 2 - n_e)} \langle S_z \rangle \\ &+ \frac{\ell(\ell+1)[\ell(\ell+1) + 2\ell'(\ell'+1) + 4] - 3(\ell'-1)^2(\ell'+2)^2}{6\ell\ell'(\ell+1)(4\ell + 2 - n_e)} \langle T_z \rangle, \end{aligned} \tag{6.9}$$

where, the magnetic dipole operator is $\hat{T}_z = \left[\sum_i \hat{\boldsymbol{s}}_i - 3\boldsymbol{r}_i(\boldsymbol{r}_i \cdot \hat{\boldsymbol{s}}_i)\right]$. The magnetic dipole term is generally much smaller than the spin moment and for most systems, it is neglected. The $\ell$ and $\ell'$ quantum numbers correspond to the valence and core orbital momentum quantum numbers respectively, $n_e$ is the number of electrons in the valence shell and $J_\pm = \ell' \pm 1/2$ represents the total angular momentum of the core shell split by the spin-orbit coupling. Here, $4\ell + 2 - n_e = n_h$, the number of holes in the $\ell$ orbital, which can be determined from the self consistent electronic structure calculation.

### 6.2.1 XMCD Employing the PAW Basis

In the projector augmented wave (PAW) method,[66] the all-electron wavefunction $|\Psi^s_{n,\boldsymbol{k}}\rangle$ is expressed in terms of a pseudo-wavefunction $|\widetilde{\Psi^s_{n,\boldsymbol{k}}}\rangle$, all-electron partial waves $|\varphi_{\ell,m}\rangle$, pseudo-partial waves $|\widetilde{\varphi_{\ell,m}}\rangle$ and projectors $|p_{\ell,m}\rangle$. The pseudo-wavefunction and the pseudo-partial waves are smooth inside the augmentation region, generally near the ion core and match the all-electron wavefunction and the all-electron partial waves respectively. The transformation between $|\Psi^s_{n,\boldsymbol{k}}\rangle$ and $|\widetilde{\Psi^s_{n,\boldsymbol{k}}}\rangle$ is:

$$|\Psi^s_{n,\boldsymbol{k}}\rangle = |\widetilde{\Psi^s_{n,\boldsymbol{k}}}\rangle + \sum_{\ell,m} \left(|\varphi_{\ell,m}\rangle - |\widetilde{\varphi_{\ell,m}}\rangle\right) \langle p_{\ell,m} | \widetilde{\Psi^s_{n,\boldsymbol{k}}}\rangle. \tag{6.10}$$

Rewriting in a simpler form and allowing for multiple projectors (index $p$) of a given $\ell$, we get:

$$|n, \boldsymbol{k}, s\rangle = |\widetilde{n, \boldsymbol{k}, s}\rangle + \sum_{p,\ell,m} \left(|p, \ell, m\rangle - |\widetilde{p, \ell, m}\rangle\right) P^{n,\boldsymbol{k},s}_{p,\ell,m}, \tag{6.11}$$

where, $P^{n,\boldsymbol{k},s}_{p,\ell,m}$ represents the projector integrated with the all-electron pseudo-wavefunction. Inside the augmentation region, the all-electron wavefunction is given by:

$$|n, \boldsymbol{k}, s\rangle = \sum_{p,\ell,m} |p, \ell, m\rangle P^{n,\boldsymbol{k},s}_{p,\ell,m}. \tag{6.12}$$

And outside the augmentation region, since the all-electron partial waves and the pseudo-partial waves match ($|\phi_{\ell,m}\rangle = |\widetilde{\phi_{\ell,m}}\rangle$), the all-electron wavefunction is given as:

$$|n, \boldsymbol{k}, s\rangle = |\widetilde{n, \boldsymbol{k}, s}\rangle. \tag{6.13}$$

We can then rewrite the probability amplitudes $\langle J, M|\hat{\boldsymbol{\varepsilon}} \cdot \hat{\boldsymbol{p}}|n, \boldsymbol{k}, s\rangle$ as:

$$\langle J, M|\hat{\boldsymbol{\varepsilon}} \cdot \hat{\boldsymbol{p}}|n, \boldsymbol{k}, s\rangle = \sum_{m',s'} C^{J,M}_{\ell',m';1/2,s'} \langle \ell', m'; 1/2, s'|\hat{\boldsymbol{\varepsilon}} \cdot \hat{\boldsymbol{p}}|n, \boldsymbol{k}, s\rangle. \tag{6.14}$$

In the above equation, we have an integral of the product of the core wavefunction and the conduction all-electron wavefunction. In the PAW representation, we can divide the overlap integral as a sum of integrals of the core wavefunction with the augmentation region and the interstitial region. In most implementations of the PAW method, including VASP, the augmentation region is defined as a region slightly *larger* than that occupied by the core wavefunctions. This means that the overlap integrals of any core wavefunction with the valence all-electron wavefunction is restricted only *within* the augmentation region. Thus, for the purpose of computing the XMCD or XAS signals, our valence wavefunction is given by Eq. 6.12 and the absorption cross-section becomes,

$$\sigma^{\hat{\boldsymbol{\varepsilon}}}(\omega) = \frac{4\pi\alpha\hbar}{m^2\omega} \sum_{M,n,\boldsymbol{k},s} \left| \sum_{p,\ell,m,m',s'} C^{J,M}_{\ell',m';1/2,s'} \langle \ell', m'; 1/2, s'|\hat{\boldsymbol{\varepsilon}} \cdot \hat{\boldsymbol{p}}|p, \ell, m\rangle P^{n,\boldsymbol{k},s}_{p,\ell,m} \right|^2 \delta(\hbar\omega - \epsilon_{n\boldsymbol{k}s} + \epsilon_{JM}). \tag{6.15}$$

In this work, the primed quantum numbers ($\ell'$, $m'$, $s'$) represent the initial core states and the unprimed numbers ($\ell$, $m$, $s$) the final conduction states. The polarisation operator is a unit vector that can be represented with a number $\mu = -1, 0, +1$, with $\pm 1$ corresponding to the circular left and right polarised states and 0 corresponding to the $z$-polarised state (see Eq. 6.1). Thus, the operator simply becomes $\hat{p}_\mu \equiv -i\hbar\nabla_\mu = \hat{\boldsymbol{\varepsilon}}_\mu \cdot \hat{\boldsymbol{p}}$. Thus, we need to compute the probability amplitude $\langle \ell', m'|\nabla_\mu|\ell, m\rangle$. To do so, we use the Wigner-Eckart theorem, which for our purposes, can be represented as:[128]

$$\langle \ell', m'|\nabla_\mu|\ell, m\rangle = (-1)^{m'} \frac{\begin{pmatrix} \ell' & 1 & \ell \\ -m' & \mu & m \end{pmatrix}}{\begin{pmatrix} \ell' & 1 & \ell \\ 0 & 0 & 0 \end{pmatrix}} \langle \ell', 0|\nabla_0|\ell, 0\rangle, \tag{6.16}$$

where, $\begin{pmatrix} j_1 & j_2 & j_3 \\ m_1 & m_2 & m_3 \end{pmatrix}$ are the Wigner 3-$j$ symbols and are linked to the Clebsch-Gordon coefficients by:

$$\begin{pmatrix} j_1 & j_2 & j_3 \\ m_1 & m_2 & m_3 \end{pmatrix} = \frac{(-1)^{j_1 - j_2 - m_3}}{\sqrt{2j_3 + 1}} C^{j_3,-m_3}_{j_1,m_1;j_2,m_2}. \tag{6.17}$$

Also, a 3-$j$ symbol is invariant under an even permutation of its columns and an odd permutation gives a phase factor $(-1)^{j_1+j_2+j_3}$. The 3-$j$ symbol is zero unless the following conditions are satisfied:

$$\begin{aligned} &m_1 + m_2 + m_3 = 0, \\ &j_1 + j_2 + j_3 \text{ is an integer , an even integer if } m_1 = m_2 = m_3 = 0, \\ &|m_i| \leq j_i. \end{aligned} \tag{6.18}$$

Thus, by using the conversion in Eq. 6.17, the amplitude in Eq. 6.16 can be written in terms of the Clebsch-Gordon coefficients as:

$$\langle \ell', m' | \nabla_\mu | \ell, m \rangle = \frac{C^{\ell',m'}_{1,\mu;\ell,m}}{C^{\ell',0}_{1,0;\ell,0}} \langle \ell', 0 | \nabla_0 | \ell, 0 \rangle. \tag{6.19}$$

Using the conditions for either the Clebsch-Gordon coefficients or the Wigner 3-$j$ symbols, Eq. 6.18 provides the selection rules for optical transitions, viz. $\ell = \ell' \pm 1$ and $m = m' - \mu$. Thus, we can now focus our attention to computing only $\langle \ell', 0 | \nabla_0 | \ell, 0 \rangle$, which is independent of $m$ and $\hat{\boldsymbol{\varepsilon}}$. If we rewrite $|\ell, m\rangle$ as a product of radial functions $\varphi_\ell(r)$ and spherical harmonics $\mathcal{Y}^m_\ell(\theta, \phi)$, we have,

$$\begin{aligned}
\langle \ell', 0 | \nabla_0 | \ell, 0 \rangle &= \int \mathcal{Y}^0_{\ell'}(\theta,\phi)\, \varphi_{\ell'}(r)\, \partial_z\ \varphi_\ell(r)\, \mathcal{Y}^0_\ell(\theta,\phi)\ \mathrm{d}\boldsymbol{r} \\
&= \int \mathcal{Y}^0_{\ell'}(\theta,\phi)\, \varphi_{\ell'}(r)\ \left( \cos\theta \partial_r - \frac{\sin\theta}{r} \partial_\theta \right)\ \varphi_\ell(r)\, \mathcal{Y}^0_\ell(\theta,\phi)\ \mathrm{d}\boldsymbol{r} \\
&= \int \mathcal{Y}^0_{\ell'}(\theta,\phi)\, \varphi_{\ell'}(r)\ \left( \cos\theta\, \mathcal{Y}^0_\ell(\theta,\phi) \partial_r \varphi_\ell(r) - \frac{\sin\theta}{r}\ \varphi_\ell(r) \partial_\theta\, \mathcal{Y}^0_\ell(\theta,\phi) \right)\ \mathrm{d}\boldsymbol{r}.
\end{aligned} \tag{6.20}$$

Here, $\partial_u = \frac{\partial}{\partial u}$. We have the following relations for the spherical harmonics:

$$\begin{aligned}
\cos\theta\, \mathcal{Y}^0_\ell(\theta,\phi) &= \frac{\ell+1}{\sqrt{(2\ell+1)(2\ell+3)}}\, \mathcal{Y}^0_{\ell+1}(\theta,\phi) + \frac{\ell}{\sqrt{(2\ell-1)(2\ell+1)}}\, \mathcal{Y}^0_{\ell-1}(\theta,\phi), \\
-\sin\theta \partial_\theta\, \mathcal{Y}^0_\ell(\theta,\phi) &= \frac{-\ell(\ell+1)}{\sqrt{(2\ell+1)(2\ell+3)}}\, \mathcal{Y}^0_{\ell+1}(\theta,\phi) + \frac{\ell(\ell+1)}{\sqrt{(2\ell-1)(2\ell+1)}}\, \mathcal{Y}^0_{\ell-1}(\theta,\phi).
\end{aligned} \tag{6.21}$$

The reference[128] contains an error in the second term on the right hand side of the second relation. Using these relations and then integrating over the spherical harmonics gives us two orthogonality conditions: $\delta_{\ell',\ell+1}$ and $\delta_{\ell',\ell-1}$. Thus, when we represent everything in terms of $\ell'$, we get:

$$\begin{aligned}
\langle l', 0 | \nabla_0 | \ell, 0 \rangle = \quad & \delta_{\ell',\ell+1} \frac{\ell'}{\sqrt{(2\ell'-1)(2\ell'+1)}} \left[ (\varphi_{\ell'}\ |\partial_r|\ \varphi_\ell) - (\ell'-1)\, (\varphi_{\ell'}\ |r^{-1}|\ \varphi_\ell) \right] \\
& + \delta_{\ell',\ell-1} \frac{\ell'+1}{\sqrt{(2\ell'+1)(2\ell'+3)}} \left[ (\varphi_{\ell'}\ |\partial_r|\ \varphi_\ell) + (\ell'+2)\, (\varphi_{\ell'}\ |r^{-1}|\ \varphi_\ell) \right],
\end{aligned} \tag{6.22}$$

where, $(\varphi_{\ell'}\ |r^\alpha|\ \varphi_\ell) = \int r^2 \varphi_{\ell'}(r) r^\alpha \varphi_\ell(r) \mathrm{d}r$. Extending this result to include the projector index $p$ for the same angular momenta $\ell$ and the projectors $P^{n,\boldsymbol{k},s}_{p,\ell,m}$ is trivial. Also, we conserve the spin, i.e. $s' = s$. Thus, the absorption spectrum for a given polarisation $\mu$ becomes,

$$\sigma^\mu(\omega) = \frac{4\pi\alpha\hbar}{m^2\omega} \sum_{M,n,\boldsymbol{k},s} \left| \sum_{p,\ell,m,m'} -i\hbar\, C^{J,M}_{\ell',m';1/2,s} \frac{C^{\ell',m'}_{1,\mu;\ell,m}}{C^{\ell',0}_{1,0;\ell,0}} \langle \ell', 0 | \nabla_0 | p, \ell, 0 \rangle P^{n,\boldsymbol{k},s}_{p,\ell,m} \right|^2 \delta(\hbar\omega - \epsilon_{n\boldsymbol{k}s} + \epsilon_{JM}). \tag{6.23}$$

where, the probability amplitude $\langle \ell', 0 | \nabla_0 | p, \ell, 0 \rangle$ is computed as in Eq. 6.22. In addition, it is required that we convert the cubic harmonics to the spherical harmonics. This is because in the VASP code,

the real cubic harmonics are used. The spherical harmonics, $\mathcal{Y}_\ell^m$, expressed in terms of the cubic harmonics, $\mathcal{Y}_{\ell,m}$, as:

$$\mathcal{Y}_\ell^m = \begin{cases} \frac{1}{\sqrt{2}}\left(-i\mathcal{Y}_{\ell,-|m|} + \mathcal{Y}_{\ell,|m|}\right) & \text{if } m < 0, \\ \mathcal{Y}_{\ell,0} & \text{if } m = 0, \\ \frac{(-1)^m}{\sqrt{2}}\left(\mathcal{Y}_{\ell,-|m|} + i\mathcal{Y}_{\ell,|m|}\right) & \text{if } m > 0. \end{cases} \tag{6.24}$$

This transformation can be rewritten using a transformation matrix $U^\ell$ as:

$$\mathcal{Y}_\ell^m = \sum_{m_1} U^\ell_{m,m_1} \mathcal{Y}_{\ell,m_1} \tag{6.25}$$

where, $U^\ell_{m,m_1}$ are the individual matrix elements. The following transformation matrix is used for transitions up to $\ell = 3$:

$$U^\ell = \begin{pmatrix} -\frac{i}{\sqrt{2}} & 0 & 0 & 0 & 0 & 0 & \frac{1}{\sqrt{2}} \\ 0 & -\frac{i}{\sqrt{2}} & 0 & 0 & 0 & \frac{1}{\sqrt{2}} & 0 \\ 0 & 0 & -\frac{i}{\sqrt{2}} & 0 & \frac{1}{\sqrt{2}} & 0 & 0 \\ 0 & 0 & 0 & 1 & 0 & 0 & 0 \\ 0 & 0 & -\frac{i}{\sqrt{2}} & 0 & -\frac{1}{\sqrt{2}} & 0 & 0 \\ 0 & \frac{i}{\sqrt{2}} & 0 & 0 & 0 & \frac{1}{\sqrt{2}} & 0 \\ -\frac{i}{\sqrt{2}} & 0 & 0 & 0 & 0 & 0 & -\frac{1}{\sqrt{2}} \end{pmatrix} \tag{6.26}$$

The transformation prefactors do not depend on $\ell$ and thus, the same matrix $U^\ell$ can be used for different a $\ell_1 \leq \ell$. It can be shown that the coefficients of the spherical harmonics are obtained by using the complex conjugate of the above matrix elements, $(U^\ell_{m,m_1})^\star$. Thus, the absorption spectrum for a given polarisation $\mu$ becomes:

$$\sigma^\mu(\omega) = \frac{4\pi\alpha\hbar^3}{m^2\omega} \sum_{M,n,\boldsymbol{k},s} \left| \sum_{p,\ell,m,m'} C^{J,M}_{\ell',m';1/2,s} \frac{C^{\ell',m'}_{1,\mu;\ell,m}}{C^{\ell',0}_{1,0;\ell,0}} \langle \ell', 0|\nabla_0|p,\ell,0\rangle \, \overline{P}^{n,\boldsymbol{k},s}_{p,\ell,m} \right|^2 \delta(\hbar\omega - \epsilon_{n\boldsymbol{k}s} + \epsilon_{JM}), \tag{6.27}$$

where, $\overline{P}^{n,\boldsymbol{k},s}_{p,\ell,m} = \sum_{m_1} (U^\ell_{m,m_1})^\star P^{n,\boldsymbol{k},s}_{p,\ell,m_1}$. Here, we used the momentum representation for calculation of our polarisation dependent absorption spectrum. We have also implemented the computation of the absorption spectrum in the position representation, the derivation of which is provided in Appendix E and can be expressed as,

$$\sigma^\mu(\omega) = 4\pi\alpha\hbar\omega \sum_{M,n,\boldsymbol{k},s} \left| \sum_{p,\ell,m,m'} \sqrt{(2\ell'+1)(2\ell+1)} \; C^{J,M}_{\ell',m';1/2,s} C^{\ell',0}_{1,0;\ell,0} C^{\ell',m'}_{1,\mu;\ell,m} \, (\varphi_{\ell'}|r|\varphi_{p\ell}) \; \overline{P}^{n,\boldsymbol{k},s}_{p,\ell,m} \right|^2 \delta(\hbar\omega - \epsilon_{n\boldsymbol{k}s} + \epsilon_{JM}). \tag{6.28}$$

## 6.3 Implementation Details

Our implementation in the VASP code[85] is based on a self-consistent calculation for a spin-polarised system. The calculation supports the inclusion of the SOC for the valence states. If however, the SOC is not included in the valence states, then the orbital moment computed by the sum rules (Eq. 6.8) is zero. VASP takes all the user inputs from the `INCAR` file and so to compute the polarisation dependent XAS spectra, the user must add the lines similar to those in Table 6.1 in the `INCAR` file.

**Table 6.1:** Lines to be added to the `INCAR` file for calculation of x-ray spectra

| Flag | Value | Explanation |
|---|---|---|
| `LXAS` | = `.TRUE.` | This parameter determines whether the XAS should be calculated. `.TRUE.` implies calculation. |
| `LXASN` | = `2` | This parameter decides the $n$ quantum number from which to excite the core electrons. Example shows an electron in the second level. |
| `LXASL` | = `1` | This parameter decides the $\ell'$ quantum number from which to excite the core electrons. Example shows an electron in the $p$ orbital. |
| `LXASNT` | = `1` | This parameter decides the atom type for which the x-ray spectra is to be computed. If there are more than one of the same type (as determined in the file `POTCAR`), the x-ray spectra is computed for each individual ion and stored in a separate file. |
| `LXASCUT` | = `6.5` | This *optional* parameter determines the cutoff energy *above* the Fermi level. The x-ray spectra is computed only up to this energy level. This parameter, if not provided, has a default value of 10 eV. |
| `LXASR` | = `2` | This *optional* parameter decides whether XAS should *also* be computed in the position representation. The default value for this parameter is `.FALSE.`. |
| `ISYM` | = `-1` | Turn off all symmetrisation, including reduction of the number of k-points in the Brillouin zone. |

VASP performs a reduction of the number of k-points in the Brillouin zone on the basis of the symmetry in the reciprocal lattice. Due to this, the individual $m$-decomposed components of the valence wavefunction are not symmetrised and need to be corrected either by applying the inverse symmetry operator to obtain each k-point and recalculating the projectors or by rotating the spherical harmonics (and then the cubic harmonics) appropriately. In order to do this, we must know each operation by which the k-points were reduced. Since, we do not have this information, we do not perform the 're-symmetrisation' of the valence wavefunction. Thus, the user must manually turn off the symmetrisation *before* computing XAS and XMCD by entering `ISYM = -1` in the `INCAR` file. The `ISYM` flag indicates the symmetrisation to be used during the run and the value of `-1` turns off all symmetrisation, including the reduction of the number of k-points.
The VASP routines used to calculate the core wavefunctions are `CL_INIT_CORE_CONF` and `SET_CORE_WF` found in the module `cl` or the file `cl_shift.F`. The core wavefunctions calculated *on-the-fly* by these routines aren't spin-orbit split (degenerate in $M$) and consist only of the radial functions. Our implementation gives one output file for $\ell' = 0$ and two output files for $\ell' > 0$ of the core state. The two output files in the second case correspond to the $J$ quantum number of the core state (spin-orbit split). Thus, we compute the spectra for the two spin-orbit states ($J = \ell' \pm \frac{1}{2}$) corresponding to a given $\ell'$ independently of each other. The user must shift the energy of the state corresponding to

$J = \ell' - \frac{1}{2}$ by an appropriate spin-orbit splitting obtained either from experiment or all-electron atomic programs towards higher energies, before adding the two output files together to obtain a complete spectrum. It is important to note that the XAS routine calculates energy values after the Fermi energy and that the energy provided in the output files begin from 0 eV. To obtain the spectrum as a function of the x-ray photon energy, the spectrum should be shifted towards higher energy by the absolute value of the core state. The broadening effects (except a default 0.1 eV broadening) due to the core-hole lifetime and photo-excited electrons are not done in the routine, since the user might want to apply different broadenings and it is not advisable to perform a VASP calculation just for a different broadening parameter. The default broadening of 0.1 eV using the (positive) derivative of the Fermi-Dirac distribution is done as an approximation to the delta function $\delta(\hbar\omega - \epsilon_{n\boldsymbol{k}s} + \epsilon_{JM})$. The output files are in the format:

`Energy (eV)` $\sigma^+$ `(a.u.)` $\sigma^-$ `(a.u.)` $\sigma^0$ `(a.u.)`

and depending on the $n$ and $\ell'$ values provided by a user, the output filenames are shown in Table 6.2.

**Table 6.2:** Output filenames depending on user input `LXASN` and `LXASL`

| $n$ | $\ell'$ | $J$ | Output Filename |
|---|---|---|---|
| 1 | 0 | $\frac{1}{2}$ | `K_edge_atom<Atom Number>`, `rK_edge_atom<Atom Number>` (for position) |
| 2 | 0 | $\frac{1}{2}$ | `L1_edge_atom<Atom Number>`, `rL1_edge_atom<Atom Number>` (for position) |
| 2 | 1 | $\frac{1}{2}$ | `L2_edge_atom<Atom Number>`, `rL2_edge_atom<Atom Number>` (for position) |
| | | $\frac{3}{2}$ | `L3_edge_atom<Atom Number>`, `rL3_edge_atom<Atom Number>` (for position) |
| $> 2$ | up to 3 | $\ell' - \frac{1}{2}$ | `Lower_edge_atom<Atom Number>`, `rLower_edge_atom<Atom Number>` (for position) |
| | | $\ell' + \frac{1}{2}$ | `Upper_edge_atom<Atom Number>`, `rUpper_edge_atom<Atom Number>` (for position) |

The XAS and XMCD spectra can be computed for any system in VASP, including bulk and supercell systems. The implementation provides output files for *each* atom, which might be useful for decomposition of an x-ray spectrum into individual site contributions. This is particularly useful in analysis of anti-ferromagnetic or ferrimagnetic systems like Gallium Ferrite, $GaFeO_3$ or Chromium Oxide, $Cr_2O_3$, where the contribution of each atom needs to be analysed to fully understand the system.

## 6.4 Test Cases

Here, we present our XAS calculation results for testing the code. The first calculation was done for computing the K-edge of *bcc*-iron, where the valence electrons were spin-polarised. For the second case, we compute the $L_{2,3}$-edges of *bcc*-iron. The valence electrons were spin-polarised and were treated with and without SOC. All calculations were done using the GGA-PBE approximation for the exchange-correlation energy as implemented in VASP.[57,58] The pseudopotentials used are in the PAW basis.[87]

### 6.4.1 Iron K-Edge

To compute the K-edge of *bcc*-iron, the lattice parameter used in the self-consistent calculations is 2.87 Å. The k-point mesh is Γ-centred and divided as 8×8×8. We have a plane wave cut-off at 700 eV and the convergence criteria for the energy is 1 $\mu$eV. The valence electrons are spin-polarised and two calculations are performed – without and with inclusion of the SOC as implemented in VASP. Because *bcc*-iron is metal, the cut-off energy for the XAS routine is set to 40 eV for the K-edge above the Fermi energy. The XAS were computed using the momentum and position representations and the comparisons of the two methods with experiment are shown in Figure 6.1.

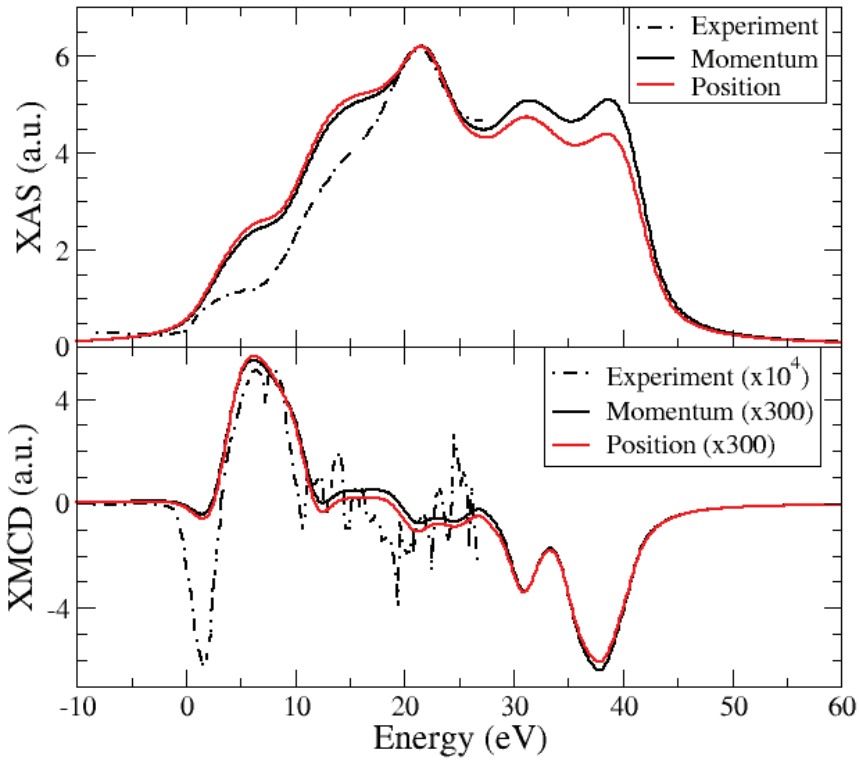


**Figure 6.1:** Computed *bcc*-iron K-edge, using the momentum operator (black) and the position operator (red), and comparison with experiment (dashed-dotted curve).

A Gaussian broadening of 1 eV and a Lorentzian broadening of 1.5 eV are used in this case. We obtain a good agreement between the two methods and experiment. The differences between the two methods is because the basis set is not complete at larger energies and require plane wave contributions for better results. These can added as shown in Appendix F to improve the results. At the moment, only the augmentation region contributions are included in the code. Our next example is a study of the Fe $L_{2,3}$ edges with and without the SOC.

### 6.4.2 Iron $L_{2,3}$-Edges without and with Spin-Orbit Coupling

To compute the $L_{2,3}$-edges for *bcc*-iron, we use the same parameters, except the energy cutoff for the XAS routines, as described in the previous subsection for the self-consistent run with VASP. The energy cutoff for the $L_{2,3}$-edges is set to 6.5 eV above the Fermi level. The comparison between the

XAS spectra for the $L_{2,3}$-edges as computed using the position and momentum operators are shown in Figure 6.2. We see that in the case of the $L_{2,3}$-edges for *bcc*-iron, there is a high level of agreement between the two methods and thus we conclude that we are within the good range of our basis set.

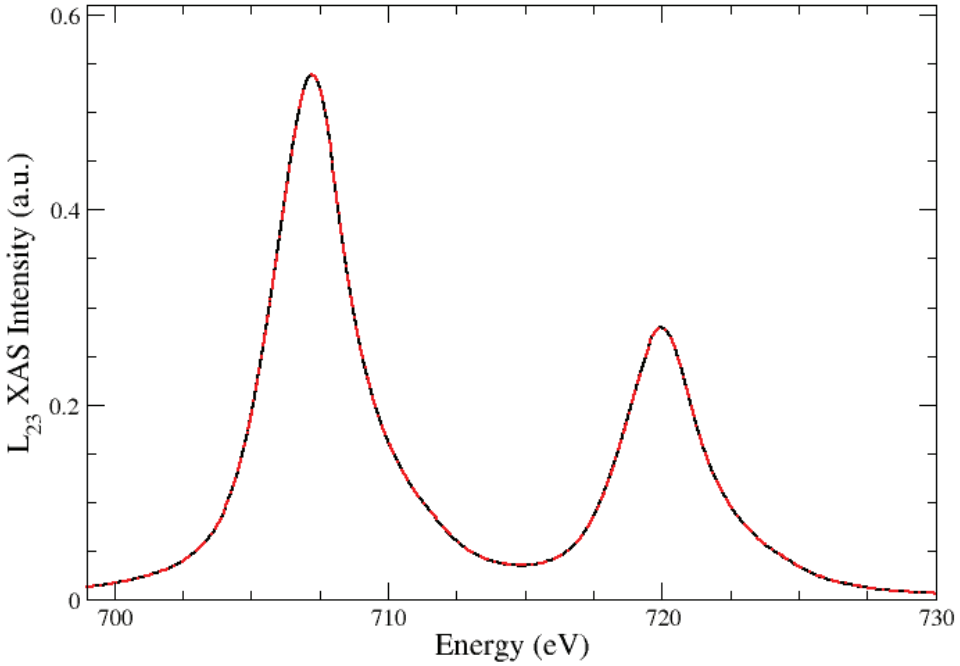


**Figure 6.2:** Computed *bcc*-iron $L_{2,3}$-edges, using the momentum operator (black) and the position operator (red).

In Figure 6.3, the polarisation dependent absorption spectrum and its comparison with experiment[129] are shown. The $L_2$ and $L_3$ plots are shifted to position themselves at the corresponding experimental peaks and the SOC difference between the $p_{1/2}$ and $p_{3/2}$ is set at 12.9 eV. A Gaussian broadening of 0.5 eV and a Lorentzian broadening of 1 eV is applied to both the plots before computing the XAS plots ($\frac{\sigma^+ + \sigma^- + \sigma^0}{3}$) and the MCD plots ($\sigma^- - \sigma^+$). For matching the XAS curves with experiment, a 'double' step function is used, described as:

$$\mu_0(E) = \frac{A_1}{1 + e^{\lambda_1 (E - E_0^1)}} + \frac{A_2}{1 + e^{\lambda_2 (E - E_0^2)}} \tag{6.29}$$

where, $A_1$, $A_2$ are the magnitudes of the individual step functions, $\lambda_1$, $\lambda_2$ are their widths and $E_0^1$, $E_0^2$ are their mean energy values of the transitions. The values for the magnitudes were chosen to match the experimental values. The remaining values were $\lambda_1 = 0.7$, $\lambda_2 = 0.8$, $E_0^1 = 710$ eV and $E_0^2 = 722.5$ eV.

In addition the sum rules were calculated using equations 6.8 and 6.9 by setting the number of holes as 3. This value of 3 was based on the charge deficit in the iron augmentation region as given

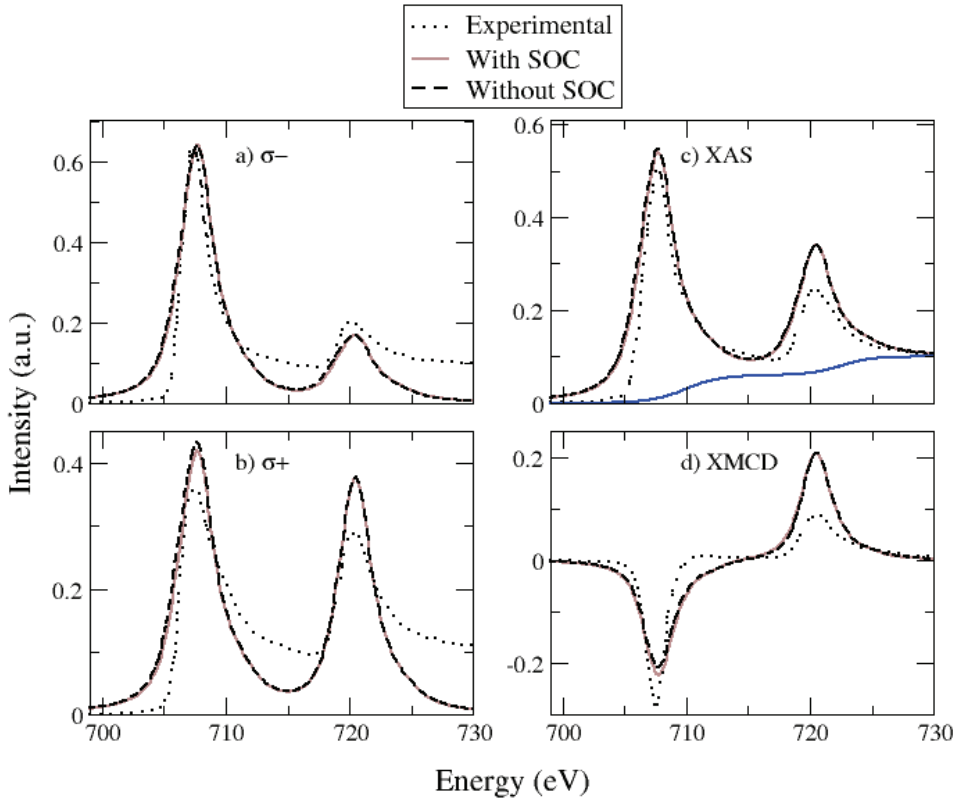


**Figure 6.3:** Momentum operator calculated *bcc*-iron bulk $L_{2,3}$ absorption spectra, without SOC (dashed black) and with SOC (solid brown) compared to experiment (dotted black) from.[129] a) and b) represent the spectra for circularly right and left polarised light respectively. c) and d) represent the XAS and the XMCD signals respectively. The solid blue curve in c) represents the double step function.

by VASP. The comparison of the sum rules from the theoretical spectra and the experimental spectra as published in[129] are provided in Table 6.3. Without SOC in the valence electrons, the cubic harmonics always give an expectation value for the $\hat{L}_z$ operator as zero. This is exactly what the sum rules indicate from the computed spectra. The spin expectation value is in good agreement as that obtained from experiment. Without the SOC, the XMCD signal obtained by us is equal at both the $L_2$ and $L_3$ locations. The inclusion of the SOC alters the XMCD signal slightly enough to provide us a non-zero orbital moment, and thereby improves our results. The spin and orbital moments are parallel to one another, exactly as expected for a *more-than-half-filled* shell. The absorption plots in Figure 6.3 are in a decent agreement with experiment.

**Table 6.3:** Comparison of the orbital and spin moments (in units of $\mu_B$) obtained using the two sum rules from the theoretical spectra with SOC and the experimental spectra.[129] Values in parentheses indicate the sum rules as obtained from the theoretical spectra without SOC

| | Theoretical | Experiment[129] |
|---|---|---|
| $m_{spin} = \langle S_z \rangle$ | 2.179 (2.034) | 1.980 |
| $m_{orb} = \langle L_z \rangle$ | 0.030 (0.000) | 0.085 |
| $\frac{m_{orb}}{m_{spin}} = \frac{\langle L_z \rangle}{\langle S_z \rangle}$ | 0.014 (0.000) | 0.043 |

## 6.5 Application to GFO

Since the code successfully (single-particle picture) reproduced the experimental spectra for Fe, we computed the $L_{2,3}$ spectra for Fe in gallium ferrite (GFO). The *ab initio* calculation details for the ideal and disordered systems were described in Chapter 4. The spectra was measured by Kim *et al.*, who also reported a large orbital moment.[79] The site occupancies reported were Fe@Fe1: 82.5 %, Fe@Fe2: 82.5 % and Fe@Ga2: 35 %. Based on our results for the site disorder studies, we assume that the electronic structure for the local Fe at the Fe2 and Ga2 sites are identical. We then compute the spectra for the Fe1 and the Fe2 sites. We then multiply the individual spectra by the site occupancies and add them up.

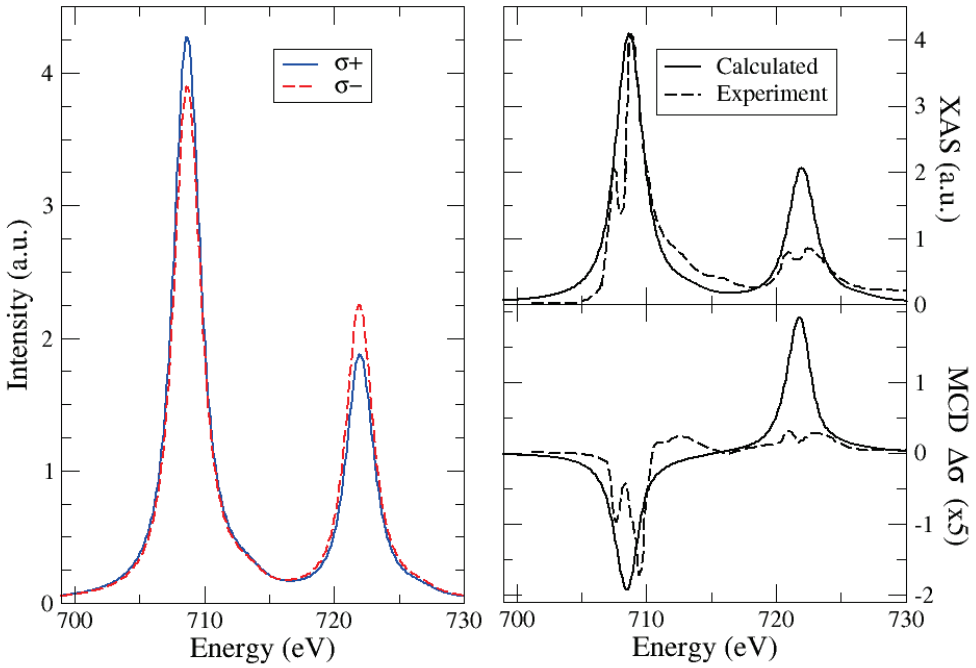


**Figure 6.4:** $L_{2,3}$-edges of Fe in GFO.

The results for the computation are provided in Fig. 6.4. The $L_{2,3}$-edges of Fe are not high in energy and as was seen earlier, the basis set was good enough for comparison with experiment. For this reason, only the momentum representation was used for computation. The experimental spectra for the individual circularly left and right polarised light was not discernible, indicating that the system is essentially antiferromagnetic. Indeed we see that the two curves are very close to each other. The computed XAS spectra was then normalised to match the experimental $L_3$-peak, and the $L_2$-peak was shifted in energy to best match the position of the experimental counterpart. We see that the experimental peaks are split, i.e. they have multiplet splitting. This behaviour occurs in $3d$ and $4f$ metal compounds because the $3d$ or $4f$ electrons are strongly correlated and localised. DFT is a single-particle picture and fails to correctly account for the localised orbitals. Based on this, we see a good agreement with experiment.
The XMCD signal was also computed after normalising the XAS and shows a dichroism indicating a net magnetic moment in the system. The sum rules were computed per Fe atom in the system and are shown in Table 6.4. The number of holes was set to 5, since Fe in GFO has an official ionic charge of +3, which amounts to a half-filled $3d$ shell. As before in the case of the Fe L-edges, we see that the spin moment agrees well with experiment, while the orbital moment is underestimated by a factor of 2.

**Table 6.4:** Comparison of the orbital and spin moments (in units of $\mu_B$) obtained using the two sum rules from the theoretical spectra with SOC and the experimental spectra[79]

| | Theoretical | Experiment[79] |
|---|---|---|
| $m_{spin} = \langle S_z \rangle$ | 0.777 | 0.870 |
| $m_{orb} = \langle L_z \rangle$ | 0.008 | 0.017 |

## 6.6 Discussion

X-ray absorption and the magnetic dichroism are highly dependent on the SOC present in the core and valence states. One way to most accurately treat the valence electrons is to use a fully relativistic approach, for example, the spin-polarised Korringa-Kohn-Rostoker (SPR-KKR) Green's function method.[111,112] In this work, the SOC is included for the valence electrons as a perturbation. However, even with the full relativistic calculations, density functional theory is known to underestimate the orbital moment.

Another point worth mentioning is that the density functional picture used is a single-particle picture and thus describes less accurately the localised $3d$ and $4f$ metal compounds. This shortcoming is due to the strong electron-correlation effects in these materials, which are not completely taken into account in DFT. Atomic model calculations within the crystal field theory, which put the Coulomb and exchange interactions on an equal footing, have shown to give an excellent agreement with x-ray absorption spectra. This agreement can be seen in multiplet calculations for the $3d$ compounds.[130–132]

Our implementation does not correctly consider the higher energy electron states. At higher energies, we require more partial all-electron and pseudo-wavefunctions. Since these are not provided in VASP, one has to work with the plane waves $|\widetilde{n, \boldsymbol{k}, s}\rangle$. At these energies, the electrons do not 'feel' the potential due to the ions and are more 'free-electron-like'. Using the PAW notation, one would

say that the all-electron partial and pseudo-wavefunctions match each other and the full all-electron wavefunction at these energies $|n, \boldsymbol{k}, s\rangle = |\widetilde{n, \boldsymbol{k}, s}\rangle$. Up to 20-30 eV above the Fermi level, the contribution due to the plane waves is negligible and so our implementation works decently well in this range. A scheme for including the plane wave contribution for high photon energies is provided in Appendix F and will be implemented in future work.

At the same time, effects due to the experimental setup or procedure can drastically alter the broadening required to fit the absorption curves. Usually the broadening effects include core-hole decays, excited electron decays and spectrometer resolution. The core-hole decays and excited electron decays are broadened with a Lorentzian function, and the spectrometer resolution is taken into consideration with a Gaussian function. In this work, we have used the same broadening parameters for the $L_{2,3}$ peaks of iron, whereas in experiments, since the $L_2$ peak is wider than the $L_3$ peak, different broadening functions should be used.

In addition to the points mentioned above, there is the saturation phenomenon that blocks the x-ray from penetrating deeper into the sample. This blocking of light causes a decrease in intensity immediately after the absorption-edge. Saturation effects can be shown to be responsible for affecting the sum rule extraction of various $3d$ metals.[133,134] These effects are also neglected in our work.

## 6.7 Conclusions and Perspectives

In this chapter, we have presented our development of a tool for the calculation of polarisation dependent X-ray absorption spectra for left and right circularly polarised, and $z$ polarised light in the electric dipole approximation for both the momentum operator $\hat{\boldsymbol{p}}$ and the position operator $\boldsymbol{r}$ matrix elements. The code supports different levels of approximations for the valence electrons – non-spin-polarised, spin-polarised without SOC and spin-polarised with SOC. As examples, we have shown the XAS and XMCD spectra for the K-edge and the $L_{2,3}$-edges of iron. These spectra have the same level of agreement with experiment as expected from single-particle calculations. Based on the success of our implementation, we computed the XAS and XMCD spectra for GFO based on experimental site occupancies. The spectra are relatively in good agreement with experiment.

As perspectives, the code can be extended to include the higher energy plane-wave-like states. This would help improve the quality of the basis set at higher energies. Since VASP is one of the fastest codes available, the XMCD of magnetic systems with many atoms per unit cell, like organic molecules on magnetic surfaces, can be computed with our code.
deuxième partie de la thèse

# 7 Conclusions and Perspectives

Relativistic effects play an important role in modern condensed matter physics and can not be ignored in quantum chemistry and recent technological developments. We address the investigation of relativistic effects, especially their application to multiferroic materials, in the present thesis.

In the second chapter, we presented a self-consistent model up to second order in $1/c$, where we coupled a semi-relativistic Hamiltonian in the mean-field approximation with the Maxwell's equations generating the mean-fields by means of a Lagrangian density. The model can also be extended to support external electromagnetic fields. By using the Lorentz gauge for the Maxwell's equations, we were able to obtain analytical expressions for the sources that generate the mean-fields. The sources consisted of two contributions, free and bound sources. There was only one correction of second order to the free sources, which came from the probability current density. The bound sources were divided into magnetization and polarization densities. The magnetization term is of zeroth order, while the polarization terms were of second order. The Darwin polarization was interpreted through an average potential that emerges due to a semi-relativistic approximation of the *Zitterbewegung*. The spin polarization can be explained as a manifestation of the magnetization term in the laboratory frame due to a semi-relativistic expansion of the Lorentz factor. Since the spin polarization has an origin in the spin-orbit coupling (SOC), the polarization term can be thought of as a consequence of the direct magnetoelectric effect.
The sources obtained were verified with the help of the continuity equation derived from three different methods, which lends credence to the model. Moreover, the same sources could be obtained by other methods, mainly the Landau's variational principle, in different gauges, indicating gauge-invariance as well as validating the sources.
There are many perspectives for the model developed. For example, the Lagrangian density can be used to create quantum hydrodynamic equations of motions through the Madelung transformation that can help describe plasmas as astrophysical objects like neutron stars. In addition, since this is a time dependent model, laser pulses, including ultrafast laser pulses, can be simulated to understand electron dynamics. Moreover, since the magnetic mean-field is included in a covariant formalism, the model can be ported to the density functional theory (DFT), where the mean-fields become a part of the effective fields.

The fourth chapter discussed our *ab initio* results using the DFT and the SOC for magnetoelectric gallium ferrite (GFO). In the initial stage, we showed that the value of the Hubbard parameter

$U = 8$ eV best describes the experimental values of the energy band gap and magnetization. This parameter controls the level of hybridisation of the electrons with the neighbouring ions and thus, controls the electronic and magnetic properties of GFO. In the following part, we demonstrated that the origin of ferrimagnetism in GFO is the presence of cationic site disorders, where the Fe and Ga cations swap places. The energy difference between the ideal and disordered systems was of the order of the thermal energy available during the synthesis of GFO, thereby indicating the difficulty involved with control of site disorders.
To study the magnetic order of the $e_g$-$t_{2g}$ orbitals of the Fe sites, we implemented the automatic rotation of the local octahedra and the crystal-field analysis. Our analysis for the Fe octahedral sites showed that the $3d$ orbitals have a tetrahedral-like splitting. This splitting was confirmed with a point-charge model and can be attributed to the high amount of distortion in the octahedral.
Towards the end of the chapter we calculated the linear dependence of the electric polarization on the temperature. Our values were in good agreement with those obtained earlier. We then performed direct magnetoelectric studies by rotating the magnetization axis. The changes in the electric polarization were very small indicating that the direct effect is not the major contribution of the magnetoelectric effect in GFO.
For perspectives, it would be helpful to perform cationic site disorder studies with excess Fe as such simulations can provide clues to control of the ferrimagnetism in GFO. In addition, the indirect effect, i.e. the magnetostrictive-induced effect, can be simulated and verified with experiment. These studies can be done with the ideal as well as disordered system to make a better connection with experiment.

In the fifth chapter, we presented our *ab initio* results for chromium oxide ($Cr_2O_3$). The studies were done with the intention of understanding the origin of spontaneous magnetization and polarization in strained nanoclusters observed in recent experiments. In the initial part, we showed that the value of the Hubbard parameter $U = 8$ eV reproduces the experimental value of the energy band gap. These studies were done for four magnetic configurations, three antiferromagnetic and one ferromagnetic. We found that the AFM1 configuration was energetically the most stable. We then performed simulations of the biaxially strains by shrinking the unit cell along the $z$- and $x$-axes. Since no net magnetization or polarization was obtained, we performed all strained calculations again with SOC to allow for spin canting. Our calculations did not show any net polarization but did provide a net magnetization which was about 40 times smaller than experiment. Based on the failure to reproduce the results, size effects or the MgO-$Cr_2O_3$ interface might be important for correctly mimicking the experimental conditions.
As perspectives, inclusion of size effects in the calculations might uncover the origin of experimental observation. This is because the nanoclusters in the experiment were very small and might not correctly described by an infinite bulk crystal. It might also be useful to include the MgO-$Cr_2O_3$ interface for more accurate computations.

The sixth chapter discussed our implementation of the computation of the x-ray absorption spectra (XAS) and the x-ray circular magnetic dichroism (XMCD). We begin by providing a theoretical description and the implementation scheme, which supports different approximations for the electron spin and can perform computations for the position or momentum representations to check the quality of the basis set. We then test our code for the Fe K-edge and $L_{2,3}$-edges. These agreed well with experiment and the basis set used was good enough. Based on this, we computed the $L_{2,3}$-edges for Fe in GFO. Our results agreed well with experiment.
For perspectives, it might be important to include the plane wave contribution in the final computation

of the spectra. This would increase the accuracy of the spectra as well as the similarity of the results from both representations. In addition, the XAS and XMCD can be computed for other multiferroic materials like $Cr_2O_3$ and $BiFeO_3$. Since the spectra are computed after the DFT convergence, they can be calculated for different site disorders or excess-Fe in GFO, and also for the strained $Cr_2O_3$ nanoclusters. It would be highly interesting to compute the spectra as function of the rotation angle or external electric or magnetic fields for comparison with experiment.

# Bibliography


[1] G. P. Zhang and W. Hübner. Laser-Induced Ultrafast Demagnetization in Ferromagnetic Metals. *Phys. Rev. Lett.*, 85:3025, 2000.

[2] B. Koopmans, J. J. M. Ruigrok, F. Dalla Longa, and W. J. M. de Jonge. Unifying Ultrafast Magnetization Dynamics. *Phys. Rev. Lett.*, 95:267207, 2005.

[3] E. Beaurepaire, J.-C. Merle, A. Daunois, and J.-Y. Bigot. Ultrafast Spin Dynamics in Ferromagnetic Nickel. *Phys. Rev. Lett.*, 76:4250, 1996.

[4] J.-Y. Bigot, M. Vomir, and E. Beaurepaire. Coherent ultrafast magnetism induced by femtosecond laser pulses. *Nat. Phys.*, 5:515, 2009.

[5] G. Schütz, W. Wagner, W. Wilhelm, and P. Kienle. Absorption of Circularly Polarized X Rays in Iron. *Phys. Rev. Lett.*, 58:737, 1987.

[6] H. Ebert, P. Strange, and B. L. Gyorffy. The influence of relativistic effects on the magnetic moments and hyperfine fields of Fe, Co and Ni. *J. Phys. F: Met. Phys.*, 18:L135, 1988.

[7] C. A. F. Vaz. Electric field control of magnetism in multiferroic heterostructures. *J. Phys.: Condens. Matter*, 24:333201, 2012.

[8] Y. Hinschberger and P.-A. Hervieux. Classical modeling of ultrafast coherent magneto-optical experiments. *Phys. Rev. B*, 88:134413, 2013.

[9] H. Vonesch and J.-Y. Bigot. Ultrafast spin-photon interaction investigated with coherent magneto-optics. *Phys. Rev. B*, 85:180407(R), 2012.

[10] J.-Y. Bigot and M. Vomir. Ultrafast magnetization dynamics of nanostructures. *Ann. Phys.*, 525:2, 2013.

[11] S. Keller, Colm T. Whelan, H. Ast, H. R. J. Walters, and R. M. Dreizler. Relativistic distorted-wave Born calculations for $(e, 2e)$ processes on inner shells of heavy atoms. *Phys. Rev. A*, 50:3865, 1994.

[12] A. K. Rajagopal. Inhomogeneous relativistic electron gas. *J. Phys. C: Solid State Phys.*, 11:L943, 1978.

[13] A. Dixit, Y. Hinschberger, J. Zamanian, G. Manfredi, and P.-A. Hervieux. Lagrangian approach to the semirelativistic electron dynamics in the mean-field approximation. *Phys. Rev. A*, 88:032117, 2013.

[14] M. Born and J. R. Oppenheimer. Quantum theory of the molecules. *Ann. d. Physik*, 84:457, 1927.

[15] J. Kohanoff. *Electronic Structure Calculations for Solids and Molecules*. Cambridge University Press, 2006.

[16] N. C. Handy and A. M. Lee. The adiabatic approximation. *Chem. Phys. Lett.*, 252:425, 1996.

[17] L. L. Foldy and S. A. Wouthuysen. On the Dirac Theory of Spin 1/2 Particles and Its Non-Relativistic Limit. *Phys. Rev.*, 78:29, 1950.

[18] K. M. Case. Some Generalizations of the Foldy-Wouthuysen Transformation. *Phys. Rev.*, 95:1323, 1954.

[19] Y. Hinschberger and P.-A. Hervieux. FoldyWouthuysen transformation applied to the interaction of an electron with ultrafast electromagnetic fields. *Phys. Lett. A*, 376:813, 2012.

[20] H. P. Dürr. Conservation laws in Lagrangian field theories with higher-order derivatives. *Il Nuovo Cimento A*, 22:386, 1974.

[21] R. Courant and D. Hilbert. *Methods of Mathematical Physics - Volume I*. Interscience Publishers, New York, 1953.

[22] P. Ramaniello and P. L. de Boeij. Relativistic two-component formulation of time-dependent current-density functional theory: Application to the linear response of solids. *J. Chem. Phys.*, 127:174111, 2007.

[23] L. D. Landau and E. M. Lifshitz. *Quantum Mechanics: Non-Relativistic Theory*. Butterworth-Heinemann, Oxford, 1977.

[24] F. A. Asenjo, J. Zamanian, M. Marklund, G. Brodin, and P. Johansson. Semi-relativistic effects in spin-1/2 quantum plasmas. *New J. Phys.*, 14:073042, 2012.

[25] P. Strange. *Relativistic Quantum Mechanics: With Applications in Condensed Matter and Atomic Physics*. Cambridge University Press, Cambridge, 2005.

[26] J. J. Sakurai. *Advanced Quantum Mechanics*. Addison-Wesley, Reading, 1967.

[27] P. Holland and H. R. Brown. The non-relativistic limits of the Maxwell and Dirac equations: the role of Galilean and gauge invariance. *Studies in History and Philosophy of Science Part B: Studies in History and Philosophy of Modern Physics*, 34:161, 2003.

[28] M. Le Bellac and J.-M. Lévy-Leblond. Galilean Electromagnetism. *Il Nuovo Cimento*, 14B:217, 1973.

[29] G. Rousseaux. Lorenz or Coulomb in Galilean electromagnetism? *Europhys. Lett.*, 71:15, 2005.

[30] M. de Montigny and G. Rousseaux. On the electrodynamics of moving bodies at low velocities. *Eur. J. Phys.*, 27:755, 2006.

[31] G. Manfredi. Non-relativistic limits of Maxwell's equations. *Eur. J. Phys.*, 34:859, 2013.

[32] Y. Hinschberger, A. Dixit, G. Manfredi, and P.-A. Hervieux. Equivalence between the semirelativistic limit of the Dirac-Maxwell equations and the Breit-Pauli model in the mean-field approximation. *Phys. Rev. A*, 91:012101, 2015.

[33] F. Haas, G. Manfredi, and M. Feix. Multistream model for quantum plasmas. *Phys. Rev. E*, 62:2763, 2000.

[34] G. Manfredi and F. Haas. Self-consistent Fluid Model for a Quantum Electron Gas. *Phys. Rev. B*, 64:075316, 2001.

[35] G. Manfredi. How to model quantum plasmas. *Fields Inst. Commun.*, 46:263, 2005.

[36] M. Marklund and G. Brodin. Dynamics of Spin-$\frac{1}{2}$ Quantum Plasmas. *Phys. Rev. Lett.*, 98:025001, 2007.

[37] G. Brodin and M. Marklund. Spin magnetohydrodynamics. *New J. Phys.*, 9:277, 2007.

[38] F. Haas, G. Manfredi, P. K. Shukla, and P.-A. Hervieux. Breather mode in the many-electron dynamics of semiconductor quantum wells. *Phys. Rev. B*, 80:073301, 2009.

[39] C. P. Ridgers, C. S. Brady, R. Duclous, J. G. Kirk, K. Bennett, T. D. Arber, and A. R. Bell. Dense electron-positron plasmas and bursts of gamma-rays from laser-generated quantum electrodynamic plasmas. *Phys. Plasmas*, 20:056701, 2013.

[40] D. R. Hartree. The Wave Mechanics of an Atom with a Non-Coulomb Central Field. Part I. Theory and Methods. *Proc. Cambridge Phil. Soc.*, 24:89, 1928.

[41] J. C. Slater. The Self Consistent Field and the Structure of Atoms. *Phys. Rev.*, 32:339, 1928.

[42] V. Fock. Näherungsmethode zur Lösung des quantenmechanischen Mehrkörperproblems. *Z. Phys.*, 61:126, 1930.

[43] J. C. Slater. Note of Hartree's Method. *Phys. Rev.*, 35:210, 1930.

[44] C. D. Sherrill and H. F. Schaefer III. The configuration interaction method: Advances in highly correlated approaches. *Adv. Quant. Chem.*, 34:143, 1999.

[45] L. H. Thomas. The calculation of atomic fields. *Proc. Cambridge Phil. Soc.*, 23:542, 1927.

[46] E. Fermi. A statistical method for the determination of some properties of the atom and its application to the theory of the periodic system of the elements. *Z. Phys.*, 48:73, 1928.

[47] P. Hohenberg and W. Kohn. Inhomogeneous Electron Gas. *Phys. Rev.*, 136:B864, 1964.

[48] W. Kohn and L. Sham. Self-Consistent Equations Including Exchange and Correlation Effects. *Phys. Rev.*, 140:A1133, 1965.

[49] A. K. Theophilou. The energy density functional formalism for excited states. *J. Phys. C: Solid State Phys.*, 12:5419, 1979.

[50] M. Petersilka, U. J. Gossmann, and E. K. U. Gross. Excitation energies from time-dependent density-functional theory. *Phys. Rev. Lett.*, 76:1212, 1996.

[51] L. Hedin. New Method for Calculating the One-Particle Green's Function with Application to the Electron-Gas Problem. *Phys. Rev.*, 139:A796, 1965.

[52] A. Görling. Density-functional theory for excited states. *Phys. Rev. A*, 54:3912, 1996.

[53] D. M. Ceperley and B. J. Alder. Ground state of the electron gas by a stochastic method. *Phys. Rev. Lett.*, 45:566, 1980.

[54] J. P. Perdew and Alex Zunger. Self-interaction correction to density-functional approximations for many-electron systems. *Phys. Rev. B*, 23:5048, 1981.

[55] A. D. Becke. Density-functional exchange-energy approximation with correct asymptotic behavior. *Phys. Rev. A*, 38:3098, 1988.

[56] J. P. Perdew and Y. Wang. Accurate and simple analytic representation of the electron-gas correlation energy. *Phys. Rev. B*, 45:13244, 1992.

[57] J. P. Perdew, K. Burke, and M. Ernzerhof. Generalized gradient approximation made simple. *Phys. Rev. Lett.*, 77:3865, 1996.

[58] J. P. Perdew, K. Burke, and M. Ernzerhof. Erratum: Generalized gradient approximation made simple. *Phys. Rev. Lett.*, 78:1396, 1997.

[59] W. E. Pickett. Electronic structure of the high-temperature oxide superconductors. *Rev. Mod. Phys.*, 61:433, 1989.

[60] W. E. Pickett. Erratum: Electronic structure of the high-temperature oxide superconductors. *Rev. Mod. Phys.*, 61:749, 1989.

[61] V. I. Anisimov, F. Aryasetiawan, and A. I. Lichtenstein. First-principles calculations of the electronic structure and spectra of strongly correlated systems: the LDA+$U$ method. *J. Phys.: Condens. Matter*, 9:767, 1997.

[62] A. I. Liechtenstein, V. I. Anisimov, and J. Zaanen. Density-functional theory and strong interactions: Orbital ordering in Mott-Hubbard insulators. *Phys. Rev. B*, 52:R5467, 1995.

[63] O. Gunarsson, O. K. Andersen, O. Jepsen, and J. Zaanen. Density-functional calculation of the parameters in the Anderson model: Application to Mn in CdTe. *Phys. Rev. B*, 39:1708, 1989.

[64] O. Gunarsson. Calculation of parameters in model Hamiltonians. *Phys. Rev. B*, 41:514, 1990.

[65] V. I. Anisimov and O. Gunarsson. Density-functional calculation of effective Coulomb interactions in metals. *Phys. Rev. B*, 43:7570, 1991.

[66] P. E. Blöchl. Projector augmented-wave method. *Phys. Rev. B*, 50:17953, 1994.

[67] P. Curie. Sur la symétrie dans les phénomènes physiques, symétrie d'un champ électrique et d'un champ magnétique. *J. Phys. Theo. Appl.*, 3:393, 1894.

[68] The best is yet to come. *Nat. Mat.*, 6:1, 2007.

[69] I. E. Dzyaloshinskii. K voprosu o magnitno-elektricheskom effekte v antiferromagnetikakh. *ZhETF*, 37:881, 1959.

[70] D. N. Astrov. Magnetoelectric Effect in Chromium Oxide. *J. Exp. Theo. Phys.*, 13:729, 1961.

[71] J. P. Remeika. $GaFeO_3$: A Ferromagnetic-Piezoelectric Compound. *J. Appl. Phys.*, 31:S263, 1960.

[72] E. A. Wood. The unit cell and space group of gallium iron oxide, a piezoelectric ferromagnetic crystal. *Acta Cryst.*, 13:682, 1960.

[73] S. C. Abrahams, J. M. Reddy, and J. L. Bernstein. Crystal Structure of Piezoelectric Ferromagnetic Gallium Iron Oxide. *J. Chem. Phys.*, 42:3957, 1965.

[74] C. H. Nowlin and R. V. Jones. Magnetism of Piezoelectric $Ga_{2-x}Fe_xO_3$. *J. Appl. Phys.*, 34:1262, 1963.

[75] G. T. Rado. Observation and Possible Mechanisms of Magnetoelectric Effects in a Ferromagnet. *Phys. Rev. Lett.*, 13:335, 1964.

[76] S. C. Abrahams and J. M. Reddy. Magnetic, Electric, and Crystallographic Properties of Gallium Iron Oxide. *Phys. Rev. Lett.*, 13:688, 1964.

[77] R. B. Frankel, N. A. Blum, S. Foner, A. J. Freeman, and M. Schieber. Ferrimagnetic Structure of Magnetoelectric $Ga_{2-x}Fe_xO_3$. *Phys. Rev. Lett.*, 15:958, 1965.

[78] T. Arima, D. Higashiyama, Y. Kaneko, J. P. He, T. Goto, S. Miyasaka, T. Kimura, K. Oikawa, T. Kamiyama, R. Kumai, and Y. Tokura. Structural and magnetoelectric properties of $Ga_{2-x}Fe_xO_3$ single crystals grown by a floating-zone method. *Phys. Rev. B*, 70:064426, 2004.

[79] J.-Y. Kim, T. Y. Koo, and J.-H. Park. Orbital and Bonding Anisotropy in a Half-Filled $GaFeO_3$ Magnetoelectric Ferrimagnet. *Phys. Rev. Lett.*, 96:047205, 2006.

[80] M. Joon Han, T. Ozaki, and J. Yu. Magnetic ordering and exchange interactions in multiferroic $GaFeO_3$. *Phys. Rev. B*, 75:060404, 2007.

[81] A. Roy, A. Garg, R. Prasad, and S. Auluck. A First-Principles Study of Structure-Property Correlation and the Origin of Ferrimagnetism in Gallium Ferrite. *Advances in Materials Physics and Chemistry*, 2:1, 2012.

[82] A. Roy, S. Mukherjee, R. Gupta, S. Auluck, R. Prasad, and A. Garg. Electronic structure, Born effective charges and spontaneous polarization in magnetoelectric gallium ferrite. *J. Phys.: Condens. Matter*, 23:325902, 2011.

[83] D. Stoeffler. First principles study of the electric polarization and of its switching in the multiferroic $GaFeO_3$ system. *J. Phys.: Condens. Matter*, 24:185502, 2012.

[84] M. Hatnean, J. Robert, M.T. Fernandez Diaz, E. Ressouche, A. Cousson, L. Pinsard-Gaudart, and S. Petit. Neutron scattering study of the magnetoelectric compound $GaFeO_3$. *Eur. Phy. J. Special Topics*, 213:69, 2012.

[85] G. Kresse and J. Furthmüller. Efficient iterative schemes for *ab initio* total-energy calculations using a plane-wave basis set. *Phys. Rev. B*, 54:11169, 1996.

[86] The vasp manual. https://www.vasp.at/index.php/documentation.

[87] G. Kresse and D. Joubert. From ultrasoft pseudopotentials to the projector augmented-wave method. *Phys. Rev. B*, 59:1758, 1999.

[88] F. Ibrahim and M. Alouani. Impact of excess iron on the calculated electronic and magnetic properties of gallium ferrite. *Phys. Rev. B*, 85:174411, 2012.

[89] D. Hobbs, G. Kresse, and J. Hafner. Fully unconstrained noncollinear magnetism within the projector augmented-wave method. *Phys. Rev. B*, 62:11556, 2000.

[90] R. Resta. Theory of the electric polarization in crystals. *Ferroelectrics*, 136:51, 1992.

[91] R. D. King-Smith and David Vanderbilt. Theory of polarization of crystalline solids. *Phys. Rev. B*, 47:1651, 1993.

[92] D. Vanderbilt and R. D. King-Smith. Electric polarization as a bulk quantity and its relation to surface charge. *Phys. Rev. B*, 48:4442, 1993.

[93] R. Resta. Macroscopic polarization in crystalline dielectrics: the geometric phase approach. *Rev. Mod. Phys.*, 66:899, 1994.

[94] R. Resta. Berry Phase in Electronic Wavefunctions. Lecture Notes. Troisième Cycle de la Physique en Suisse Romande, Année Académique 1995–96.

[95] D. Vanderbilt and R. D. King-Smith. Electronic polarization in the ultrasoft pseudopotential formalism. *Unpublished Report*, 1998.

[96] A. M. Kalashnikova, R. V. Pisarev, L. N. Bezmaternykh, V. L. Temerov, A. Kirilyuk, and Th. Rasing. Optical and Magneto-Optical Studies of a Multiferroic $GaFeO_3$ with a High Curie Temperature. *JETP Letters*, 81:452, 2005.

[97] O. Eriksson, M. S. S. Brooks, and B. Johansson. Orbital polarization in narrow-band systems: Application to volume collapses in light lanthanides. *Phys. Rev. B*, 41:7311, 1990.

[98] R. Masrour, E. K. Hlil, M. Hamedoun, A. Benyoussef, O. Mounkachi, and H. El Moussaoui. Electronic and magnetic structures of $Fe_3O_4$ ferrimagnetic investigated by first principle, mean field and series expansions calculations. *J. Magn. Magn. Mat.*, 378:37, 2015.

[99] A. Roy, R. Prasad, S. Auluck, and A. Garg. Effect of site-disorder on magnetism and magneto-structural coupling in gallium ferrite: A first-principles study. *J. Appl. Phys.*, 111:043915, 2012.

[100] C. Bradley and A. Cracknell. *The Mathematical Theory of Symmetry in Solids*. Oxford University Press, 2010.

[101] J. D. Jackson. *Classical Electrodynamics*. John Wiley & Sons, Inc., 1962.

[102] S. Mukherjee, A. Garg, and R. Gupta. Probing magnetoelastic coupling and structural changes in magnetoelectric gallium ferrite. *J. Phys.: Condens. Matter*, 23:445403, 2011.

[103] N. A. Spaldin. A beginner's guide to the modern theory of polarization. *J. Solid State Chem.*, 195:2, 2012.

[104] B. Kundys, F. Roulland, C. Lefèvre, C. Mény, A. Thomasson, and N. Viart. Room temperature polarization in the ferrimagnetic $Ga_{2-x}Fe_xO_3$ ceramics. *J. Eur. Ceram. Soc.*, 35:2277, 2015.

[105] Yu. F. Popov, A. M. Kadomtseva, G. P. Vorob'ev, V. A. Timofeeva, and D. M. Ustinin. Magnetoelectric effect and toroidal order in $Ga_{2-x}Fe_xO_3$. *J. Exp. Theo. Phys.*, 87:146, 1998.

[106] A. Malashevich, S. Coh, I. Souza, and D. Vanderbilt. Full magnetoelectric response of $Cr_2O_3$ from first principles. *Phys. Rev. B*, 86:094430, 2012.

[107] Y. Guo, S. J. Clark, and J. Robertson. Electronic and magnetic properties of $Ti_2O_3$, $Cr_2O_3$, and $Fe_2O_3$ calculated by the screened exchange hybrid density functional. *J. Phys: Condens. Mat.*, 24:325504, 2012.

[108] D. Halley, N. Najjari, H. Majjad, L. Joly, P. Ohresser, F. Scheurer, C. Ulhaq-Bouillet, S. Berciaud, B. Doudin, and Y. Henry. Size-induced enhanced magnetoelectric effect and multiferroicity in chromium oxide nanoclusters. *Nat. Comm.*, 5:3167, 2014.

[109] C. S. G. Cousins. The corundum structure: internal strain tensors and cluster configurations under stress. *J. Phys. C: Solid State Phys.*, 14:1585, 1981.

[110] S. L. Dudarev, G. A. Botton, S. Y. Savrasov, C. J. Humphreys, and A. P. Sutton. Electron-energy-loss spectra and the structural stability of nickel oxide:An $LSDA+U$ study. *Phys. Rev. B*, 57:1505, 1998.

[111] H. Ebert. Fully Relativistic Band Structure Calculations for Magnetic Solids - Formalism and Application. In Hugues Dreyssé, editor, *Electronic Structure and Physical Properties of Solids*, volume 535 of *Lecture Notes in Physics*, page 191. Springer Berlin Heidelberg, 2000.

[112] J. Minárt and H. Ebert. Magnetic circular dichroism in X-ray absorption: theoretical description and applications. *Appl. Phys. A*, 78:847, 2004.

[113] M. Alouani, J. M. Wills, and J. W. Wilkins. Scaling of the $L_{2,3}$ circular magnetic x-ray dichroism of Fe nitrides. *Phys. Rev. B*, 57:9502, 1998.

[114] V. Kanchana, G. Vaitheeswaran, and M. Alouani. Calculated electronic structure and x-ray magnetic circular dichroism of $CrO_2$. *J. Phys.: Condens. Matter*, 18:5155, 2006.

[115] M. Altarelli. Orbital-mangetization sum rule for x-ray circular dichroism: A simple proof. *Phys. Rev. B*, 47:597, 1993.

[116] A. Ankudinov and J. J. Rehr. Sum rules for polarization-dependent x-ray absorption. *Phys. Rev. B*, 51:1282, 1995.

[117] G. van der Laan. 25 Years of Magnetic X-Ray Dichroism. In Eric Beaurepaire, Hervé Bulou, Loic Joly, and Fabrice Scheurer, editors, *Magnetism and Synchrotron Radiation: Towards the Fourth Generation Light Sources*, volume 151 of *Springer Proceedings in Physics*, page 257. Springer International Publishing, 2013.

[118] N. V. Smith, C. T. Chen, F. Sette, and L. F. Mattheiss. Relativistic tight-binding calculations of x-ray absorption and magnetic circular dichroism at the $L_2$ and $L_3$ edges of nickel and iron. *Phys. Rev. B*, 46:1023, 1992.

[119] B. T. Thole, P. Carra, and G. van der Laan. X-ray circular dichroism as a probe of orbital magnetization. *Phys. Rev. Lett.*, 68:1943, 1992.

[120] P. Carra, B. T. Thole, M. Altarelli, and X. Wang. X-ray circular dichroism and local magnetic fields. *Phys. Rev. Lett.*, 70:694, 1993.

[121] J. L. Erskine and E. A. Stern. Calculation of the $M_{23}$ magneto-optical absorption spectrum of ferromagnetic nickel. *Phys. Rev. B*, 12:5016, 1975.

[122] C. T. Chen, F. Sette, Y. Ma, and S. Modesti. Soft-x-ray magnetic circular dichroism at the $L_{2,3}$ edges of nickel. *Phys. Rev. B*, 42:7262, 1990.

[123] O. Bunău and M. Calandra. Projector augmented wave calculation of x-ray absorption spectra at the $L_{2,3}$ edges. *Phys. Rev. B*, 87:205105, 2013.

[124] L. Pardini, V. Bellini, F. Manghi, and C. Ambrosch-Draxl. First-principles calculation of X-ray dichroic spectra within the full-potential linearized augmented planewave method: An implementation into the Wien2k code. *Comp. Phys. Comm.*, 183:628, 2012.

[125] P. A. M. Dirac. The Quantum Theory of the Emission and Absorption of Radiation. *Proceedings of the Royal Society of London A: Mathematical, Physical and Engineering Sciences*, 114(767):243–265, 1927.

[126] E. Fermi. *Nuclear Physics*. University of Chicago Press, 1950.

[127] D. J. Griffiths. *Introduction to Quantum Mechanics*. Pearson Prentice Hall, 2005.

[128] A. R. Edmonds. *Angular Momentum in Quantum Mechanics*. Princeton University Press, 1974.

[129] C. T. Chen, Y. U. Idzerda, H.-J. Lin, N. V. Smith, G. Meigs, E. Chaban, G. H. Ho, E. Pellegrin, and F. Sette. Experimental Confirmation of the X-Ray Magnetic Circular Dichroism Sum Rules for Iron and Cobalt. *Phys. Rev. Lett.*, 75:152, 1995.

[130] G. van der Laan, B. T. Thole, G. A. Sawatzky, and M. Verdaguer. Multiplet structure in the $L_{2,3}$ x-ray-absorption spectra: A fingerprint for high- and low-spin $Ni^{2+}$ compounds. *Phys. Rev. B*, 37:6587, 1988.

[131] B. T. Thole, G. van der Laan, and P. H. Butler. Spin-mixed ground state of Fe phthalocyanine and the temperature-dependent branching ratio in X-ray absorption spectroscopy. *Chem. Phys. Lett.*, 149:295, 1988.

[132] G. van der Laan and I. W. Kirkman. The 2p absorption spectra of 3d transition metal compounds in tetrahedral and octahedral symmetry. *J. Phys.: Condens. Matter.*, 4:4189, 1992.

[133] R. Nakajima, J. Stöhr, and Y. U. Idzerda. Electron-yield saturation effects in $L$-edge x-ray magnetic circular dichroism spectra of Fe, Co and Ni. *Phys. Rev. B*, 59:6421, 1999.

[134] V. Chakarian and Y. U. Idzerda. Total electron yield method in x-ray absorption spectroscopy: A closer look at the saturation/self-absorption effects (abstract). *J. Appl. Phys.*, 81:4709, 1997.

[135] R. M. Martin. Comment on calculations of electric polarization in crystals. *Phys. Rev. B*, 9:1998, 1974.

[136] F. Schwabl. *Advanced Quantum Mechanics*. Springer-Verlag Berlin Heidelberg, 2007.

# A

# Derivation of the Extended-Pauli Equation

Here we derive the extended Pauli equation with the Foldy-Wouthuysen transformation that is exact up to second order in $1/c$. We rewrite the Dirac Hamiltonian as,

$$\hat{H} = \beta mc^2 + c\boldsymbol{\alpha}\cdot(\hat{\boldsymbol{p}} - q\boldsymbol{A}) + q\phi = \beta mc^2 + \hat{O} + \mathcal{E}, \tag{A.1}$$

where $\hat{O}$ represents the *odd* operator $c\boldsymbol{\alpha}\cdot(\hat{\boldsymbol{p}} - q\boldsymbol{A})$ and $\mathcal{E}$ represents the scalar potential, an *even* operator. To obtain a Hamiltonian using the Hadamard lEmma, Eq. 2.7, the transformation $S = -\frac{i\beta\hat{O}}{2mc^2}$ is used such that $[\beta mc^2, S] = -\hat{O}$. This is the same transformation as was used to obtain the zeroth order Pauli equation, Eq. 2.14. The expansion is now done up to second order in $1/c$ as,

$$\hat{H}_1 = \hat{H} + i[S,\hat{H}] + \frac{i^2}{2!}\Big[S,[S,\hat{H}]\Big] + \frac{i^3}{3!}\Big[S,\Big[S,[S,\hat{H}]\Big]\Big] + \frac{i^4}{4!}\Big[S,\Big[S,\Big[S,[S,\hat{H}]\Big]\Big]\Big] - \dot{S} - \frac{i}{2!}[S,\dot{S}]. \tag{A.2}$$

The individual terms are,

$$\begin{aligned}
i[S,\hat{H}] &= -\hat{O} + \frac{\beta\hat{O}^2}{mc^2} + \frac{\beta}{2mc^2}[\hat{O},\mathcal{E}], && \text{(A.3)}\\
\frac{i^2}{2!}\Big[S,[S,\hat{H}]\Big] &= -\frac{\beta\hat{O}^2}{2mc^2} - \frac{\hat{O}^3}{2m^2c^4} - \frac{1}{8m^2c^4}\Big[\hat{O},[\hat{O},\mathcal{E}]\Big], && \text{(A.4)}\\
\frac{i^3}{3!}\Big[\Big[S,[S,\hat{H}]\Big]\Big] &= \frac{\hat{O}^3}{6m^2c^4} - \frac{\beta\hat{O}^4}{6m^3c^6}, && \text{(A.5)}\\
\frac{i^4}{4!}\Big[\Big[\Big[S,[S,\hat{H}]\Big]\Big]\Big] &= \frac{\beta\hat{O}^4}{24m^3c^6}, && \text{(A.6)}\\
\dot{S} &= \frac{i\beta\dot{\hat{O}}}{2mc^2}, && \text{(A.7)}\\
\frac{i}{2!}[S,\dot{S}] &= \frac{i}{8m^2c^4}[\hat{O},\dot{\hat{O}}], && \text{(A.8)}
\end{aligned}$$

where the identities $\hat{O}\beta = -\beta\hat{O}$ and $\beta\mathcal{E} = \mathcal{E}\beta$ were used to reach these results. Collecting these and after some manipulation, we get,

$$\hat{H}_1 = \beta mc^2 + \mathcal{E} + \frac{\beta\hat{O}^2}{2mc^2} - \frac{\beta\hat{O}^4}{8m^3c^6} - \frac{1}{8m^2c^4}\Big[\hat{O},[\hat{O},\mathcal{E}]\Big] - \frac{i}{8m^2c^4}[\hat{O},\dot{\hat{O}}] + \frac{\beta}{2mc^2}[\hat{O},\mathcal{E}] - \frac{\hat{O}^3}{3m^2c^4} - \frac{i\beta\dot{\hat{O}}}{2mc^2}. \tag{A.9}$$

We see that there are no odd operators up to order $c^0$. The last three terms in the previous equation are the only odd operators and they are each of order $1/c$. Thus, another transformation $S'$ is needed to remove these terms. We rewrite the Hamiltonian $\hat{H}_1$ as,

$$\hat{H}_1 = \beta mc^2 + \mathcal{E}' + \hat{O}', \tag{A.10}$$

where,

$$\mathcal{E}' = \mathcal{E} + \frac{\beta\hat{O}^2}{2mc^2} - \frac{\beta\hat{O}^4}{8m^3c^6} - \frac{1}{8m^2c^4}\left[\hat{O},[\hat{O},\mathcal{E}]\right] - \frac{i}{8m^2c^4}[\hat{O},\dot{\hat{O}}], \tag{A.11}$$

$$\hat{O}' = \frac{\beta}{2mc^2}[\hat{O},\mathcal{E}] - \frac{\hat{O}^3}{3m^2c^4} - \frac{i\beta\dot{\hat{O}}}{2mc^2}. \tag{A.12}$$

Similarly as before now, we define $S' = \frac{i\beta\hat{O}'}{2mc^2}$, so that $i[S,\beta mc^2] = -\hat{O}'$. Using the Hadamard lemma again and stopping the expansion at second order in $1/c$ gives us,

$$\hat{H}_2 = \hat{H}_1 + i[S',\hat{H}_1] = \beta mc^2 + \mathcal{E}', \tag{A.13}$$

or

$$\hat{H}_2 = \beta mc^2 + \mathcal{E} + \frac{\beta\hat{O}^2}{2mc^2} - \frac{\beta\hat{O}^4}{8m^3c^6} - \frac{1}{8m^2c^4}\left[\hat{O},[\hat{O},\mathcal{E}]\right] - \frac{i}{8m^2c^4}[\hat{O},\dot{\hat{O}}] \tag{A.14}$$

Evaluting the operator products in the above Hamiltonian gives us,

$$\frac{\beta\hat{O}^2}{2mc^2} = \frac{\beta(\hat{\boldsymbol{p}}-q\boldsymbol{A})^2}{2m} - \frac{\beta q\hbar}{2m}\boldsymbol{\Sigma}\cdot\boldsymbol{B}, \tag{A.15}$$

$$-\frac{\beta\hat{O}^4}{8m^3c^6} = -\frac{\beta(\hat{\boldsymbol{p}}-q\boldsymbol{A})^4}{8m^3c^2}, \tag{A.16}$$

$$\begin{aligned}-\frac{1}{8m^3c^6}\left[\hat{O},\left([\hat{O},\mathcal{E}]-i\dot{\hat{O}}\right)\right] = &-\frac{q\hbar}{8m^2c^2}\boldsymbol{\sigma}\cdot[\boldsymbol{E}\times(\hat{\boldsymbol{p}}-q\boldsymbol{A}) - (\hat{\boldsymbol{p}}-q\boldsymbol{A})\times\boldsymbol{E}] \\ &-\frac{q\hbar^2}{8m^2c^2}\boldsymbol{\nabla}\cdot\boldsymbol{E},\end{aligned} \tag{A.17}$$

where the definitions of $\boldsymbol{E} = -\boldsymbol{\nabla} - \partial_t\boldsymbol{A}$ and $\boldsymbol{B} = \boldsymbol{\nabla}\times\boldsymbol{A}$ were used for reaching the final expressions. Combining these terms and using $\hat{H}$ in place of $\hat{H}_2$ gives us,

$$\begin{aligned}\hat{H} = &mc^2 + q\phi + \frac{(\hat{\boldsymbol{p}}-q\boldsymbol{A})^2}{2m} - \frac{q\hbar}{2m}\boldsymbol{\sigma}\cdot\boldsymbol{B} - \frac{(\hat{\boldsymbol{p}}-q\boldsymbol{A})^4}{8m^3c^2} - \frac{q\hbar^2}{8m^2c^2}\boldsymbol{\nabla}\cdot\boldsymbol{E} \\ &-\frac{q\hbar}{8m^2c^2}\boldsymbol{\sigma}\cdot[\boldsymbol{E}\times(\hat{\boldsymbol{p}}-q\boldsymbol{A}) - (\hat{\boldsymbol{p}}-q\boldsymbol{A})\times\boldsymbol{E}],\end{aligned} \tag{A.18}$$

which is the extended Pauli equation used in Eq. 2.15.

# B

# Derivation of the Extended Pauli Equation from the Lagrangian Density

Here we show that the Lagrangian density provided in Eq. 2.20 does return the extended Pauli equation when we consider the Euler-Lagrange equation for $\Psi^\dagger$. Computing each term of the Euler-Lagrange equations yields,

$$\begin{aligned}\frac{\partial \mathcal{L}_P}{\partial \Psi^\dagger} = &\frac{i\hbar}{2}\dot{\Psi} - (mc^2 + q\phi)\Psi + \frac{1}{2m}q\boldsymbol{A}\cdot(\hat{\boldsymbol{p}} - q\boldsymbol{A})\Psi + \left[\frac{q\hbar}{2m}\epsilon_{ijk}\sigma_i\partial_j A_k - \frac{q\hbar^2}{8m^2c^2}\partial_k^2\phi - \frac{q\hbar^2}{8m^2c^2}\partial_t\partial_k A_k\right]\Psi \\ &+ \epsilon_{ijk}\left[\frac{q\hbar}{4m^2c^2}\sigma_i\partial_j\phi q A_k + \frac{q\hbar}{4m^2c^2}\sigma_i\partial_t A_j q A_k\right]\Psi - \frac{q\hbar}{8m^2c^2}\epsilon_{ijk}\left[\Psi^\dagger\sigma_i(\partial_j\phi + \partial_t A_j)\hat{p}_k\Psi\right],\end{aligned} \tag{B.1}$$

$$\partial_t\frac{\partial \mathcal{L}_P}{\partial(\partial_t\Psi^\dagger)} = -\frac{i\hbar}{2}\partial_t\Psi, \tag{B.2}$$

$$\partial_k\frac{\partial \mathcal{L}_P}{\partial(\partial_k\Psi^\dagger)} = \frac{1}{2m}\hat{\boldsymbol{p}}\cdot(\hat{\boldsymbol{p}} - q\boldsymbol{A}\boldsymbol{A})\Psi - \frac{q\hbar}{8m^2c^2}\hat{\boldsymbol{p}}\cdot[(\boldsymbol{\nabla} + \partial_t\boldsymbol{A})\times\boldsymbol{\sigma}\Psi]. \tag{B.3}$$

When we combine the above terms and insert them into Eq. 2.23, we obtain, after som algebra,

$$\begin{aligned}i\hbar\dot{\Psi} = &(mc^2 + q\phi)\Psi + \frac{(\hat{\boldsymbol{p}} - q\boldsymbol{A})^2}{2m}\Psi - \frac{q\hbar}{2m}\boldsymbol{\sigma}\cdot(\boldsymbol{\nabla}\times\boldsymbol{A})\Psi + \frac{q\hbar^2}{8m^2c^2}\Delta\phi\Psi + \frac{q\hbar^2}{8m^2c^2}\boldsymbol{\nabla}\cdot\partial_t\boldsymbol{A}\Psi \\ &+ \frac{q\hbar}{4m^2c^2}\boldsymbol{\sigma}\cdot\{(\boldsymbol{\nabla}\phi + \partial_t\boldsymbol{A})\times(\hat{\boldsymbol{p}} - q\boldsymbol{A})\}\Psi - \frac{q\hbar}{8m^2c^2}\boldsymbol{\sigma}\cdot(\hat{\boldsymbol{p}}\times\partial_t\boldsymbol{A})\Psi,\end{aligned} \tag{B.4}$$

which is the expected extended Pauli equation. The Hermitian conjugate form of this equation can be obtained by taking the Euler-Lagrange equation for $\Psi$.

# C

# Derivation of Rotation Matrix for d-states

Rotation causes a change of the Cartesian coordinates as,

$$\boldsymbol{r}' = \hat{R}\boldsymbol{r}. \tag{C.1}$$

The prime and bar indicate rotated variables, observables, basis, etc. $\boldsymbol{r} = (x, y, z)$ and $\hat{R}$ is any general rotation matrix along a given axis. This then gives us,

$$\begin{aligned} x' &= R_{11}x + R_{12}y + R_{13}z \\ y' &= R_{21}x + R_{22}y + R_{23}z \\ z' &= R_{31}x + R_{32}y + R_{33}z \end{aligned} \tag{C.2}$$

Let us assume that the real spherical harmonics for a given $\ell$ can be expressed in terms of a rotated real spherical harmonics set for the same $\ell$. That is,

$$\overline{\mathcal{Y}_{\ell m}} = A\mathcal{Y}_{\ell m}, \tag{C.3}$$

where we denote the rotation matrix as $A$, we have a $5 \times 5$ matrix for $\ell = 2$. If we write out the full form of the spherical harmonics (we use $(r')^2 = r^2$), we have,

$$\begin{bmatrix} \frac{1}{2}\sqrt{\frac{15}{\pi}}\frac{x'y'}{r^2} \\ \frac{1}{2}\sqrt{\frac{15}{\pi}}\frac{y'z'}{r^2} \\ \frac{1}{4}\sqrt{\frac{5}{\pi}}\frac{2(z')^2-(x')^2-(y')^2}{r^2} \\ \frac{1}{2}\sqrt{\frac{15}{\pi}}\frac{z'x'}{r^2} \\ \frac{1}{4}\sqrt{\frac{15}{\pi}}\frac{(x')^2-(y')^2}{r^2} \end{bmatrix} = \begin{bmatrix} a_{11} & a_{12} & a_{13} & a_{14} & a_{15} \\ a_{21} & a_{22} & a_{23} & a_{24} & a_{25} \\ a_{31} & a_{32} & a_{33} & a_{34} & a_{35} \\ a_{41} & a_{42} & a_{43} & a_{44} & a_{45} \\ a_{51} & a_{52} & a_{53} & a_{54} & a_{55} \end{bmatrix} \begin{bmatrix} \frac{1}{2}\sqrt{\frac{15}{\pi}}\frac{xy}{r^2} \\ \frac{1}{2}\sqrt{\frac{15}{\pi}}\frac{yz}{r^2} \\ \frac{1}{4}\sqrt{\frac{5}{\pi}}\frac{2z^2-x^2-y^2}{r^2} \\ \frac{1}{2}\sqrt{\frac{15}{\pi}}\frac{zx}{r^2} \\ \frac{1}{4}\sqrt{\frac{15}{\pi}}\frac{x^2-y^2}{r^2} \end{bmatrix}. \tag{C.4}$$

By multiplying out this matrix and expanding the primed coordinates in terms of unprimed (i.e. by using equation C.2), we can compare the coefficients on the right and left sides of the equation to represent $a_{ij}$ in terms of $R_{mn}$. Note that we have six polynomials ($x^2$,$y^2$,$z^2$,$xy$,$yz$,$zx$) but we wish to represent only 5 coefficients. This implies that we have a *double* solution for one coefficient. Indeed, if we follow through the calculation, we get two solutions for every $a_{i3}$. Below is the list of all the elements of matrix $A$:

1. $m' = -2$:

$$\begin{aligned}
a_{11} &= R_{11}R_{22} + R_{12}R_{21} \\
a_{12} &= R_{12}R_{23} + R_{13}R_{22} \\
a_{13} &= \sqrt{3}R_{13}R_{23} = -\sqrt{3}(R_{11}R_{21} + R_{12}R_{22}) \\
a_{14} &= R_{11}R_{23} + R_{13}R_{21} \\
a_{15} &= R_{11}R_{21} - R_{12}R_{22}.
\end{aligned}$$

2. $m' = -1$:

$$\begin{aligned}
a_{21} &= R_{21}R_{32} + R_{22}R_{31} \\
a_{22} &= R_{22}R_{33} + R_{23}R_{32} \\
a_{23} &= \sqrt{3}R_{23}R_{33} = -\sqrt{3}(R_{21}R_{31} + R_{22}R_{32}) \\
a_{24} &= R_{23}R_{31} + R_{21}R_{33} \\
a_{25} &= R_{21}R_{31} - R_{22}R_{32}.
\end{aligned}$$

3. $m' = 0$:

$$\begin{aligned}
a_{31} &= \frac{1}{\sqrt{3}}(2R_{31}R_{32} - R_{11}R_{12} - R_{21}R_{22}) \\
a_{32} &= \frac{1}{\sqrt{3}}(2R_{32}R_{33} - R_{12}R_{13} - R_{22}R_{23}) \\
a_{33} &= \frac{1}{2}(2R_{33}^2 - R_{13}^2 - R_{23}^2) = -\frac{1}{2}(2R_{32}^2 - R_{12}^2 - R_{22}^2 + 2R_{31}^2 - R_{11}^2 - R_{21}^2) \\
a_{34} &= \frac{1}{\sqrt{3}}(2R_{31}R_{33} - R_{11}R_{13} - R_{21}R_{23}) \\
a_{35} &= \frac{1}{\sqrt{3}}(2R_{31}^2 - R_{11}^2 - R_{21}^2 - 2R_{32}^2 + R_{12}^2 + R_{22}^2).
\end{aligned}$$

4. $m' = 1$:

$$\begin{aligned}
a_{41} &= R_{31}R_{12} + R_{32}R_{11} \\
a_{42} &= R_{32}R_{13} + R_{33}R_{12} \\
a_{43} &= \sqrt{3}R_{33}R_{13} = -\sqrt{3}(R_{31}R_{11} + R_{32}R_{12}) \\
a_{44} &= R_{33}R_{11} + R_{31}R_{13} \\
a_{45} &= R_{31}R_{11} - R_{32}R_{12}.
\end{aligned}$$

5. $m' = 2$:

$$\begin{aligned}
a_{51} &= R_{11}R_{12} - R_{22}R_{22} \\
a_{52} &= R_{12}R_{13} - R_{23}R_{23} \\
a_{53} &= \frac{\sqrt{3}}{2}(R_{13}^2 - R_{23}^2) = -\frac{\sqrt{3}}{2}(R_{11}^2 - R_{21}^2 + R_{12}^2 - R_{22}^2) \\
a_{54} &= R_{13}R_{11} - R_{23}R_{21} \\
a_{55} &= \frac{1}{2}(R_{11}^2 - R_{21}^2 - R_{12}^2 + R_{22}^2).
\end{aligned}$$

We now derive the form of $A$ for rotations about each of the Cartesian axes. Since any rotation can always be represented in terms of rotations about the Cartesian axes, $R_z$, $R_y$ and $R_x$, the $A$ matrices can be used for all cases. As is shown, the double solution obtained for $a_{i3}$ are always identical and thus, all rotations of the spherical harmonics can also be represented in terms of $A_z$, $A_y$ and $A_x$.

We begin by considering a rotation about the $z$-axis. In the real spherical harmonics basis, $\hat{R}_z(\theta) \rightarrow A_z(\theta)$. The $R$ matrix in Cartesian basis is,

$$R_z(\theta) = \begin{bmatrix} \cos\theta & -\sin\theta & 0 \\ \sin\theta & \cos\theta & 0 \\ 0 & 0 & 1 \end{bmatrix}. \tag{C.5}$$

It can be easily verified that the double solutions for $a_{i3}$ are in fact identical for this case (and for the following two cases as well). Thus, the $A_z(\theta)$ matrix is,

$$A_z(\theta) = \begin{bmatrix} \cos 2\theta & 0 & 0 & 0 & \sin 2\theta \\ 0 & \cos\theta & 0 & \sin\theta & 0 \\ 0 & 0 & 1 & 0 & 0 \\ 0 & -\sin\theta & 0 & \cos\theta & 0 \\ -\sin 2\theta & 0 & 0 & 0 & \cos 2\theta \end{bmatrix}. \tag{C.6}$$

We now consider a general rotation about the $y$-axis. In the real spherical harmonics basis, $\hat{R}_y(\theta) \rightarrow A_y(\theta)$. The $R$ matrix in Cartesian basis is,

$$R_y(\theta) = \begin{bmatrix} \cos\theta & 0 & \sin\theta \\ 0 & 1 & 0 \\ -\sin\theta & 0 & \cos\theta \end{bmatrix}. \tag{C.7}$$

The $A_y(\theta)$ matrix is,

$$A_y(\theta) = \begin{bmatrix} \cos\theta & \sin\theta & 0 & 0 & 0 \\ -\sin\theta & \cos\theta & 0 & 0 & 0 \\ 0 & 0 & \frac{1}{2}(3\cos^2\theta - 1) & -\frac{\sqrt{3}}{2}\sin 2\theta & \frac{\sqrt{3}}{2}\sin^2\theta \\ 0 & 0 & \frac{\sqrt{3}}{2}\sin 2\theta & \cos 2\theta & -\frac{1}{2}\sin 2\theta \\ 0 & 0 & \frac{\sqrt{3}}{2}\sin^2\theta & \frac{1}{2}\sin 2\theta & \frac{1}{2}(1+\cos^2\theta) \end{bmatrix}. \tag{C.8}$$

We now consider a rotation about the $x$-axis. In the real spherical harmonics basis, $\hat{R}_x(\theta) \rightarrow A_x(\theta)$. The $R$ matrix in Cartesian basis is,

$$R_x(\theta) = \begin{bmatrix} 1 & 0 & 0 \\ 0 & \cos\theta & -\sin\theta \\ 0 & \sin\theta & \cos\theta \end{bmatrix}. \tag{C.9}$$

The $A_x(\theta)$ matrix is,

$$A_x(\theta) = \begin{bmatrix} \cos\theta & 0 & 0 & -\sin\theta & 0 \\ 0 & \cos 2\theta & -\frac{\sqrt{3}}{2}\sin 2\theta & 0 & -\frac{1}{2}\sin 2\theta \\ 0 & \frac{\sqrt{3}}{2}\sin 2\theta & \frac{1}{2}(3\cos^2\theta - 1) & 0 & -\frac{\sqrt{3}}{2}\sin^2\theta \\ \sin\theta & 0 & 0 & \cos\theta & 0 \\ 0 & -\frac{1}{2}\sin 2\theta & -\frac{\sqrt{3}}{2}\sin^2\theta & 0 & \frac{1}{2}(1+\cos^2\theta) \end{bmatrix}. \tag{C.10}$$

Just like with the $R$ matrices, the $A$ matrices can be multiplied in the order of rotation. This is a faster way to generate the net rotation matrix since the individual matrices are simpler. One can of course, first create a net $R$ matrix by multiplying the individual $R$ matrices and then using the $A$ matrix element definitions to create the $A$ matrix, i.e. $A_{Z-Y-Z}(\alpha,\beta,\gamma) = A_z(\gamma)A_y(\beta)A_z(\alpha)$. The order is important since matrix multiplication is not commutative. Here, we list the individual matrix elements after the final multiplication.

$$\begin{aligned}
a_{11} &= \cos 2\gamma\cos\beta\cos 2\alpha - \frac{1}{2}\sin 2\gamma(1+\cos^2\beta)\sin 2\alpha \\
a_{12} &= \cos 2\gamma\sin\beta\cos\alpha - \frac{1}{2}\sin 2\gamma\sin 2\beta\sin\alpha \\
a_{13} &= \frac{\sqrt{3}}{2}\sin 2\gamma\sin^2\beta \\
a_{14} &= \cos 2\gamma\sin\beta\sin\alpha + \frac{1}{2}\sin 2\gamma\sin 2\beta\sin\alpha \\
a_{15} &= \cos 2\gamma\cos\beta\sin 2\alpha + \frac{1}{2}\sin 2\gamma(1+\cos^2\beta)\cos 2\alpha
\end{aligned}$$

$$\begin{aligned}
a_{21} &= -\cos\gamma\sin\beta\cos 2\alpha + \frac{1}{2}\sin\gamma\sin 2\beta\sin 2\alpha \\
a_{22} &= \cos\gamma\cos\beta\cos\alpha - \sin\gamma\cos 2\beta\sin\alpha \\
a_{23} &= \frac{\sqrt{3}}{2}\sin\gamma\sin 2\beta \\
a_{24} &= \cos\gamma\cos\beta\sin\alpha + \sin\gamma\cos 2\beta\cos\alpha \\
a_{25} &= -\cos\gamma\sin\beta\sin 2\alpha - \frac{1}{2}\sin\gamma\sin 2\beta\cos 2\alpha
\end{aligned}$$

$$\begin{aligned}
a_{31} &= -\frac{\sqrt{3}}{2}\sin^2\beta\sin 2\alpha \\
a_{32} &= \frac{\sqrt{3}}{2}\sin 2\beta\sin\alpha \\
a_{33} &= \frac{1}{2}(3\cos^2\beta - 1) \\
a_{34} &= -\frac{\sqrt{3}}{2}\sin 2\beta\cos\alpha \\
a_{35} &= \frac{\sqrt{3}}{2}\sin^2\beta\cos 2\alpha
\end{aligned}$$

$$
\begin{aligned}
a_{41} &= \sin\gamma \sin\beta \cos 2\alpha + \frac{1}{2}\cos\gamma \sin 2\beta \sin 2\alpha \\
a_{42} &= -\sin\gamma \cos\beta \cos\alpha - \cos\gamma \cos 2\beta \sin\alpha \\
a_{43} &= \frac{\sqrt{3}}{2}\cos\gamma \sin 2\beta \\
a_{44} &= -\sin\gamma \cos\beta \sin\alpha + \cos\gamma \cos 2\beta \cos\alpha \\
a_{45} &= \sin\gamma \sin\beta \sin 2\alpha - \frac{1}{2}\cos\gamma \sin 2\beta \cos 2\alpha
\end{aligned}
$$

$$
\begin{aligned}
a_{51} &= -\sin 2\gamma \cos\beta \cos 2\alpha - \frac{1}{2}\cos 2\gamma(1+\cos^2\beta)\sin 2\alpha \\
a_{52} &= -\sin 2\gamma \sin\beta \cos\alpha - \frac{1}{2}\cos 2\gamma \sin 2\beta \sin\alpha \\
a_{53} &= \frac{\sqrt{3}}{2}\cos 2\gamma \sin^2\beta \\
a_{54} &= -\sin 2\gamma \sin\beta \sin\alpha + \frac{1}{2}\cos 2\gamma \sin 2\beta \cos\alpha \\
a_{55} &= -\sin 2\gamma \cos\beta \sin 2\alpha + \frac{1}{2}\cos 2\gamma(1+\cos^2\beta)\cos 2\alpha.
\end{aligned}
$$

In our implementation, we use this matrix directly after computing the Euler angles $\alpha$, $\beta$ and $\gamma$.

# D

# Overview of Electric Polarisation

The electric polarisation $\boldsymbol{P}$ is defined as the dipole moment per unit volume. We begin by writing the classical expression for calculating the dipole moment $\boldsymbol{d}$, of a collection of charges, $q_i$, at positions $\boldsymbol{r}_i$ as,

$$\boldsymbol{d} = \sum_i q_i \boldsymbol{r}_i, \tag{D.1}$$

which can be extended for continuous electronic charge densities $e\,\rho(\boldsymbol{r})$ as,

$$\boldsymbol{d} = \int e\,\rho(\boldsymbol{r})\,\boldsymbol{r}\,\mathrm{d}\boldsymbol{r}, \tag{D.2}$$

where $e$ is the electronic charge and $\rho(\boldsymbol{r})$ is the probability density of the electrons. This definition of the dipole moment can easily be used for finite systems such as molecules, but is not well defined when applied to bulk solids, due to their infinite sizes.[93,103,135] One can then adopt an alternative viewpoint by considering a macroscopic but finite, piece of matter and define its polarisation $\boldsymbol{P}$ as,

$$\boldsymbol{P} = \frac{1}{\mathcal{V}}\left[e\sum_{i=1}^{n_a} Z_i \boldsymbol{R}_i - e\int \boldsymbol{r}\,\rho(\boldsymbol{r})\,\mathrm{d}\boldsymbol{r}\right], \tag{D.3}$$

where $\mathcal{V}$ is the volume of the sample, $eZ_i$ are the bare ionic charges and $n_a$ is the number of atomic sites. However it should be noted that though the above expression is well defined, $\boldsymbol{P}$ is not a bulk property, since it depends upon the truncation and shape of the sample. In fact, *variations* of $\boldsymbol{P}$ are measured as bulk material properties in most circumstances. The first step towards the modern theory of polarisation was made by Resta,[90] who cast $\Delta\boldsymbol{P}$ as an integrated macroscopic current. Later work by King-Smith and Vanderbilt[91,92] identified a geometric quantum phase (Berry phase) in $\Delta\boldsymbol{P}$. Further information can be found in the lecture notes by Resta[94] as well as in a review by Spaldin.[103] In this work, we only present an outline of the electric polarisation.

$\Delta\boldsymbol{P}$ is generally defined as the difference between the macroscopic polarisation (dipole moment per unit volume) of two different states of the same solid, usually a non-polar state and a polar state. Since the dipole moments can be expressed in terms of ionic and electronic parts (Eq. D.1), we have,

$$\Delta\boldsymbol{P} = \Delta\boldsymbol{P}_{\mathrm{ion}} + \Delta\boldsymbol{P}_{\mathrm{el}}, \tag{D.4}$$

where the electronic part for the finite sample is,

$$\Delta\boldsymbol{P}_{\mathrm{el}} = -\frac{e}{\mathcal{V}}\int \boldsymbol{r}\,\Delta\rho(\boldsymbol{r})\,\mathrm{d}\boldsymbol{r}, \tag{D.5}$$

and the ionic part is simply

$$\Delta \boldsymbol{P}_{\text{ion}} = \frac{e}{\mathcal{V}} \sum_{i=1}^{n_a} \left[ Z_i \boldsymbol{r}_i^{\text{polar}} - Z_i \boldsymbol{r}_i^{\text{non-polar}} \right]. \tag{D.6}$$

Thus, calculating the ionic contribution is relatively easy. For the electronic part, it is easier to consider the maximally localised Wannier functions, $w_n(\boldsymbol{r})$ corresponding to band $n$. In unit cell $\boldsymbol{R}$, it is given as,

$$\begin{aligned} w_n(\boldsymbol{r} - \boldsymbol{R}) &= \frac{\mathcal{V}_{\text{cell}}}{(2\pi)^3} \int_{BZ} e^{-i\boldsymbol{k}\cdot\boldsymbol{R}} \Psi_{n\boldsymbol{k}}(\boldsymbol{r}) \, \mathrm{d}\boldsymbol{k} \\ &= \frac{\mathcal{V}_{\text{cell}}}{(2\pi)^3} \int_{BZ} e^{i\boldsymbol{k}\cdot(\boldsymbol{r}-\boldsymbol{R})} u_{n\boldsymbol{k}}(\boldsymbol{r}) \, \mathrm{d}\boldsymbol{k}, \end{aligned} \tag{D.7}$$

where $\Psi_{n\boldsymbol{k}}(\boldsymbol{r}) = e^{i\boldsymbol{k}\cdot\boldsymbol{r}} u_{n\boldsymbol{k}}(\boldsymbol{r})$ are the Bloch functions written in terms of the cell-periodic part $u_{n\boldsymbol{k}}(\boldsymbol{r})$. $\mathcal{V}_{\text{cell}}$ is the unit cell volume and the integral is over the Brillouin zone. Since we now have localised Wannier functions instead of the completely delocalised Bloch functions, we can work out the average position of the electrons in the Wannier function and treat them as being present at that point, the *Wannier centre*, $\bar{\boldsymbol{r}}_n$, which is the expectation value of the position operator for the Wannier function,

$$\bar{\boldsymbol{r}}_n = \int w_n^\star(\boldsymbol{r}) \, \boldsymbol{r} \, w_n(\boldsymbol{r}) \, \mathrm{d}\boldsymbol{r}. \tag{D.8}$$

Using the momentum representation, where the position operator is $\boldsymbol{r} = -i\frac{\partial}{\partial \boldsymbol{k}}$, we have from Eqs. D.8 and D.7,

$$\bar{\boldsymbol{r}}_n = i\frac{\mathcal{V}_{\text{cell}}}{(2\pi)^3} \int_{BZ} e^{i\boldsymbol{k}\cdot(\boldsymbol{r}-\boldsymbol{R})} \langle u_{n\boldsymbol{k}} | \frac{\partial u_{n\boldsymbol{k}}}{\partial \boldsymbol{k}} \rangle \, \mathrm{d}\boldsymbol{k}. \tag{D.9}$$

Thus, we can now extend our definition of the polarisation for the ions to the electrons as,

$$\begin{aligned} \boldsymbol{P}_{\text{el}} &= -\frac{1}{\mathcal{V}_{\text{cell}}} \sum_{n}^{\text{occupied}} q_n \bar{\boldsymbol{r}}_n \\ &= -\frac{2ie}{(2\pi)^3} \sum_{n}^{\text{occupied}} \int_{BZ} e^{-i\boldsymbol{k}\cdot\boldsymbol{R}} \langle u_{n\boldsymbol{k}} | \frac{\partial u_{n\boldsymbol{k}}}{\partial \boldsymbol{k}} \rangle \, \mathrm{d}\boldsymbol{k}, \end{aligned} \tag{D.10}$$

and thus, $\Delta \boldsymbol{P}_{\text{el}}$ is given by,

$$\Delta \boldsymbol{P}_{\text{el}} = -\frac{2ie}{(2\pi)^3} \sum_{n}^{\text{occupied}} \int_{BZ} e^{-i\boldsymbol{k}\cdot\boldsymbol{R}} \left[ \langle u_{n\boldsymbol{k}}^{\text{polar}} | \frac{\partial u_{n\boldsymbol{k}}^{\text{polar}}}{\partial \boldsymbol{k}} \rangle - \langle u_{n\boldsymbol{k}}^{\text{non-polar}} | \frac{\partial u_{n\boldsymbol{k}}^{\text{non-polar}}}{\partial \boldsymbol{k}} \rangle \right] \mathrm{d}\boldsymbol{k}. \tag{D.11}$$

The factor of two appears because in a general covalent case, the (more) positively charged cation and the (more) negatively charged electron density move apart together, resulting in a larger *effective* displacement of the ions and hence a larger polarisation.

At the Kohn-Sham level, the one-electron wavefunctions are available in standard electronic codes, including VASP, and thus, the polarisation $\boldsymbol{P}$ can be calculated with relative ease. However, to compare with experiment it is important to calculate $\Delta \boldsymbol{P}$, the difference of $\boldsymbol{P}^{\text{polar}}$ and $\boldsymbol{P}^{\text{non-polar}}$.

Since the electric polarisation is multi-valued, more specifically, electric polarisation values lie on a polarisation lattice, it is important to calculate the difference given in D.4 on the same branch of the polarisation lattice. In the case of GFO, this can be complicated due to the presence of many non-polar unit cells near the polar structure. To resolve this, it is usually necessary to compute the polarisation at multiple points on a path connecting the two structures. Formally, this can be expressed as,

$$\Delta \boldsymbol{P} = \int_0^1 \boldsymbol{P}(\lambda)\, \mathrm{d}\lambda, \tag{D.12}$$

where $\lambda$ denotes the different points on the path connecting the non-polar structure, $\lambda = 0$, with the polar structure, $\lambda = 1$. Alternatively, one can carefully compute along the branch of the polarisation lattice by making sure that the polarisation values between two successive points do not change drastically, as was done by Stoeffler[83] for GFO.

# E

# XAS Using the Position Representation

To obtain the x-ray absorption in the position representation, we use the commutation relation between $\boldsymbol{p}$ and $\boldsymbol{r}$ given as:

$$\left[\boldsymbol{r}, \hat{H}_0\right] = \frac{i\hbar}{m}\hat{\boldsymbol{p}}. \tag{E.1}$$

Note that the commutation relation holds if and only if the basis set is complete. For simplicity, we compute the transition probability $D_{if}^{\hat{\boldsymbol{\varepsilon}}} = |\langle i|\hat{\boldsymbol{\varepsilon}} \cdot \hat{\boldsymbol{p}}|f\rangle|^2 \ \delta(\hbar\omega - \epsilon_f + \epsilon_i)$, i.e. transitions from state $\langle i|$ to state $|f\rangle$, without the scaling constants. Thus, we have:

$$\begin{aligned}
D_{if}^{\hat{\boldsymbol{\varepsilon}}} &= \frac{m^2}{\hbar^2}\left|\langle i|\hat{\boldsymbol{\varepsilon}} \cdot \left[\boldsymbol{r}, \hat{H}_0\right]|f\rangle\right|^2 \delta(\hbar\omega - \epsilon_f + \epsilon_i) && \text{(E.2)}\\
&= \frac{m^2}{\hbar^2}\left|\sum_m \langle i|\hat{\boldsymbol{\varepsilon}}|m\rangle \cdot \left(\langle m|\boldsymbol{r}\hat{H}_0|f\rangle - \langle m|\hat{H}_0\boldsymbol{r}|f\rangle\right)|f\rangle\right|^2 \delta(\hbar\omega - \epsilon_f + \epsilon_i) && \text{(E.3)}\\
&= \frac{m^2}{\hbar^2}\left|\sum_m \hat{\boldsymbol{\varepsilon}} \cdot \langle i|m\rangle\,(\epsilon_f - \epsilon_m)\,\langle m|\boldsymbol{r}|f\rangle\right|^2 \delta(\hbar\omega - \epsilon_f + \epsilon_i) && \text{(E.4)}\\
&= \frac{m^2}{\hbar^2}\left|\sum_m \hat{\boldsymbol{\varepsilon}} \cdot \delta_{im}\,(\epsilon_f - \epsilon_m)\,\langle m|\boldsymbol{r}|f\rangle\right|^2 \delta(\hbar\omega - \epsilon_f + \epsilon_i) && \text{(E.5)}\\
&= \frac{m^2}{\hbar^2}\left|\hbar\omega\langle i|\hat{\boldsymbol{\varepsilon}} \cdot \boldsymbol{r}|f\rangle\right|^2 \delta(\hbar\omega - \epsilon_f + \epsilon_i). && \text{(E.6)}\\
\therefore\ D_{if}^{\hat{\boldsymbol{\varepsilon}}} &= m^2\omega^2\left|\langle i|\hat{\boldsymbol{\varepsilon}} \cdot \boldsymbol{r}|f\rangle\right|^2 \delta(\hbar\omega - \epsilon_f + \epsilon_i). && \text{(E.7)}
\end{aligned}$$

And our absorption spectrum is given as:

$$\sigma^{\hat{\boldsymbol{\varepsilon}}}(\omega) = 4\pi\alpha\hbar\omega \sum_{if} \left|\langle i|\hat{\boldsymbol{\varepsilon}} \cdot \boldsymbol{r}|f\rangle\right|^2 \delta(\hbar\omega - \epsilon_f + \epsilon_i). \tag{E.8}$$

The probability amplitudes for the absorption spectrum in the $|\ell, m\rangle$ basis for $\mu = +1, 0, -1$ in the position representation are simpler to calculate because we can directly represent them in terms

of spherical harmonics with $\ell = 1$ as:

$$r_{+1} = \frac{-1}{\sqrt{2}}(\hat{x} + i\hat{y}) = \sqrt{\frac{4\pi}{3}}\, r\mathcal{Y}_1^{+1}(\theta,\phi), \tag{E.9}$$

$$r_{-1} = \frac{1}{\sqrt{2}}(\hat{x} - i\hat{y}) = \sqrt{\frac{4\pi}{3}}\, r\mathcal{Y}_1^{-1}(\theta,\phi), \tag{E.10}$$

$$r_0 = \hat{z} = \sqrt{\frac{4\pi}{3}}\, r\mathcal{Y}_1^{0}(\theta,\phi). \tag{E.11}$$

Thus, our amplitudes $\langle \ell', m' | r_\mu | \ell, m \rangle$ are:

$$\langle \ell', m' | r_\mu | \ell, m \rangle = \int \mathcal{Y}_{\ell'}^{-m'}(\theta,\phi)\ \varphi_{\ell'}(r)\sqrt{\frac{4\pi}{3}}\, r\mathcal{Y}_1^{\mu}(\theta,\phi)\ \mathcal{Y}_{\ell}^{m}(\theta,\phi)\ \varphi_\ell(r)\ \mathrm{d}\Omega\ \mathrm{d}r \tag{E.12}$$

$$= \sqrt{\frac{4\pi}{3}}\ (\varphi_{\ell'}|r|\varphi_\ell) \int \mathcal{Y}_{\ell'}^{-m'}(\theta,\phi)\ \mathcal{Y}_1^{\mu}(\theta,\phi)\ \mathcal{Y}_{\ell}^{m}(\theta,\phi)\ \mathrm{d}\Omega, \tag{E.13}$$

where $(\varphi_{\ell'}|r|\varphi_\ell)$ is the radial integral. The integral of the product of three spherical harmonics gives us the Gaunt coefficient and can be written with the Wigner 3-$j$ symbols as:[128]

$$\int \mathcal{Y}_{\ell_1}^{m_1}(\theta,\phi)\ \mathcal{Y}_{\ell_2}^{m_2}(\theta,\phi)\ \mathcal{Y}_{\ell_3}^{m_3}(\theta,\phi)\ \mathrm{d}\Omega = \sqrt{\frac{(2\ell_1+1)(2\ell_2+1)(2\ell_3+1)}{4\pi}} \begin{pmatrix} \ell_1 & \ell_2 & \ell_3 \\ 0 & 0 & 0 \end{pmatrix} \begin{pmatrix} \ell_1 & \ell_2 & \ell_3 \\ m_1 & m_2 & m_3 \end{pmatrix}. \tag{E.14}$$

Thus, using Eq. 6.17, our probability amplitudes can be simplified as:

$$\langle \ell', m' | r_\mu | \ell, m \rangle = \sqrt{(2\ell'+1)(2\ell+1)}\ C^{\ell',0}_{1,0;\ell,0}\ C^{\ell',m'}_{1,\mu;\ell,m}\,(\varphi_{\ell'}|r|\varphi_\ell)\,. \tag{E.15}$$

Here, the selection rules are exactly the same as those in the momentum representation, viz. $\ell = \ell' \pm 1$ and $m = m' - \mu$. The extension of the derivation to involve the projector index $p$ of the same angular momentum and the projectors $P^{n,\boldsymbol{k},s}_{p,\ell,m}$ is trivial. This form is obviously easier to compute as it does not involve differentiating the valence wavefunction as in the case of the momentum representation. However, it is worth reiterating that the two representations are equivalent *if and only if* the basis set is complete. We have implemented both the methods and the momentum representation is always computed. The comparison between the two representations provides a check on the quality of the basis set.

# F

# Inclusion of Higher Energy States for XAS

At higher energies, the electron states are less affected by the ionic potential and the electron state is more 'wave-like'. For this reason, the all-electron partial waves and pseudo-partial waves are provided only up to a given energy level in VASP. For studying the electron states above this energy, we must consider the plane wave basis, i.e. the all-electron partial waves and pseudo-partial waves match each other. Then, the full all-electron wavefunction $\Psi^s_{n,\boldsymbol{k}}(\boldsymbol{r})$ in the plane wave basis is given by Eq. 6.13:

$$\Psi^s_{n,\boldsymbol{k}}(\boldsymbol{r}) = \langle \boldsymbol{r} | \widetilde{n, \boldsymbol{k}, s} \rangle = \sum_{\boldsymbol{G}} A^s_{n,\boldsymbol{k}+\boldsymbol{G}} e^{i(\boldsymbol{k}+\boldsymbol{G})\cdot\boldsymbol{r}}. \tag{F.1}$$

Here, $A^s_{n,\boldsymbol{k}+\boldsymbol{G}}$ are the eigenvalues obtained in the plane wave basis after the Hamiltonian diagonalisation. In Eq. F.1, the plane waves are written in terms of a global coordinate system $\boldsymbol{r}$, while the core states in the $\langle \ell', m'; 1/2, s'|$ basis are in terms of a local coordinate system $\boldsymbol{r}'$ of an atom with a global position $\boldsymbol{\tau}_a$, where $\boldsymbol{r} = \boldsymbol{r}' + \boldsymbol{\tau}_a$. Using this in Eq. F.1, we get,

$$\langle \boldsymbol{r}' | \widetilde{n, \boldsymbol{k}, s} \rangle = \sum_{\boldsymbol{G}} A^s_{n,\boldsymbol{k}+\boldsymbol{G}} e^{i(\boldsymbol{k}+\boldsymbol{G})\cdot\boldsymbol{\tau}_a} e^{i(\boldsymbol{k}+\boldsymbol{G})\cdot\boldsymbol{r}'} = \sum_{\boldsymbol{G}} A^s_{n,\boldsymbol{k}+\boldsymbol{G}} e^{i(\boldsymbol{k}+\boldsymbol{G})\cdot\boldsymbol{\tau}_a} \langle \boldsymbol{r}' | \boldsymbol{k}+\boldsymbol{G} \rangle, \tag{F.2}$$

where $|\boldsymbol{k}+\boldsymbol{G}\rangle$ is the plane wave represented in terms of $\boldsymbol{r}'$. We can expand the exponential in terms of spherical harmonics $\mathcal{Y}^m_\ell$ to get:[136]

$$e^{i(\boldsymbol{k}+\boldsymbol{G})\cdot\boldsymbol{r}'} = 4\pi \sum_{\ell=0}^{\infty} \sum_{m=-\ell}^{+\ell} i^\ell j_\ell(|\boldsymbol{k}+\boldsymbol{G}|r) \mathcal{Y}^{m\star}_\ell(\widehat{\boldsymbol{k}+\boldsymbol{G}}) \mathcal{Y}^m_\ell(\hat{\boldsymbol{r}'}), \tag{F.3}$$

where, $\widehat{\boldsymbol{k}+\boldsymbol{G}}$ and $\hat{\boldsymbol{r}'}$ denote the unit vectors along $\boldsymbol{k}+\boldsymbol{G}$ and $\boldsymbol{r}'$ respectively. $j_\ell(x)$ are the spherical Bessel functions linked to the ordinary Bessel functions $J_\ell$ as $j_\ell(x) = \sqrt{\frac{\pi}{2x}} J_{\ell+\frac{1}{2}}(x)$. The spherical Bessel functions can also be written as:

$$j_\ell(x) = (-x)^\ell \left( \frac{1}{x} \frac{\mathrm{d}}{\mathrm{d}x} \right)^\ell \frac{\sin(x)}{x}. \tag{F.4}$$

We must now compute the probability amplitudes $\langle \ell', m'; 1/2, s' | \hat{p}_\mu | n, \boldsymbol{k}, s \rangle$ for transitions under the polarisation $\mu = \pm 1, 0$. Thus,

$$\langle \ell', m'; 1/2, s' | \hat{p}_\mu | \widetilde{n, \boldsymbol{k}, s} \rangle = \langle \ell', m'; 1/2, s' | \hat{p}_\mu \sum_{\boldsymbol{G}} A^s_{n,\boldsymbol{k}+\boldsymbol{G}} e^{i(\boldsymbol{k}+\boldsymbol{G})\cdot\boldsymbol{\tau}_a} | \boldsymbol{k}+\boldsymbol{G} \rangle \tag{F.5}$$

$$= \sum_{\boldsymbol{G}} A^s_{n,\boldsymbol{k}+\boldsymbol{G}} e^{i(\boldsymbol{k}+\boldsymbol{G})\cdot\boldsymbol{\tau}_a} \hbar(k_\mu + G_\mu) \langle \ell', m'; 1/2, s' | \boldsymbol{k}+\boldsymbol{G} \rangle \delta_{s,s'}. \tag{F.6}$$

Using Eq. F.3 and carrying out the integration over the spherical harmonics gives us $\delta_{\ell,\ell'}$ and $\delta_{m,m'}$. Simplifying with some algebra gives us the probability amplitudes as,

$$\langle \ell', m'; 1/2, s' | \hat{p}_\mu | \widetilde{n, \boldsymbol{k}, s} \rangle = \sum_{\boldsymbol{G}} \hbar(k_\mu + G_\mu)\ e^{i(\boldsymbol{k}+\boldsymbol{G})\cdot\boldsymbol{\tau}_a}\ B^{\ell',m',s}_{n,\boldsymbol{k}+\boldsymbol{G}}\ \delta_{s,s'}, \tag{F.7}$$

where,

$$B^{\ell',m',s}_{n,\boldsymbol{k}+\boldsymbol{G}} = 4\pi i^{\ell'} A^s_{n,\boldsymbol{k}+\boldsymbol{G}} \mathcal{Y}^{m\prime\star}_{\ell'}(\widehat{\boldsymbol{k}+\boldsymbol{G}}) \int \varphi_{\ell'}(r') j_{\ell'}(|\boldsymbol{k}+\boldsymbol{G}|r') r'^2\, \mathrm{d}r'.$$

The development shown here is that of the plane wave contribution of the wavefunction in PAW. To generalise the implementation, we should consider the full PAW transformation as in Eq. 6.10 and sum the contributions from the all-electron partial waves, the pseudo-partial waves and the plane waves. The development to compute the pseudo-partial wave contribution is similar to the all-electron partial waves as shown through Eqs. 6.16-6.27. We then have three probability amplitudes, which can be summed up to give the transition probabilities for the absorption spectrum. The final absorption spectrum in the momentum representation can then be written as:

$$\begin{aligned}\sigma^\mu(\omega) = \frac{4\pi\alpha\hbar^2}{m^2\omega} \sum_{M,n,\boldsymbol{k},s} \Bigg| \sum_{\ell,m,m'} C^{J,M}_{\ell',m';1/2,s} \Bigg\{ -i \frac{C^{\ell',m'}_{1,\mu;\ell,m}}{C^{\ell',0}_{1,0;\ell,0}} \sum_p \langle \ell', 0 | \nabla_0 \left( |p,\ell,0\rangle - |\widetilde{p,\ell,0}\rangle \right) \overline{P}^{n,\boldsymbol{k},s}_{p,\ell,m} \\ + \sum_{\boldsymbol{G}} (k_\mu + G_\mu)\ e^{i(\boldsymbol{k}+\boldsymbol{G})\cdot\boldsymbol{\tau}_a}\ B^{\ell',m',s}_{n,\boldsymbol{k}+\boldsymbol{G}} \Bigg\} \Bigg|^2 \delta(\hbar\omega - \epsilon_{n\boldsymbol{k}s} + \epsilon_{JM}).\end{aligned} \tag{F.8}$$

To work in the position representation, we get,

$$\begin{aligned}\langle \ell', m'; 1/2, s' | r_\mu | \widetilde{n, \boldsymbol{k}, s} \rangle &= \langle \ell', m'; 1/2, s' | r_\mu \sum_{\boldsymbol{G}} A^s_{n,\boldsymbol{k}+\boldsymbol{G}} e^{i(\boldsymbol{k}+\boldsymbol{G})\cdot\boldsymbol{\tau}_a} | \boldsymbol{k}+\boldsymbol{G} \rangle & \text{(F.9)} \\ &= \sum_{\boldsymbol{G}} A^s_{n,\boldsymbol{k}+\boldsymbol{G}} e^{i(\boldsymbol{k}+\boldsymbol{G})\cdot\boldsymbol{\tau}_a} \langle \ell', m'; 1/2, s' | r_\mu | \boldsymbol{k}+\boldsymbol{G} \rangle \delta_{s,s'}. & \text{(F.10)}\end{aligned}$$

Using Eq. F.3 and carrying out the integration over the spherical harmonics gives us the Gaunt coefficients and the selection rules identical to those obtained in Appendix E. With some algebra, we get the probability amplitudes,

$$\langle \ell', m'; 1/2, s' | r_\mu | \widetilde{n, \boldsymbol{k}, s} \rangle = \sum_{\boldsymbol{G}} \sum_{\ell,m} \sqrt{(2\ell'+1)(2\ell+1)}\ e^{i(\boldsymbol{k}+\boldsymbol{G})\cdot\boldsymbol{\tau}_a}\ C^{\ell',0}_{1,0;\ell,0} C^{\ell',m'}_{1,\mu;\ell,m} B^{\ell,m,s}_{n,\boldsymbol{k}+\boldsymbol{G}}\ \delta_{s,s'}. \tag{F.11}$$

The full absorption spectrum in the position representation then becomes,

$$\begin{aligned}\sigma^\mu(\omega) = 4\pi\alpha\hbar\omega \sum_{M,n,\boldsymbol{k},s} \Bigg| \sum_{\ell,m,m'} C^{JM}_{\ell',m';1/2,s} C^{\ell',0}_{1,0;\ell,0} C^{\ell',m'}_{1,\mu;\ell,m} \sqrt{(2\ell'+1)(2\ell+1)} \Bigg\{ \sum_p \left(\varphi_{\ell'}|r|\phi_{p\ell}\right) \overline{P}^{n,\boldsymbol{k},s}_{p,\ell,m} \\ + \sum_{\boldsymbol{G}}\ e^{i(\boldsymbol{k}+\boldsymbol{G})\cdot\boldsymbol{\tau}_a} B^{\ell,m,s}_{n,\boldsymbol{k}+\boldsymbol{G}} \Bigg\} \Bigg|^2 \delta(\hbar\omega - \epsilon_{n\boldsymbol{k}s} + \epsilon_{JM}),\end{aligned} \tag{F.12}$$

where, $\phi_{p\ell}(r) = \varphi_{p\ell}(r) - \widetilde{\varphi_{p\ell}(r)}$. The calculation of the plane wave contribution is computationally very expensive, since it involves an integration of a spherical Bessel function with the radial core wavefunction for every $\boldsymbol{G}$-vector for every k-point. Moreover, the plane wave contribution becomes significant only at higher energies, the calculation of which requires a higher plane wave cutoff, and can be neglected for systems with small band gaps.

# Résumé Étendu

Ce travail de thèse concerne l'étude de la physique des matériaux où les interactions relativistes sont très importantes. Dans les récents développements technologiques, les effets relativistes jouent un rôle prépondérant. Ces développements concernent, sans en être limités, les lasers femto-secondes, les matériaux multiferroïques ou encore les phénomènes de transport de spin dans différents matèriaux. Les courtes échelles de temps des interactions lumière-matière peuvent désormais être sondées avec une grande précision, mais ces échelles de temps ainsi que les interactions lumière-matière ne peuvent pas être correctement décrites sans tenir compte des effets relativistes.

Lorsque nous développons l'équation de Dirac relativiste au second ordre en $1/c$, où $c$ est la vitesse de la lumière, nous obtenons le terme de couplage spin-orbite (SOC) et le terme de Darwin. Le terme de SOC montre que le moment de spin et le moment cinétique d'orbite ne sont pas conservés individuellement, seule leur somme vectorielle l'est. Les conséquences physiques sont très intéressantes. Par exemple, lorsque des impulsions laser ultra-rapides interagissent avec un gaz d'électrons d'un matériau ferromagnétique, on observe le phénomène de désaimantation spontanée. D'autre part, pour expliquer les phénomènes multiferroïques dans différents matériaux, il est nécessaire d'inclure le couplage du moment de spin au moment d'orbite dans les calculs *ab initio*.

Dans le chapitre 2, nous avons développé un modèle semi-relativiste au second ordre en 1/c pour étudier des systèmes électroniques à plusieurs corps. Nous avons commencé avec l'équation de Dirac dans l'approximation de Hartree, qui a été ensuite réécrite en puissances de $1/c$ en utilisant la transformation Foldy-Wouthuysen, qui se fonde sur le lemme Hadamard,

$$\begin{aligned} e^{iS}\hat{Q}e^{-iS} =& \hat{Q} + i[S,\hat{Q}] + \frac{i^2}{2!}[S,[S,\hat{Q}]] + \frac{i^3}{3!}[S,[S,[S,\hat{Q}]]] + \cdots \\ & - \left(\dot{S} + \frac{i}{2!}[S,\dot{S}] + \frac{i^2}{3!}[S,[S,\dot{S}]] + \cdots\right), \end{aligned} \tag{1}$$

où, $\hat{Q}$ est l'opérateur qui est transformé par une transformation unitaire $S$. Cette transformation découple les interactions matière-antimatière et nous permet de nous concentrer sur les effets semi-relativistes jusqu'à l'ordre souhaité. Il est également plus simple de travailler avec deux spineurs (spin-up et spin-down de l'électron) au lieu de quatre vecteurs bi-spineurs. A l'ordre zéro, la seule correction à l'équation de Schrödinger vient du terme Zeeman, qui couple le spin de l'électron au

champ magnétique. Les effets du second ordre, comme les termes du SOC et de Darwin, sont essentiels à la bonne compréhension des processus de la magnéto-optique et sont par conséquent conservés dans notre modèle.

$$\begin{aligned}\hat{H} =& mc^2 + q\phi + \frac{(\hat{\boldsymbol{p}} - q\boldsymbol{A})^2}{2m} - \frac{q\hbar}{2m}\boldsymbol{\sigma}\cdot\boldsymbol{B} - \frac{(\hat{\boldsymbol{p}} - q\boldsymbol{A})^4}{8m^3c^2} - \frac{q\hbar}{8m^2c^2}\boldsymbol{\nabla}\cdot\boldsymbol{E} \\ & - \frac{q\hbar}{8m^2c^2}\boldsymbol{\sigma}\cdot\left[\boldsymbol{E}\times(\hat{\boldsymbol{p}} - q\boldsymbol{A}) - (\hat{\boldsymbol{p}} - q\boldsymbol{A})\times\boldsymbol{E}\right],\end{aligned} \tag{2}$$

où les champs électromagnétiques sont definis: $\boldsymbol{E} = -\boldsymbol{\nabla}\phi - \partial_t\boldsymbol{A}$ et $\boldsymbol{B} = \boldsymbol{\nabla}\times\boldsymbol{A}$. Nous avons ensuite réécrit les équations de Maxwell en termes de potentiels scalaire et vectoriel, et utilisé la jauge de Lorentz pour obtenir deux équations découplées de ces potentiels:

$$-\Delta\phi + \frac{1}{c^2}\partial_t^2\phi = \frac{q\rho}{\varepsilon_0} \tag{3}$$

$$-\Delta\boldsymbol{A} + \frac{1}{c^2}\partial_t^2\boldsymbol{A} = \mu_0 q\boldsymbol{j}. \tag{4}$$

Le Lagrangien pour le système semi-relativiste et les équations de Maxwell ont ensuite été développés pour coupler le système avec les champs auto-générés:

$$\begin{aligned}\mathcal{L} =& \frac{i\hbar}{2}(\Psi^\dagger\dot{\Psi} - \dot{\Psi}^\dagger\Psi) - \Psi^\dagger(mc^2 + q\phi)\Psi - \frac{1}{2m}\left[(i\hbar\partial_k - qA_k)\Psi^\dagger(-i\hbar\partial_k - qA_k)\Psi\right] \\ & + \frac{q\hbar}{2m}\Psi^\dagger\epsilon_{ijk}\sigma_i\partial_j A_k\Psi - \frac{q\hbar^2}{8m^2c^2}\left[\partial_k^2\phi + \partial_t\partial_k A_k\right]\Psi^\dagger\Psi + \frac{q\hbar}{4m^2c^2}\Psi^\dagger\epsilon_{ijk}\left[\sigma_i\partial_j\phi q A_k + \sigma_i\partial_t A_j q A_k\right]\Psi \\ & - \frac{q\hbar}{8m^2c^2}\epsilon_{ijk}\left[\Psi^\dagger\sigma_i\partial_j\phi\hat{p}_k\Psi - \partial_j\phi\hat{p}_k\Psi^\dagger\sigma_i\Psi + \Psi^\dagger\sigma_i\partial_t A_j\hat{p}_k\Psi - \partial_t A_j\hat{p}_k\Psi^\dagger\sigma_i\Psi\right] \\ & + \frac{\varepsilon_0}{2}(\partial_k\phi)^2 - \frac{\varepsilon_0}{2c^2}(\partial_t\phi)^2 - \frac{1}{2\mu_0}(\partial_j A_k)^2 + \frac{1}{2\mu_0 c^2}(\partial_t A_k)^2.\end{aligned} \tag{5}$$

L'équation d'Euler-Lagrange de cette densité de Lagrange pour une variable $\varphi$ nous donne son équation de mouvement:[20,21]

$$\frac{\partial\mathcal{L}}{\partial\varphi} - \sum_\mu \partial_\mu\frac{\partial\mathcal{L}}{\partial(\partial_\mu\varphi)} + \sum_\mu \partial_\mu^2\frac{\partial\mathcal{L}}{\partial(\partial_\mu^2\varphi)} + \sum_{\substack{\mu,\nu \\ \mu\neq\nu}} \partial_\mu\partial_\nu\frac{\partial\mathcal{L}}{\partial(\partial_\mu\partial_\nu\varphi)} = 0. \tag{6}$$

Par exemple, l'équation d'Euler-Lagrange pour la variable $\Psi^\dagger$ nous donne l'hamiltonien semi-relativiste comme indiqué à l'annexe B. Pour déterminer les sources de charges, nous avons calculé les équations d'Euler-Lagrange de cette densité de Lagrange pour les potentiels scalaire $\phi$ et vectoriel $\boldsymbol{A}$. La densité de probabilité est donc définie comme,

$$\begin{aligned}q\rho =& q\Psi^\dagger\Psi + \frac{q\hbar}{4mc^2}\boldsymbol{\nabla}\cdot\left[\frac{q}{m}\boldsymbol{A}\times(\Psi^\dagger\boldsymbol{\sigma}\Psi) - \frac{i\hbar}{2m}\left\{(\boldsymbol{\nabla}\Psi^\dagger)\times\boldsymbol{\sigma}\Psi + \Psi^\dagger\boldsymbol{\sigma}\times(\boldsymbol{\nabla}\Psi)\right\}\right] \\ & + \frac{q\hbar}{4mc^2}\boldsymbol{\nabla}\cdot\left\{\frac{\hbar}{2m}\boldsymbol{\nabla}(\Psi^\dagger\Psi)\right\} \\ =& q\rho^{\text{free}} - \boldsymbol{\nabla}\cdot\boldsymbol{P}_{\text{spin}} - \boldsymbol{\nabla}\cdot\boldsymbol{P}_{\text{Darwin}},\end{aligned} \tag{7}$$

et de courant comme,

$$\begin{aligned} q\boldsymbol{j} =& \frac{qi\hbar}{2m}\left[(\boldsymbol{\nabla}\Psi^\dagger)\Psi - \Psi^\dagger(\boldsymbol{\nabla}\Psi)\right] - \frac{q^2}{m}\boldsymbol{A}\Psi^\dagger\Psi + \frac{q\hbar}{2m}\left[\boldsymbol{\nabla}\times(\Psi^\dagger\boldsymbol{\sigma}\Psi)\right] + \frac{q^2\hbar}{4m^2c^2}\left[\boldsymbol{E}\times(\Psi^\dagger\boldsymbol{\sigma}\Psi)\right] \\ & - \frac{q\hbar}{4m^2c^2}\partial_t\left[\frac{q}{m}\boldsymbol{A}\times(\Psi^\dagger\boldsymbol{\sigma}\Psi) - \frac{i\hbar}{2m}\left\{(\boldsymbol{\nabla}\Psi^\dagger)\times\boldsymbol{\sigma}\Psi + \Psi^\dagger\boldsymbol{\sigma}\times(\boldsymbol{\nabla}\Psi)\right\}\right] - \frac{q\hbar}{4m^2c^2}\partial_t\left[\frac{\hbar}{2m}\boldsymbol{\nabla}(\Psi^\dagger\Psi)\right] \\ =& q\boldsymbol{j}^{\text{free}} + \boldsymbol{\nabla}\times\boldsymbol{M} + \partial_t\boldsymbol{P}_{\text{spin}} + \partial_t\boldsymbol{P}_{\text{Darwin}} \end{aligned} \tag{8}$$

Ces sources ont été définies en termes de fonctions d'onde de particules individuelles qui sont solutions du système semi-relativiste et ont été écrites en termes de composantes non liées (*free*) et liées (*bound*). Les sources contiennent en plus une densité de courant non liée de second ordre et des sources liées. Les sources liées ont été réécrites en tant que quantités d'aimantation et de polarisation électrique.
Le terme d'aimantation est dû aux spins des électrons dans le champ moyen. Les termes de polarisation électrique ont deux contributions – la première est due au terme Darwin et la deuxième à l'aimantation magnétique. La polarisation électrique du terme de Darwin a été interprétée comme un potentiel moyen créé par le mouvement de tremblement des électrons (*Zitterbewegung*). Ce mouvement est dû à l'interaction entre les solutions de matière-antimatière de l'équation de Dirac et agit en tant que potentiel (le terme de Darwin) dans la limite semi-relativiste.

Pour mieux comprendre cela, nous considérons les fluctuations $\delta\boldsymbol{r}(t)$ autour de la trajectoire moyenne $\overline{\boldsymbol{r}(t)}$ de l'électron:

$$\boldsymbol{r}(t) = \overline{\boldsymbol{r}(t)} + \delta\boldsymbol{r}(t), \tag{9}$$

où $\boldsymbol{r}(t)$ est la position instantanée au temps $t$. En développant la distribution de probabilité autour de la trajectoire moyenne, nous obtenons,

$$\rho(\boldsymbol{r}) = \Psi^\dagger(\overline{\boldsymbol{r}})\Psi(\overline{\boldsymbol{r}}) + \boldsymbol{\nabla}\left[\Psi^\dagger(\overline{\boldsymbol{r}})\Psi(\overline{\boldsymbol{r}})\right]\cdot\delta\boldsymbol{r} + \frac{1}{2}\frac{\partial^2\left[\Psi^\dagger(\overline{\boldsymbol{r}})\Psi(\overline{\boldsymbol{r}})\right]}{\partial r_i\partial r_j}\delta r_i\delta r_j + \cdots, \tag{10}$$

où nous négligeons la dépendance temporelle. La perturbation est ainsi, $\rho_Z = \overline{\rho(\boldsymbol{r})} - \Psi^\dagger(\overline{\boldsymbol{r}})\Psi(\overline{\boldsymbol{r}})$. Puisque *Zitterbewegung* est isotrope, le terme linéaire disparaît lorsque l'on considère la moyenne,

$$\rho_Z = \overline{\rho(\boldsymbol{r})} - \Psi^\dagger(\overline{\boldsymbol{r}})\Psi(\overline{\boldsymbol{r}}) = \frac{1}{2}\frac{\partial^2\left[\Psi^\dagger(\overline{\boldsymbol{r}})\Psi(\overline{\boldsymbol{r}})\right]}{\partial r_i\partial r_j}\delta r_i\delta r_j. \tag{11}$$

L'amplitude des oscillations peut être estimée de l'ordre de la longueur d'onde Compton,

$$\overline{\delta\boldsymbol{r}^2} \equiv \frac{\hbar^2}{m^2c^2}, \tag{12}$$

ce qui nous donne,

$$\rho_Z \equiv \frac{\hbar^2}{6m^2c^2}\delta_{ij}\frac{\partial^2\left[\Psi^\dagger(\overline{\boldsymbol{r}})\Psi(\overline{\boldsymbol{r}})\right]}{\partial r_i\partial r_j} = \frac{\hbar^2}{6m^2c^2}\Delta(\Psi^\dagger\Psi) = -\boldsymbol{\nabla}\cdot\left[-\frac{\hbar^2}{6m^2c^2}\boldsymbol{\nabla}(\Psi^\dagger\Psi)\right], \tag{13}$$

et une densité de polarisation électrique,

$$\boldsymbol{P}_Z = -\frac{\hbar^2}{6m^2c^2}\boldsymbol{\nabla}(\Psi^\dagger\Psi). \tag{14}$$

En comparaison avec $\boldsymbol{P}_{\text{Darwin}}$, nous observons que la dépendance fonctionnelle est correcte. La discordance de la constante multiplicatif (3/4) se pose en raison de l'estimation brute des fluctuations.

Le terme de polarisation électrique en raison de l'aimantation a été interprété comme une expansion semi-relativiste de la transformation de Lorentz du tenseur aimantation-polarisation électrique. Ce terme apparaît en raison de l'inclusion du SOC. Pour mieux comprendre l'origine, on considère deux systèmes référentiels qui se déplacent avec une vitesse v par rapport à l'autre. Les transformations de Lorentz pour la densité d'aimantation $\boldsymbol{M}$ et la densité de polarisation $\boldsymbol{P}$ dans le cas pleinement relativiste sont,[25]

$$\boldsymbol{P} = \gamma\left(\boldsymbol{P}' + \frac{\boldsymbol{v}\times\boldsymbol{M}'}{c^2}\right) - \frac{\gamma^2}{1+\gamma}\left(\frac{\boldsymbol{P}'\cdot\boldsymbol{v}}{c}\right)\frac{\boldsymbol{v}}{c}, \tag{15}$$

$$\boldsymbol{M} = \gamma(\boldsymbol{M}' - \boldsymbol{v}\times\boldsymbol{P}') - \frac{\gamma^2}{1+\gamma}\left(\frac{\boldsymbol{M}'\cdot\boldsymbol{v}}{c}\right)\frac{\boldsymbol{v}}{c}, \tag{16}$$

où $\gamma = \frac{1}{\sqrt{1-v^2/c^2}}$ est le facteur de Lorentz. Pour $v \ll c$ et $|\boldsymbol{M}| \gg c|\boldsymbol{P}|$ (limite électrique), nous obtenons,

$$\boldsymbol{P} = \boldsymbol{P}' + \frac{\boldsymbol{v}\times\boldsymbol{M}'}{c^2}, \tag{17}$$

$$\boldsymbol{M} = \boldsymbol{M}'. \tag{18}$$

Dans le système référentiel de repos de l'électron (les variables de la forme $x'$), il y a une densité d'aimantation $\boldsymbol{M}' = \boldsymbol{M}_{\text{spin}}$, mais aucune polarisation électrique, $\boldsymbol{P}' = 0$. Ainsi, dans le référentiel du laboratoire, nous obtenons,

$$\boldsymbol{P} = \frac{\boldsymbol{v}\times\boldsymbol{M}_{\text{spin}}}{c^2}, \tag{19}$$

$$\boldsymbol{M} = \boldsymbol{M}_{\text{spin}}. \tag{20}$$

Ceci est purement classique, car $\boldsymbol{v}$, $\boldsymbol{M}$ et $\boldsymbol{P}$ sont des nombres réels, et non des opérateurs. Pour comparer avec le résultat de la mécanique quantique,[24] nous définissons l'opérateur de vitesse comme,

$$\hat{\boldsymbol{v}} = \frac{(\hat{\boldsymbol{p}} - q\boldsymbol{A})}{m}, \tag{21}$$

et l'opérateur de densité d'aimantation comme,

$$\hat{\boldsymbol{M}}_{\text{spin}} = \frac{q\hbar}{2m}\boldsymbol{\sigma}. \tag{22}$$

Par conséquent, nous pouvons definir l'opérateur de densité de polarisation électrique dans le système référentiel de laboratoire,

$$\begin{aligned}\hat{\boldsymbol{P}}_{\text{spin}} &= \frac{\hat{\boldsymbol{v}}\times\hat{\boldsymbol{M}}_{\text{spin}}}{c^2} \\ &= -\frac{q\hbar}{2m^2c^2}\left(q\boldsymbol{A}\times\boldsymbol{\sigma} - \frac{1}{2}\hat{\boldsymbol{p}}\times\boldsymbol{\sigma} + \frac{1}{2}\boldsymbol{\sigma}\times\hat{\boldsymbol{p}}\right).\end{aligned} \tag{23}$$

Multipliant à droite par $\Psi$ et à gauche par $\Psi^\dagger$ nous obtenons:

$$\Psi^\dagger\hat{\boldsymbol{P}}_{\text{spin}}\Psi = -\frac{q\hbar}{2mc^2}\left[\frac{q}{m}\boldsymbol{A}\times(\Psi^\dagger\boldsymbol{\sigma}\Psi) - \frac{i\hbar}{2m}\left\{(\boldsymbol{\nabla}\Psi^\dagger)\times\boldsymbol{\sigma}\Psi + \Psi^\dagger\boldsymbol{\sigma}\times(\boldsymbol{\nabla}\Psi)\right\}\right], \tag{24}$$

qui est identique à $\boldsymbol{P}_{\text{spin}}$ obtenu précédemment, sauf pour un facteur de 2. Ce facteur a la même origine que la correction de Thomas, bien connue dans l'hamiltonien spin-orbite.

Nos résultats sont en très bon accord avec ceux de Y. Hinschberger obtenus en utilisant l'approche hamiltonienne en jauge de Coulomb. Nos résultats sont par conséquent universels et indépendants de la jauge utilisée. Ensuite, nous avons vérifié ces sources avec 3 formes de l'équation de continuité obtenues à partir d'un) l'hamiltonien, b) les équations de Maxwell et c) le théorème de Noether. Les trois équations étaient identiques donnée par,

$$i\hbar\partial_t(\Psi^\dagger\Psi) = -\frac{1}{2m}\left[(\hat{\boldsymbol{p}}^2\Psi^\dagger)\Psi - \Psi^\dagger(\hat{\boldsymbol{p}}^2\Psi)\right] - \frac{\hat{\boldsymbol{p}}}{m}\cdot(q\boldsymbol{A}\Psi^\dagger\Psi) + \frac{q\hbar}{4m^2c^2}\hat{\boldsymbol{p}}\cdot\left[\boldsymbol{E}\times(\Psi^\dagger\boldsymbol{\sigma}\Psi)\right], \tag{25}$$

et seules les sources non liées apparaissent dans cette équation. Le fait que les lois de conservation obtenus à partir de l'hamiltonien semi-relativiste et le théorème de Noether coïncident avec la conservation de la charge implicite dans les équations de Maxwell avec des sources de second ordre, est une caractéristique intéressante de notre modèle et renforce notre confiance dans la validité du modèle.

Vers la fin du chapitre (section 2.6), nous avons également étendu les équations de Maxwell et nous avons suggéré trois versions différentes du modèle, qui peuvent être utilisées en fonction des propriétés des sources nécessaires, y compris la possibilité d'inclure des champs électromagnétiques externes dépendant du temps.

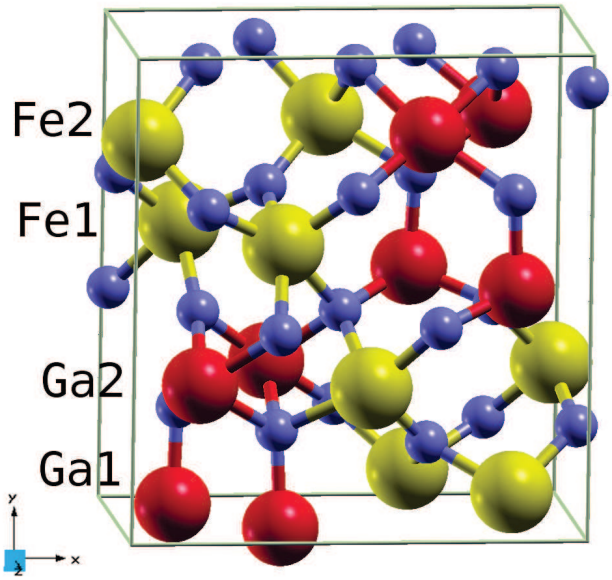


**Figure 1:** Structure cristalline de GFO.

Dans le chapitre 4, nous avons effectué des calculs *ab initio*, utilisant le code VASP (*Vienna Ab initio Simulation Package*),[85,86] pour comprendre la structure électronique des systèmes multiferroïques, tels que $GaFeO_3$ (GFO). Les matériaux multiferroïques sont des systèmes où deux ou plusieurs paramètres d'ordre ferroïques (ferromagnétisme, ferroélectricité, etc.) sont couplés. Le GFO a été découvert dans les années 1960 et possède des propriétés ferrimagnétique et ferroélectrique.[71,72,77]

Il a été largement étudié, aussi bien expérimentalement[71–79,84] que théoriquement,[80–83,88] mais une compréhension totale du couplage entre les ordres magnétique et électrique fait encore défaut. Ce matériau contient deux sites de fer (Fe1 et Fe2) et deux sites de gallium (Ga1 et Ga2). Les sites de Fe1, Fe2 et Ga2 forment avec les atomes d'oxyène qui les entourent, des octaèdres déformés, tandis que le site du Ga1 forme un tétraèdre déformé (voir figure 1).

Pour étudier ce système, nous avons utilisé la méthode des ondes planes augmentées par projection (PAW), implémentée dans le code VASP.[66,87] Pour inclure le terme d'échange et de corrélation électronique nous avons utilisé l'approximation de la densité locale (LDA)[54] ou l'approximation du gradient généralisé (GGA)[57,58] et, afin de mieux décrire les électrons corrélés 3*d* du Fe,[59–61] nous avons rajouté un terme de Hubbard à l'hamiltonien.[62] Pour confirmer les résultats précédents et obtenir les paramètres de notre modèle, nous avons fixé le terme d'échange J = 0,9 eV et calculé l'énergie de bande interdite et les moments magnétiques pour les deux valeurs de l'interaction de Hubbard $U$ = 4 eV et 8 eV). Cela nous a permis de confirmer les résultats expérimentaux de Arima *et al.*,[78] et les résultats théoriques de Ibrahim et Alouani.[88]

**Table 1:** Bande interdite, moments de spin et d'orbite de GFO calculés en LDA+U et GGA+U, comparés aux valeurs expérimentales

| | Exp. | LDA | | GGA | |
|---|---|---|---|---|---|
| | | $U = 4$ eV | $U = 8$ eV | $U = 4$ eV | $U = 8$ eV |
| Bande interdite (eV) | 3.2[96] | 1.5 | 3.0 | 2.0 | 3.2 |
| Moment magnétique de spin Fe1 ($\mu_B$) | -3.9[78] | -4.02 | -4.41 | -4.10 | -4.44 |
| Moment magnétique de spin Fe2 ($\mu_B$) | 4.5[78] | 4.02 | 4.41 | 4.10 | 4.44 |
| Moment magnétique d'orbite ($\mu_B$) | - | ±0.027 | ±0.020 | ±0.022 | ±0.017 |

Pour GGA+U (U = 8 eV), nous avons obtenu un très bon accord avec l'expérience pour les valeurs de la bande interdite et du moment magnétique de spin Fe2 (voir tableau 1). La valeur du moment magnétique de spin Fe1 n'est pas en accord avec l'expérience et le désaccord est expliqué avec les désordres de sites cationiques Ga and Fe.
Pour expliquer le ferrimagnétisme observé expérimentalement dans GFO, nous avons effectué des études de désordre du Fe1 et du Fe2 en se basant sur les observations expérimentales de Hatneal *et al.*[84] Nous avons utilisé la structure cristalline pour GFO avec les désordres des sites comme indiqué dans la figure 2. Un modèle simple a également été créé, où l'aimantation d'un site individuel peut être calculée en multipliant l'occupation du site par le moment magnétique de l'ion de Fe correspondant. Le tableau 2 montre les résultats des deux méthodes ainsi que les résultats expérimentaux.

**Table 2:** Résultats *ab initio* de l'aimantation par site, comparés avec l'expérience et ceux obtenus par le modèle.

| Site | Exp.[84] | *Ab initio* | Modèle simple |
|---|---|---|---|
| Fe1 | -4.0 | -3.335 | -3.375 |
| Fe2 | 3.5 | 3.346 | 3.375 |
| Ga1 | 0.0 | 0.00 | 0.0 |
| Ga2 | 2.7 | 2.243 | 2.250 |

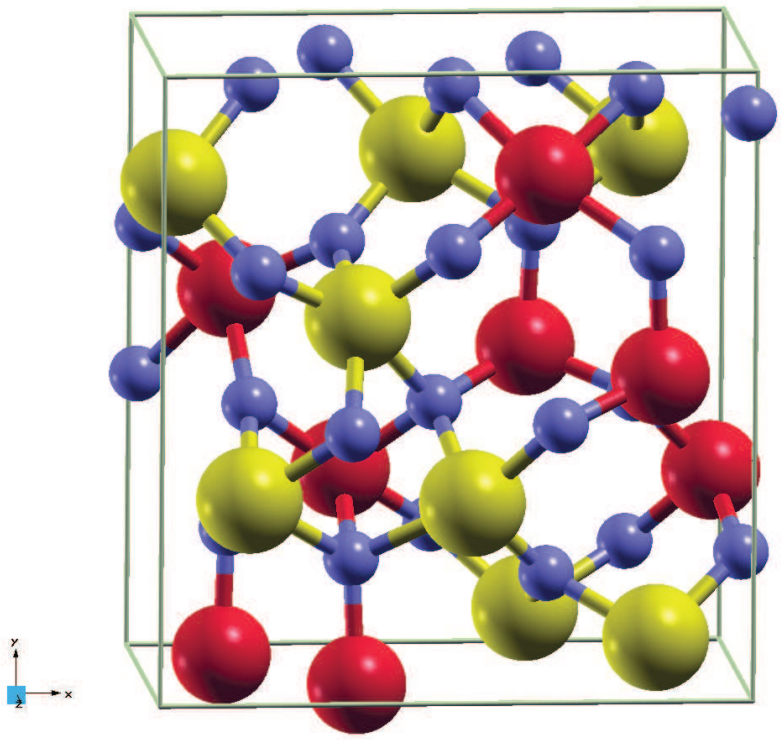

**Figure 2:** La structure cristalline de GFO avec les désordres des sites cationiques.

Nous observons un désaccord de $-0.665$ et $0.457$ $\mu_B$ pour les moments magnétiques sur les sites Fe1 et Ga2. Cependant, le moment magnétique sur le site Fe2 et l'aimantation du système sont en bon accord avec l'expérience. Par ailleurs, les résultats du calcul simple, décrit précédemment, sont en très bon accord avec les résultats *ab initio*.
Lorsque nous comparons les énergies de l'état fondamental pour la structure idéale (voir figure 1) et la structure désordonnée (voir figure 2), nous obtenons une différence de 231 meV (environ $\sim$ 2700 K), qui est inférieure à la somme des valeurs respectives de 25 meV et 400 meV pour les Fe2-Ga2 et Fe1-Ga2 prédites par Roy *et al.*[99]

En se basant sur des valeurs moyennes expérimentales de 2.7 $\mu_B$ du fer sur le site de Ga2, avec une occupaton de 50%, on obtient un moment magnétique par atome de Fe de 5.4 $\mu_B$. Un moment suréstimé, car le moment magnétique maximum que le Fe peut posséder est de 5.0 $\mu_B$. Le même est vrai pour la valeur moyenne de -4.0 $\mu_B$ rapportée pour le site Fe1, qui correspond à un moment individuel de -5.33 $\mu_B$, en se basant sur une occupation de fer de 75%. Le moment magnétique obtenu est d'environ 10 $\mu_B$ par cellule unitaire, et par conséquent, nous concluons que l'origine du ferrimagnétisme dans GFO est due au désordre des sites cationiques.

Afin d'améliorer notre compréhension des électrons $3d$ dans le GFO, nous avons effectué une analyse du champ cristallin sur les sites octaédriques. A l'état d'ion libre, l'élément de fer présente cinq orbtiales $3d$ dégénérées, mais en environement octaédrique, on observe une levée de dégénérescence des états $e_g$ (doublement dégénérés) de plus haute énergie, et $t_{2g}$ (triplement dégénérés) de plus basse énergie. Dans le cas d'un environement tétraédrique, on obtient une séparation énergétique inverse.

Ces séparations sont présentées dans la figure 3.

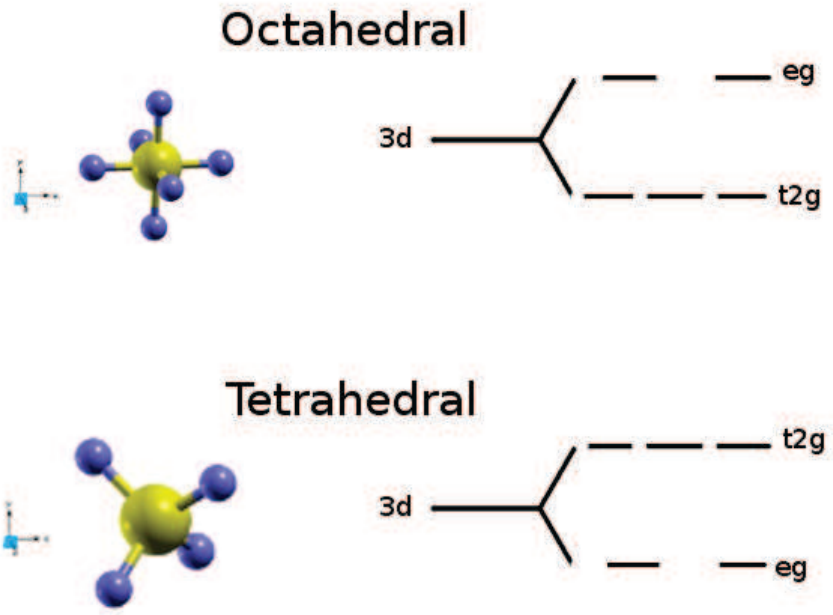


**Figure 3:** Séparation des orbitales 3d dans les environnements octaédriques et tétraédriques.

Deux détails importants doivent être soulignés ici. D'une part, les orbitales $e_g$ et $t_{2g}$ sont décrites en utilisant les harmoniques sphériques réelles, et d'autre part, celles-ci sont définies par leur nombre quantique $m$, soit la valeur propre de l'opérateur $\hat{L}_z$, qui dépend du système de coordonnées. Le deuxième point est visualisé dans la figure 3, avec l'aide d'un référentiel. Si le système de coordonnées n'est pas comme représenté sur la figure, alors les orbitales $d$ obtenues seraient une superposition des orbitales $3d$ et la séparation ne peut pas être clairement définie comme étant celle des $e_g$ et $t_{2g}$. Pour obtenir les vecteurs propres $e_g$ et $t_{2g}$, un référentiel est défini en tournant les harmoniques sphériques pour aligner les anions appropriés suivant les axes. Nous avons donc une matrice de rotation pour les vraies harmoniques sphériques analogues à la matrice de rotation du système de coordonnées cartésiennes. Nous avons implémenté le changement de référentiel par rotation directe des harmoniques sphériques réelles dans le code VASP. Les détails sont fournis dans la section 4.6.1.

Nous avons effectué une rotation locale et la projection des orbitales atomiques sur le site de l'octaèdre pour déterminer leur séparation en énergie. En raison de la forte distorsion de l'octaèdre, pour les états occupés, le calcul montre que la levée de dégénérescence devient alors similaire à celle d'un environnement tétraédrique, comme indiqué dans la figure 4. Cette séparation persiste pour les états occupés sur tous les sites octaédriques, et elle n'est pas influencée par l'inclusion de SOC.

Nous avons par conséquent développé un modèle dit de charges électriques ponctuelles, afin d'analyser et de comprendre le champ cristallin dans un octaèdre très déformé. Nous avons réécrit le potentiel de Coulomb dû aux six atomes d'oxygène les plus proches du centre de l'octaèdre en termes

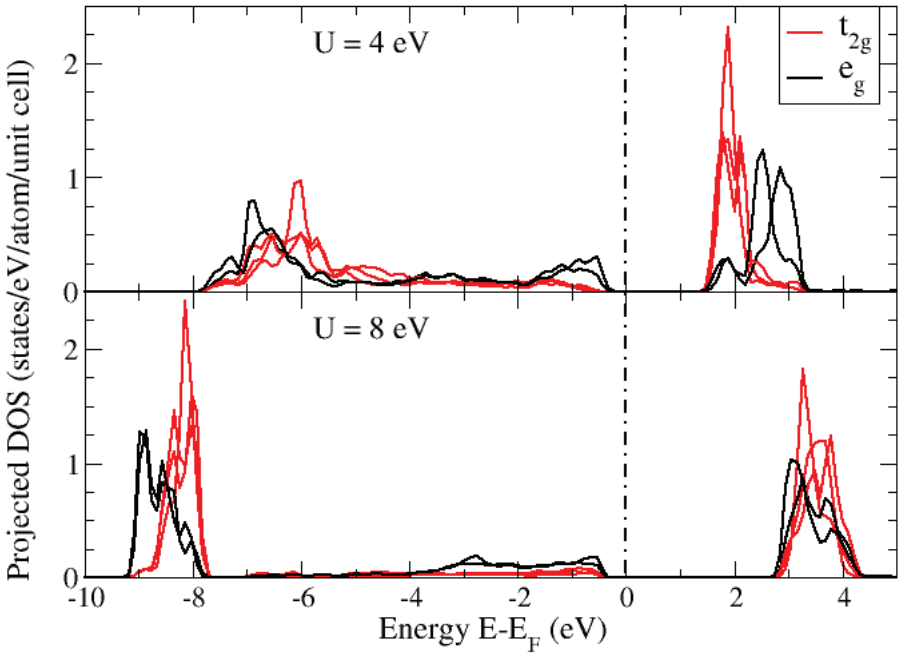


**Figure 4:** Densité d'états décomposée en états $e_g$ et $t_{2g}$ du site de Fe2 octaédrique.

d'harmoniques sphériques:

$$V(\boldsymbol{r}) = \sum_{i=1}^{6} \frac{q_i}{|\boldsymbol{r} - \boldsymbol{R}_i|} = \sum_{i=1}^{6} \sum_{\ell=0}^{\infty} \sum_{m=-\ell}^{\ell} (-1)^m \frac{4\pi q_i}{2\ell+1} \mathcal{Y}_\ell^{-m}(\boldsymbol{r})\, \mathcal{Y}_\ell^m(\boldsymbol{R}_i)\, \frac{R_i^\ell}{r^{\ell+1}}, \tag{26}$$

où $q_i$ est la charge formelle sur l'atome i des ligands qui forment l'octaèdre, qui vaut $-2e$ par ion d'oxygène dans GFO, les $\mathrm{Y}_\ell^m$ sont les harmoniques sphériques, et $\boldsymbol{R}_i$ est le vecteur qui donne la distance de l'atome central au ligand $i$. En utilisant l'expression ci-dessus, nous pouvons calculer les éléments de matrice $M_{m,m''}$ des orbitales $3d$:

$$M_{m,m''} = \int \sum_{i=1}^{6} \sum_{\ell,m'} (-1)^{m+m'} \frac{5 q_i R_i^\ell}{r^{\ell+1}} \sqrt{\frac{4\pi}{2\ell+1}} |r\phi|^2 \begin{pmatrix} 2 & 2 & \ell \\ 0 & 0 & 0 \end{pmatrix} \begin{pmatrix} 2 & 2 & \ell \\ m'' & -m & -m' \end{pmatrix} \mathrm{d}r, \tag{27}$$

où $\begin{pmatrix} j_1 & j_2 & j_3 \\ m_1 & m_2 & m_3 \end{pmatrix}$ sont les symboles 3-$j$ de Wigner exprimés en termes de coefficients Clebsch-Gordon comme,

$$\begin{pmatrix} j_1 & j_2 & j_3 \\ m_1 & m_2 & m_3 \end{pmatrix} = \frac{(-1)^{j_1 - j_2 - m_3}}{\sqrt{2j_3+1}} \langle j_3, -m_3 | j_1, m_1; j_2, m_2 \rangle. \tag{28}$$

Ils sont non nuls si les conditions suivantes sont satisfaites:

$$m_1 + m_2 + m_3 = 0, \tag{29}$$

$$j_1 + j_2 + j_3 \quad \text{est un nombre entier, et pair si } m_1 = m_2 = m_3 = 0, \tag{30}$$

$$|m_i| \leq j_i. \tag{31}$$

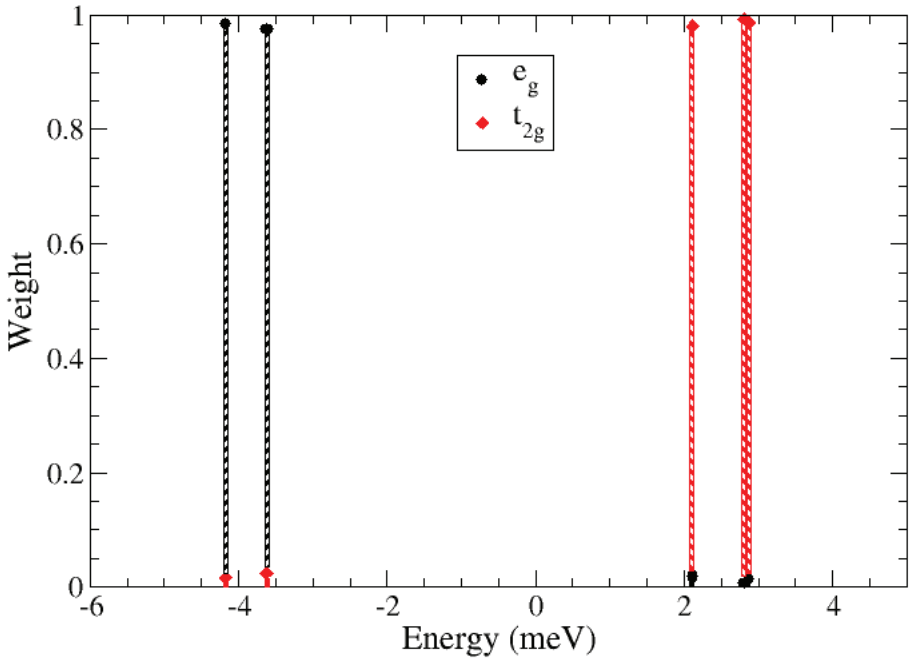


**Figure 5:** Les niveaux d'énergies obtenus par notre modèle.

Nous avons ensuite calculé les éléments de matrice de l'hamiltonien pour les électrons 3*d* puis nous avons diagonalisé cet hamiltonien pour déterminer les vecteurs et les valeurs propres. Pour les sites de Fe, nous constatons une séparation énergétique similaire à celle obtenue par le calcul *ab initio* (voir figure 5). Nous avons conclu que la déformation provoque un environement de type tétraédrique avec des charges asymétriques.

Dans le but de comprendre le couplage entre les ordres ferroïques (magnétique et électrique), nous avons effectué des calculs *ab initio* pour la polarisation électrique pour différentes directions de l'aimantation. Un bref aperçu de la théorie moderne de la polarisation est fourni dans l'annexe D. Pour simuler un effet de la température, on suppose une interpolation linéaire des positions atomiques et les paramètres de maille entre 4 K et 230 K. Ces valeurs des positions atomiques à 4 K et à 230 K ont été mesurées avec la diffractométrie de neutrons par Arima *et al.*[78] Il y a très peu de changement dans les positions atomiques et les vecteurs de maille. Le changement de volume, par exemple, est inférieur à 0.2 %, ce qui justifie l'approximation linéaire entre ces deux températures.

Les valeurs absolues de la polarisation électrique pour le système idéal en fonction de la température sont présentées dans la figure 6. Le vecteur de polarisation est aligné le long de l'axe $y$ négatif, avec une amplitude d'environ 23.5 $\mu$C/cm$^2$, proche de la valeur de 25 $\mu$C/cm$^2$ calculée par Stoeffler.[83] On voit que lorsque la température augmente, l'amplitude de la polarisation diminue, car l'augmentation de la température entraîne une augmentation des distances inter-atomiques, ce qui provoque une

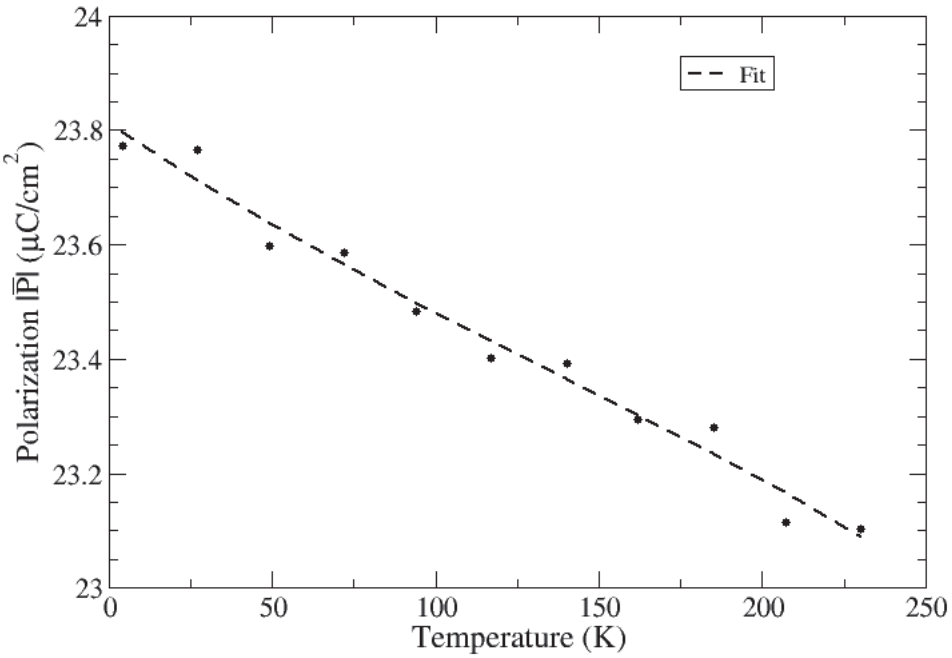


**Figure 6:** Polarisation électrique dans GFO en fonction de la température.

diminution de l'hybridation. Puisque la polarisation est une mesure de la distance entre les charges, une localisation des électrons à proximité des ions implique une diminution de l'amplitude de la polarisation électrique.

Les polarisations électriques obtenues sont en bon accord avec les études théoriques antérieures.[83] Des études expérimentales récentes ont été effectuées sur $Ga_{2-x}Fe_xO_3$ pour $x = 1,1$, indiquant des valeurs de polarisation autour de 33 $\mu C/cm^2$, proches de nos valeurs. Ces confirmations théoriques et expérimentales nous encouragent à étudier les effets magnétoélectriques dans GFO.

Il existe deux types d'effets magnétoélectriques, direct et indirect. L'effet magnétoélectrique direct provient du SOC, qui couple le spin et la structure cristalline. Quand un champ magnétique externe est appliqué, les électrons se déplacent ce qui provoque un changement de la polarisation électrique. Cet effet ne nécessite pas le changement des positions ioniques et est une conséquence directe du champ magnétique externe, d'où l'appelation de terme direct. D'autre part, l'effet magnétoélectrique peut être une conséquence indirecte de champ magnétique externe par un déplacement des ions qui modifie le volume de la maille élémentaire. Cet effet est souvent appelé effet magnétoélectrique magnétostrictif. Sur la base des expériences réalisées dans les années 1960, il a été émis l'hypothèse que les effets magnétoélectrique observés sont dus au mécanisme indirect dans GFO.[75] Cependant, dans les années 1990, Popov *et al.* ont indiqué que le mécanisme direct est responsable des effets magnétoélectriques observés dans GFO.[105]
On commence par faire tourner l'axe de magnétisation dans le plan $y$-$z$, à partir de l'axe $z$ positif (la configuration originale), à l'axe $z$ négatif par l'axe $y$ positif. Pour vérifier si le mécanisme direct est responsable des effets observés magnétoélectriques, les calculs ont été effectués en gardant les

ions fixes. En conséquence, toute variation de la polarisation électrique est due à la variation de la polarisation électronique.

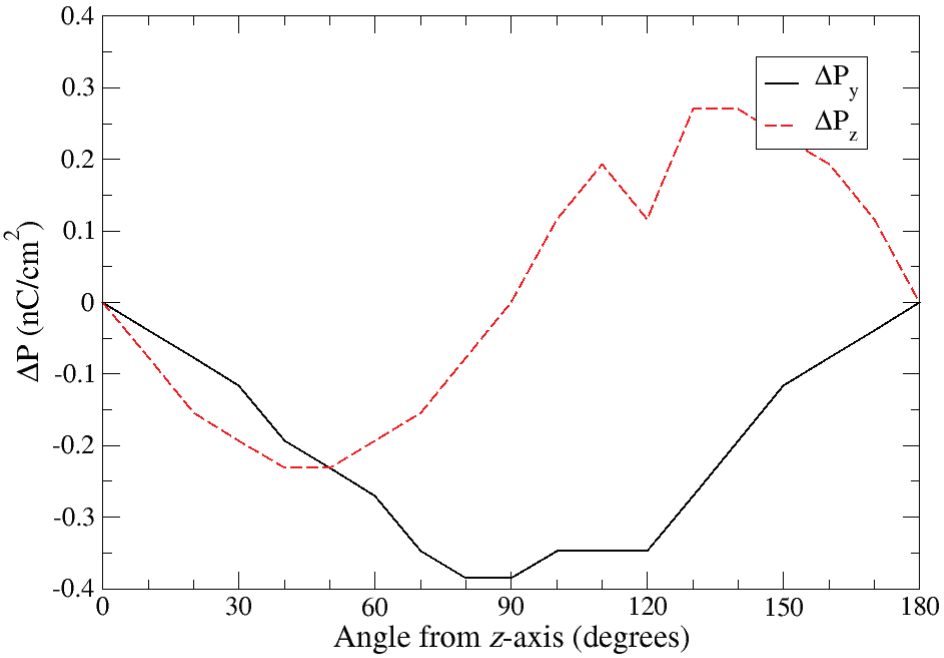


**Figure 7:** Modification des polarisations électriques le long des axes $y$ et -$z$ dans GFO en fonction de la rotation de l'axe d'aimantation.

La figure 7 montre la variation de la polarisation électrique le long des axes $y$ et $z$ dans GFO. Alors qu'une tendance claire existe dans les deux courbes, le changement est inférieur à 0.4 nC/cm$^2$, cinq ordres de grandeur inférieurs à la polarisation électrique spontanée déterminée précédemment (23.5 $\mu$C/cm$^2$). En outre, il est très difficile de mesurer ces petites valeurs. On peut conclure que le mécanisme directe est loin d'être suffisant pour expliquer les effets magnétoélectriques dans GFO. Le mécanisme indirect peut être la principale cause des effets observés. Cette hypothèse est étayée par les calculs de la dépendance de température, où le changement de volume de l'ordre de 0.2 % provoque un changement de la polarisation électrique d'environ 0.6 $\mu$C/cm$^2$ ou 2.5 %.

Nous avons également effectué des simulations sur $Cr_2O_3$, pour lesquelles nous avons utilisé des techniques similaires pour déterminer l'origine du ferromagnétisme dans un système antiferromagnétique, en appliquant de fortes compressions biaxiales sur la cellule unitaire. La première prédiction théorique de l'existence de l'effet magnétoélectrique a été fournie par Dzyaloshinskii en 1959 pour $Cr_2O_3$,[69] et a été suivie par une observation expérimentale en 1961 par Astrov.[70] Depuis, de nombreuses études ont été réalisées sur ce système.[106,107]

Des expériences récentes par Halley *et al.* sur les nanoclusters de $Cr_2O_3$ dans MgO ont donné des résultats intéressants, et ont le potentiel d'être utilisées dans de nouveaux dispositifs électroniques.

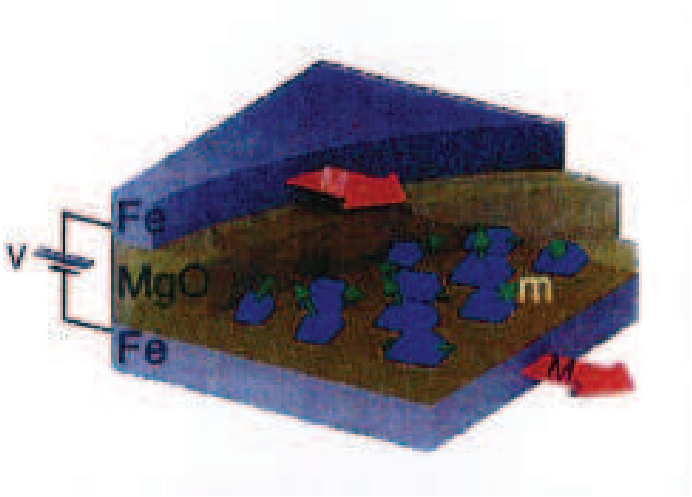


**Figure 8:** Schéma expérimental[108] de nanoclusters $Cr_2O_3$ incorporé dans MgO entre deux électrodes ferromagnétiques de Fe. Reproduit avec la permission de Macmillan Publishers Ltd: Nature Communications, 2014

La figure 8 représente le schéma expérimental, où on a observé un effet magnétoélectrique induit par la taille des nanoclusters de $Cr_2O_3$ (observation d'une aimantation et d'une polarisation électrique spontanées). Ces résultats ne sont pas observés pour un cristal massif sans compression. Les origines du ferromagnétisme et de la polarisation sont supposées par conséquent provenir des systèmes $Cr_2O_3$ très compressés, plutôt que de l'interface MgO-$Cr_2O_3$.

Les calculs *ab initio* ont été effectués en utilisant le code VASP[85,86] et l'approche GGA+$U$.[57,58,110] Quatre valeurs de $U$ ont été étudiées (3, 4, 6 et 8 eV). Il y a quatre atomes de Cr alignés par maille unitaire, et par conséquent quatre configurations magnétiques sont possibles. On les désigne comme AFM1 (+, -, +, -), AFM2 (+, -, -, +), AFM3 (+, +, -, -) et FM (+, +, +, +), où les signes +/- indiquent l'orientation magnétique le long de l'axe $z$. La bande d'énergies interdites du système est montrée dans le tableau 3.

**Table 3:** La bande interdite (eV) de $Cr_2O_3$ en fonction de $U$. La valeur expérimentale est 3.4 eV[107]

| $U$ | AFM1 $+-+-$ | AFM2 $+--+$ | AFM3 $++--$ | FM $++++$ |
|---|---|---|---|---|
| 3 | 1.8 | 1.7 | 1.7 | 2.2 |
| 4 | 2.4 | 2.4 | 2.4 | 2.4 |
| 6 | 3.0 | 3.2 | 3.3 | 2.7 |
| 8 | 3.5 | 3.6 | 3.6 | 3.1 |

Comme on le voit dans le cas de GFO, la bande interdite augmente avec U en raison de l'abaissement de l'hybridation qui provoque la localisation des orbitales 3d. Nous constatons que la valeur $U = 8$ eV reproduit la valeur expérimentale 3.4 eV.[107] Il faut noter que le moment magnétique total pour la configuration de l'état fondamental de $Cr_2O_3$ est nul, ce qui correspond à un état antiferromagnétique. Dans l'intention de déterminer l'origine du ferromagnétisme dans ce système, nous avons effectué des calculs de la structure électronique pour des compressions biaxiales. En se basant sur les valeurs

expérimentales, la maille unitaire a été comprimée par 0 %, 3 %, 4 %, 5 % et 6 % le long de l'axe $z$, et par 0 %, 5 %, 10 % et 15 % dans le plan $x$-$y$. Ces calculs ont été initialement faits sans SOC. Comme ces calculs montrent une aimantation totale nulle, nous les avons refaits avec SOC. Ce qui permet de coupler le spin au réseau, et eventuellement de générer des moments magnétiques noncollinéaires. Le graphe de l'aimantation totale pour différentes compressions est montré dans la figure 9.

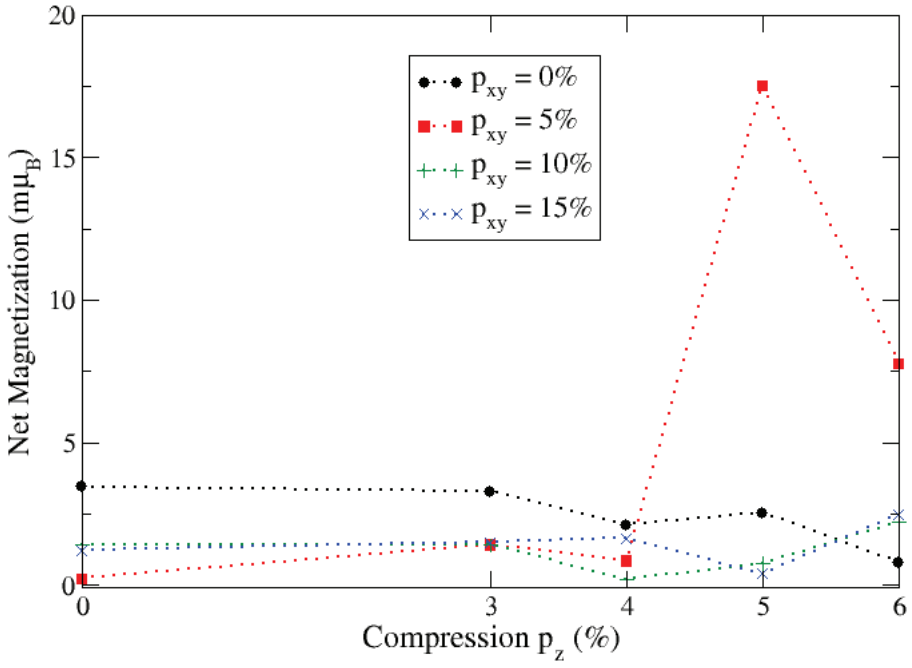


**Figure 9:** Aimantation (SOC inclus) en fonction de la contrainte de compression le long de l'axe $z$. Les différentes courbes correspondent à des contraintes de compression de 0 % (cercles noirs), 5 % (carrés rouges), 10 % (points positifs verts) et 15 % (croix bleues) le long de l'axe $x$.

Il n'y a pas de corrélation entre les composantes $y$ des moments magnétiques individuels, car ils sont trop faibles. D'autre part, les composantes $x$ présentent une configuration AFM2 le long de l'axe -$x$. Ces composants $x$ augmentent également avec la contrainte de compression.

La figure 10 montre les moments de spin moyens et les moments magnétiques d'orbites pour le Cr en fonction des contraintes de compression. Bien que la composante $z$ se comporte d'une manière similaire au cas sans SOC, il n'y a pas corrélation entre les autres composantes. Puisque Cr a une couche $3d$ moins que demi-remplie, les moments d'orbites sont anti-parallèles aux moments de spin. On observe une augmentation de la composante $x$ du moment de spin pour une contrainte de compression de l'ordre de 3-5 % le long de l'axe $z$. La valeur maximale est d'environ 10 m$\mu_B$ par atome de Cr, comparée à une valeur expérimentale de 80 m$\mu_B$ par atome Cr.[108] De plus, si la cause d'une aimantation est le ferrimagnétisme par opposition au ferromagnétisme, le moment physique réel par atome de Cr peut être plus élevé. En général, nos calculs des moments individuels par atome de Cr sont sous estimés par rapport aux valeurs expérimentales par un facteur d'environ 40.

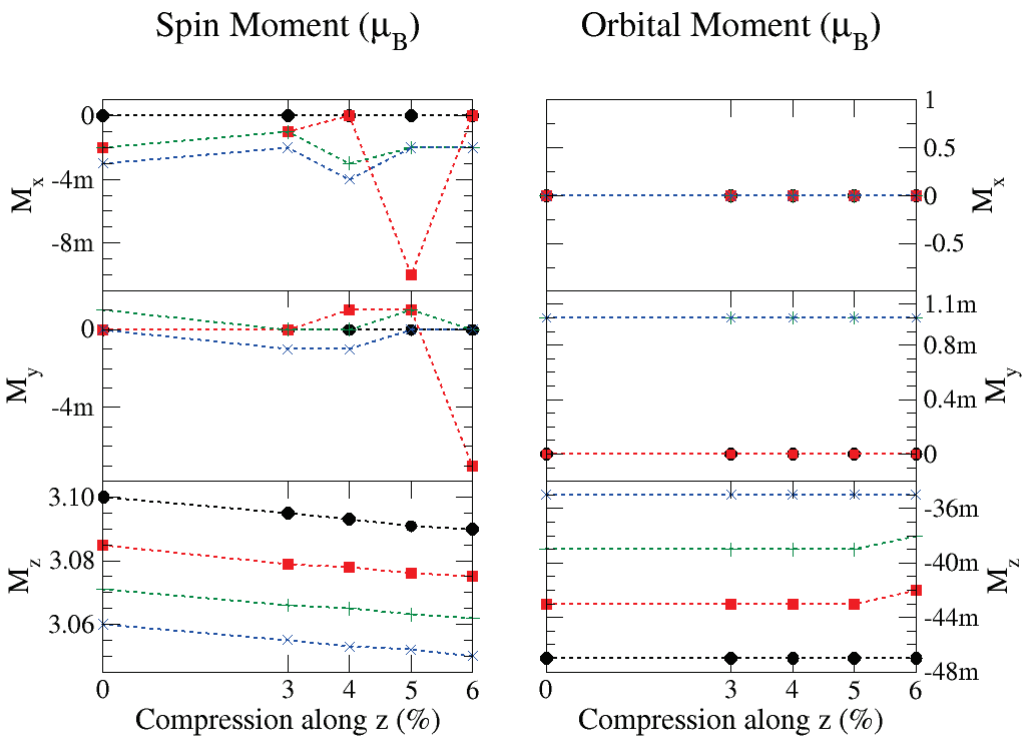


**Figure 10:** Les composants $x$ (haut), $y$ (milieu) et $z$ (bas) des moments de spin (gauche) et de orbitale (droit) de Cr en fonction de compressions le long de l'axe $z$. Les différentes courbes correspondent à des contraintes de compression de 0 % (cercles noirs), 5 % (carrés rouges), 10 % (points positifs verts) et 15 % (croix bleues) le long de l'axe $x$.

L'incapacité de reproduire l'observation expérimentale peut être attribuée au fait que nous avons négligé la taille des nanoclusters, l'excès d'oxygène, ou à l'interface MgO-$Cr_2O_3$. D'autres études seraient nécessaires pour vérifier chacune de ces hypothèses.

Pour expliquer les résultats spectroscopiques, nous avons implémenté le calcul des spectres d'absorption des rayons X (XAS) pour différentes polarisations de la lumière. Cette implémentation a été réalisée en utilisant l'approximation dipolaire électrique. Le XAS dépend fortement du couplage spin-orbite des électrons des états profonds. La différence entre les spectres polarisés circulairement à gauche et circulaire à droite est appelée dichroïsme circulaire magnétique de rayons X (XMCD). Les rayons X excitent les électrons des états profonds et provoquent des transitions vers les états de conduction. les excitations électroniques sont par conséquent très spécifiques au type d'atome. Les méthodes XAS et XMCD ont été intensivement utilisées, à la fois théoriquement et expérimentalement,[111–118] pour étudier les matériaux magnétiques. Le XMCD fournit également des informations sur le moment magnétique de spin et le moment d'orbite des états de conduction de chaque atome magnétique à l'aide des règles de sommes.[119,120] Le spectre d'absorption $\sigma^\mu$ pour une polarisation $\mu$ dans le PAW, est donné par:

$$\sigma^{\mu}(\omega) = \frac{4\pi\alpha\hbar^3}{m^2\omega} \sum_{M,n,\boldsymbol{k},s} \left| \sum_{p,\ell,m,m'} C^{J,M}_{\ell',m';1/2,s} \frac{C^{\ell',m'}_{1,\mu;\ell,m}}{C^{\ell',0}_{1,0;\ell,0}} \langle \ell', 0 | \nabla_0 | p, \ell, 0 \rangle \, \overline{P}^{n,\boldsymbol{k},s}_{p,\ell,m} \right|^2 \delta(\hbar\omega - \epsilon_{n\boldsymbol{k}s} + \epsilon_{JM}), \qquad (32)$$

où, $m$, dans le premier facteur, est la masse de l'électron, $\omega$ la fréquence de la lumière incidente, $\hbar$ la constante réduite de Planck, $\alpha$ la constante de structure fine, $\ell$ le nombre quantique secondaire, $m$ le nombre quantiques magnétique, $p$ le type de projecteur et $\epsilon_i$ l'énergie de l'état $i$. Cette équation est exprimée en représentation impulsion $\hat{\boldsymbol{p}}$. Pour vérifier le calcul, nous avons également implémenté le XAS et XMCD dans la représentation position (voir annexe E). Plusieurs détails sur notre implémentation sont fournis dans la section 6.3

Nos résultats préliminaires, pour le seuil K et les seuils $L_{2,3}$ du fer massif de structure cubique centrée, sont en bon accord avec l'expérience (voir figures 11 et 12).

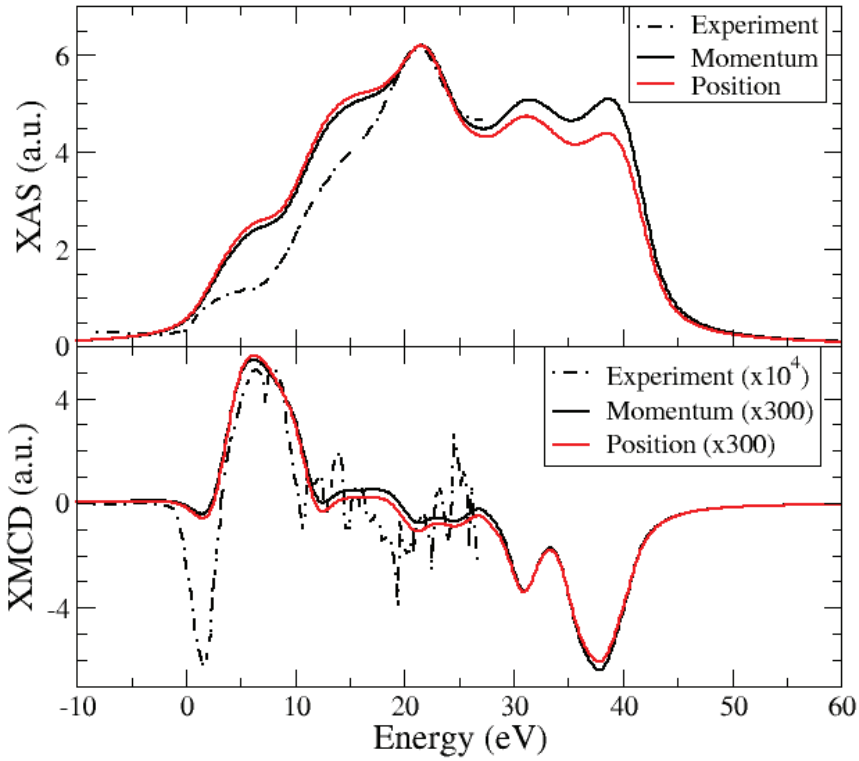


**Figure 11:** XAS et XMCD au seuil-K du fer massif, calculés en répresentations impulsion (noir) et position (rouge), comparés aux spectres expérimentaux (pointillés mixtes).

Nous avons également calculé les moments magnétiques de spin et d'orbite en ustilisant les règles de sommes (équations 6.8 et 6.9), comme indiqué dans le tableau 4.

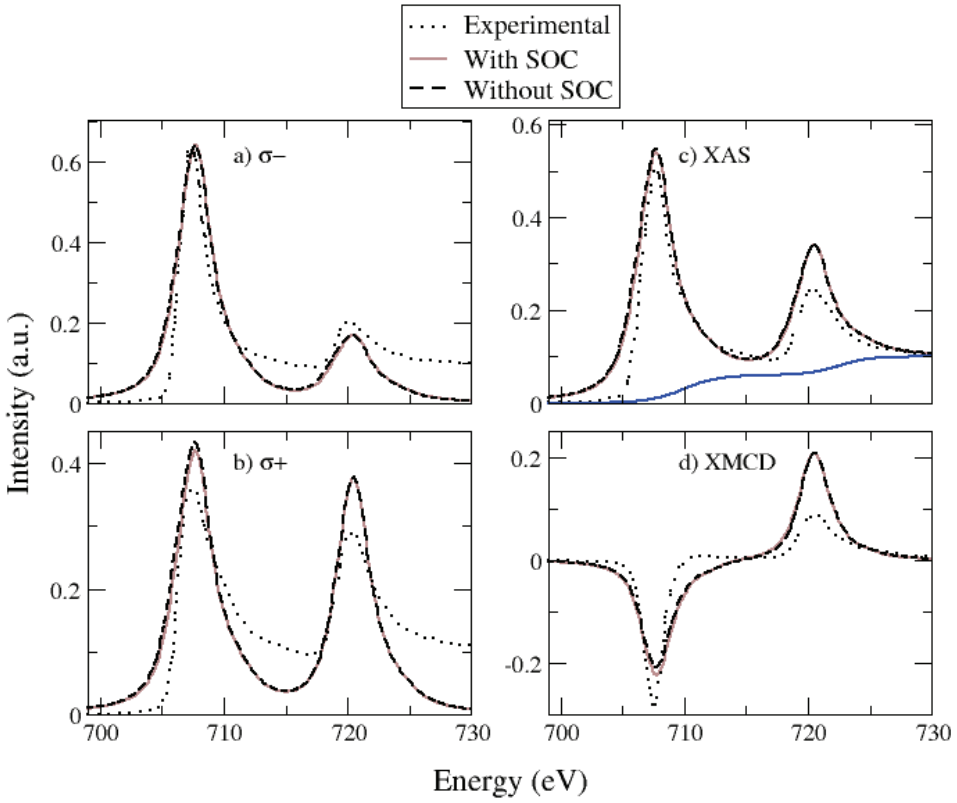


**Figure 12:** XAS et XMCD aux seuils $L_{2,3}$ du fer bcc massif, calculés en répresentations impulsion, sans (courbe noir pointillée) et avec SOC (courbe marron), comparés à l'expérience (courbe pointillée).[129] () et (b) representent les spectres avec une polarisation circulaire à droite et à gauche, respectivement, (c) et (d) representent les spectres XAS et XMCD, respectivement. La courbe bleue en (c) resprésente la fonction double saut pour rajouter la contribution de fond.

**Table 4:** Comparaison des moments magnétiques de spin et d'orbite (en $\mu_B$) obtenus des spectres théoriques (avec SOC) et les spectres expérimentaux.[129] Les valeurs entre parenthèses indiquent les valeurs obtenues des règles de sommes à partir des spectres théoriques sans SOC

| | Théorique | Expérimentale[129] |
|---|---|---|
| $m_{spin} = \langle S_z \rangle$ | 2.179 (2.034) | 1.980 |
| $m_{orb} = \langle L_z \rangle$ | 0.030 (0.000) | 0.085 |
| $\frac{m_{orb}}{m_{spin}} = \frac{\langle L_z \rangle}{\langle S_z \rangle}$ | 0.014 (0.000) | 0.043 |

Puisque le code reproduit les spectres expérimentaux pour Fe avec succès, nous avons calculé les spectres aux seuils-$L_{2,3}$ pour le Fe dans GFO. Les spectres ont été mesurés par Kim *et al.*[79] Les occupations des sites rapportés étaient Fe@Fe1: 82.5 %, Fe@Fe2: 82.5 % et Fe@Ga2: 35 %. Basé sur nos résultats pour les études des désordres de site, nous supposons que les structures électroniques de Fe sur les sites Fe2 et Ga2 sont identiques. Ensuite nous avons calculé les spectres pour les sites Fe1 et Fe2, et multiplié les spectres individuels par les occupations des sites avant de les additionner.

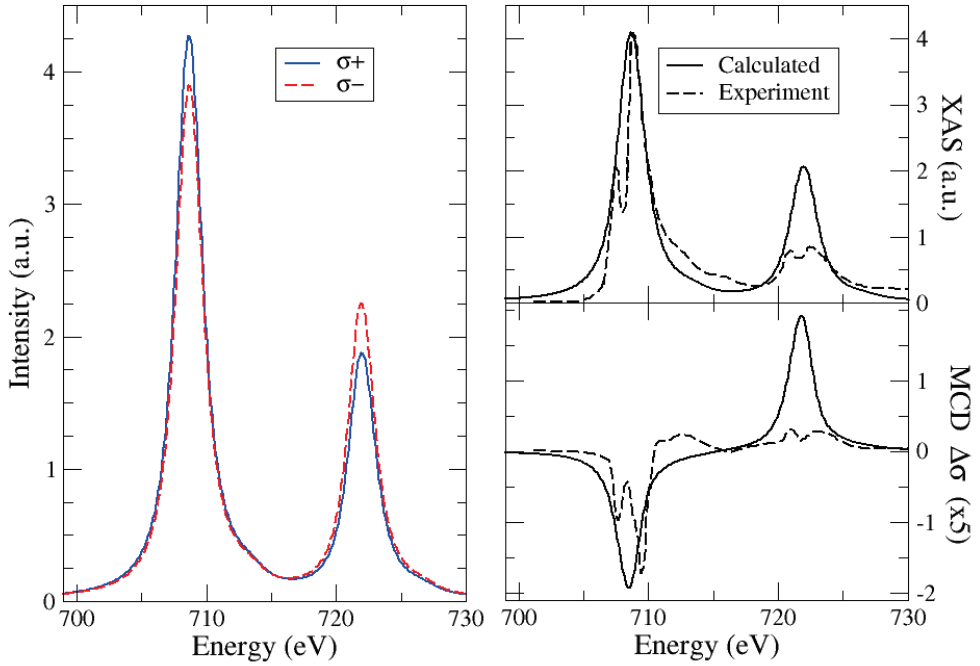


**Figure 13:** Les seuils $L_{2,3}$ de Fe dans GFO.

Les résultats de calcul sont fournis dans la figure 13. Nous voyons que les pics expérimentaux sont répartis, à savoir qu'ils ont une structure de multiplet. Ce problème se produit dans les composés des métaux $3d$ et $4f$ car ces électrons sont fortement corrélés et localisés. DFT est une approximation de particules indépendantes et ne décrit pas correctement les corrélations électronique de ces orbitales localisées. En faisant abstraction de cette limitation, nous constatons un bon accord avec l'expérience. Le signal XMCD a également été calculé, après normalisation du XAS, et montre une amplitude non nulle. Ce qui indique une aimantation totale dans le GFO. Les règles de somme ont été utilisées pour déterminer les moments de spin et d'orbite par atome de Fe, et sont résumées dans le tableau 5.

**Table 5:** Comparaison des moments magnétiques de spin et d'orbitale (en $\mu_B$) et les spectres expémentaux.[79]

| | Théorique | Expérimentale[79] |
|---|---|---|
| $m_{spin} = \langle S_z \rangle$ | 0.777 | 0.870 |
| $m_{orb} = \langle L_z \rangle$ | 0.008 | 0.017 |

Pour conclure, cette thèse a été surtout consacrée à des développement de méthodes et de programmes numériques pour calculer les spectres d'absorption de rayons X et de XMCD. L'implémentation est faite dans un des codes *ab initio* de calcul de la structure électronique, parmi les plus rapides au monde. Nos programmes numériques seront disponibles pour la communauté scientifique de calcul de la structure électronique, pour déterminer le XAS et le XMCD des matériaux magnétiques les plus complexes.

Anant DIXIT

# Effets relativistes : applications aux matériaux multiferroïques


## Résumé

Notre étude porte sur des matériaux à effets relativistes importants. L'hamiltonien semi-relativiste, couplé aux équations de Maxwell (EM), permet de déduire les sources de courant et de densité, incluant des termes de second ordre (polarisations de spin et de Darwin). Différents modèles sont développés par expansion des EM. L'étude ab initio montre que (1) le désordre atomique peut produire le ferrimagnétisme (FM) dans GaFeO3 (GFO) multiferroïque, (2) les états 3d Fe des octaèdres déformés ont une levée de dégénérescence tétraédrique (théorie du champ cristallin), (3) la polarisation électrique concorde avec l'expérience, (4) le mécanisme magnétoélectrique (ME) direct est insuffisant pour expliquer le ME observé. Pour Cr2O3, le calcul de l'état massif sous contraintes biaxiales n'explique pas son FM, la taille de l'échantillon ou l'excès d'oxygène pourrait de fait être important. Enfin, nous avons développé le XAS et le XMCD dans le code VASP et calculé ces spectres pour GFO.


Mot-clés : Couplage spin-orbit, Multiferroïque, Gallium ferrite, Oxyde de chrome, Lagrange, dynamique des électrons semi-relativiste, Dirac Maxwell, XAS XMCD


## Résumé en anglais

We studied the physics of materials where relativistic effects are important. We first coupled the semi-relativistic Hamiltonian with the Maxwell's equations, and derived the current and density sources, which included second-order terms like the spin and Darwin polarizations. Different models were developed, by expanding the Maxwell's equations. We then performed ab initio studies to explain (1) site disorders as the origin of ferrimagnetism in multiferroic GaFeO3 (GFO), (2) crystal-field theory where the Fe 3d states at the deformed octahedra have tetrahedral splittings, (3) the electric polarization as a function of temperature, and (4) the insufficiency of the direct magnetoelectric (ME) mechanism to explain observed ME behavior. For Cr2O3, bulk calculations for different biaxial strains failed to explain its ferromagnetism, indicating that size or excess-O effects might be important. Finally, we implemented XAS and XMCD in VASP and computed these spectra for GFO.


Keywords: Spin Orbit Coupling, Multiferroic, Gallium Ferrite, Chromium Oxide, Lagrangian, Semi-relativistic Electron Dynamics, Dirac Maxwell, XAS XMCD